



Journal of INNOVATIVE SCIENCE and ENGINEERING

Volume 6
Issue 2
Year 2022

E-ISSN: 2602-4217

www.jise.btu.edu.tr

Image-Based Control of 2-DOF Ball Balancing System

Hüseyin Can GURSOY¹ , Nurettin Gökhan ADAR^{2*} 

^{1,2*} *Department of Mechatronics Engineering, Bursa Technical University, 16310 Bursa, TURKEY*

Abstract

In this study, the Ball-Plate stabilization system is designed to control with image processing algorithms. The position of the ball is aimed to control by tilting the plate on which the ball is located at a certain position and velocity. The system has two rotational degrees of freedom and is unstable. In the system, two DC motors are used as an actuator, and a camera is used as a feedback sensor. The camera captures the position of the ball and image processing algorithm calculates the that position to blance the plate..PID control is selected for servo motors. Thus, the position of the ball can be controlled so that it converges to the desired point on the plate. Real-time tests are conducted, and Maximum Overshoot and Steady State Error are calculated for both the x and y-axis, and results are given in figures. For the setpoint (15 cm, 15 cm) the Maximum Overshoot and Steady State Error were measured at 40.6% - 8% on the x-axis and 48.6% - 8.6% on the y-axis, while for the setpoint (10 cm, 10 cm) The Maximum Overshoot and Steady State Error were measured at 40.6% - 8% on the x-axis and 48.6% - 8.6% on the y axis.

Keywords: Ball&Plate, PID Control, Image Processing

Cite this paper as:

Gursoy C. H. and Adar, G. N. (2022).
*Image-Based Control of 2-DOF Ball
Balancing System*. Journal of Innovative
Science and Engineering.6(2):160-174

*Corresponding author: Nurettin Gökhan
Adar
E-mail: gokhan.adar@btu.edu.tr

Received Date:27/03/2022
Accepted Date:05/10/2022
© Copyright 2022 by
Bursa Technical University. Available
online at <http://jise.btu.edu.tr/>



The works published in Journal of
Innovative Science and Engineering
(JISE) are licensed under a Creative
Commons Attribution-NonCommercial 4.0
International License.

1. Introduction

Automatic control systems are an indispensable part of today's autonomous systems and are used in all areas where human beings develop technologically, such as input-output control of reactions in chemical and biological studies, power generation facilities, position and velocity control of aircraft in aviation, and space industries. Image processing is one of the important issues of our age, which gives very efficient results when used with automatic control systems. In recent years, these two phenomena have been used together, and visual servoing has been studied frequently in the engineering literature. The information needed by the control system can be obtained by using image processing techniques. By filtering the raw images taken from the camera and by performing mathematical operations, objects can be tracked and detected, and necessary information can be obtained. The Ball and Plate system is an example of visual servoing. The position information of the ball is obtained using the images. After processing the images necessary information is calculated to control the servo motors. The system tries to stabilize the ball by updating the information it receives from the camera.

Awtar et al. discuss the basic design and development of a classical Ball-Plate system according to mechatronic design principles. The realization of the design touches on basic facts such as cost, performance, and functionality. It studies a completely dynamic system review, hardware design, sensor and actuator selection, system modeling, parameter identification, and controller design for the top-plate system. The touchscreen is used to track the ball coordinate instead of the camera [1]. Brezina et al. discuss developing the classic Ball-Plate system. Different methods are tried to improve the system hardware and software. The study especially focuses on the effect of different image processing algorithms on cycle times and delays [2]. Itani designed a ball stabilization system using two Servo Motors, ARDUINO as a microprocessor and a camera for feedback. The transfer function was calculated by mathematical modeling of the system, and a PID controller was designed with a transfer function. The system was implemented in real-time, and the stability and efficiency of the system were shown with graphs [3]. Ho et al. designed both a real-time prototype and a virtual simulation of the Ball-Plate system. A detailed dynamic model of the system was created and the system was calculated with the coefficients obtained from the dynamic model. The accuracy of the system in the prototype and simulation were examined and compared [4]. Taifour et al. studied on a real-time system design for ball balancing on a single axis. In the system, a Servo Motor was used as an actuator, while an ultrasonic distance sensor was used for feedback and ARDUINO as a microcontroller. PID was preferred as the controller, and the study aims to experimentally measure the system response and stability according to the changing P, I, and D coefficients [5]. Kocaoğlu designed a Ball Beam system that aims to keep the ball at any selected point on the rod. The current state of the ball was measured by using different sensors, and the ball is displaced by changing the rod's angle through various motors. By applying different control algorithms, the positioning of the ball at the desired point was tried to be ensured appropriately. Settling time, maximum overshoot, and steady-state error were tried to be kept in optimum condition. The PID control method was applied, and the experimental setup was conducted [6]. Fabregas et al. focused on the variable set point for the Ball-Plate system in a simulation. While the position of the ball was usually controlled with a fixed point, the setpoint was changed to a certain trajectory (like a square, circle, or ellipse). Both ball position control and trajectory tracking were performed by different controllers [7]. Fan et al. designed a Ball-Plate system using the Hierarchical Fuzzy Control method. A setup of the system was designed, and the system was run in real-time. While an empty and flat plate was

used in general Ball-Plate systems, obstacles were placed on the plate in this study, and the ball was ensured to reach another point from a certain point. The trajectory of the ball was determined by the Fuzzy Logic Control method [8]. Chen et al. studied the control of Ball-Plate systems on a robot that moved on rough terrain instead of on a fixed ground. The design of a walking robot with 6 parallel legs and the mathematical model of the movement were combined with the model of the classical Ball-Plate system. An experimental setup was conducted, and the system was examined in real-time [9]. Chi-Cheng et al. manufactured the plate of ball balancing system move with a design different from classical methods. Ball coordinates were obtained with image processing algorithms. To stabilize the plate, a manipulator with two degrees of freedom was preferred rather than a Servo Motor. Linear Quadratic Regulator (LQR) was designed as the controller, and experimental studies were performed to increase the stability of the system [10].

Park and Lee, used a 6-degree-of-freedom Robot Manipulator as an actuator to move the plate instead of servo motors. Ball coordinates are obtained with Image Processing algorithms. The experimental setup is implemented in real-time [11]. Kassem et al designed a Ball-Plate system using the 6 DOF Stewart Platform. PID, LQR, Sliding Mode, and Fuzzy Logic Controller are used separately to control the ball position in the system. Four control methods are compared in terms of efficiency and accuracy when the system is being operated both for a fixed setpoint and for following a trajectory. The system is tested both in the simulation and on the experimental setup [12].

In this study, the position of the ball on the plate with two degrees of freedom was automatically controlled with image processing techniques. The system consisted of two Servo motors, a camera, a controller, a plate, and mechanical parts that enable the system to move. Servo Motors rotated the plate in two different axes, and the ball could move as the force (gravity) acting on the ball changes. To calculate the change in the position of the ball against the angle change of the motors, the mathematical modeling of the system was derived, and the Transfer Function was obtained. A PID-based controller was designed using the transfer function. The position information of the ball was obtained by using image processing algorithms through a camera placed on the system, and this coordinate was used as feedback. Maximum Overshoot and Steady State Error were calculated for both the x and y axes, and the results are given in figures.

2. Materials and Methods

2.1. Experimental Setup and Mathematical Model of Ball Balancing Table

The experimental setup of the ball-plate system consisted of the servo motors, Arduino Uno, camera, and mechanical parts, and was given in Figure 1. TowerPro MG996 servo motors were used as actuators. HXSJ A870 webcam having a resolution of 640x480 pixels was preferred, and a connection was established via the USB port. The top plate was made of 30x30x3 mm wood. Mechanical parts were manufactured by using the additive manufacturing technique with PLA filament at 80% fill rate and 0.2 mm layer thickness. The system was an example of an electromechanical system, and its mathematical modeling was examined, and the transfer function of the system was calculated to design a controller.

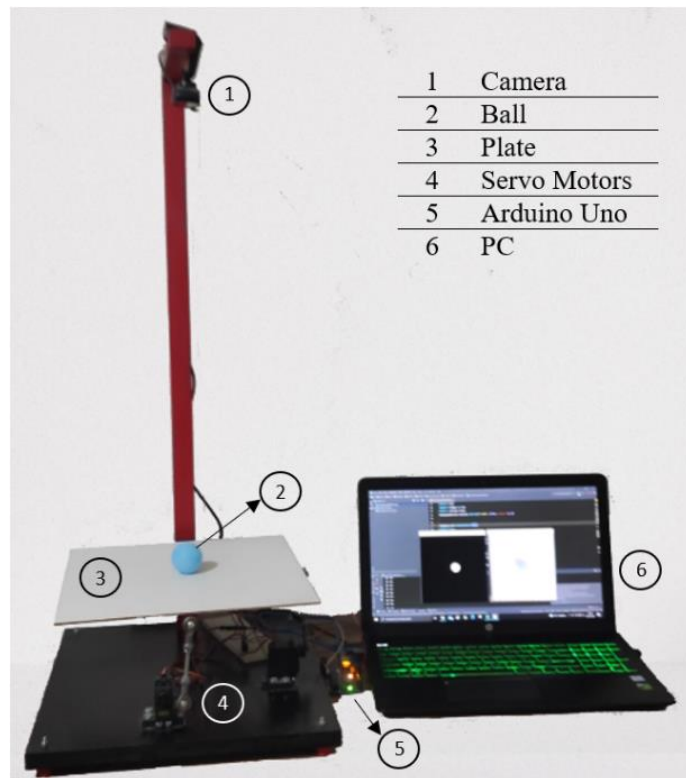


Figure 1. Experimental Setup

The plate on which the ball was located can move in two axes. However, since both axes were symmetrical with respect to each other, their dynamic equations were considered the same, and the system could only be modeled on one axis [11]. Therefore, the mathematical modeling and transfer function were calculated only for the x-axis. The ball and plate system model was presented in Figure 2.

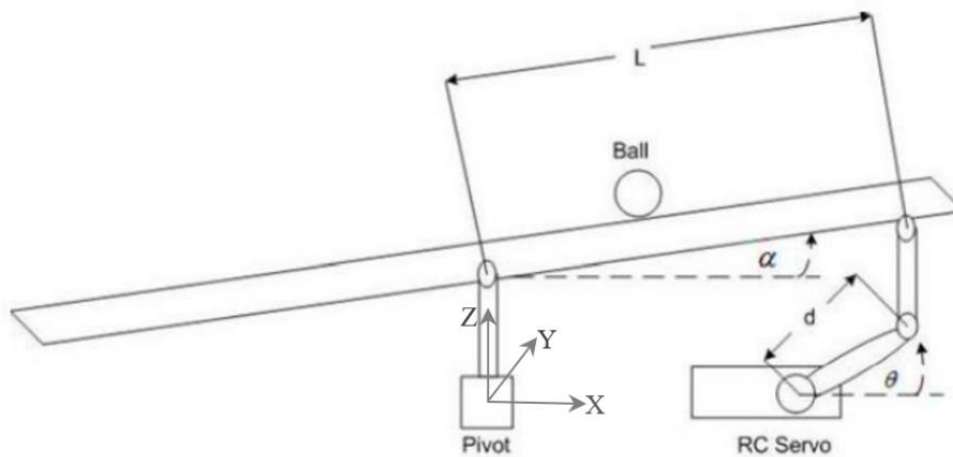


Figure 2. Dynamic Model of the System (x-axis) [3]

The parameters of the system are given in Table 1.

Table 1. Parameters of The System

Parameters	Value
$m_b(\text{kg})$	0.0025
$r_b(\text{m})$	0.02
$g(\text{m/s}^2)$	9.81
$I_b(\text{kg.m}^2)$	3.2×10^{-6}
$L_p(\text{m})$	0.3
$r_a(\text{m})$	0.024

In this study, the dynamical model of the system is derived with Euler-Lagrange Equations.

$$\frac{d}{dt} \left(\frac{\partial \mathcal{L}}{\partial \dot{q}_i} \right) - \frac{\partial \mathcal{L}}{\partial q_i} = Q_i \quad (1)$$

and the Lagrangian is as:

$$\mathcal{L} = T - V \quad (2)$$

where T is Kinetic Energy, and V is the Potential Energy of the system, respectively.

The kinetic energy of a ball and the table are calculated as follows:

$$T_b = \frac{1}{2} [m_b(\dot{x}_b^2 + \dot{y}_b^2) + \frac{I_b}{r_b^2}(\dot{x}_b^2 + \dot{y}_b^2)] = \frac{1}{2} (m_b + \frac{I_b}{r_b^2})(\dot{x}_b^2 + \dot{y}_b^2) \quad (3)$$

$$T_p = \frac{1}{2} (I_p + I_b)(\dot{\alpha}^2 + \dot{\beta}^2) + \frac{1}{2} m_b(x_b^2 \dot{\alpha}^2 + 2x_b \dot{\alpha} y_b \dot{\beta} + y_b^2 \dot{\beta}^2) \quad (4)$$

where T_b is the kinetic energy of the ball, T_p is the kinetic energy of plate, m_b is the mass of the ball, r_b is the radius of the ball, x_b is the position of the ball on the x-axis, y_b is the position of the ball on the y-axis, \dot{x}_b is the velocity of the ball on the x-axis, \dot{y}_b is the velocity of the ball on the y-axis, I_b is the ball's moment of inertia, I_p is the moment of inertia of the plate, α is the angle of the plate on the x-axis, and β is the angle of the plate on the y-axis.

The total kinetic energy of a system is a sum of the kinetic energy of a ball and the kinetic energy of a table and is as follows:

$$T = T_b + T_p = \frac{1}{2} (m_b + \frac{I_b}{r_b^2})(\dot{x}_b^2 + \dot{y}_b^2) + \frac{1}{2} (I_p + I_b)(\dot{\alpha}^2 + \dot{\beta}^2) + \frac{1}{2} m_b(x_b^2 \dot{\alpha}^2 + 2x_b \dot{\alpha} y_b \dot{\beta} + y_b^2 \dot{\beta}^2) \quad (5)$$

The total Potential Energy of a system occurs with the ball because the reference is selected as the pivot point of the plate. The potential energy of the system is calculated:

$$V_b = m_b g h = m_b g (x_b \sin \alpha + y_b \sin \beta) \quad (6)$$

where g (m/s^2) is gravity.

Using Equations (5) and (6), The Lagrangian is expressed as:

$$\begin{aligned} \mathcal{L} = & \frac{1}{2} \left(m_b + \frac{I_b}{r_b^2} \right) (\dot{x}_b^2 + \dot{y}_b^2) + \frac{1}{2} (I_p + I_b) (\dot{\alpha}^2 + \dot{\beta}^2) \\ & + \frac{1}{2} m_b (x_b^2 \dot{\alpha}^2 + 2x_b \dot{\alpha} y_b \dot{\beta} + y_b^2 \dot{\beta}^2) - m_b g (x_b \sin \alpha + y_b \sin \beta) \end{aligned} \quad (7)$$

Equations (8), (9), and (10) are calculated by taking the derivatives of Equation (7) according to the time, the position of the ball, and the velocity of the ball.

$$\frac{\partial \mathcal{L}}{\partial \dot{x}_b} = \left(m_b + \frac{I_b}{r_b^2} \right) \dot{x}_b \quad (8)$$

$$\frac{\partial}{\partial t} \frac{\partial \mathcal{L}}{\partial \dot{x}_b} = \left(m_b + \frac{I_b}{r_b^2} \right) \ddot{x}_b \quad (9)$$

$$\frac{\partial \mathcal{L}}{\partial x_b} = m_b (x_b \dot{\alpha} + y_b \dot{\beta}) \dot{\alpha} - m_b g \sin \alpha \quad (10)$$

If the equations (9) and (10) are substituted into equation (1) and rearranged, the dynamical model of the system is obtained as:

$$\left(m_b + \frac{I_b}{r_b^2} \right) \ddot{x}_b - m_b (x_b \dot{\alpha} + y_b \dot{\beta}) \dot{\alpha} + m_b g \sin \alpha = 0 \quad (11)$$

Equation (11) is a non-linear mathematical model. To derive the Transfer Function of the system, linear model is needed. The small deviation of α and β in Equation (12) is linearized as:

$$\left(m_b + \frac{I_b}{r_b^2} \right) \ddot{x}_b + \frac{m_b g r_a}{L_p} \theta_x = 0 \quad (12)$$

Since the system is symmetrical, the mathematical model of the y-axis is the same as the x-axis and is as follows:

$$\left(m_b + \frac{I_b}{r_b^2} \right) \ddot{y}_b + \frac{m_b g r_a}{L_p} \theta_y = 0 \quad (13)$$

When the Laplace transform is applied to the expression in Equation (12) and $X_b(s)$ and $\theta_x(s)$ are selected as output and input of a system, the transfer function of a system is calculated as:

$$P(s) = \frac{\text{output}}{\text{input}} = \frac{X_b(s)}{\theta_x(s)} = -\frac{m_b g r_a}{L_p(m_b + \frac{I_b}{r_b^2})s^2} \frac{\text{rad}}{\text{m}} \quad (14)$$

According to the parameters in Table 1, the transfer function is defined as:

$$\text{TF} = G(s) = \frac{0.107 \text{ deg}}{s^2 \text{ cm}} \quad (15)$$

The servo motor was worked in real-time and the data set was obtained as input voltage and output velocity. Using this data, the transfer function of the servo motor was calculated as follows:

$$G_M(s) = \frac{\vartheta(s)}{V_M(s)} = \frac{K_M}{\tau s + 1} = \frac{100}{0.01s + 1} \quad (16)$$

where K_M is the motor gain coefficient, and τ is the time constant of the motor.

2.1.1. PID Controller Design

The mathematical model of the PID controller is as follows:

$$u(t) = K_p e(t) + K_i \int_0^t e(s) ds + K_d \frac{de(t)}{dt} \quad (17)$$

where $u(t)$ is the output of the controller, $e(t)$ is the control error, K_p is the proportional coefficient, K_i is the integral coefficient, and K_d is the derivative coefficient.

The closed-loop block diagram of the system is given in Figure 3 where $G(s)$, and $G_M(s)$ is the system's and servo motor's transfer functions. PD controller is selected to control the system.

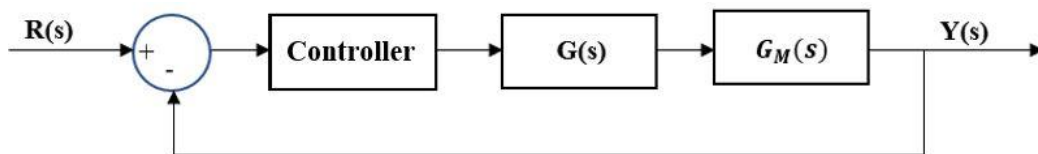


Figure 3. Closed-Loop Block Diagram of the System

The close-loop transfer function and the characteristic equation of the system are given below in Equation (18) and Equation (19), respectively. If the denominator of the closed-loop transfer function is set to zero, the characteristic equation is calculated as follows:

$$\frac{Y(s)}{R(s)} = \frac{(K_p + K_d s)(G(s))(G_M(s))}{1 + (K_p + K_d s)(G(s))(G_M(s))} \quad (18)$$

$$0.01s^3 + s^2 + 10.7K_d s + 10.7K_p = 0 \quad (19)$$

Since the characteristic equation in (19) is the third order and the general characteristic equation formula is the second order, the factor $(a*s + b)$ is added to the general characteristic equation.

$$P_D(s) = (as + b) (s^2 + 2\xi\omega_n s + \omega_n^2) \quad (20)$$

where ξ is the damping ratio, and ω_n is the undamped natural frequency.

“ ξ ” and “ ω_n ” values are calculated using “overshoot” and “settling time” parameters. The overshoot value and the settling time are chosen as %2 and 1 second, respectively. The ξ is calculated as 0.7797 and the ω_n value as 5.12. Since the ξ is less than 1, it is expected that the system will oscillate and reach the set point. With the calculated values, the formula is rearranged, and Equality (21) is obtained as follows:

$$P_D(s) = s^2 + 8s + 26.32 \quad (21)$$

$$P_C(s) = P_D(s) \quad (22)$$

If the equality in (22) is achieved and both equations are equalized, a, b, K_p , and K_d coefficients are obtained as follows:

$$a=0.01 \quad b=0.92 \quad K_p = 2.45 \quad K_d = 0.69 \quad (23)$$

As obtained in Equation (23), the “ K_p ” value was 2.45, and the “ K_d ” value was 0.69. While the system was running, steady-state error was always detected because of the friction forces that were neglected while creating the dynamic model of the system and the gaps in the mechanical connections. The “I” coefficient of the PID works to eliminate this continuous steady-state error. Therefore, the controller was designed as PD, but the “I” coefficient was experimentally optimized and used as $K_i=0.03$.

2.2. Image Processing

Image processing is a set of operations for making meaningful inferences from an image. These operations are obtained by using mathematical operations to be performed on the pixels that make up the image. With different algorithms, a lot of information can be obtained from the image and used for different purposes such as control of the mechatronics systems. In this study, image processing is used for object recognition and object tracking. Algorithms are written on the PYTHON.

2.2.1. Color Spaces and Masking

To analyze the concept of color in the digital world and to correspond to a mathematical equivalent, there is more than one characterization method. Each of these methods is called Color Space. Each Color Space is used for different

purposes. The raw image obtained from the camera is in “RGB” Color Space format. In this format, each color is obtained as a result of combining the red, green, and blue colors in different proportions.

However, since different light sources was used in the study, a Color Space with the light intensity (brightness) parameter was chosen. “HSV” Color Space format was selected to solve this problem. In this format, each color was expressed in terms of hue, saturation, and brightness. In this way, different brightness values could be detected, and a protection algorithm could be written in response to light level changes. The ball on the table image from the camera was in “RGB” format. Then the image was converted form “”RGB” to “HSV” format, and was given in Figure 4.

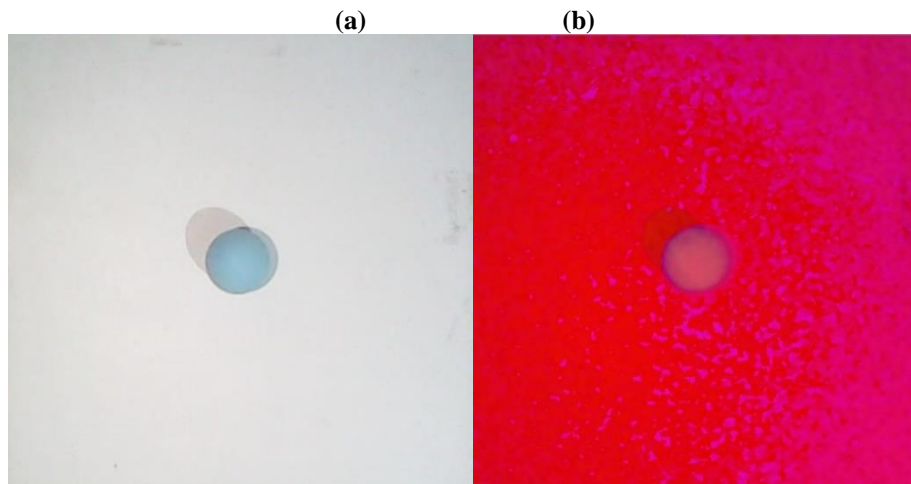


Figure 4. a) “RGB” Color Space Image b) “HSV” Color Space Image

In ideal light conditions, the average “HSV” values in pixels containing the ball were measured as (102, 67, 216), respectively. “HSV” threshold values were determined to operate system in different light conditions. . This process was calculated by experimentally measuring the “HSV” values of the pixels of the ball under different light conditions like unstable brightness levels, changeable light color and intensity. Measurements were made under the extreme conditions that could occur, and a more stable algorithm was established in this way. These threshold values were limited to a minimum of (90,50,50) and a maximum of (110, 255, 255) to be “H”, “S”, and “V”, respectively.

To make edge detection operations easier, masking was done with the determined threshold values. The purpose of masking was to make the pixel values of different surface pixels more observable. Pixels within the range (ball) were obtained in white, and pixels out of the range (plane) were obtained in black. Figure 5 shows the image with the masking process.

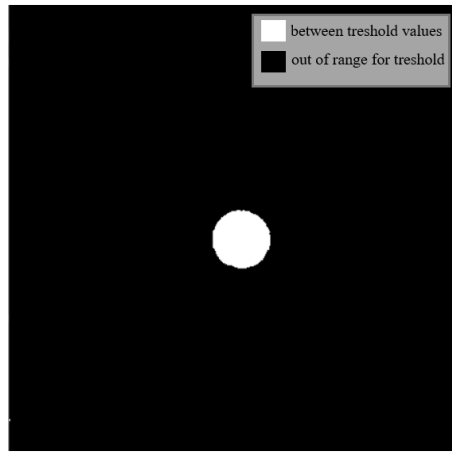


Figure 5. Masked Image

2.2.2. Coordinate Detection

The ball coordinates, which was input to the control algorithm and then used as feedback, were obtained at this stage. To obtain the position information of the ball, the boundaries between the ball and the ground were determined. An edge detection algorithm was used to determine the boundaries. This process was done by frequency analysis and the separation of color regions of different intensities. The function detected the sudden color transition from 0 black pixels to 255 white pixels as border pixels. In this way, the white ball in the image was separated from the black background. The border-image of the spherical ball in the 2D image was a regular circle, and the center point of this circle was the desired coordinate information. To find the center point of the circle, the smallest rectangle that could contain the borders drawn. This rectangle was a square. The center point of the drawn square could be accepted as the center point of the circle. In this way, the coordinate information of the center point of the ball was calculated. In Figure 6, there is the image of the ball whose coordinate was found.



Figure 6. The Center Point of The Ball

3. Results and Discussion

The real-time image taken from the camera is processed with image processing algorithms. The first of these algorithms is pre-processing. The image is resized to the desired size and converted from “RGB” color space to “HSV” format. Then, maximum and minimum threshold values are obtained using the experimentally measured “HSV” pixel values of the ball. Masking processing is done by using threshold values. Finally, the edges of the ball are found by an edge finder function that performs frequency analysis of the pixel values in the masked, black and white image. The center point of the ball is obtained from the found edges.

The input of the transfer function is calculated in “cm” as length units. However, the ball coordinate information is obtained as pixel size. Therefore, an appropriate conversion is made from the pixel size to the length dimension. The 30x30 cm sized plate is measured as 440 pixels in the image from the camera, and the coordinate information is multiplied by a calculated coefficient and converted to “cm”. The coefficient is found as “0.0682” by doing 30 cm divided by 440 pixels.

The position information of the ball is sent to two separate PID controllers for the x and y axes, and the angle values of the servo motors are obtained at the controller output. The whole system works in real-time. The general block diagram of the system is given in Figure 7.

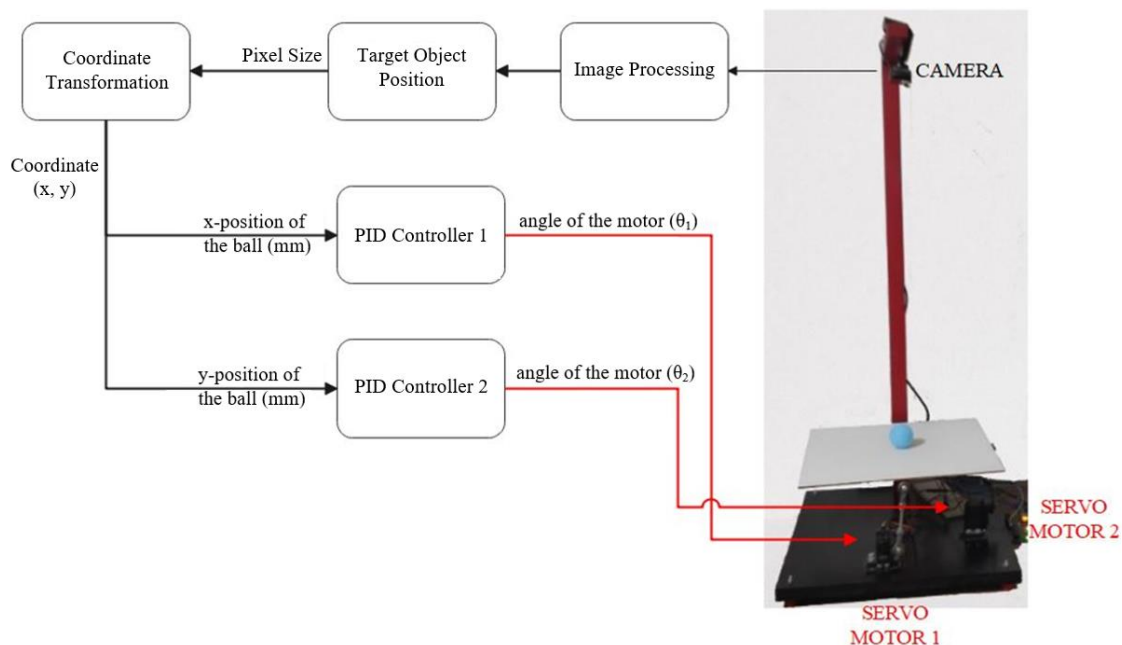


Figure 7. General Block Diagram of System

The K_p and K_d values calculated in Equation (22) are theoretical values that are found for optimum operating conditions in the system. However, the system does not work satisfactorily with these calculated values in real-time. While creating the dynamic model of the system, some forces such as friction were ignored, and it was assumed that the ball would move without slipping. The gap in the structure of the U-joint used at the pivot point caused some losses and errors.

Therefore, the theoretically calculated PID coefficients are different from the most ideal coefficients in practice. The parameters which the system can operate in the most optimized way in practice are tested on the PID controller and are obtained as $K_p=2.1$, $K_d=1.1$, and $K_i=0.03$. In theory, a “PD” controller is designed, but since a “steady-state error” is encountered in the system, a PID controller is used in practice by adding the “integral value (K_i)”.

In the real-time system, the position graphs of the ball are obtained for different setpoints. In Figure 8 and Figure 9, there are position-time graphs on the x-axis and y-axis of the ball that the setpoint is set to be in the middle of the plate (15 cm, 15 cm). In this graph, the Maximum Overshoot for the X-axis is 40.6%, and the Steady State Error is 8%, while the Maximum Overshoot for Y-Axis is 48.6%, and the Steady-State Error is 8.6%.

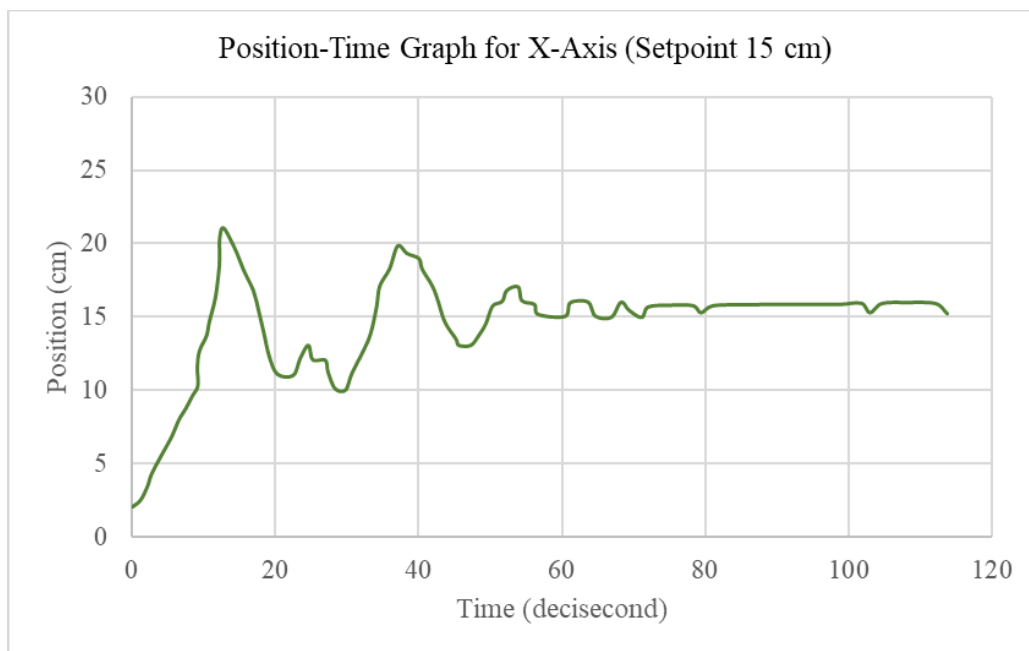


Figure 8. Position-Time Graph for x-Axis (Setpoint 15 cm)

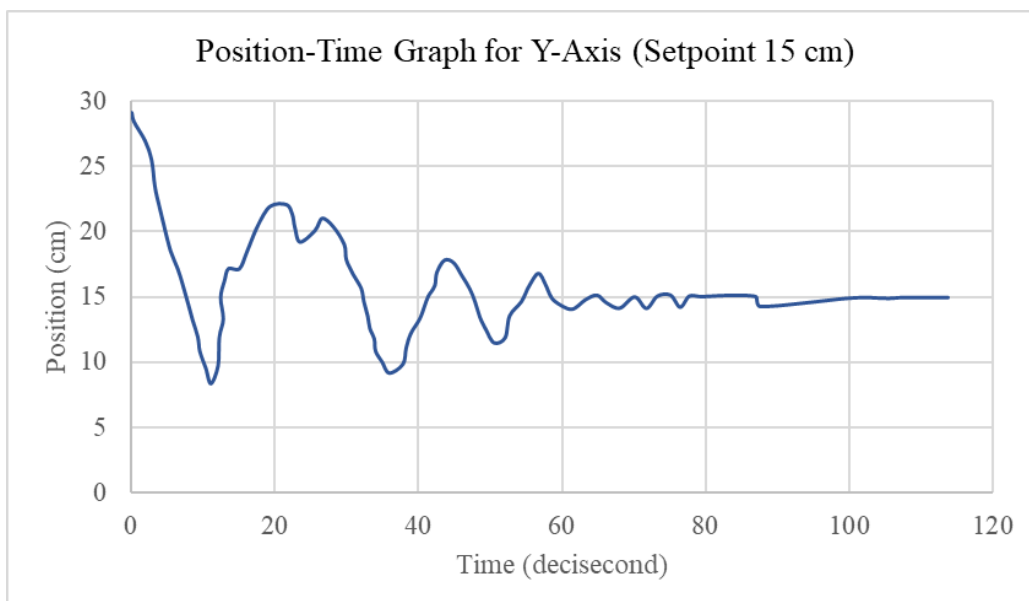


Figure 9. Position-Time Graph for y-Axis (Setpoint 15 cm)

In Figure 10 and Figure 11, there are position-time graphs of the ball on the x-axis and y-axis where the setpoint is set at 10 cm for the x-axis and 10 cm for the y-axis. The Maximum Overshoot for the x-axis is 25%, and the Steady State Error is 5%, while the Maximum Overshoot for y-Axis is 49.5%, and the Steady State Error is 6%.

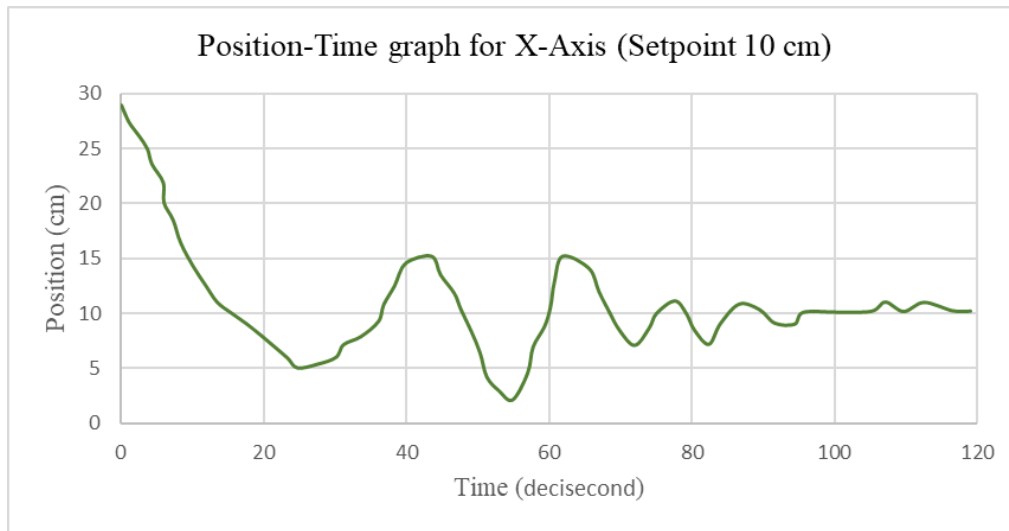


Figure 10. Position-Time Graph for x-Axis (Setpoint 10 cm)

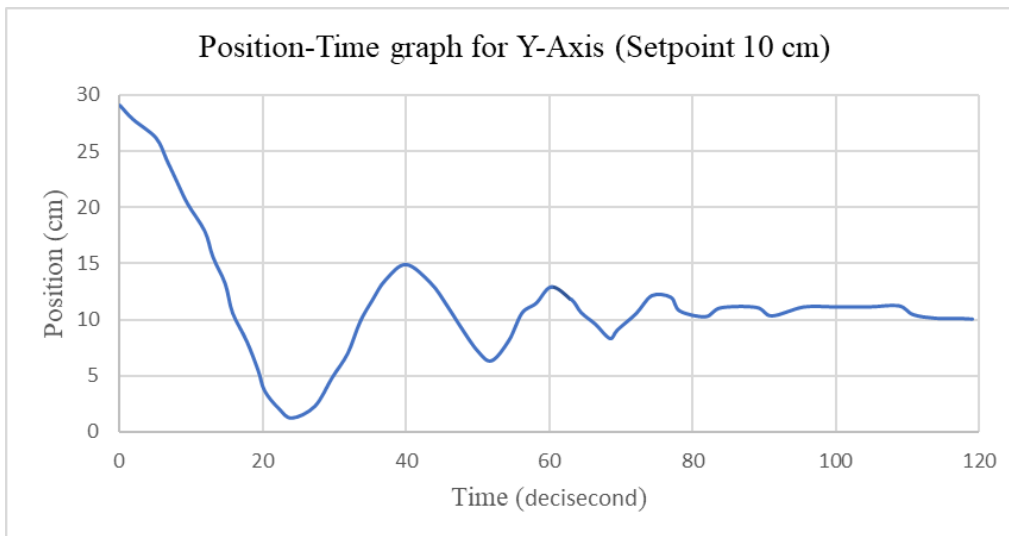


Figure 11. Position-Time Graph for y-Axis (Setpoint 10 cm)

4. Conclusions

In this study, a ball balancing system was designed by using image processing. The system included two Servo Motors as an actuator and a camera as a feedback sensor. The instantaneous coordinates of the ball were found by processing the image taken from the camera.

The dynamic model of the system was calculated using Lagrange-Euler Equations and the transfer function was obtained to compute the PD coefficients. A PD controller was designed with $K_p = 2.45$ and $K_d = 0.69$. In the real-time

implementation, the PD controller was not satisfied. Thus PID controller was selected as $K_p = 2.45$, $K_d = 0.69$ and $K_i = 0.003$.

The time-dependent position of the ball was given with figures for each setpoint. When the setpoint was given as the midpoint of the plate, Maximum Overshoot was 25%-49.5%, and the Steady State Error was 5%-6% in the x and y axes, respectively.

The gaps in the U-joint used in the system cause the plate to rotate around its axis. This important mechanical problem causes the system not to work stably in the regions far from the center. If the mechanical problem is eliminated, the system will operate more stable.

NOMENCLATURE

α	: Slope of the plate at x-axis
β	: Slope of the plate at y-axis
m_b	: Mass of the ball
r_b	: Radius of the ball
x_b	: Position of the ball at x-axis
y_b	: Position of the ball at y-axis
\mathcal{L}	: Lagrange
q_i	: Joint variable
T	: Kinetic energy of the system
V	: Potential energy of the system
Q	: Generalized forces
T_b	: Kinetic energy of the ball
I_b	: Inertia moment of the ball
x_b'	: Linear velocity of the ball at the x-axis
y_b'	: Linear velocity of the ball at the y-axis
w_x	: Angular velocity of the ball at the x-axis
w_y	: Angular velocity of the ball at the y-axis
r_a	: Arm length of the servo motor
L_p	: Length of the plate
θ_x	: Angle of the servo motor
ξ	: Damping ratio
ω_n	: Undamped natural frequency
t_s	: Settling time

References

- [1] Awtar, S., Bernard, C., Boklund, N., Master, A., Ueda, D., Craig K. (2002). Mechatronic Design Of A Ball-On-Plate Balancing System. *Mechatronics*, 12(2), 217-228 p.
- [2] Brezina, A., Tkacik, M., Tkacik, T., Jadlovska S. (2019). Upgrade of the Ball and Plate Laboratory Model. *IFAC-PapersOnLine*, 52(27), 277-282 p.
- [3] Itani, A. (2017). Ball Plate Balancing System Using Image Processing.
- [4] Ho, M., Rizal, Y., Chu, L. (2013). Visual Servoing Tracking Control of a Ball and Plate System: Design, Implementation and Experimental Validation. *International Journal of Advanced Robotic Systems*, 10(7).
- [5] Taifour, A., Ahmed, A., Almahdi, H., Osama, A., Naseraldeen, A. (2017). Design and Implementation of Ball and Beam System Using PID Controller. *Automatic Control and Information Sciences*, 3(1), 1-4 p.
- [6] Kocaoğlu, S. (2013). Pıd Kontrollü Top Çubuk Sisteminin Tasarımı ve Kontrolü Üzerine Bir Araştırma.
- [7] Fabregas, E., Chacón, J., Dormido-Canto, S., Farias, S., Dormido G. (2015). Virtual Laboratory of the Ball and Plate System. *IFAC-PapersOnLine*, 48(29), 152-157 p.
- [8] Fan, X., Zhang, N., Teng, S. (2004). Trajectory Planning And Tracking Of Ball And Plate System Using Hierarchical Fuzzy Control Scheme. *Fuzzy Sets and Systems*, 144(2), 297-312p.
- [9] Chen, Z., Gao F., Sun, Q., Tian, Y., Liu, J., Zhao, Y. (2019). Ball-on-plate motion planning for six-parallel-legged robots walking on irregular terrains using pure haptic information. *Mechanism and Machine Theory*, Volume 141, 136-150 p.
- [10] Chi-Cheng, C., Tsai, C. (2016). Visual Servo Control for Balancing a Ball-Plate System. *International Journal of Mechanical Engineering and Robotics Research*, 5(1).
- [11] Park, J., Lee, Y. (2003). Robust Visual Servoing For Motion Control Of The Ball On A Plate. *Mechatronics*, 13(7), 723-738 p.
- [12] Kassem, A., Haddad, H., Albitar, C. (2015). Comparison Between Different Methods of Control of Ball and Plate System with 6DOF Stewart Platform. *IFAC-PapersOnLine*, 48(11), 47-52 p.
- [13] Gözde, H. (2019). Evolutionary Computation Based Control For Ball And Plate Stabilization System. *Balkan Journal Of Electrical & Computer Engineering*, 7(1), 45-46 p.
- [14] Kuo, B. (1999). *Otomatik Kontrol Sistemleri*, Litaratür, 7th edition, 88-90 p. ISBN:975-8431-64-1.

The Structural Characterization, Radioluminescence Results, and Thermoluminescence Kinetic Parameters of Aventurine

Ilker Cetin KESKIN^{1*} 

^{1*} Department of Electricity and Energy, Soma Vocational School, Manisa Celal Bayar University, Soma 45500, Manisa, Turkey.

Abstract

In this study, in which the optical and luminescence properties of aventurine, a silicate-based mineral, were examined, the crystal structure of the mineral was examined by XRD analysis, its rheological properties and the elements it contained were determined by SEM-EDX analysis, and its structural properties were examined by FT-IR analysis. In order to determine the luminescence properties, radioluminescence (RL) and thermoluminescence (TL) methods were used and kinetic parameters were calculated. In the measurements taken in bulk and powder form of Aventurine, it was observed that the powder sample had a much better spectrum intensity, it was observed that the emission around 570 nm became much more pronounced in the powder sample. On the other hand, similar emissions were detected in both samples, though at different intensities. In TL analysis, it was observed that Aventurine was responsive to both X-ray and ultraviolet radiation at three different doses. While after X-ray irradiation, Aventurine exhibited TL glow curves with peaks at maximum temperatures of 90 oC and 250 oC, under UV irradiation the TL glow curves concentrated in the high-temperature region which is around 300 oC observed. Also; the TL kinetic parameters were reported; activation energy (E), the order of kinetics (b), and frequency factor (s) of the first peak have been determined in detail by using Computerized Glow Curve Deconvolution (CGCD) method.

Keywords: Quartz, Structural Characterization, Thermal Analysis Radioluminescence (RL), Thermoluminescence (TL)

Cite this paper as:

Keskin, Ç. I. (2022). *The Structural Characterization, Radioluminescence Results, and Thermoluminescence Kinetic Parameters of Aventurine*. Journal of Innovative Science and Engineering.6(2):175-189

*Corresponding author: Ilker Cetin Keskin
E-mail: ilker.keskin@cbu.edu.tr

Received Date:13/04/2021
Accepted Date:03/06/2022
© Copyright 2022 by
Bursa Technical University. Available
online at <http://jise.btu.edu.tr/>



The works published in Journal of Innovative Science and Engineering (JISE) are licensed under a Creative Commons Attribution-NonCommercial 4.0 International License.

1. Introduction

Aventurine is a mineral that has been used for many years as a glazing material. Aventurine, which is a silicon-based (SiO_2) mineral, contains elements such as chromium, iron, magnesium, aluminum, and potassium, but also contains trace amounts of different elements. Aventurine, a type of quartz, is found in nature in green, orange, gray, and blue tones. Aventurine, which is frequently seen in green examples, has a granular structure with metallic lusters. It has a scaly appearance, has a microcrystalline structure, and also contains hematite and mica. Due to its silicate structure, it shows different colors depending on the number of impurity atoms that serve as color centers in the crystal structure. When we look at the studies on aventurine, it is seen that there are some characterization studies in general terms, but there are intense thermal studies on this mineral because it is widely used as a glazing material [1–4].

In a study on Beryl, one of the silicate group minerals, it was reported that it has a wide emission range between 300 and 800 nm, with maximum peaks around 470 nm and 580 nm in the cathodoluminescence (CL) spectrum. It has been stated that the Cr^{3+} ion plays an important role in the color centers of the green-colored beryl mineral [5]. In the study on chalcedony, one of the most well-known minerals of the quartz family, a maximum TL peak was recorded at 110 °C for white chalcedony and 121 °C for blue chalcedony in the TL studies taken after X-ray excitation [6]. In TL measurements taken after irradiation of onyx mineral, which is also a variation of chalcedony, with gamma radiation, peaks were detected at 150 and 210 °C [7].

Since aventurine is a feldspar group and a mineral found in different colors in nature and used as a glaze material by heat treatment, the effect of the presence of color centers on the optical properties (radioluminescence) of the mineral is interesting for research. On the other hand, the investigation of thermoluminescence properties, which occur as a result of the thermal effect of interaction with radiation, gives a different perspective to the optical properties of aventurine minerals.

In this study, unlike the literature, the optical and luminescence properties of aventurine are emphasized. In terms of luminescence, it has been observed that it has a strong thermoluminescence response due to radiation excitation. In addition, some characterization analyzes are also included. Radioluminescence and thermoluminescence properties of aventurine samples excited by X-ray and short-wavelength ultraviolet radiation were examined and kinetic parameter calculations were made on the glow curve. As stated above, no dosimetric and optical characterization studies of aventurine have been found in the literature. The sample used in the study was obtained commercially and is known to have been mined from the Mysore region of India.



Figure 1. Bulk and powder form Aventurine.

Figure 1 shows the bulk and powder forms of aventurine minerals. In the press used for pellet preparation, the mechanically crushed mineral was powdered and sieved with a pore size of 150 microns. A powder sample was used in all analyzes. In order to compare the RL emissions of both, the bulk sample was also analyzed in the RL measurement only. In our previous studies on minerals, it was observed that better luminescence results were obtained from powdered samples.

2. Materials and Methods

PANalytical Empyrean brand X-ray diffraction (XRD) device was used to determine the crystal structure of aventurine and to determine the major or minor phases present. The step scan range was determined as 10° – 80° when the XRD pattern was taken from the powdered aventurine sample. Working conditions of diffractometer; current is determined as 40 mA and voltage as 45 kV. The X-ray source of the device has a Cu-K α anode and has a wavelength of 1.5405 Å. The FTIR spectra were carried out with a potassium bromide (KBr) disc for absorbance in the region 400 – 4000 cm^{-1} using a Perkin Elmer Spectrum 100 FTIR spectrophotometer. Gemini SEM500 device was used to examine the surface morphology and to obtain EDX spectrum of the aventurine.

TL glow curves of the aventurine exposed to short-wavelength UV light (254 nm) and X-rays were recorded in the range of 50 $^{\circ}\text{C}$ to 400 $^{\circ}\text{C}$ in a dark room with an RA94 Reader / Analyzer system in N_2 atmosphere. In order to obtain the TL glow curve of the powder sample, thin aluminum pots prepared in a way that would not create a surface gap with the thermocouple in the sample room of the device were used. The TL responses of aventurine according to different excitation were taken at a heating rate of 2 $^{\circ}\text{C}/\text{s}$ after 10, 20, and 30 min irradiation for both sources.

In the radioluminescence (RL) system, the X-rays obtained from the tungsten target by operating the Machlett OEG-50A X-ray tube at 30 kV and 15 mA, which have a dose value of 30 Gy per minute, are directed to the sample. The occurring scintillation is transmitted to the Jobin Yvon spectrophotometer thanks to the optical path positioned at an angle. Signals are collected by a CCD (Charge Coupled Device) detector cooled with liquid nitrogen, and the luminescence spectrum is obtained by this process.

3. Results and Discussion

3.1. XRD Analysis of Aventurine

The X-ray diffraction (XRD) pattern and phase analysis of the aventurine was performed and represented in Figure 2. Quartz is a non-clay mineral commonly and invariably found in all specimens. Aventurine is a silicate-based mineral. The result of phase analysis for aventurine powder X'Pert Highscore Plus program was matched that planes of the hexagonal Silicon Dioxide (SiO_2) such as (010), (011), (111), (112), (121), and (220) with XRD pattern of aventurine. In addition, low-intensity phases of cubic Fe^{2+} and tetragonal CrO_2 referred to with ICSD cards no (96-900-6607) and (01-076-1232) respectively, were detected in the XRD pattern.

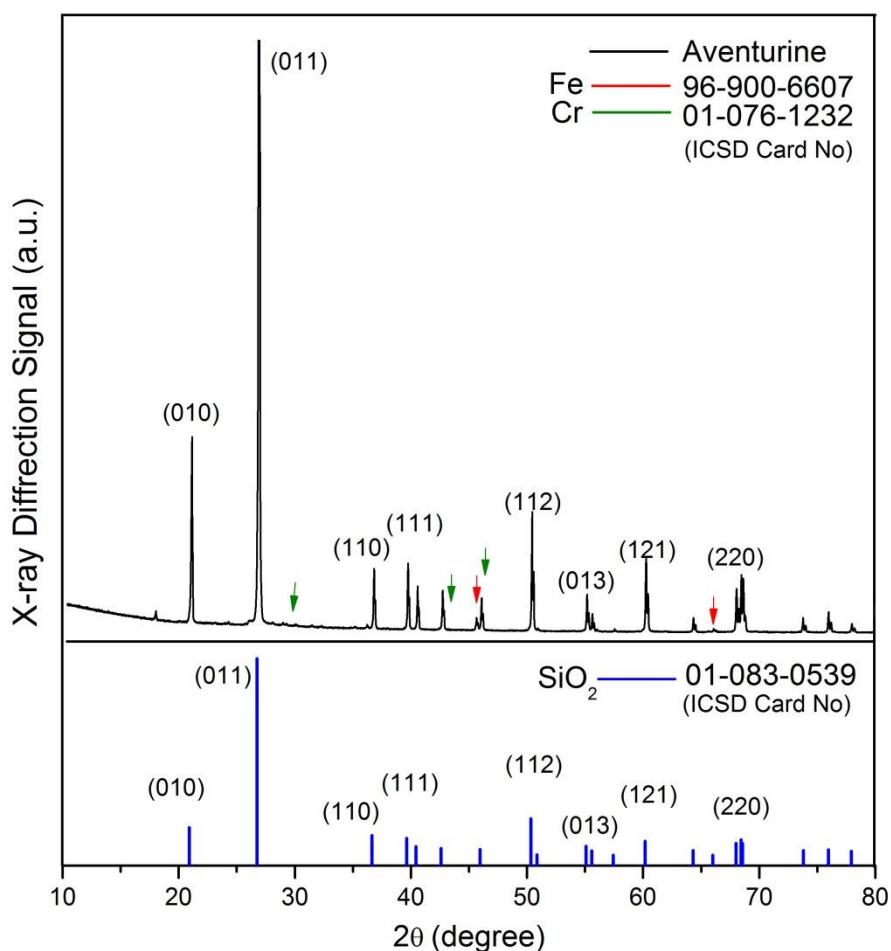


Figure 2. X-ray diffraction (XRD) pattern of aventurine.

The Debye-Scherrer's equation was used to calculate the average crystallite sizes of aventurine powder (1):

$$D = \frac{k\lambda}{\beta \cos\theta} \quad (1)$$

where D is the crystallite size (nm), $k=0.94$, $\lambda_{\text{Cu}} = 0.15406$ nm, β is the full width at half-maximum of the peak in radians corrected from instrumental broadening, and θ is the peak angle [6,8]. To calculate the average crystallite size,

(011) plane of the XRD pattern was used because of it has strongest intensity. The average crystallite size was found 90.57 nm. The data used for calculation; Peak max (2θ): 26.5517221, θ_2 : 26.5912564, θ_1 : 26.4971291, FWHM: 0.0941273, Cos (θ): 0.973276.

3.2. FT-IR Spectrum of Aventurine

Figure 3 shows the FTIR spectrum of aventurine. In accordance with the literature, the marked peaks which are Si-O interactions and the band assignment peaks of Al and Mg in the structure of the quartz-based aventurine mineral were specified. The findings are listed in Table 1.

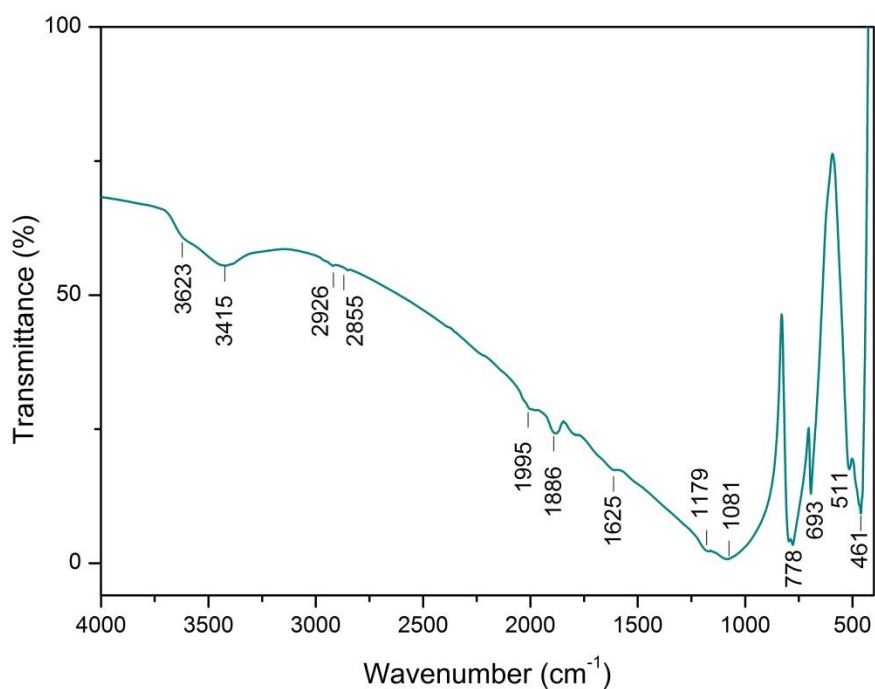


Figure 3. FTIR spectrum of Aventurine

Table 1. FT-IR transmission bands assignments of aventurine [9,10].

Wavenumber (cm ⁻¹)	Probable Band Assignment
461, 511	asymmetrical bending vibrations of Si-O
693	symmetrical bending vibrations of Si-O
778	symmetrical stretching vibrations of Si-O
1081,1179	asymmetrical stretching vibrations of Si-O due to low Al for Si substitution
1625	inbound molecular water to Al or Mg.
1886, 1995	combination of vibrations of the Si-O network
2855, 2926	organic carbon
3415	O--H group
3623	stretching vibration of O-H

3.3. SEM Images and EDX Spectrum of Aventurine

Fig. 4 is shown the morphology and composition of aventurine were assigned under scanning electron microscopy and energy-dispersive X-ray spectroscopy (SEM-EDX). This analysis gave valuable information about atoms that composed the mineral and that allowed the observation of the morphological structure of the aventurine mineral. The SEM images of microstructural features of two different sides (Fig. 4 a-b) were taken at a magnification 5000X, and it's seen that the aventurine has a layered microstructure.

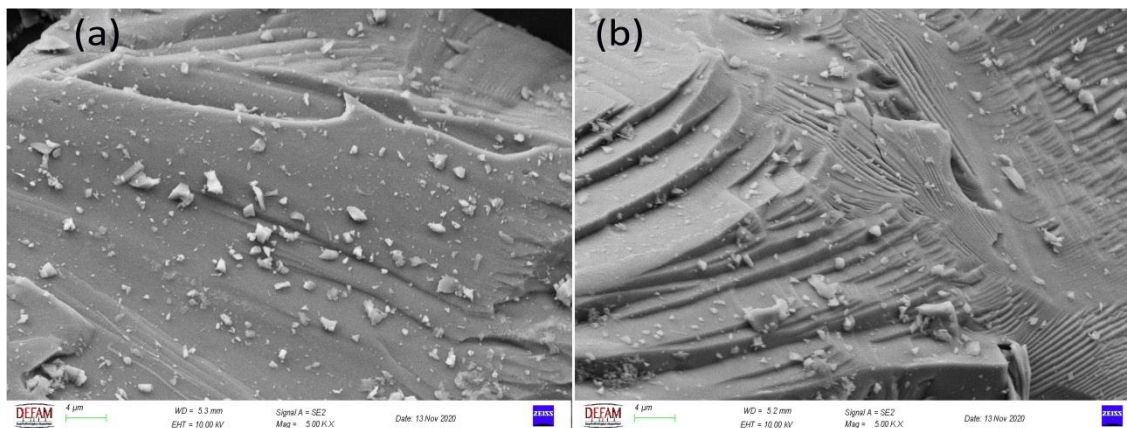


Figure 4. SEM images of Aventurine from different sides same diameter, and magnification.

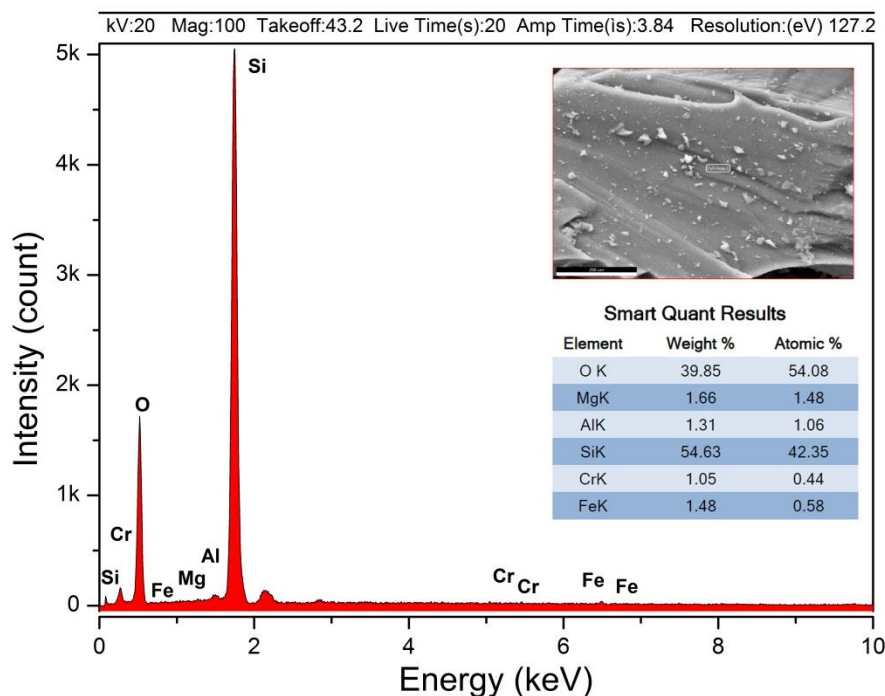


Figure 5. EDX spectrum of Aventurine.

As seen in Fig.5, as expected according to the quantitative results, the presence of a high amount of Si shows itself. Following Si, Mg, Al, Fe, and Cr impurities have been detected. These atoms directly affect the luminescence properties of the mineral.

The coloration in minerals is due to defects in the crystal structure, impurity atoms, or both. The electrons that produce color by the absorption of light can sometimes be found on a foreign atom or in a defective crystal. An impurity or structural defect can create energy levels locally between the valence and conduction bands. If the energy differences between this energy level and the conductivity and valence bands are in visible light, coloration occurs. Thus, light energy stimulated an electron; providing an energy transition and causing the electron to transition to a higher energy level. The formation of coloration occurs by the absorption of some of the wavelengths that make up the light. These impurity atoms act as color centers. Atoms detected in EDX analysis can exist in ionic states with different charges. The emission behaviors of the ionic states of these detected atoms are discussed under the title of RL properties.

3.4. TL Dose Responses and Kinetic Parameters

The thermoluminescence formation mechanism can be briefly defined as the first exposure of the material to radiation and then the obtaining of a glow curve with thermal excitation. According to the band model; Absorption of radiation means the formation of electron-hole pairs. The energy storage property is due to the presence of crystal defects such as impurities or vacancies. These defects are formed during the irradiation process and can trap electrons and holes. The material is excited with a radiation source such as an X-ray, β , γ , or UV light. As a result of the excitation, the electrons are trapped in the traps originating from the impurity atoms in the material. After the excitation process, by thermally stimulating the material the electrons in these traps are released and a glow curve is obtained. The glow curve gives information about the characteristic properties such as activation energy and trap depth.

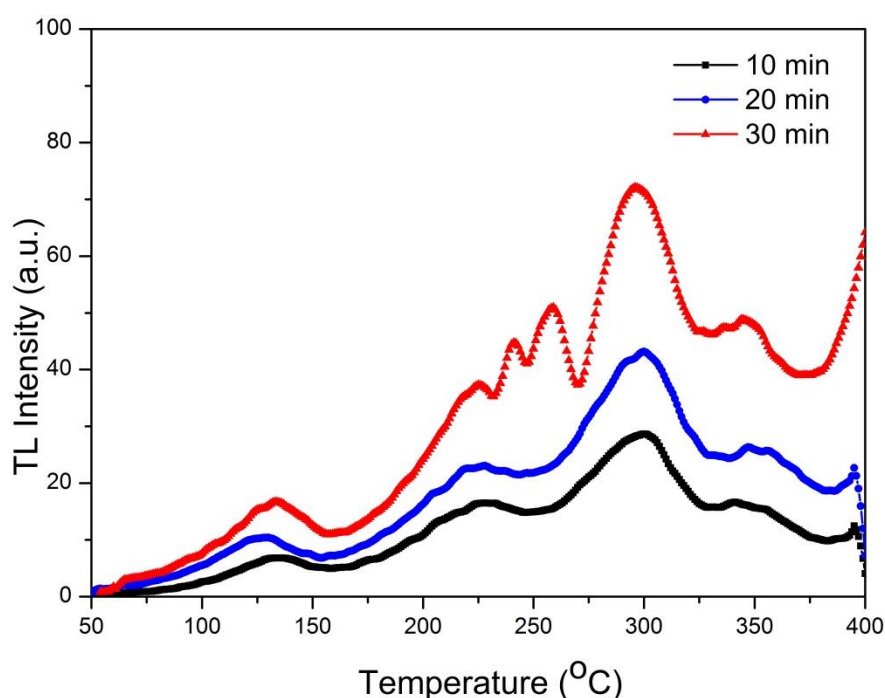


Figure 6. TL curves of Aventurine taken after 254 nm UV irradiation at 10, 20, 30 min.

Figure 6 shows the TL glow curves from 50 °C up to 400 °C of the powder aventurine irradiated with shortwave UV light for 10, 20, and 30 min. The glow curves have been recorded at a heating rate of 2 °C/s following irradiation. In Table 2, the maximum peak points of the glow curves obtained after UV irradiation are given. This peak became more

pronounced with the increasing dose of aventurine, which retained its general glow characteristic of around 350 °C. Also, it has been observed that new trap levels occur at 241 and 258 °C.

Table 2. The maximum TL curves of aventurine irradiated with UV light.

Irradiation Time (min)		Maximum Points of TL Peaks (°C)				
10	135	228	-	-	300	350
20	127	223	-	-	299	353
30	133	224	241	258	295	345

An important detail that draws attention to the glow curve formed as a result of 30 minutes of irradiation; The rise starting from 375 °C is the presence of peaks of possible new trap levels at higher temperatures. However, the current device's inability to measure over 400 °C does not make it possible to observe this peak.

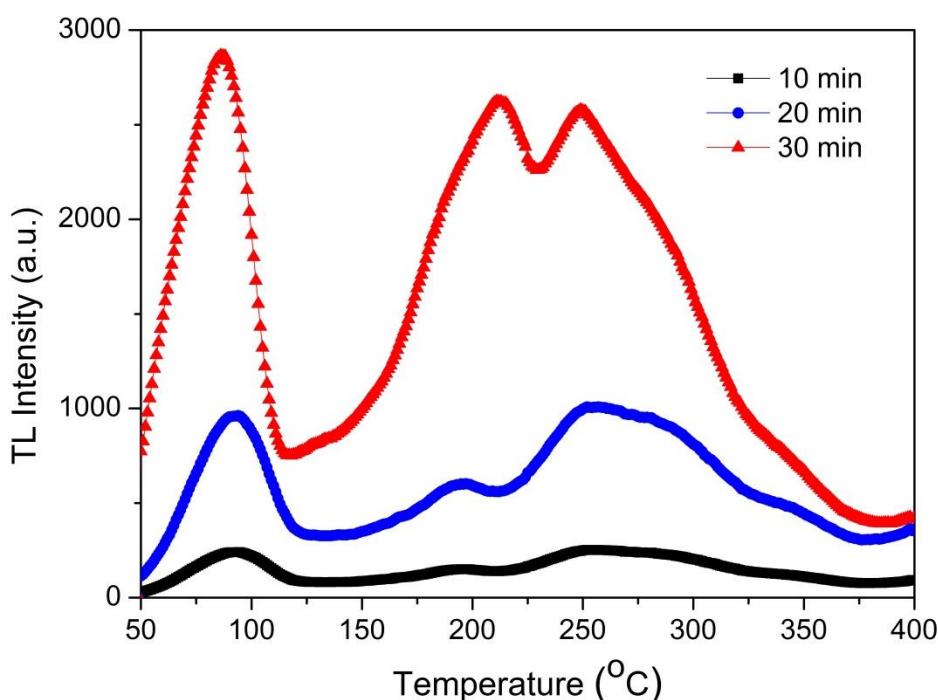


Figure 7. TL curves of Aventurine at different doses under X-ray excitation.

As seen in Figure 7, the TL glow curves from 50 °C up to 400 °C of the powder aventurine irradiated with X-rays for three different doses (300 Gy, 600 Gy, 900 Gy). The glow curves have been recorded at a heating rate of 2 °C/s following irradiation. In Table 3, the maximum peak points of the glow curves obtained after each X-ray irradiation are given.

Table 3. The maximum TL curves of aventurine irradiated with X-ray.

Irradiation Time (min)		Maximum Points of TL Peaks (°C)				
10	94	193	259	-	344	
20	91	195	252	-	345	
30	86	212	249	289	343	

As the irradiation increased, it was observed that the FWHM value of the glow curve of around 90 °C, characteristically encountered in quartz-based minerals, decreased and became more pronounced. The wide peak with a maximum point of around 250 °C and a shoulder around 195 °C, indicating the presence of deep traps, behaved like a single wide peak with the increase in dose. In the glow curve obtained after 900 Gy irradiation, it is noteworthy that a deep trap is evident at 212 °C degrees. Depending on the dose increase, it is expected that new deep traps will become evident or that existing ones will behave as a component of a single glow curve.

The luminescence glow curve of the sample from which TL measurement was taken is the combined state of many different luminescence peaks of the traps arising from the impurity atoms and crystalline dislocations in that mineral. In order to determine the activation energies and intensities of each of the peak components that make up this main radiation curve, the CGDC method is a frequently used method and there are many programs for this application. Of course, when deconvoluting the complex structure of the main glow curve, the correct number of peaks and the correct position of each peak is an important factor in the calculation of TL kinetic parameters. [11–13]. Since TL signal intensity exhibits a significant peak at both high and low temperatures and also has a good dose-response to X-ray radiation for dosimetric studies, the TL glow curve obtained as a result of 900 Gy dosing was deconvoluted. (Fig.8)

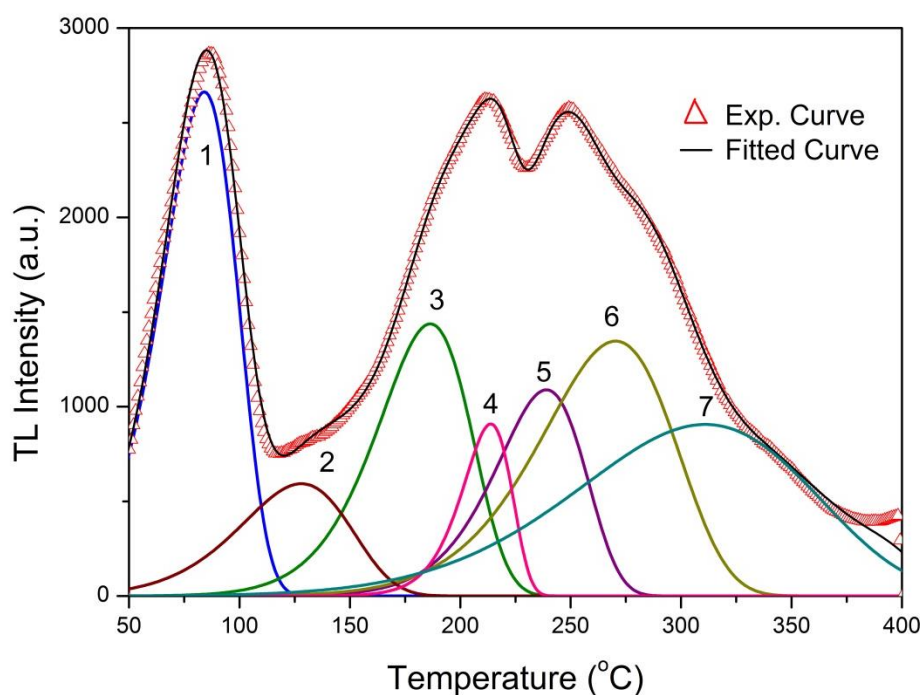


Figure 8. TL glow curve of the aventurine fitted with seven multiparameter functions.

The parameters (T_m , T_1 , T_2 , τ , δ , ω , μ , γ) which are calculated for each peak under deconvoluted experimental glow curve of aventurine are seen in Table 4. The symmetry factor (μ_g) determines the kinetic order of the thermoluminescence glow curve. The kinetic order is determined depending on the radiation peak shape. If the calculated μ_g value is found as 0.42, this is defined as first-order kinetic, and if it is 0.52, it is defined as second-order kinetic. [11]. The γ value defined as $\gamma = \delta/\tau$ is another important factor in determining the kinetic orders. The range of $\gamma = 0.7-0.8$ is for first-order kinetics, and the range of $\gamma = 1.05-1.20$ is the value for second-order kinetics [14]. The parameter called the

merit number (FOM) determines the accuracy and suitability of the deconvolution process. The classification for FOM of deconvolution determined by this values; 0.0% - 2.5% the fit is good, 2.5% - 3.5% is small flow and > 3.5% is bad fit. [15,16].

Table 4. Kinetic parameters of aventurine for each deconvolution peak (FOM: 1.06).

Peak No	$T_m(^{\circ}\text{C})$	T_1	T_2	τ	δ	ω	μ_g	γ	$E_{avg}(\text{eV})$	$s (s^{-1})$
1	84±1.2	61	102	23	18	41	0.439	0.782	0.663±0.013	2.76x10 ⁸
2	127±3.1	94	154	33	27	60	0.450	0.818	0.580±0.024	1.70x10 ⁶
3	186±2.4	157	208	29	22	51	0.431	0.758	0.857±0.014	2.42x10 ⁸
4	214±1.5	198	225	16	11	27	0.407	0.687	1,707±0,046	7,73x10 ¹⁶
5	239±2.6	211	260	28	21	49	0.428	0.750	1,109±0,009	8,10x10 ⁹
6	270±3.2	229	301	41	31	72	0.430	0.756	0.833±0.024	3.53x10 ⁶
7	310±3.6	240	368	70	58	128	0.453	0.828	0.556±0.046	2.43x10 ³

3.5. Radioluminescence Properties

Radioluminescence (RL) is the luminescence that occurs when a material is excited by photon sources such as X-rays or gamma rays. In the radioluminescence process, X-ray or gamma beam excitation provides information about the whole sample, because penetrates the entire volume of the sample. With the radioluminescence spectrum, the emission intensity as a function of the wavelength of the excitation light, the excitation intensity as a function of the emitted wavelength, the polarization of the emission, and the quantum yield are examined. Ionizing radiation simultaneously activates existing optical centers, which enables the investigation of a material's luminescence properties. [17,18]. RL or X-ray excited luminescence is useful for determining defects of minerals. X-ray radiation penetrates and induces the whole volume of the sample, forming new luminescence defects. The radioluminescence emissions of minerals (for this research aventurine) or other luminescent materials (phosphors, ceramics, glass, fibers, etc.) were measured on a high-sensitivity wavelength-multiplexed CCD detector which is capable of detection range from 200 to 1200 nm. So, in particular, the emission spectra of minerals with different impurity atoms can be determined in detail [19].

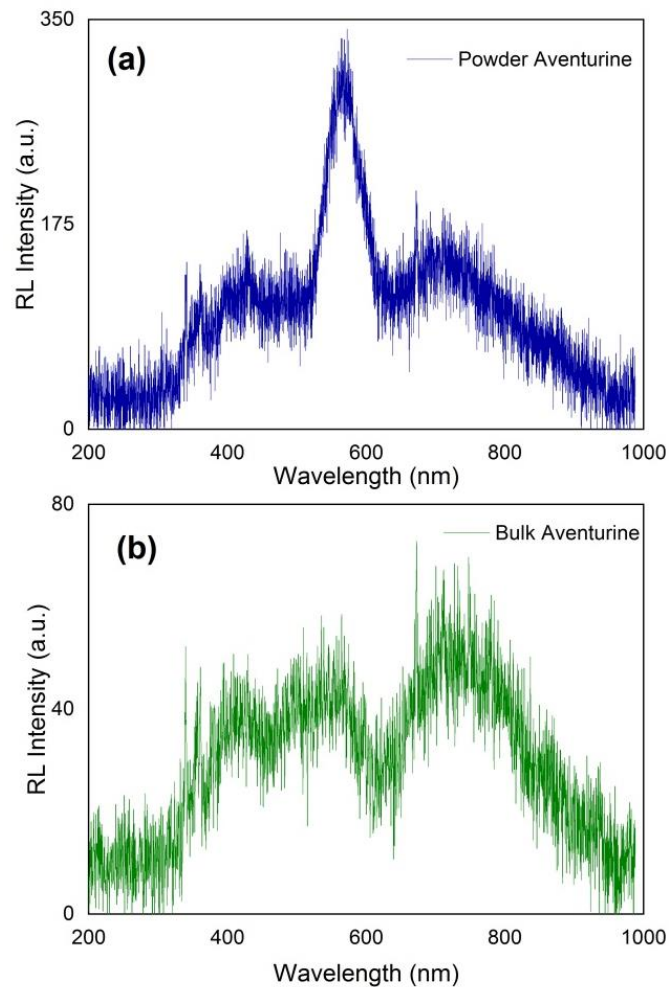


Figure 9. RL spectra of powder and bulk aventurine samples.

Fig. 9 shows the RL spectra of bulk and powder samples of aventurine. Aventurine has a quite broad emission range from about 300 to 1000 nm. Figure 9 (a) shows the emission bands of powder Aventurine with maximum peak intensities at approximately 360, 430, 570, 720, 870, and 890 nm. In Figure 9 (b), bulk aventurine exhibited emissions in almost the same regions, although the amount of noise was high due to the weakness of the detected luminescence. It is seen that the emission intensity of the powder sample is five times higher than that of the bulk. In addition, although it is common to both the emission band with a peak maximum at 570 nm (quite weak in the bulk sample) became dominantly evident. In powder material, due to the easier penetration of X-rays compared to the bulk material, the reduction of the particle size, and the enlargement of the surface area, the luminescence collected by the detector as a result of volumetric interaction has a higher intensity.

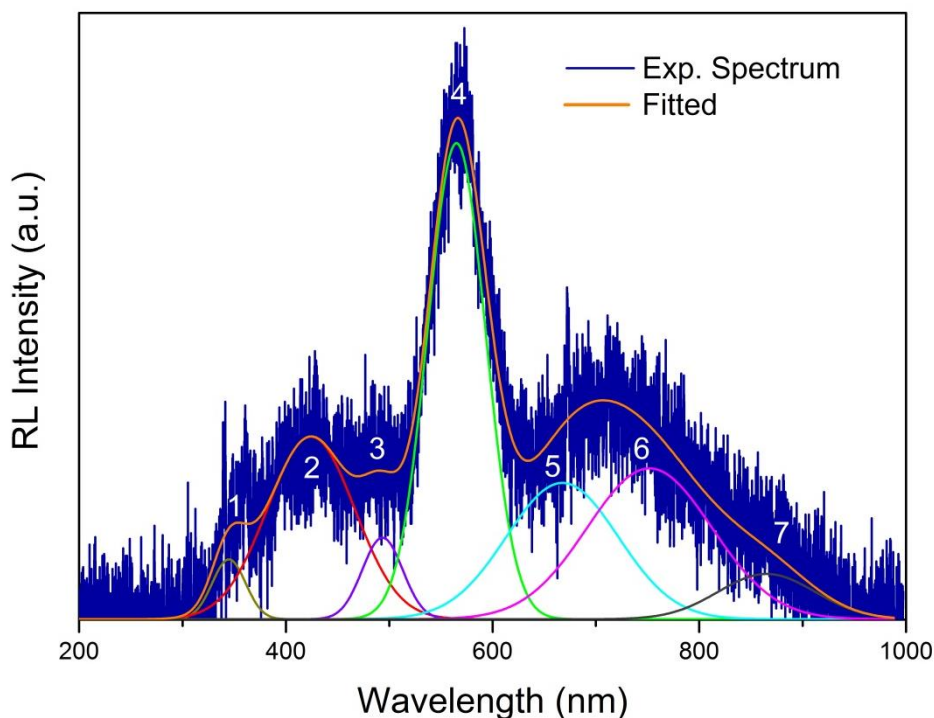


Figure 9. Fitted RL spectrum of powder aventurine.

In Fig. 10, suitable for the RL measurements is possible to determine, despite the complex structure of the RL emission behavior, that there are only a limited number of specific bands. The experimental RL spectrum, in the range of 200–1000 nm, was fitted by a sum of seven Gaussian functions using the fitting program. The factors involved in the luminescence phenomenon, which are emission spectra, lifetime, and efficiency, are the important parameters covered by luminescence. These parameters are directly dependent on the crystal phase, which is affected by factors such as temperature and pressure. Thus, minor changes in the lattice structure, such as impurities, the presence of surface defects or substitute ions, and inclusions at ppm concentrations, can cause changes in the intensity and wavelength position of the emission spectra [18].

Table 5. Parameters of possible peaks under the RL spectrum of aventurine.

Peak No	λ_{\max} (nm)	I_{\max} (a.u.)	A (peak area)	FWHM
1	344.83 ± 1.38	59.07 ± 2.11	1286.12 ± 153.30	37.96 ± 4.21
2	424.28 ± 1.81	124.42 ± 1.08	10287.39 ± 258.33	99.43 ± 7.79
3	493.46 ± 1.69	70.62 ± 1.27	2125.80 ± 132.38	46.02 ± 5.41
4	565.11 ± 0.60	280.68 ± 0.42	17840.35 ± 1093.79	66.12 ± 2.12
5	667.51 ± 2.66	99.78 ± 0.94	9822.08 ± 611.44	127.20 ± 1.38
6	751.93 ± 3.65	107.49 ± 1.12	12161.63 ± 1418.47	142.35 ± 7.69
7	865.14 ± 85.48	51.34 ± 2.07	2823.17 ± 563.18	110.04 ± 7.80

* Adj. R-Square 0.96513, λ_{\max} : the position of the maxima, I_{\max} : intensity of the maxima, FWHM: full-width at half maximum

In Table 5 the parameters of the resolved possible peaks under the RL spectrum were given. Of course, it is possible to obtain many different variations apart from this deconvolution. Considering that each of the 7 individual peaks

corresponds to the emissions of impurity atoms contained in aventurine. We cannot say with certainty that the observed emission originates from a certain metal ion with a certain valence, but we should compare how well these overlap with examples in the literature. In Table 6, the emission wavelength values of Si, Mg, Fe, Al, and Ca ions, which were determined by the EDX analysis to be present in aventurine, are given in order from the highest intensity to the lowest. When Table 6 is examined, it is seen that there are emission values that are exactly compatible with the resolved peaks.

Table 6. The most intense spectral lines arranged according to wavelength [20].

Cations	Si ¹⁺	Si ²⁺	Si ³⁺	Mg ¹⁺	Mg ²⁺	Fe ¹⁺	Fe ²⁺	Fe ³⁺	Al ¹⁺	Al ²⁺	Al ³⁺
Wavelength (nm)	742	637	455	880	789	868	645	437	396	466	360
	728	566	386	518	448	649	624	592	877	600	414
	703	505	573	552	439	751	730	416	783	559	452
	594	413	482	382	-	718	542	428	669	835	569
	625	333	348	-	-	667	-	360	-	342	-
	855	784	761	-	-	-	-	-	-	-	-

Under stress structures with Si-O bonding, such as aventurine, have some unbounded oxygen or silicon-vacancy centers or some Si-O bonding defects, which cause UV emission. As for Cr, one of the important metals in Aventurine; Cr²⁺ ions exhibit a line emission at about 650 nm at room temperature. It is thought that this impurity emission may result from the ³E→⁵E transition of the Cr²⁺ ion [21]. Although the measurement was taken at room temperature, it is known that the weak infrared emission at about 820 nm at low temperatures is related to the ³E→³T₁ transition of the Cr³⁺ ion [22].

A trivalent chromium ion (Cr³⁺) is a significant transition metal member of the group. Chromium's 3d³ electron configuration has a really engaging combination of the spin doublet and spin-quartet states. Cr³⁺ has exhibited a wide emission from 650 nm to 850 nm in synthesized alumina-based phosphor. The stated wide emission band originated from the ⁴T_{2g}-⁴A_{2g} transition of Cr³⁺ [23]. It has been observed that the fluorescence spectra of glass-based optical fiber structures containing Cr³⁺ have a maximum peak around 540 nm in the range of 500-800 nm in the emission spectrum obtained as a result of 474 nm excitation [24].

4. Conclusions

Aventurine is a translucent form of quartz known for its bright containments which give it a sheeny look. The aventurine comes from the presence of chrome-bearing fuchsite, which adds a silvery green or silvery blue sheen to the crystal. Hematite or goethite subsumptions form orange and brown crystals. Aventurine can thus be found in various colors such as orange, blue, gray, brown, and yellow, but it is most often green. Minor phases of Fe and Cr were observed in the XRD analysis of Aventurine, a silicon oxide-based mineral. In the EDX spectrum, the presence of Mg, Al, Cr, and Fe was detected, except for Si and O. TL glow curves of the sample irradiated with UV light and X-ray radiation for 10, 20, and 30 minutes were examined. As a result of UV irradiation, it was observed that deep traps at high temperatures were more prominent and had a main peak with a maximum intensity of about 300 oC. It has been determined that both shallow traps and deep traps are strongly present in the glow curves obtained after X-ray irradiation. CGDC analysis

was performed on the curve obtained after 900 Gy dosing, and it was observed that the resolved peaks were first-order kinetic levels, varying from 0.663 ± 0.013 eV to 1.707 ± 0.046 eV. The RL spectra of powder and bulk Aventurine samples generally showed similar emissions, but the powder sample has a strong emission of around 560 nm. In order to determine the possible positions of the Gaussian peaks which are forming this main emission spectrum consists of and the caused by the impurity atoms, the RL spectrum was also deconvolved. Depending on the presence of ions in aventurine, the formation mechanism of emissions is discussed.

References

- [1] B. Karasu, B. Sarıcaoğlu, Aventurin Sırlarına Genel Bir Bakış, El-Cezeri Fen ve Mühendislik Derg. 2019 (2019) 140–155. doi:10.31202/ecjse.460093.
- [2] M.J.O. Donoghue, eJournal of Gemmology Gemmological Association Of Great Britain, 20 (1986).
- [3] A. Gozalbo, M.J. Orts, S. Mestre, P. Agut, F. Lucas, A. Belda, C. Blanco, Ceramic Glazes With Aventurine Effect, *Cycle*. (2006) 189–202.
- [4] M.D. Shcheglova, Mechanism of aventurine formation in copper-containing alkali-leadsilicate glass, *Glas. Ceram.* 53 (1996) 14–17.
- [5] M.I. Kati, M. Türemis, I.C. Keskin, B. Tastekin, R. Kibar, A. Çetin, N. Can, Luminescence behaviour of beryl (aquamarine variety) from Turkey, *J. Lumin.* 132 (2012). doi:10.1016/j.jlumin.2012.03.058.
- [6] İ.Ç. Keskin, M.İ. Kati, M. Türemiş, A. Çetin, Y. Tuncer Arslanlar, R. Kibar, Determination of Thermoluminescence Kinetic Parameters of White and Blue Chalcedony Exposed to X-ray Irradiation, *Radiat. Phys. Chem.* (2018). doi:10.1016/j.radphyschem.2018.05.031.
- [7] M.I. Teixeira, D.N. Souza, L.V.E. Caldas, Onyx as radiation detector for high doses, *Radiat. Meas.* 46 (2011) 1894–1896. doi:10.1016/j.radmeas.2011.07.021.
- [8] S. Gültekin, S. Yıldırım, O. Yılmaz, İ.Ç. Keskin, M.İ. Kati, E. Çelik, Structural and optical properties of SrAl₂O₄: Eu²⁺/Dy³⁺ phosphors synthesized by flame spray pyrolysis technique, *J. Lumin.* 206 (2019) 59–69. doi:10.1016/j.jlumin.2018.10.011.
- [9] R. Ullah, B.K. Deb, M. Yousuf, A. Mollah, Synthesis and Characterization of Silica Coated Iron-Oxide Composites of Different Ratios, *Int. J. Compos. Mater.* 4 (2014) 135–145. doi:10.5923/j.cmaterials.20140402.13.
- [10] V. Ramasamy, P. Rajkumar, V. Ponnusamy, Depth wise analysis of recently excavated Vellar river sediments through FTIR and XRD studies, *Indian J. Phys.* 83 (2009) 1295–1308. doi:10.1007/s12648-009-0110-3.
- [11] C. Pagonis, Vasilis, Kitis, George, Furetta, Numerical and Practical Exercises in Thermoluminescence, Springer New York, New York, NY, 2006. doi:10.1007/0-387-30090-2.
- [12] T. Sakurai, R.K. Gartia, Method of computerized glow curve deconvolution for analysing thermoluminescence, *J. Phys. D. Appl. Phys.* 36 (2003) 2719–2724. doi:10.1088/0022-3727/36/21/020.
- [13] N.D. Sang, N. Van Hung, T. Van Hung, N.Q. Hien, Using the computerized glow curve deconvolution method and the R package tgcd to determination of thermoluminescence kinetic parameters of chilli powder samples by GOK model and OTOR one, *Nucl. Instruments Methods Phys. Res. Sect. B Beam Interact. with Mater. Atoms.* 394 (2017) 113–120. doi:10.1016/j.nimb.2017.01.012.

- [14] M. Balarin, Half-width and asymmetry of glow peaks and their consistent analytical representation, *J. Therm. Anal.* 17 (1979) 319–332. doi:10.1007/BF01914023.
- [15] H.G. Balian, N.W. Eddy, Figure-of-merit (FOM), an improved criterion over the normalized chi-squared test for assessing goodness-of-fit of gamma-ray spectral peaks, *Nucl. Instruments Methods.* 145 (1977) 389–395. doi:10.1016/0029-554X(77)90437-2.
- [16] S.K. Misra, N.W. Eddy, IFOM, a formula for universal assessment of goodness-of-fit of gamma ray spectra, *Nucl. Instruments Methods.* 166 (1979) 537–540. doi:10.1016/0029-554X(79)90546-9.
- [17] A.T.Y. Arslanlar Tuncer Y., Kibar R., Çetin A., Canımoğlu A., Radioluminescence Properties of Copper- and Terbium-Implanted Strontium Titanate Radioluminescence Properties of Copper- and Terbium-Implanted Strontium Titanate, *Lett. Spectrosc.* (2013) 364–366. doi:10.1080/00387010.2012.738278.
- [18] Y. Rodríguez-Lazcano, V. Correcher, J. Garcia-Guinea, Thermo- and cathodoluminescence properties of lepidolite, *Spectrochim. Acta - Part A Mol. Biomol. Spectrosc.* 113 (2013) 281–285. doi:10.1016/j.saa.2013.04.107.
- [19] Y. Tuncer Arslanlar, J. Garcia-Guinea, R. Kibar, A. Çetin, M. Ayvacikli, N. Can, Luminescence behavior and Raman characterization of jade from Turkey, *Appl. Radiat. Isot.* 69 (2011) 1299–1306. doi:10.1016/j.apradiso.2011.05.011.
- [20] A.R. Striganov, N.S. Sventitskii, *Tables of Spectral Lines of Neutral and Ionized Atoms*, Springer US, Boston, MA, 1968. doi:10.1007/978-1-4757-6610-3.
- [21] Y.T. Arslanlar, *Doğal Taşların Ve Sentetiklerinin Karakteristik Ve Optik Özelliklerinin İncelenmesi Doktora Tezi Yasemin Tuncer Arslanlar*, Celal Bayar Üniversitesi Fen Bilimleri Enstitüsü, 2011.
- [22] T.C. Vanoy, A.M. Levert, G.L. McPherson, Luminescence spectra of crystals of RbMnCl_3 , Rb_2MnCl_4 and CsMnBr_3 doped with Cr^{2+} : exciton trapping at luminescent Cr^{2+} centres, *J. Phys. C Solid State Phys.* 21 (1988) 2969–2979. doi:10.1088/0022-3719/21/15/027.
- [23] L. Zhang, S. Zhang, Z. Hao, X. Zhang, G. Pan, Y. Luo, H. Wu, J. Zhang, A high efficiency broad-band near-infrared $\text{Ca}_2\text{LuZr}_2\text{Al}_3\text{O}_{12}:\text{Cr}^{3+}$ garnet phosphor for blue LED chips, *J. Mater. Chem. C.* 6 (2018) 4967–4976. doi:10.1039/C8TC01216D.
- [24] D. Dutta, A. Dhar, A. V. Kir'yanov, S. Das, S. Bysakh, M.C. Paul, Fabrication and characterization of chromium-doped nanophase separated yttria-alumina-silica glass-based optical fibers, *Phys. Status Solidi.* 212 (2015) 1836–1844. doi:10.1002/pssa.201532017.

The Impact of Orientation Angle and Number of Layers on Electromagnetic Shielding Characteristics of Carbon Fiber Composites

Yucel Coskun ^{1*} , Mehmet Baris Tabakcioglu ² 

^{1*} Department of Electronics and Communication Engineering, Beykent University, 34398, Istanbul, Turkey

² Department of Electrical and Electronics Engineering, Bursa Technical University, 16310, Bursa, Turkey

Abstract

In this study, electromagnetic shielding characteristics for orientation angle and number of plies of carbon fiber reinforced epoxy composites were investigated in the frequency range between 900 and 6000 MHz. Both unidirectional and bidirectional carbon fiber fabrics were utilized as reinforcement materials to manufacture the composite samples. Twill bidirectional glass fiber fabrics were also used in order to provide a large amount of flexibility. To prepare the composite laminates for measurement, hand lay-up method was preferred. Measurements were carried out by using DFG 4060 signal generator and HF 60105 spectrum analyzer. In the proposed frequency range, electromagnetic shielding effectiveness (EMSE) up to 62.13 dB was achieved. This value is accepted in the literature as a good level of shielding. According to the measurements, it was observed that EMSE was very higher when the orientation angle of the carbon fiber was 90°, as compared to 0°. Another parameter that affects EMSE is whether the carbon fiber fabric used is unidirectional or bidirectional because it was observed that the bidirectional fabric increased EMSE. In addition, it was determined that the number of plies has less effect on EMSE than the orientation angle.

Keywords: Carbon fiber; Hand lay-up method; Orientation angle; Electromagnetic shielding.

Cite this paper as:

Coskun, Y., Tabakcioglu, M.B. (2022). *The Impact of Orientation Angle and Number of Layers on Electromagnetic Shielding Characteristics of Carbon Fiber Composites*. Journal of Innovative Science and Engineering. 6(2): 190-200

*Corresponding author: Yucel Coskun
E-mail: yucelcoskun@beykent.edu.tr

Received Date: 05/08/2021

Accepted Date: 09/02/2022

© Copyright 2022 by

Bursa Technical University. Available
online at <http://jise.btu.edu.tr/>



The works published in Journal of Innovative Science and Engineering (JISE) are licensed under a Creative Commons Attribution-NonCommercial 4.0 International License.

1. Introduction

Recently, due to extensive utilization of electromagnetic waves in electronic devices and communication equipment, electromagnetic interference (EMI) has become a serious issue [1]. It can cause important malfunctions in electronic systems. Especially in the military applications, malfunctions caused by EMI are vital, as there are critical platforms such as helicopters, battle tanks, unmanned aerial vehicles, frigates and jet aircrafts including electronic warfare and radar systems, control panels and avionics. Therefore, various materials have been used for the purpose of shielding critical systems and preventing safety problems [2, 3]. These materials are mainly conductor metals, surface spreading film materials coated metal, ferromagnetic materials, and composite materials [4]. Although the use of metals offers a high level of protection against EMI, it is not preferred in some industries, such as aviation [5-7] because there is a rising requirement to reduce aircraft weight and provide excellent mechanical properties, as well as a good level of electromagnetic shielding [6, 8]. Carbon fiber reinforced polymer composites (CFRP) are being increasingly used in EMI shielding due to their light weight, design flexibility, compression strength, and tensile strength [8,9]. In CFRP, the matrix is most often epoxy resin to bind carbon fibers together. Epoxy is a thermoset polymer that has low cost [10, 11]. Luo and Chung studied on carbon fiber reinforced carbon matrix composites, and they showed that shielding effectiveness of 124 dB was achieved in the frequency range between 0.3 MHz and 1.5 GHz. However, since carbon matrix materials are expensive, polymer matrix composites are preferred [12,13]. In some applications where a higher breaking point is required, glass fibers can also be used with carbon fibers.

The implementation of an EMI shielding material is decided by measuring its EMSE. EMSE can be expressed as the sum of three factors called reflection loss (R_{dB}), absorption loss (A_{dB}), and multiple internal reflections loss (M_{dB}). Reflection loss occurs due to impedance differences of two different media and depends on the electrical conductivity of the material. Absorption loss depends on the thickness and skin depth of the material. Multiple internal reflections loss is usually at negligible level. The illustration of EMI shielding mechanism is shown in Figure 1 [14]. The expression for EMSE, which includes R_{dB} , A_{dB} , and M_{dB} terms is given as:

$$EMSE_{dB} = 20 \log \left| \frac{\eta_0}{4\eta_s} \right| + 20 \log |e^{t/\delta}| + 20 \log |1 - e^{-2t/\delta}| \quad (1)$$

In equation (1), the skin depth is related to frequency, relative permeability, and conductivity as:

$$\delta = \frac{1}{\sqrt{\pi f \mu \sigma_c}} \quad (2)$$

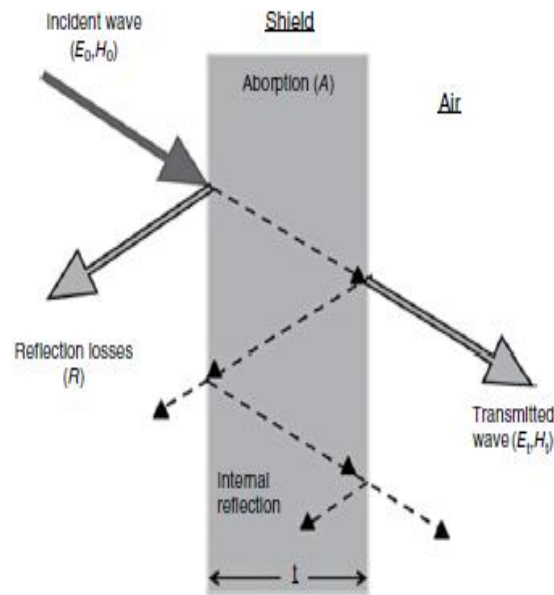


Figure 1. EMI shielding mechanism.

In this study, firstly, a total of eight carbon fiber epoxy composite samples with different orientation angle and number of plies were prepared, using hand lay-up method, and then measurements were carried out to investigate the effects of the orientation angle, the number of plies, and fabric type on EMSE in the proposed frequency range.

2. Experimental Setup

2.1. Sample Manufacturing

Unidirectional carbon fiber fabric with a real weight of 300 g/m² and epoxy resin, which consists of epoxy resin and hardener were employed to prepare first four laminates (25 x 25 cm). The volume fraction of carbon fiber was targeted to be in the range of 0.45-0.50. Total weight of epoxy resin was found by calculating its specific gravity. Epoxy resin and hardener were mixed in weight ratio of 5:3. In order to manufacture the four laminates designed with different stacking sequences, unidirectional plies were rotated in different directions at 90°. Configurations of samples of 2 plies and 3 plies manufactured in this way were arranged as [0°, 0°], [0°, 90°], [0°, 0°, 0°], and [0°, 90°, 0°]. All samples were manufactured by using hand lay-up method as shown in Figure 2.

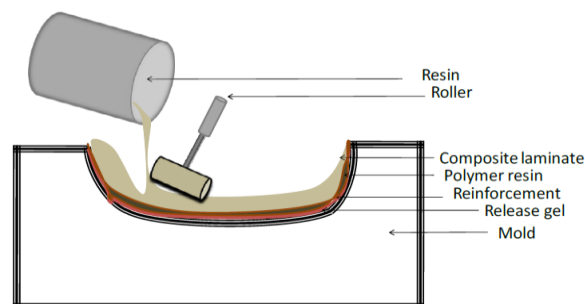


Figure 2. The schematic of hand lay-up method [15].

Bidirectional carbon fiber fabric with a real weight of 200 g/m², twill bidirectional glass fiber fabric and epoxy resin, which consists of epoxy resin and hardener, were employed to prepare the other four laminates (25 x 25 cm). The volume

fraction of carbon fiber was targeted to be in the range of 0.35-0.40. Total weight of epoxy resin was again found from its specific gravity. Epoxy resin and hardener were mixed in weight ratio of 5:3. Configurations of samples of 2 plies, 3 plies, and 5 plies manufactured were arranged as $[0^\circ/90^\circ, 0^\circ/90^\circ]$, $[0^\circ/90^\circ, 0^\circ/90^\circ, 0^\circ/90^\circ]$, $[0^\circ/90^\circ, (0^\circ/90^\circ)_G, 0^\circ/90^\circ]$, and $[0^\circ/90^\circ, (0^\circ/90^\circ)_G, 0^\circ/90^\circ, (0^\circ/90^\circ)_G, 0^\circ/90^\circ]$. The subscript G represents glass fiber fabric.

The fiber fabrics used in the manufacturing process are illustrated in Figure 3.

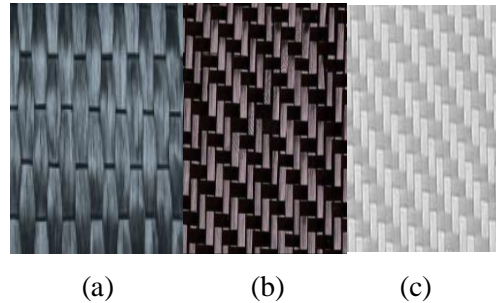


Figure 3. Unidirectional and bidirectional fiber fabrics: (a) Unidirectional carbon fiber fabric, (b) Bidirectional $0^\circ/90^\circ$ carbon fiber fabric, (c) Bidirectional $0^\circ/90^\circ$ glass fiber fabric.

2.2 Measurements

The measurement method is based on the signal loss of the samples placed between the transmitting and receiving antennas. Firstly, the signal loss of the free space between the antennas was measured, and then measurements of the samples were performed. Electromagnetic shielding effectiveness (EMSE) of the samples was defined as the ratio between power received from interference source with no shield and power passing through the shielding material.

$$EMSE = 10 \log_{10} \frac{\text{Power received from interference source with no shield}}{\text{Power passing through the shielding material}} \quad (3)$$

EMSE measurement setup is illustrated in Figure 4.

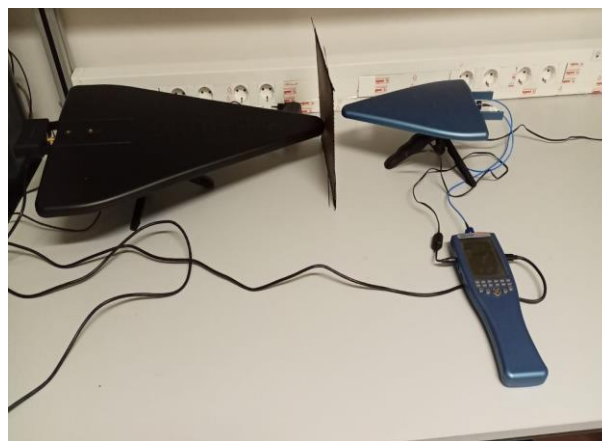


Figure 4. EMSE measurement setup.

As shown in Figure 4, there is a receiving antenna and a spectrum analyzer in left hand side, and a transmitting antenna and directional field generator in right hand side.

3. Results and discussion

The attenuation values in dB for the free space and the first four samples between the antennas are given in Table 1 [16].

Table 1. Attenuation values

Frequency (MHz)	Free Space (dB)	[0°,0°] (dB)	[0°,90°] (dB)	[0°,0°,0°] (dB)	[0°,90°,0°] (dB)
900	-18.82	-22.57	-28.14	-23.38	-27.87
1000	-26.77	-30.81	-34.74	-31.63	-33.51
1100	-18.16	-23.10	-28.74	-25.83	-27.74
1200	-24.55	-28.64	-36.41	-29.98	-34.14
1300	-11.25	-20.22	-31.57	-21.14	-33.11
1400	-10.23	-19.47	-33.03	-20.31	-34.80
1500	-11.20	-18.91	-40.52	-20.59	-33.47
1600	-10.01	-18.08	-36.55	-19.88	-33.95
1700	-11.11	-19.29	-33.88	-20.37	-35.82
1800	-10.44	-18.35	-34.14	-19.64	-35.14
1900	-10.48	-18.59	-34.79	-20.45	-36.29
2000	-8.07	-16.52	-35.01	-18.01	-36.01
2100	-11.01	-20.44	-38.61	-21.52	-40.69
2200	-10.69	-22.13	-41.06	-22.41	-40.97
2300	-9.98	-21.68	-47.78	-22.04	-43.61
2400	-11.46	-21.54	-48.46	-21.87	-45.24
2500	-4.89	-14.16	-48.03	-14.42	-41.70
2600	-16.75	-21.39	-50.77	-21.20	-49.84
2700	-16.28	-21.81	-47.86	-21.81	-61.93
2800	-16.52	-21.70	-50.26	-21.58	-49.90
2900	-15.67	-20.99	-54.34	-20.86	-47.15
3000	-17.27	-23.70	-57.96	-23.16	-51.72
3100	-16.58	-21.77	-50.01	-21.52	-50.42
3200	-16.97	-22.75	-50.30	-22.02	-47.84
3300	-17.29	-22.67	-62.32	-22.30	-61.66
3400	-17.10	-22.97	-55.79	-22.31	-60.07
3500	-17.51	-23.00	-61.06	-22.51	-52.43
3600	-25.64	-31.44	-64.77	-30.87	-66.24
3700	-15.80	-21.40	-61.55	-20.92	-59.91
3800	-15.90	-21.73	-55.55	-21.13	-60.38
3900	-15.51	-20.82	-65.59	-20.41	-61.75
4000	-14.93	-21.06	-56.47	-20.53	-54.60
4100	-14.31	-20.18	-59.35	-19.74	-61.80
4200	-15.53	-21.64	-59.76	-20.74	-57.93
4300	-15.48	-21.17	-69.29	-20.76	-60.89
4400	-15.08	-21.76	-60.27	-20.61	-56.74
4500	-14.89	-20.83	-59.74	-19.95	-62.90
4600	-15.77	-22.14	-60.80	-21.35	-69.98
4700	-16.89	-23.80	-59.60	-22.70	-58.53
4800	-15.47	-21.37	-60.46	-20.64	-63.96
4900	-15.12	-21.56	-66.66	-20.78	-75.46
5000	-16.03	-21.95	-64.93	-21.16	-59.01
5100	-15.80	-21.70	-67.32	-21.40	-75.05
5200	-15.37	-21.84	-60.37	-20.57	-64.73
5300	-15.45	-21.32	-64.54	-20.53	-57.23
5400	-15.28	-21.62	-69.26	-20.89	-69.98
5500	-16.06	-21.75	-66.33	-20.84	-71.26
5600	-14.27	-19.72	-65.53	-19.11	-56.91
5700	-15.73	-21.81	-65.22	-21.01	-66.48
5800	-17.14	-21.99	-67.04	-21.19	-60.19
5900	-15.38	-21.76	-63.90	-20.44	-58.04
6000	-14.38	-20.14	-61.16	-19.57	-67.62

As it can be seen in Table 1, the leftmost column gives the operating frequency. The next column shows the free space loss. The next 4 columns illustrate the received signal strength passing through carbon fiber materials with different orientation respectively, [0°, 0°], [0°, 90°], [0°, 0°, 0°], and [0°, 90°, 0°].

It can be seen from the table that orientation is highly effective. For example, at 900 MHz and [0°, 0°] orientation (both carbon fiber plies are in the same direction) loss is -22.57 dB; however, at [0°,90°] orientation (carbon fiber plies are

perpendicular to each other) loss is -28.14 dB. As another example, if the operating frequency is selected as 6000 MHz, at $[0^\circ, 0^\circ]$ orientation, loss is -20.14 dB, but, at $[0^\circ, 90^\circ]$ orientation, loss is -61.16 dB. Therefore, it can be concluded that when the orientation is changed, loss will change too. Especially at 90° orientation angle, as electromagnetic wave propagation direction is perpendicular to fiber orientation, total loss increases because of increasing absorption losses. Moreover, as the operating frequency is increased, loss will increase enormously. The reason for this increase is that mechanism of shielding for conductive materials is absorption depending on decreasing skin depth in high frequencies. Also it can be seen in the Table 1 that number of plies has affected the electromagnetic shielding effectiveness (EMSE). For example, at 2300 MHz and $[0^\circ, 0^\circ]$ orientation (both carbon fiber plies are in the same direction) loss is -21.68 dB; however, at $[0^\circ, 0^\circ, 0^\circ]$ orientation (three carbon fiber plies are in the same direction) loss is -22.04 dB. As another example, if the operating frequency is selected as 6000 MHz, at $[0^\circ, 0^\circ]$ orientation, loss is -20.14 dB, but, at $[0^\circ, 0^\circ, 0^\circ]$ loss is -19.57 dB. Therefore, it can be concluded that when the third layer is added in order to investigate the effect of number of plies of the composite samples on EMSE, loss will change less. According to the absorption loss equation, the ability to absorb electromagnetic waves of the materials depends on their thicknesses.

According to the measurements performed in the 900-6000 MHz frequency range, the attenuation graph of electromagnetic wave for $[0^\circ, 0^\circ]$ and $[0^\circ, 0^\circ, 0^\circ]$ orientation is illustrated in Figure 5.

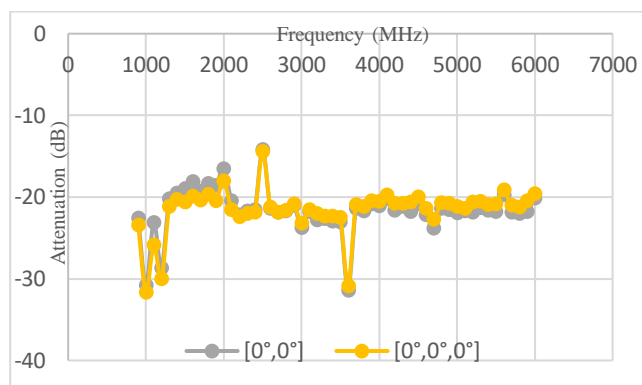


Figure 5. Attenuation for the samples in $[0^\circ, 0^\circ]$ and $[0^\circ, 0^\circ, 0^\circ]$ orientation.

As can be seen in Figure 5, there is almost the same pattern between 2-layered and 3-layered materials in the same orientation. According to the measurements performed in the 900-6000 MHz frequency range, the attenuation graph of electromagnetic wave for $[0^\circ, 0^\circ]$ and $[0^\circ, 90^\circ]$ orientation is depicted in Figure 6.

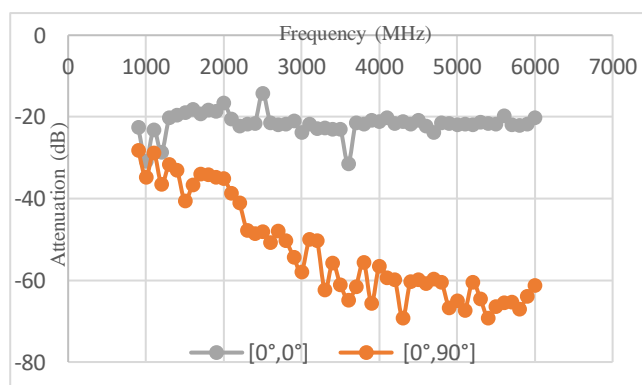


Figure 6. Attenuation for the samples in $[0^\circ, 0^\circ]$ and $[0^\circ, 90^\circ]$ orientation.

As can be seen in Figure 6, attenuation patterns of the materials are very different. Especially in high frequencies, there is approximately 40 dB difference. According to the measurements performed in the 900-6000 MHz frequency range, the attenuation graph of electromagnetic wave for the free space and $[0^\circ, 90^\circ, 0^\circ]$ orientation is demonstrated in Figure 7.

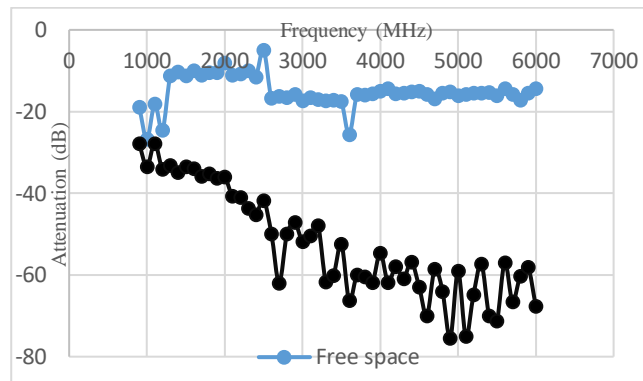


Figure 7. Attenuation for the samples in free space and $[0^\circ, 90^\circ, 0^\circ]$ orientation.

As it is seen in Figure 7, attenuation patterns of the material oriented in $[0^\circ, 90^\circ, 0^\circ]$ and free space are very different. Especially in high frequencies, there is approximately 60 dB difference. The reasons for this difference are reflection, absorption, and multiple internal reflection losses the material provides.

After measuring the first four samples manufactured with unidirectional carbon fiber fabrics, measurements of the other four samples manufactured with bidirectional carbon fiber fabrics were carried out in order to compare two different fabric types in terms of EMI shielding. The attenuation values in dB for the free space and the other four samples between the antennas are given in Table 2.

Table 2. Attenuation values

Frequency	Free Space	$[0^\circ/90^\circ, 0^\circ/90^\circ]$	$[0^\circ/90^\circ, 0^\circ/90^\circ, 0^\circ/90^\circ]$	$[0^\circ/90^\circ, (0^\circ/90^\circ)_{G'}, 0^\circ/90^\circ]$	$[0^\circ/90^\circ, (0^\circ/90^\circ)_{G'}, (0^\circ/90^\circ)_{G'}, 0^\circ/90^\circ]$
900	-18.82	-25.07	-24.84	-25.37	-24.93
1000	-26.77	-30.93	-30.83	-30.85	-30.71
1100	-18.16	-26.94	-26.18	-26.72	-26.68
1200	-24.55	-33.04	-32.93	-32.35	-32.74
1300	-11.25	-30.39	-31.03	-30.51	-30.75
1400	-10.23	-33.20	-35.82	-34.30	-34.67
1500	-11.20	-33.46	-33.73	-34.39	-35.14
1600	-10.01	-33.39	-33.06	-33.68	-33.43
1700	-11.11	-32.99	-32.99	-32.76	-33.75
1800	-10.44	-33.70	-33.29	-33.45	-33.80
1900	-10.48	-35.00	-35.30	-34.80	-36.21
2000	-8.07	-36.08	-36.78	-35.88	-37.28
2100	-11.01	-41.1	-41.27	-40.88	-41.46
2200	-10.69	-39.62	-40.73	-40.21	-40.65
2300	-9.98	-41.83	-42.48	-42.44	-43.67
2400	-11.46	-43.27	-44.14	-43.98	-43.51
2500	-4.89	-39.82	-40.47	-41.81	-40.05
2600	-16.75	-47.20	-49.48	-49.31	-47.86
2700	-16.28	-53.04	-53.39	-53.26	-51.96
2800	-16.52	-54.14	-53.47	-54.35	-58.33
2900	-15.67	-48.53	-48.07	-48.26	-49.97

3000	-17.27	-51.20	-51.48	-51.99	-51.80
3100	-16.58	-47.18	-47.66	-48.09	-47.26
3200	-16.97	-46.62	-46.64	-47.13	-46.56
3300	-17.29	-53.15	-55.48	-55.55	-51.19
3400	-17.10	-53.83	-54.50	-55.37	-53.81
3500	-17.51	-57.20	-59.06	-57.53	-56.62
3600	-25.64	-67.30	-65.67	-67.53	-65.74
3700	-15.80	-65.19	-62.99	-63.15	-63.24
3800	-15.90	-59.35	-60.67	-60.04	-62.02
3900	-15.51	-61.41	-59.47	-61.18	-62.49
4000	-14.93	-56.22	-53.94	-55.48	-56.21
4100	-14.31	-58.72	-59.58	-60.33	-57.54
4200	-15.53	-60.21	-58.37	-60.15	-60.13
4300	-15.48	-67.11	-73.46	-72.87	-67.15
4400	-15.08	-55.72	-55.03	-55.12	-55.71
4500	-14.89	-55.08	-53.93	-56.30	-54.84
4600	-15.77	-65.41	-63.67	-67.06	-59.85
4700	-16.89	-59.83	-61.98	-61.19	-59.78
4800	-15.47	-72.95	-76.95	-74.36	-77.60
4900	-15.12	-73.31	-69.15	-67.44	-68.75
5000	-16.03	-65.14	-61.63	-60.72	-64.04
5100	-15.80	-69.88	-69.50	-72.66	-65.33
5200	-15.37	-67.74	-68.00	-67.93	-64.78
5300	-15.45	-70.82	-62.06	-62.39	-65.32
5400	-15.28	-68.02	-67.43	-69.45	-63.90
5500	-16.06	-61.30	-60.64	-60.80	-61.03
5600	-14.27	-58.69	-57.06	-56.97	-57.64
5700	-15.73	-69.51	-69.72	-67.59	-67.75
5800	-17.14	-64.62	-61.82	-61.73	-61.45
5900	-15.38	-62.41	-65.53	-61.55	-62.09
6000	-14.38	-70.69	-70.93	-70.71	-71.66

As it can be seen in Table 2, the leftmost column gives the operating frequency. The next column shows the free space loss. The next 4 columns illustrate the received signal strength passing carbon fiber materials with different orientation respectively, $[0^\circ/90^\circ, 0^\circ/90^\circ]$, $[0^\circ/90^\circ, 0^\circ/90^\circ, 0^\circ/90^\circ]$, $[0^\circ/90^\circ, (0^\circ/90^\circ)_G, 0^\circ/90^\circ]$, and $[0^\circ/90^\circ, (0^\circ/90^\circ)_G, 0^\circ/90^\circ, (0^\circ/90^\circ)_G, 0^\circ/90^\circ]$.

It can be seen from Table 2 that loss values in the frequency range between 900 and 6000 MHz did not change significantly compared to the samples in $[0^\circ, 90^\circ]$ and $[0^\circ, 90^\circ, 0^\circ]$ orientation prepared with unidirectional carbon fiber fabrics although the volume fraction of carbon fiber was decreased in the samples in $[0^\circ/90^\circ, 0^\circ/90^\circ]$ and $[0^\circ/90^\circ, 0^\circ/90^\circ, 0^\circ/90^\circ]$ orientation prepared with bidirectional carbon fiber fabrics. On the other hand, according to equation (3), shielding effectiveness up to 58.19 dB was achieved with the sample in $[0^\circ/90^\circ, 0^\circ/90^\circ]$ orientation, whereas the sample in $[0^\circ, 90^\circ]$ orientation showed maximum 53.98 dB shielding efficiency. Similarly, maximum shielding effectiveness of 61.48 dB was achieved with the sample in $[0^\circ/90^\circ, 0^\circ/90^\circ, 0^\circ/90^\circ]$ orientation, whereas the sample in $[0^\circ, 90^\circ, 0^\circ]$ orientation showed maximum 60.34 dB shielding efficiency. Therefore, it can be concluded that bidirectional fabric increased EMSE. According to the measurements performed in the 900-6000 MHz frequency range, the attenuation graph of electromagnetic wave for $[0^\circ, 90^\circ]$ and $[0^\circ/90^\circ, 0^\circ/90^\circ]$ orientation is depicted in Figure 8.

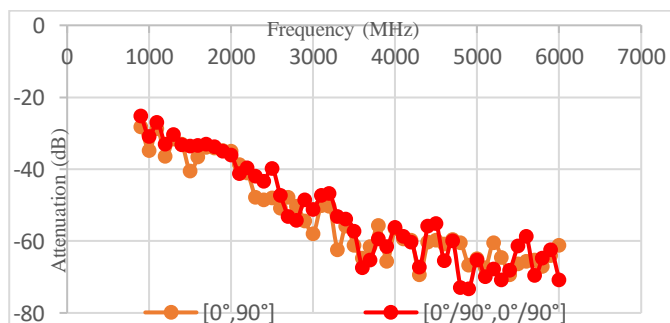


Figure 8. Attenuation for the samples in $[0^\circ, 90^\circ]$ and $[0^\circ/90^\circ, 0^\circ/90^\circ]$ orientation.

According to the measurements performed in the 900-6000 MHz frequency range, the attenuation graph of electromagnetic wave for $[0^\circ, 90^\circ, 0^\circ]$ and $[0^\circ/90^\circ, 0^\circ/90^\circ, 0^\circ/90^\circ]$ orientation is depicted in Figure 9.

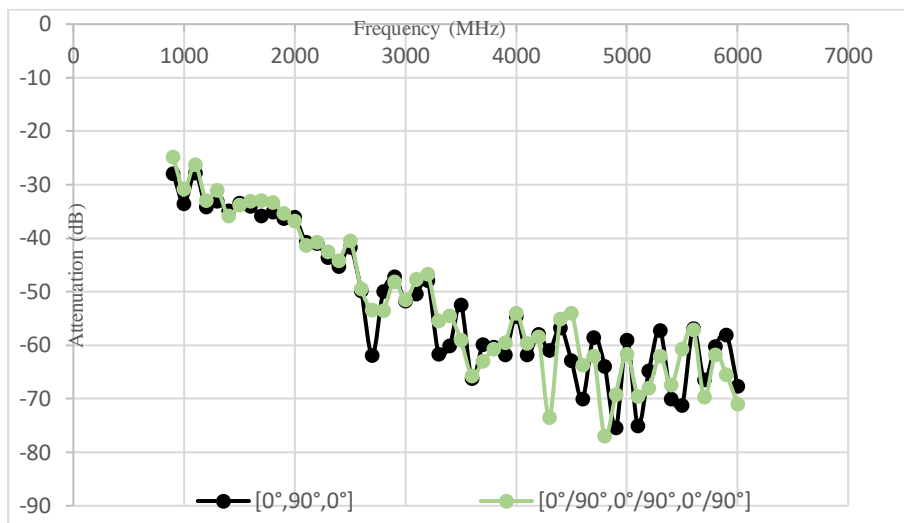


Figure 9. Attenuation for the samples in $[0^\circ, 90^\circ, 0^\circ]$ and $[0^\circ/90^\circ, 0^\circ/90^\circ, 0^\circ/90^\circ]$ orientation.

Also, it can be seen in the table that the use of bidirectional glass fiber has not contributed significantly to EMI shielding. For example, at 2000 MHz and $[0^\circ/90^\circ, 0^\circ/90^\circ]$ orientation, loss is -36,08 dB; however, at orientation $[0^\circ/90^\circ, (0^\circ/90^\circ)_G, 0^\circ/90^\circ]$, loss is -35.88 dB. As another example, if the operating frequency is selected as 6000 MHz, at $[0^\circ/90^\circ, 0^\circ/90^\circ]$ orientation, loss is -70.69 dB, but, at $[0^\circ/90^\circ, (0^\circ/90^\circ)_G, 0^\circ/90^\circ]$, loss is -70.71 dB.

According to the measurements performed in the 900-6000 MHz frequency range, the attenuation graph of electromagnetic wave for $[0^\circ/90^\circ, 0^\circ/90^\circ]$ and $[0^\circ/90^\circ, (0^\circ/90^\circ)_G, 0^\circ/90^\circ]$ orientation is illustrated in Figure 10.

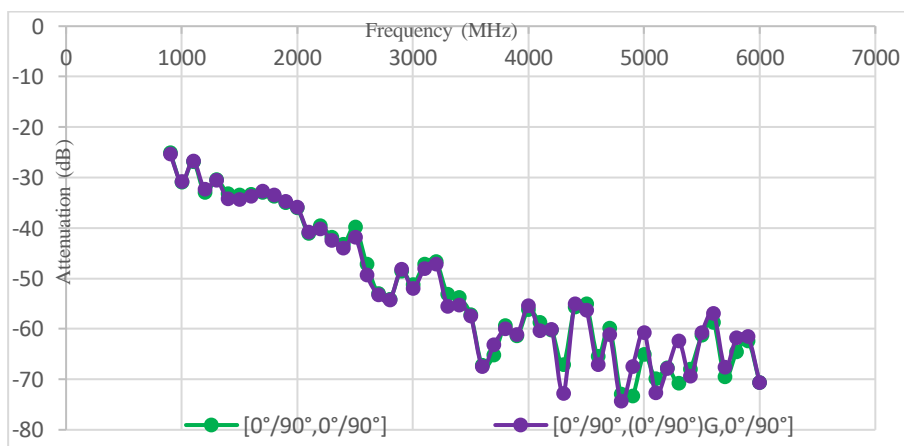


Figure 10. Attenuation for the samples in $[0^\circ/90^\circ, 0^\circ/90^\circ]$ and $[0^\circ/90^\circ, (0^\circ/90^\circ)_G, 0^\circ/90^\circ]$ orientation.

As can be seen in Figure 10, there is almost the same pattern between the samples. According to the measurements performed in the 900-6000 MHz frequency range, the attenuation graph of electromagnetic wave for the free space and $[0^\circ/90^\circ, (0^\circ/90^\circ)_G, 0^\circ/90^\circ, (0^\circ/90^\circ)_G, 0^\circ/90^\circ]$ orientation is depicted in Figure 11.

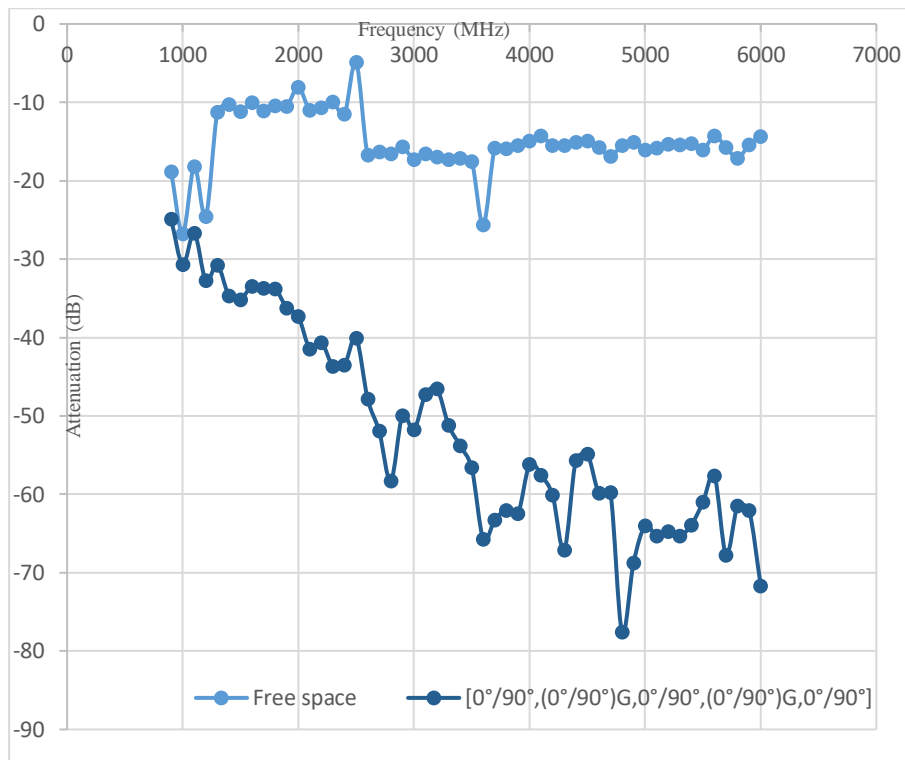


Figure 11. Attenuation for the samples in free space and $[0^\circ/90^\circ, (0^\circ/90^\circ)_G, 0^\circ/90^\circ, (0^\circ/90^\circ)_G, 0^\circ/90^\circ]$ orientation.

As it is seen in Figure 11, attenuation patterns of the material oriented in $[0^\circ/90^\circ, (0^\circ/90^\circ)_G, 0^\circ/90^\circ, (0^\circ/90^\circ)_G, 0^\circ/90^\circ]$ and free space are highly different. Especially in high frequencies, there is more than 60 dB difference.

4. Conclusion

In this study, the electromagnetic interference (EMI) shielding characteristics of carbon fiber epoxy composite samples manufactured were investigated. The measurement results indicated that carbon fiber could be utilized as a shielding material. In order to increase the shielding abilities of carbon fiber reinforced polymer composites (CFRP), it was verified that the fiber orientation was one of the most effective parameters. It was observed that the electromagnetic shielding effectiveness (EMSE) increased since the absorption loss of electromagnetic wave increased when the orientation angle is 90° , which is perpendicular to the electromagnetic wave propagation direction. Another parameter that affected the EMI shielding was fabric type. It was observed that use of bidirectional fabrics increased the EMSE. Furthermore, according to the results, the number of plies has fewer effects on EMSE than the orientation angle. Therefore, when designing composite laminates involving carbon fibers, determining the most effective fiber orientation, rather than increasing the number of plies, is suggested to provide a better shielding. Also, the cost will reduce since the use of the redundant fiber fabric and epoxy resin is avoided.

Acknowledgement

This work is supported partially by Scientific Research Projects Department (BAP) of Bursa Technical University under the grant no. 200Y013.

References

- [1] Chung, D. D. L. (2001). Electromagnetic interference shielding effectiveness of carbon materials. *Carbon*, 39: 279-285.
- [2] Kim, H. G., Shin, H. J., Kim, G. C., Park, H. J., Moon, H. J. and Kwac, L. K. (2014). Electromagnetic interference shielding characteristics for orientation angle and number of plies of carbon fiber reinforced plastic. *Carbon letters*, 15: 268-276.
- [3] Arik, E. and Tabakcioglu, M.B. (2017). Reducing emi by multiple slits shielding, *9th International Conference on Electronics, Computers and Artificial Intelligence*, pp. 1-4.
- [4] Ding, S.J., Zhao, Y.Z., Ge, D.B. (2008). Research progress in electromagnetic shielding materials. *Materials Review* 22.4.
- [5] Williams, N., Varadan, V.K., Ghodgaonkar, D. and Varadan, V.V. (1990). Measurement of transmission and reflection of conductive lossy polymers at millimeter-wave frequencies. *IEEE transactions on electromagnetic compatibility*, 32: 236-240.
- [6] Rea, S., Linton, D., Orr, E. and McConnell, J. (2005). Electromagnetic shielding properties of carbon fibre composites in avionic systems. *Mikrotalasna revija*, 11: 29-32.
- [7] Amran, Y. M., Alyousef, R., Alabduljabbar, H., Alaskar, A., & Alrshoudi, F. (2020). Properties and water penetration of structural concrete wrapped with CFRP. *Results in Engineering*, 5, 100094.
- [8] Liu, Z., Zhou, Z., & Hou, Q. (2021, October). Improvement on Electric Conductivity of Carbon Fiber Reinforced Plastic Composites. In *2021 IEEE 5th Information Technology, Networking, Electronic and Automation Control Conference (ITNEC)* (Vol. 5, pp. 632-635). IEEE.
- [9] Jana, P. B., Mallick, A. K. and De, S. K. (1992). Effects of sample thickness and fiber aspect ratio on emi shielding effectiveness of carbon fiber filled polychloroprene composites in the x-band frequency range. *IEEE transactions on electromagnetic compatibility*, 34: 478-481.
- [10] Jones, R. M. (1975). *Mechanism of composites materials*, McGraw-Hill Book Co., New York, 2nd Edition.
- [11] Mohan, L., Kumar, T. N., Karakkad, S., & Krishnan, S. T. (2021). Development of Cost-Effective Carbon Nanofiber Epoxy Nanocomposites for Lightweight Wideband EMI Shielding Application. *IEEE Transactions on Nanotechnology*, 20, 627-634.
- [12] Luo, X., & Chung, D. D. L. (1999). Electromagnetic interference shielding using continuous carbon-fiber carbon-matrix and polymer-matrix composites, *Composites Part B: Engineering*, 30(3), 227-231.
- [13] Ucar, N., Kayaoğlu, B. K., Bilge, A., Gurel, G., Sencandan, P., & Paker, S. (2018). Electromagnetic shielding effectiveness of carbon fabric/epoxy composite with continuous graphene oxide fiber and multiwalled carbon nanotube. *Journal of Composite Materials*, 52(24), 3341-3350.
- [14] Jaroszewski, M, Thomas, S., Rane, A.V. (2018). *Advanced materials for electromagnetic shielding: fundamentals, properties, and applications*. John Wiley & Sons.
- [15] Sultan Aljibori, H.S., Mohamad Alosfur, F.K., Ridha, N.J. and Salim, S. (2016). A study on thermal diffusivity and dielectric properties of epoxy matrix reinforced by fibers material. *Journal of Kerbala University*, 12: 42-53.
- [16] Coskun, Y. and Tabakcioglu, M.B. (2021). Electromagnetic Shielding Characteristics of Oriented Carbon Fiber Epoxy Composites”, *EMC Turkey Conference*, Submitted.



Self-Healing Carbon Fiber Composites with Thermoplastic Polymers

Gokcenur Saglam^{1*}  Ayse Celik Bedeloglu² 

^{1,2} *Department of Polymer Materials Engineering, Bursa Technical University, 16310 Bursa, TURKEY*

Abstract

The utilization areas of composite materials are increasing day by day. However, these materials are difficult and expensive to manufacture. In addition, since they are thermoset structures, their recycling is very limited in case of damage. Self-healing materials are the ones that automatically and independently heal or repair the damage caused by any factors, without external intervention. Self-healing polymeric materials are in the range of smart materials. Research on self-healing polymers and polymer composites using this effect has increased rapidly in recent years due to the advantages such as cost reduction and less labour requirement that the current topic provides. In this review, first of all, brief information about self-healing mechanisms used in composites will be given in the light of the studies in literature, then the use of stitch method in composites and self-healing composites will be mentioned and finally, the test methods of self-healing composites will be addressed.

Keywords: 3-Dimensional reinforcement, carbon fibre reinforced polymers (CFRPs), self-healing, self-repairing, self-mendable, stitching process, filament

Cite this paper as:

Saglam, G. and Bedeloglu Celik, A. (2022). *Healing Carbon Fiber Composites with Thermoplastic Polymers*. Journal of Innovative Science and Engineering, 6(2):201-219

*Corresponding author: Gokcenur Saglam
E-mail: gkc.nur_saglam@hotmail.com

Received Date:01/07/2021
Accepted Date:09/11/2021
© Copyright 2022 by
Bursa Technical University. Available
online at <http://jise.btu.edu.tr/>



The works published in Journal of Innovative Science and Engineering (JISE) are licensed under a Creative Commons Attribution-NonCommercial 4.0 International License.

1. Introduction

Recent studies show that fossil fuels are a significant contributor to the greenhouse effect, accounting for about a quarter of total carbon dioxide emissions [1]. The European Union aims to reduce greenhouse gas emission values below 60% by 2050 within the scope of the Kyoto Protocol [2]. There is a legal obligation in the automotive industry in this regard. Decreasing the CO₂ emission level to 95 g/km in 2021 has become the most important issue for vehicle manufacturers today. The most common work done on this topic is to lightweight [3].

Due to its high strength, good fatigue resistance, lightweight and easy processability, composite materials have growing use in important sectors such as automotive, machinery, aviation, space, defence, white goods, and rail systems[4], [5]. This multi-phase system consists of matrix material including polymer, metal, inorganic non-metallic materials and reinforcing materials including fibres and particles, as shown in figure 1. The matrix material is a structure that binds the reinforcement materials together. It also ensures that the load on it is evenly distributed to the reinforcement materials [3].

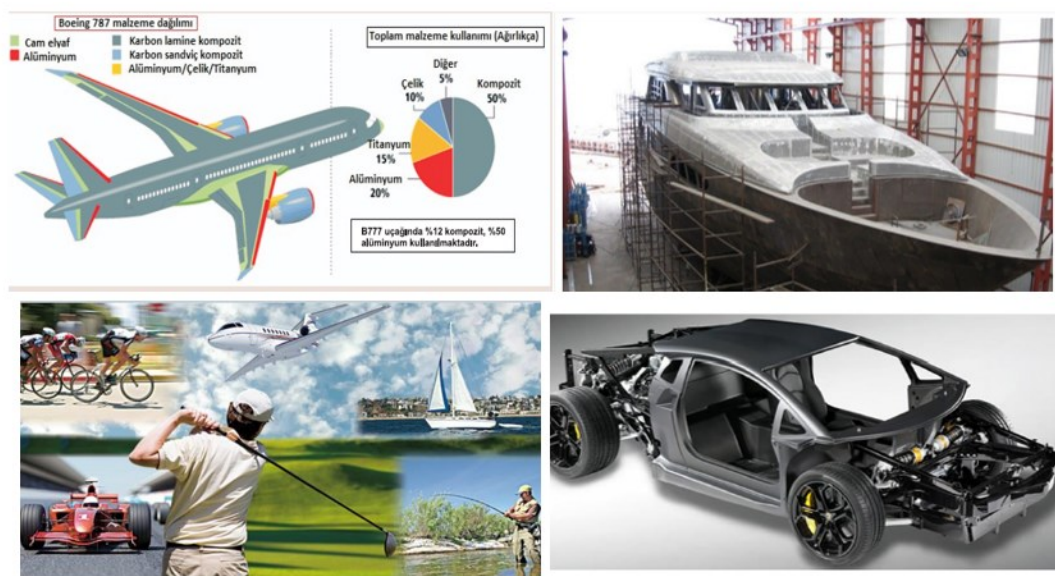


Figure 1. Utilization areas of composite materials [6]

Various fibres such as carbon fibres, glass fibres, aramid fibres, polyethylene fibres, cellulose-based fibres including banana, jute, sisal, flax and hemp, boron fibres, silicon carbide fibres, alumina fibres, etc. are often used to obtain fibre-reinforced composites with advanced or functional composites [7].

Among all different types of composites, fibre-reinforced polymer composites are preferable in many areas since they have high specific strength, high specific modulus, good fatigue resistance, high damage tolerance and good damping characteristics. Fibre-reinforced polymer composites (FRPCs) are mostly formed by overlapping multiple FRPC or prepreg layers and curing them under heat and pressure [9]. With the help of their tailorable and adjustable properties, advanced composites can provide some important advantages including weight reduction, longer shell and usage life compared to conventional composites, (i.e. electrical or thermal)[8]. However, material and manufacturing costs are

high to develop and produce in advanced composites. Besides, the matrix materials are still too weak to fulfil high-performance applications and also, reuse or recycling of both matrix and reinforcement can be difficult [8]. Another important point is that the long-term durability of FRPCs materials is still problematic. As shown in figure 2, stresses occurring during the production and use of composites, as well as deterioration, decay, and wearing due to environmental conditions (such as temperature, humidity, UV, scratches) lead to the straightforward emergence of the existing matrix crack or delamination in FRPCs while controlling and repairing these damages, which is difficult and costly [10]–[12]. The formation of these cracks leads to a decrease in the mechanical properties of the material and a shorter service life [13].

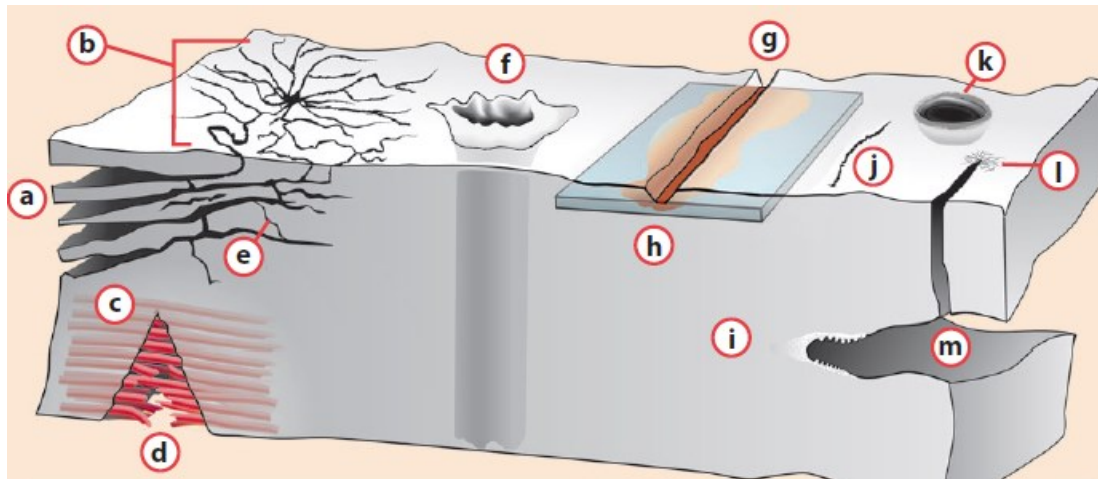


Figure 2. Damage modes in polymer composites [14]

In such cases, damaged parts are tried to be repaired with patch, welding, resin curing and bonding techniques [15]. However, these methods are not self-actualized. That is, they are not automatic and also expensive, technically difficult and time-consuming [16], [17]. This issue is an important research topic worldwide as the repair of the damage creates a serious financial problem. Developing countries are doing various studies on this subject. Among these studies, self-healing materials gain importance. Market analyses on this subject are shown in figure 3. It is estimated that the self-healing composites market will have grown 45.30% from 2021 to 2028 [18].



Figure 3. Global self-healing composites market [18].

Therefore, different approaches including self-healing processes were studied to improve the material properties and process.

2. Self-Healing Mechanisms in Composites

Self-healing can be defined as the ability of a material to heal the damage automatically and autonomously without the need for any external intervention [19]. In literature, several terms are used to describe such property in materials, such as self-repairing/healing/mendable, autonomic healing/repair. Self-healing materials range from polymers to metals and ceramics. Polymers are of great interest, especially in the field of self-healing composites due to their advantages including easy processability and low cost. As polymers can have very different improvement mechanisms compared to a wide range of application areas and other material classes, intensive studies are carried out in this field [20].

2.1. Extrinsic Self-Healing

For a long time, several studies have been carried out to eliminate the mechanical breakage and delamination problems of FRPCs and improve their service life; these efforts continue to improve the properties of existing composites or to heal the damaged composites [20]. If we look at the latter, studies are proceeding on two different methods: external and internal self-healing for the self-healing of composite materials [19], [21], [22]. Among them, the extrinsic self-healing method is divided into microcapsule [23]–[25] and microvascular method (Figure 4) [12], [26], [27]. Fluids are used as a healing agent in both methods. The main mechanism of these techniques can be expressed as follows [28]:

- 1-Breakdown of the capsule / vascular structure as a result of damage
- 2-Spreading of the self-healing liquid over the damaged area
- 3-Reaction of the healing agent in the damaged area.

In the self-healing mechanism of composites with microcapsules, the properties of shell and core materials are the most important parameters that determine the performance of this mechanism [29]–[32]. A wide variety of microcapsulation techniques is classified as in situ polymerization, interfacial polymerization, collecting emulsion polymerization, miniemulsion polymerization, solvent evaporation / solvent extraction and sol-gel polymerization based on the wall formation mechanism to encapsulate healing agents as mentioned in literature [33]. Among the microencapsulated healing agents, efficient healing systems are as follows: Single capsule system, Capsule/dispersed catalyst system, Phase-separated droplet/capsule system, double capsule system and all-in-one capsule system [34]. The main disadvantage of this method is that if the self-healing agent is released from the capsule/vascular system, the existing healing agent is depleted and in this way, a single local undesired healing occurs [35].



Figure 4. a) microencapsulation of healing agents and b) intrinsic self-healing mechanism [36]

2.2. Intrinsic Self-Healing

Unlike extrinsic self-healing mechanisms, intrinsic self-healing mechanism does not include a stored healing agent. However, this mechanism is based on the specific molecular structures of the materials and the performance of the polymers. Intrinsic healing mechanism is based on different approaches such as thermally reversible reactions (Diels–Alder (DA)) [21], [37], dynamic covalent bond reformation and reshuffling [38], ionomers [39], [40], dynamics of supramolecular chemistry or combinations [41], photochemical [42]–[44], dispersion of meltable thermoplastic materials [10], [45], [46], solvents and etc. [47]. A schematic representation of the Diels–Alder based shape memory assisted self-healing process is depicted in Fig. 5. [48].

The intrinsic mechanism is less complicated than the extrinsic self-healing mechanism, since the intrinsic mechanism may perform more than one healing process while there is no need to have the stored healing agent for this repair. Besides, the need for external stimuli (such as heat, light, UV) is a disadvantage [49] and internal self-healing is often limited to repairing a small damaged area [50].

Moreover, among the other healing agents, EMAA has been found to be the most effective and durable curing agent, since the acid group in its structure reacts strongly with hydroxyl groups in the epoxy [64].

3. Self-Healing Composites by Stitching

3.1. Stitching Process in Composites

Carbon fiber reinforced composite (CFRC) materials are used in many different industries to provide high mechanical properties and significant weight savings due to their high in-plane specific strength and stiffness. However, carbon fiber is relatively expensive compared to other reinforcement materials. In addition, composite materials have low fracture toughness and low damage tolerance due to their high sensitivity to out-of-plane fracture. For this reason, researchers are working on different methods to increase translaminar strength and reduce delamination formation. In composites, the use of fabrics produced by weaving, knitting or braiding with different weave types, or stitching composites with special threads and filaments and then laminating them can increase the strength of the structure and prevent crack propagation [65] [66].

The type and structure of the seam applied to composite materials is one of the most important parameters affecting the performance of the composite. As seen in Figure 6, 4 different stitching types are applied: Lock stitch, Modified Lock stitch, Chain stitch and Dual lock stitch. While lock stitches are used in the fabric industry, other stitch types are frequently used in the composite industry. [67].

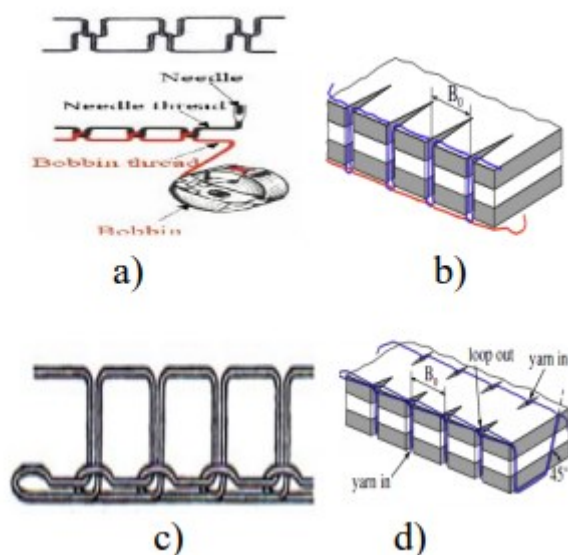


Figure 6. Stitching Types (a) Lock stitch; (b) Modified Lock stitch; (c) Chain stitch and (d) Dual lock stitch [68]

Stitching the composites is advantageous over other textile processes as it allows the stitching of both dry fabric and uncured prepreg layers [69]. Constructing structural parts such as fittings from composite materials requires more mechanical strength. Delamination damage caused by impact occurs at joints or load application centres of structural parts made of composite materials. In the future, a technology that allows a specific and local effect on the three-dimensional properties of the material will be required to form increasingly complex composite structures [70].

Through-the-thickness stitching is the most effective method for joining composite structures such as stiffeners, lap joints and wing/spar joints is shown in Figure 7. This method increases high in-plane strength, interlaminar fracture toughness, impact damage tolerance [71], low cost, high in-plane strength, interlaminar fracture toughness and tensile strength in composite materials [72]–[74]. It also has a higher resistance to delamination cracking under low energy, high energy, dynamic loading and ballistic effects [75], [76].

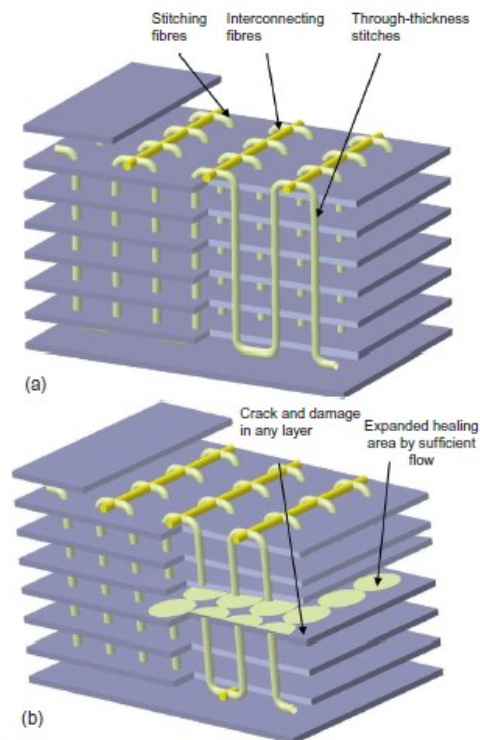


Figure 7. Architecture of the EMAA stitches in the carbon fibre–epoxy composite (a) before (b) after [77]

Stitched FRPC materials have an advantages as well as disadvantages [78]. Especially when the stitching needle passes through the prepreg tape or fabric, a gap is formed in the area and the fibres are separated from each other. Also needles do not easily pass through in the prepreg or tape and therefore the formation of resin-rich regions, porosity, voids, slippage of in-plane and out-of-plane fibres, fracture of fibres and crack formation between the resin occur [79].

In general the damage to composite materials, can be controlled depending on the stitching yarn type and density of stitching, filament structure and diameter, needle size and diameter, the orientation of the stitch rows [80] and processing technique [81].

3.2. Self-Healing Performance by Stitching

The self-healing thermoplastic polymers in the review will be summarized separately as particles and filament forms. While different thermoplastic polymers are used in granular form, only EMMA thermoplastic polymer is used in filament form. EMMA is preferred because its molecular structure plays a better role in the improvement of the delamination

regions formed between the layers and the filament form of EMMA, which makes it more suitable for the stitching method and more effective in recovery [56], [60], [82].

On the other hand, the use of other thermoplastic polymers other than EMMA in the form of particles for self-healing purposes can be summarized as follows: Pingkarawat et al. [56] investigated the effect of different types of healing agents (EMMA, EVA and PEGMA) on the compression, heal and tensile properties of composite materials by using different concentrations (5%, 10%, 15%). Varley et al. [62] investigated the healing mechanisms of self-healing materials using different thermoplastic polymers to investigate the healing efficiency and mechanical properties of composite materials. In this study, thermoplastic healing agents such as EMMA, EVA, SEBS, PEGMA, PVB and ABS were selected because of their chemical structures. Pingkarawat et al. [61] selected EMMA, EVA, PEGMA and ABS thermoplastic polymers as repairing agents and examined the effect of interlayered damage on composite materials and their mechanical properties. The initial healing process was PVB > EVA > SEBS ~ ABS ~ EMMA > PEGMA. However, the successive recovery ability was listed as EVA > EMAA > PEGMA > PVB > SEBS ~ ABS. Thus, it was concluded that EMMA, EVA and PEGMA are reproducible healing agents.

The molecular structures of ABS, EVA and EMMA are shown in Figure 8 [83]. Acrylonitrile–butadiene–styrene is an opaque, amorphous polymer. It is composed of the polymerization of styrene, acrylonitrile and butadiene elements as shown in Figure 7 [83]. ABS includes unsaturated hydrocarbon, nitrile, maleic anhydride and cyanide functional groups which react with epoxy groups. However, due to its high melting temperature, high viscosity, low glass transition temperature and poor adhesion, its self-healing efficiency is low [62].

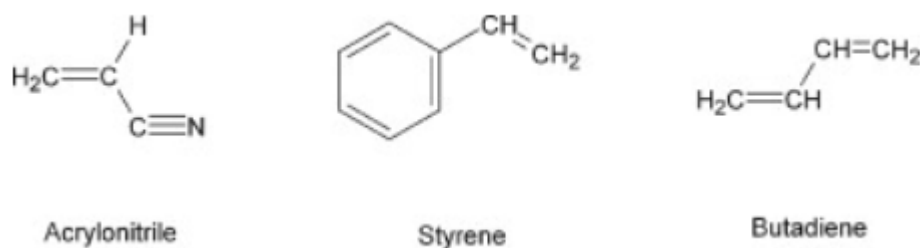


Figure 8. Chemical structure of ABS raw materials [83]

EVA is a random copolymer and it is made of with varying amounts vinyl acetate (VA) and ethylene. The end property depends on vinyl acetate (VA) content. The elastomeric grade of EVA consists of VA content varying from 40–60 wt %, which is used in adhesives. In EVA, as the VA content increases, its crystallinity decreases, so T_m lowers [84]. The increase in VA proportion in EVA causes the growth of oxygen and O/C contribution. Corona discharges cause the emergence of new C=O groups and the creation of RCOO⁻ groups. EVA does not fully react with epoxy, but when RCOO⁻ groups are formed in its structure, the reaction takes place [85]. Compared to other thermoplastics, it has a much lower viscosity in the presence of heat and exhibits a fluid-like behaviour, so that it can easily penetrates into cracks and heal by reacting with the damaged surface [56], [62].

EMAA is used as the most effective repair agent due to its low melting point, toughness and high melt flow index [52]. It is used in the form of particles, films, fibres or filaments dispersed in the epoxy matrix and composite materials. In

general, the repair mechanism takes place in the presence of heat (about 150 ° C) between the hydroxyl group in the epoxy and the acid groups in the EMMA structure. It produces water vapour in the matrix in the presence of heat. Molten EMMA is spread to the damaged area under the influence of water vapour and is healed by reacting with the damaged structure [85]. EMMA does not run out during the reaction and a reproducible process occurs.

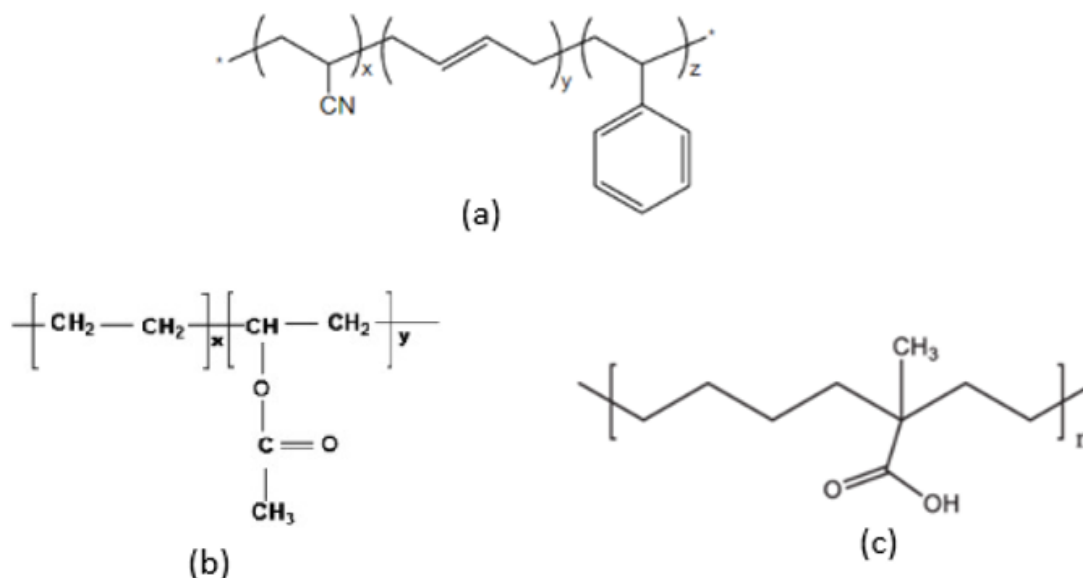


Figure 9. Chemical structure of the thermoplastic healing agents used in this work showing the range of functional group and polymer architectures. (a) acrylonitrile butadiene styrene (ABS) [86], (b) ethylene vinyl acetate (EVA) [87], (c) Poly(ethylene-co-methacrylic acid) (EMAA) [88]

As shown in the studies mentioned below, self-healing composite material development studies were examined with the stitching method. The effect of stitch density on inter-layer fracture toughness and self-healing properties of carbon-epoxy composite materials was investigated [59]. By using the EMMA filament, the stitching increased the interlaminar fracture toughness during delamination by forming a large diameter crack bridging traction zone, as shown in Figure 10.

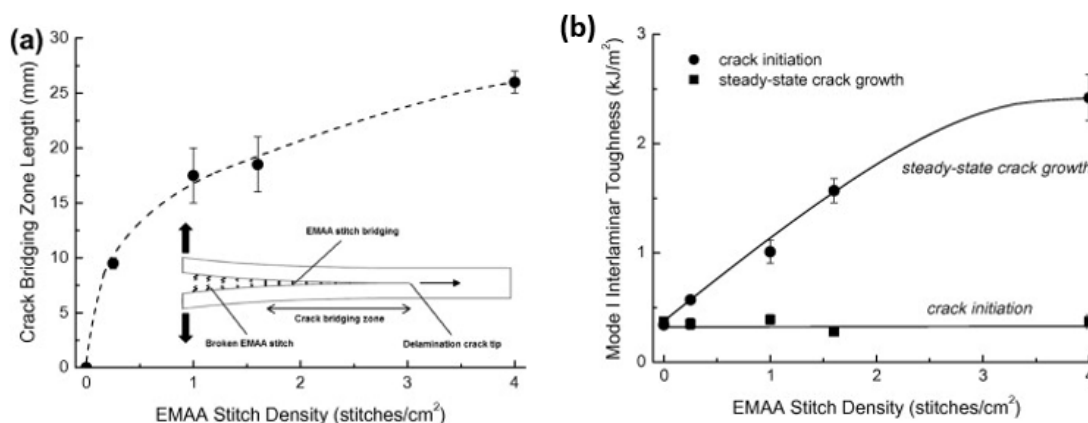


Figure 10. Effect of EMMA stitch density on the (a) length of the crack bridging zone and (b) number of stitches within the interlaminar fracture toughness [89]

Pingkarawat et al. [90] investigated the effect of stitching with EMMA filaments in carbon-epoxy laminate on self-healing and delamination toughness. According to the results, fracture toughness was completely recovered by stitching EMMA filaments. When the stitch density reached 4 stitches/cm², resistance to fatigue and fracture toughness increased due to the rise in the crack bridging zone. In another study [91], EMAA filaments with a diameter of 1.5 mm were stitched with carbon prepregs to form self-healing composite materials as shown in Figure 11.

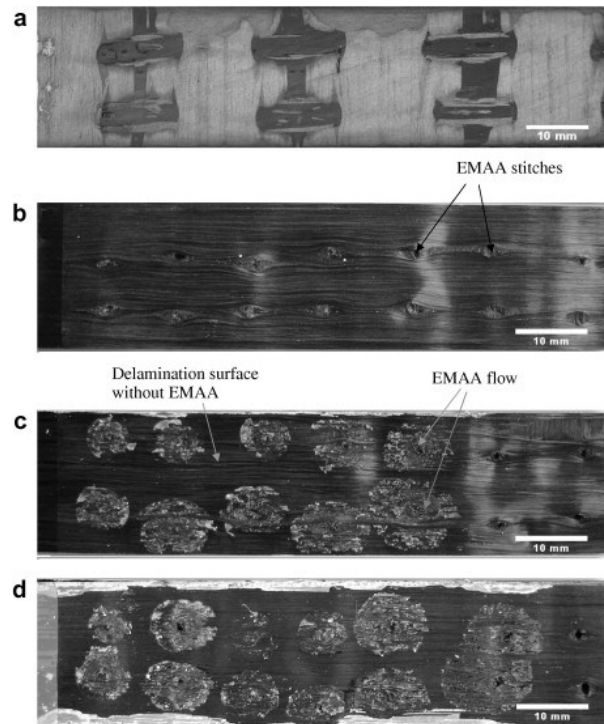


Figure 11. (a) The top surface interconnected EMAA fibres, (b) the fracture surfaces before healing, (c) after first healing and (d) after second healing [92].

In another study, self-healing efficiency, delamination toughness and mechanical properties of composite materials stitched using four different EMMA filament diameters were investigated [58]. As the diameter of the filament increases, the thickness (mm) of the composite material increases while the carbon density in it decreases and thus its mechanical properties decrease. Yang et al. [93] developed a 3-dimensional composite T-joint, through-thickness direction stitching with EMMA filaments.

4. Testing of Self-Healing Composites

Various characterization techniques are used in the evaluation of self-healing properties and performance. The most commonly used thermal characterization techniques can be summarized as follows:

1. Dynamic Mechanical Analysis (DMA) is used to determine self-healing materials, glass transition temperature and viscoelastic properties [94]
2. Differential Scanning Calorimeters (DSC) is used to measure the melting and glass transition temperature besides examining the thermal properties and curing behaviour of the matrix and self-healing agents [94]

3. Thermal Gravimetric Analysis (TGA) is widely used to determine the composition and thermal stability of the matrix and self-healing agents [94].
4. The fibre content of the laminates is measured by using the resin combustion test according to ASTM D2548-11 specifications [95].

The main mechanical characterization techniques;

1. Tensile testing determines the semi-static mechanical properties of a material according to ASTM D3039 specifications. It provides the ability to understand tensile strength and stress-strain behaviour such as stress, elongation or Young's modulus as a function of temperature, time and stress ratio [96].
 1. Mode I and Mode II interlaminar fracture toughness and self-healing efficiency are achieved using a double cantilever beam (DCB) and End-Notched Flexure (ENF) test in accordance with ASTM D5528-01 and ASTM D7905 / D7905M specifications respectively [97] [98].
 2. The three-point bending test is performed in accordance with ASTM D7264/D7264M-07 specifications to find the flexural strength properties and flexural modulus of flexure of hybrid composites [99].

Besides, the molecular structure of the self-healing composite materials is examined using Fourier transform infrared spectroscopy (FT-IR) and Scanning Electron Microscopy (SEM) is investigated before and after the formation of microbubbles formed in the material, pore structure [91].

5. Conclusion

In this article, the effects of the use of thermoplastic polymers in the form of stitches in composite materials on self-healing efficiency and other properties are presented. As a result of stitching composites with thermoplastic filaments, it has been proven that mechanical properties and repair efficiency are greatly affected. The parameters such as type and diameter of the needle and filament, seam density, laminate thickness and fabric/prepreg structure affect the properties of the self-repairing composite material to be created. Also, due to the stitching process, filament breakage, misalignment and too tight / loose stitching, many different damages on composite materials, such as resin-intensive zone formation, seam distortions, microcracking, excessive looseness or tightness can be caused. Therefore, more studies are needed in this area. In particular, optimization of stitch parameters to increase interlaminar delamination resistance has not yet been studied with a strong theoretical approach and studies are ongoing in this respect.

References

- [1] "Greenhouse gas emissions: drivers and impacts - Canada.ca." <https://www.canada.ca/en/environment-climate-change/services/environmental-indicators/greenhouse-gas-emissions-drivers-impacts.html> (accessed Aug. 16, 2021).
- [2] "Sera gazı emisyonlarının azaltımı — Avrupa Çevre Ajansı." <https://www.eea.europa.eu/tr/themes/climate/intro> (accessed Aug. 16, 2021).

- [3] “Fuel Quality | Climate Action.” https://ec.europa.eu/clima/policies/transport/fuel_en (accessed Aug. 16, 2021).
- [4] G. S. Cole and A. M. Sherman, “Light weight materials for automotive applications,” *Materials Characterization*, 1995, doi: 10.1016/1044-5803(95)00063-1.
- [5] C. Soutis, “Fibre reinforced composites in aircraft construction,” *Progress in Aerospace Sciences*, vol. 41, no. 2. Elsevier Ltd, pp. 143–151, 2005. doi: 10.1016/j.paerosci.2005.02.004.
- [6] M. Zor, “Kompozit Malzemelerle İlgili Genel Bilgiler”, doi: 10.01.2018.
- [7] G. Lubin, *Handbook of Composites*. 1982. doi: 10.1007/978-1-4615-7139-1.
- [8] Y. di Boon and S. C. Joshi, “A review of methods for improving interlaminar interfaces and fracture toughness of laminated composites,” *Materials Today Communications*, vol. 22, Mar. 2020, doi: 10.1016/j.mtcomm.2019.100830.
- [9] S. A. Hayes, F. R. Jones, K. Marshiya, and W. Zhang, “A self-healing thermosetting composite material,” *Composites Part A: Applied Science and Manufacturing*, 2007, doi: 10.1016/j.compositesa.2006.06.008.
- [10] R. Luterbacher, T. S. Coope, R. S. Trask, and I. P. Bond, “Vascular self-healing within carbon fibre reinforced polymer stringer run-out configurations,” *Composites Science and Technology*, vol. 136, pp. 67–75, 2016, doi: 10.1016/j.compscitech.2016.10.007.
- [11] G. J. Williams, “Self-Healing Functionality for Cfrp,” no. April, pp. 1–8, 2007.
- [12] A. C. Garg, “Delamination-a damage mode in composite structures,” *Engineering Fracture Mechanics*, 1988, doi: 10.1016/0013-7944(88)90181-6.
- [13] B. J. Blaiszik, S. L. B. Kramer, S. C. Olugebefola, J. S. Moore, N. R. Sottos, and S. R. White, “Self-healing polymers and composites,” *Annual Review of Materials Research*, 2010, doi: 10.1146/annurev-matsci-070909-104532.
- [14] D. Y. Wu, S. Meure, and D. Solomon, “Self-healing polymeric materials: A review of recent developments,” *Progress in Polymer Science (Oxford)*. 2008. doi: 10.1016/j.progpolymsci.2008.02.001.
- [15] Y. Chen, A. M. Kushner, G. A. Williams, and Z. Guan, “Multiphase design of autonomic self-healing thermoplastic elastomers,” *Nature Chemistry*, 2012, doi: 10.1038/nchem.1314.
- [16] K. Pingkarawat, C. H. Wang, R. J. Varley, and A. P. Mouritz, “Self-healing of delamination fatigue cracks in carbon fibre-epoxy laminate using mendable thermoplastic,” *Journal of Materials Science*, vol. 47, no. 10, pp. 4449–4456, 2012, doi: 10.1007/s10853-012-6303-8.
- [17] “Kendi Kendini İyileştiren Kompozitler Pazarı – Küresel Endüstri Eğilimleri ve 2028’e Kadar Tahmin | Veri Köprüsü Pazar Araştırması.” <https://www.databridgemarketresearch.com/reports/global-self-healing-composites-market> (accessed Aug. 16, 2021).
- [18] S. K. Ghosh, *Self-Healing Materials: Fundamentals, Design Strategies, and Applications*. 2009. doi: 10.1002/9783527625376.
- [19] F. H. Gojny, M. H. G. Wichmann, B. Fiedler, W. Bauhofer, and K. Schulte, “Influence of nano-modification on the mechanical and electrical properties of conventional fibre-reinforced composites,” *Composites Part A: Applied Science and Manufacturing*, vol. 36, no. 11, pp. 1525–1535, Nov. 2005, doi: 10.1016/j.compositesa.2005.02.007.

- [20] D. G. Bekas, K. Tsirka, D. Baltzis, and A. S. Paipetis, "Self-healing materials: A review of advances in materials, evaluation, characterization and monitoring techniques," *Composites Part B: Engineering*, vol. 87, pp. 92–119, 2016, doi: 10.1016/j.compositesb.2015.09.057.
- [21] N. J. Kanu, E. Gupta, U. K. Vates, and G. K. Singh, "Self-healing composites: A state-of-the-art review," *Composites Part A: Applied Science and Manufacturing*. 2019. doi: 10.1016/j.compositesa.2019.04.012.
- [22] E. N. Brown, S. R. White, and N. R. Sottos, "Microcapsule induced toughening in a self-healing polymer composite," *Journal of Materials Science*, 2004, doi: 10.1023/B:JMSC.0000016173.73733.dc.
- [23] M. R. Kessler, N. R. Sottos, and S. R. White, "Self-healing structural composite materials," *Composites Part A: Applied Science and Manufacturing*, vol. 34, no. 8, pp. 743–753, 2003, doi: 10.1016/S1359-835X(03)00138-6.
- [24] S. R. White et al., "Autonomic healing of polymer composites," *Nature*. 2001. doi: 10.1038/35057232.
- [25] J. W. C. Pang and I. P. Bond, "A hollow fibre reinforced polymer composite encompassing self-healing and enhanced damage visibility," *Composites Science and Technology*, 2005, doi: 10.1016/j.compscitech.2005.03.008.
- [26] K. S. Toohey, N. R. Sottos, J. A. Lewis, J. S. Moore, and S. R. White, "Self-healing materials with microvascular networks," *Nature Materials*, 2007, doi: 10.1038/nmat1934.
- [27] K. S. Toohey, N. R. Sottos, J. A. Lewis, J. S. Moore, and S. R. White, "Self-healing materials with microvascular networks," *Nature Materials*, 2007, doi: 10.1038/nmat1934.
- [28] A. Ebrahiminiya, M. Khorram, S. Hassanajili, and M. Javidi, "Modeling and optimization of the parameters affecting the in-situ microencapsulation process for producing epoxy-based self-healing anti-corrosion coatings," *Particuology*, 2018, doi: 10.1016/j.partic.2017.01.010.
- [29] H. Li, Y. Cui, Z. Li, Y. Zhu, and H. Wang, "Fabrication of microcapsules containing dual-functional tung oil and properties suitable for self-healing and self-lubricating coatings," *Progress in Organic Coatings*, 2018, doi: 10.1016/j.porgcoat.2017.11.019.
- [30] X. M. Tong, T. Zhang, M. Z. Yang, and Q. Zhang, "Preparation and characterization of novel melamine modified poly(urea-formaldehyde) self-repairing microcapsules," *Colloids and Surfaces A: Physicochemical and Engineering Aspects*, 2010, doi: 10.1016/j.colsurfa.2010.09.009.
- [31] E. N. Brown, M. R. Kessler, N. R. Sottos, and S. R. White, "In situ poly(urea-formaldehyde) microencapsulation of dicyclopentadiene," *Journal of Microencapsulation*, 2003, doi: 10.1080/0265204031000154160.
- [32] S. K. Ghosh, *Self-Healing Materials: Fundamentals, Design Strategies, and Applications*. 2009. doi: 10.1002/9783527625376.
- [33] D. Y. Zhu, M. Z. Rong, and M. Q. Zhang, "Self-healing polymeric materials based on microencapsulated healing agents: From design to preparation," *Progress in Polymer Science*. 2015. doi: 10.1016/j.progpolymsci.2015.07.002.
- [34] T. C. Mauldin and M. R. Kessler, "Self-healing polymers and composites," *International Materials Reviews*, 2010, doi: 10.1179/095066010X12646898728408.
- [35] L. Zhai, A. Narkar, and K. Ahn, "Self-healing polymers with nanomaterials and nanostructures," *Nano Today*, vol. 30. Elsevier B.V., p. 100826, Feb. 01, 2019. doi: 10.1016/j.nantod.2019.100826.

- [36] G. Postiglione, S. Turri, and M. Levi, "Effect of the plasticizer on the self-healing properties of a polymer coating based on the thermoreversible Diels-Alder reaction," *Progress in Organic Coatings*, vol. 78, pp. 526–531, 2015, doi: 10.1016/j.porgcoat.2014.05.022.
- [37] X. Chen et al., "A thermally re-mendable cross-linked polymeric material," *Science*, 2002, doi: 10.1126/science.1065879.
- [38] S. J. Kalista and T. C. Ward, "Thermal characteristics of the self-healing response in poly(ethylene-co-methacrylic acid) copolymers," *Journal of the Royal Society Interface*, vol. 4, no. 13, pp. 405–411, 2007, doi: 10.1098/rsif.2006.0169.
- [39] R. J. Varley and S. van der Zwaag, "Towards an understanding of thermally activated self-healing of an ionomer system during ballistic penetration," *Acta Materialia*, 2008, doi: 10.1016/j.actamat.2008.08.008.
- [40] R. P. Sijbesma et al., "Reversible polymers formed from self-complementary monomers using quadruple hydrogen bonding," *Science*, 1997, doi: 10.1126/science.278.5343.1601.
- [41] *,† Chan-Moon Chung, † Young-Suk Roh, † and Sung-Youl Cho, and J.-G. Kim‡, "Crack Healing in Polymeric Materials via Photochemical [2+2] Cycloaddition," 2004, doi: 10.1021/CM049394+.
- [42] N. Oya, P. Sukarsaatmadja, K. Ishida, and N. Yoshie, "Photoinduced mendable network polymer from poly(butylene adipate) end-functionalized with cinnamoyl groups," *Polymer Journal*, 2012, doi: 10.1038/pj.2012.18.
- [43] J. Ling, M. Z. Rong, and M. Q. Zhang, "Coumarin imparts repeated photochemical remendability to polyurethane," *Journal of Materials Chemistry*, 2011, doi: 10.1039/c1jm13467a.
- [44] M. C. Li and A. C. Loos, "The Effects of Processing on Interply Bond Strength of Thermoplastic Composites," *Journal of Reinforced Plastics and Composites*, 1992, doi: 10.1177/073168449201101006.
- [45] S. A. Hayes, W. Zhang, M. Branthwaite, and F. R. Jones, "Self-healing of damage in fibre-reinforced polymer-matrix composites," *Journal of the Royal Society Interface*, 2007, doi: 10.1098/rsif.2006.0209.
- [46] D. Y. Wu, S. Meure, and D. Solomon, "Self-healing polymeric materials: A review of recent developments," *Progress in Polymer Science (Oxford)*. 2008. doi: 10.1016/j.progpolymsci.2008.02.001.
- [47] G. Rivero, L. T. T. Nguyen, X. K. D. Hillewaere, and F. E. du Prez, "One-pot thermo-remendable shape memory polyurethanes," *Macromolecules*, 2014, doi: 10.1021/ma402471c.
- [48] P. C. JE et al., "Manufacturing challenges in self-healing technology for polymer composites — a review," *Journal of Materials Research and Technology*, vol. 9, no. 4, pp. 7370–7379, Jul. 2020, doi: 10.1016/j.jmrt.2020.04.082.
- [49] N. Zhong and W. Post, "Self-repair of structural and functional composites with intrinsically self-healing polymer matrices: A review," *Composites Part A: Applied Science and Manufacturing*. 2015. doi: 10.1016/j.compositesa.2014.11.028.
- [50] G. Rivero, L. T. T. Nguyen, X. K. D. Hillewaere, and F. E. Du Prez, "One-pot thermo-remendable shape memory polyurethanes," *Macromolecules*, 2014, doi: 10.1021/ma402471c.
- [51] S. Meure, D. Y. Wu, and S. Furman, "Polyethylene-co-methacrylic acid healing agents for mendable epoxy resins," *Acta Materialia*, vol. 57, no. 14, pp. 4312–4320, Aug. 2009, doi: 10.1016/j.actamat.2009.05.032.

- [52] K. Pingkarawat, C. H. Wang, R. J. Varley, and A. P. Mouritz, "Self-healing of delamination cracks in mendable epoxy matrix laminates using poly[ethylene-co-(methacrylic acid)] thermoplastic," *Composites Part A: Applied Science and Manufacturing*, 2012, doi: 10.1016/j.compositesa.2012.03.010.
- [53] C. L. Nogueira, J. M. F. de Paiva, and M. C. Rezende, "Effect of the interfacial adhesion on the tensile and impact properties of carbon fiber reinforced polypropylene matrices," *Materials Research*, 2005, doi: 10.1590/S1516-14392005000100015.
- [54] G. Li and H. Meng, Recent advances in smart self-healing polymers and composites. 2015. doi: 10.1016/C2013-0-16515-4.
- [55] K. Pingkarawat, C. H. Wang, R. J. Varley, and A. P. Mouritz, "Mechanical properties of mendable composites containing self-healing thermoplastic agents," *Composites Part A: Applied Science and Manufacturing*, 2014, doi: 10.1016/j.compositesa.2014.05.015.
- [56] I. L. Hia, V. Vahedi, and P. Pasbakhsh, "Self-Healing Polymer Composites: Prospects, Challenges, and Applications," *Polymer Reviews*. 2016. doi: 10.1080/15583724.2015.1106555.
- [57] K. Pingkarawat and A. P. Mouritz, "Stitched mendable composites: Balancing healing performance against mechanical performance," *Composite Structures*, 2015, doi: 10.1016/j.compstruct.2014.12.034.
- [58] K. Pingkarawat, C. H. Wang, R. J. Varley, and A. P. Mouritz, "Effect of mendable polymer stitch density on the toughening and healing of delamination cracks in carbon-epoxy laminates," *Composites Part A: Applied Science and Manufacturing*, 2013, doi: 10.1016/j.compositesa.2013.02.014.
- [59] M. Ravandi, W. S. Teo, L. Q. N. Tran, M. S. Yong, and T. E. Tay, "The effects of through-the-thickness stitching on the Mode I interlaminar fracture toughness of flax/epoxy composite laminates," *Materials and Design*, 2016, doi: 10.1016/j.matdes.2016.07.093.
- [60] Khomkrit Pingkarawat, "THERMOPLASTIC FIBRE STITCHING: A NEW SELF-HEALING METHOD FOR CARBON-EPOXY COMPOSITES," 2013.
- [61] R. J. Varley, D. A. Craze, A. P. Mouritz, and C. H. Wang, "Thermoplastic healing in epoxy networks: Exploring performance and mechanism of alternative healing agents," *Macromolecular Materials and Engineering*, 2013, doi: 10.1002/mame.201200394.
- [62] K. Pingkarawat, C. H. Wang, R. J. Varley, and A. P. Mouritz, "Healing of fatigue delamination cracks in carbon-epoxy composite using mendable polymer stitching," *Journal of Intelligent Material Systems and Structures*, vol. 25, no. 1, pp. 75–86, 2014, doi: 10.1177/1045389X13505005.
- [63] S. Meure, S. Furman, and S. Khor, "Poly[ethylene-co-(methacrylic acid)] healing agents for mendable carbon fiber laminates," *Macromolecular Materials and Engineering*, vol. 295, no. 5, pp. 420–424, 2010, doi: 10.1002/mame.200900345.
- [64] F. Dau, M. L. Dano, and Y. Duplessis-Kergomard, "Experimental investigations and variability considerations on 3D interlock textile composites used in low velocity soft impact loading," *Composite Structures*, 2016, doi: 10.1016/j.compstruct.2016.06.034.
- [65] H. Ahn and W. R. Yu, "Mechanical analysis of 3D braided and woven composites using fiber-based continuum analysis," *Composite Structures*, 2017, doi: 10.1016/j.compstruct.2016.11.003.
- [66] A. Saboktakin, "3D textile preforms and composites for aircraft structures: A review," *International Journal of Aviation, Aeronautics, and Aerospace*, 2019, doi: 10.15394/ijaaa.2019.1299.

- [67] A. R. Horrocks and S. C. Anand, *Handbook of technical textiles*. 2000. doi: 10.1533/9781855738966.
- [68] L. K. Jain, K. A. Dransfield, and Y. W. Mai, "On the effects of stitching in CFRPs - II. Mode II delamination toughness," *Composites Science and Technology*, 1998, doi: 10.1016/S0266-3538(97)00186-3.
- [69] C. Sickinger and A. Herrmann, "Structural Stitching as a Method to design High-Performance Composites in Future."
- [70] Y. Tada and T. Ishikawa, "Experimental evaluation of the effects of stitching on CFRP laminate specimens with various shapes and loadings," *Mechanical and corrosion properties. Series A, Key engineering materials*, 1989, doi: 10.4028/www.scientific.net/kem.37.305.
- [71] T. J. Kang and S. ho Lee, "Effect of Stitching on the Mechanical and Impact Properties of Woven Laminate Composite," *Journal of Composite Materials*, 1994, doi: 10.1177/002199839402801604.
- [72] W. C. Chung, B. Z. Jang, T. C. Chang, L. R. Hwang, and R. C. Wilcox, "Fracture behavior in stitched multidirectional composites," *Materials Science and Engineering A*, 1989, doi: 10.1016/0921-5093(89)90355-9.
- [73] K. Dransfield, C. Baillie, and Y. W. Mai, "Improving the delamination resistance of CFRP by stitching-a review," *Composites Science and Technology*, 1994, doi: 10.1016/0266-3538(94)90019-1.
- [74] L. K. Jain and Y. W. Mai, "On the effect of stitching on mode I delamination toughness of laminated composites," *Composites Science and Technology*, 1994, doi: 10.1016/0266-3538(94)90103-1.
- [75] A. P. Mouritz, "The damage to stitched GRP laminates by underwater explosion shock loading," *Composites Science and Technology*, 1995, doi: 10.1016/0266-3538(95)00122-0.
- [76] K. Pingkarawat and A. P. Mouritz, "Stitched mendable composites: Balancing healing performance against mechanical performance," *Composite Structures*, 2015, doi: 10.1016/j.compstruct.2014.12.034.
- [77] K. Dransfield, C. Baillie, and Y. W. Mai, "On stitching as a method for improving the delamination resistance of CFRPs," 1993.
- [78] H. B. Dexter and J. G. Funk, "Impact resistance and interlaminar fracture toughness of through-the-thickness reinforced graphite/epoxy," Jan. 1986, Accessed: Jun. 24, 2020. [Online]. Available: <http://ntrs.nasa.gov/search.jsp?R=19860054139>
- [79] "5th Australian Aeronautical Conference: Preprints of Papers - Tensile Properties of Thin Stitched Carbon/Epoxy Composites (Engineering Collection) - Informit." <https://search.informit.com.au/documentSummary;dn=559510268154395;res=IELENG> (accessed Dec. 14, 2019).
- [80] K. W. Furrow, A. C. Loos, and R. J. Cano, "Environmental effects on stitched RTM textile composites," *Journal of Reinforced Plastics and Composites*, 1996, doi: 10.1177/073168449601500403.
- [81] Y. Yang and M. W. Urban, "Self-healing polymeric materials," *Chemical Society Reviews*, 2013, doi: 10.1039/c3cs60109a.
- [82] V. Kostopoulos, A. Kotrotsos, S. Tsantzalis, P. Tsokanas, T. Loutas, and A. W. Bosman, "Toughening and healing of continuous fibre reinforced composites by supramolecular polymers," *Composites Science and Technology*, vol. 128, pp. 84–93, 2016, doi: 10.1016/j.compscitech.2016.03.021.
- [83] L. W. McKeen, "Styrenic Plastics," *Fatigue and Tribological Properties of Plastics and Elastomers*, pp. 51–71, Jan. 2010, doi: 10.1016/B978-0-08-096450-8.00004-1.

- [84] A. Emblem, "Plastics properties for packaging materials," *Packaging Technology*, pp. 287–309, Jan. 2012, doi: 10.1533/9780857095701.2.287.
- [85] J. Izdebska, "Corona Treatment," *Printing on Polymers: Fundamentals and Applications*, pp. 123–142, Jan. 2016, doi: 10.1016/B978-0-323-37468-2.00008-7.
- [86] S. Meure, R. J. Varley, D. Y. Wu, S. Mayo, K. Nairn, and S. Furman, "Confirmation of the healing mechanism in a mendable EMAA-epoxy resin," *European Polymer Journal*, 2012, doi: 10.1016/j.eurpolymj.2011.11.021.
- [87] C. Mariano Domingues da Silva, A. L. A. Silva, R. Pacheco, and A. M. Rocco, "Conductivity and Thermal Behaviour of Sulfonated ABS Membranes for Fuel Cell Applications," *ECS Transactions*, 2019, doi: 10.1149/1.3210642.
- [88] S. Rashtchi, P. D. Ruiz, R. Wildman, and I. Ashcroft, "Measurement of moisture content in photovoltaic panel encapsulants using spectroscopic optical coherence tomography: a feasibility study," 2012. doi: 10.1117/12.928959.
- [89] N. K. James, U. Lafont, S. van der Zwaag, and W. A. Groen, "Piezoelectric and mechanical properties of fatigue resistant, self-healing PZT-ionomer composites," *Smart Materials and Structures*, 2014, doi: 10.1088/0964-1726/23/5/055001.
- [90] K. Pingkarawat, C. H. Wang, R. J. Varley, and A. P. Mouritz, "Effect of mendable polymer stitch density on the toughening and healing of delamination cracks in carbon-epoxy laminates," *Composites Part A: Applied Science and Manufacturing*, 2013, doi: 10.1016/j.compositesa.2013.02.014.
- [91] "Thermoplastic fibre stitching: a new self-healing method for carbon-epoxy composites." https://www.researchgate.net/publication/257836051_Thermoplastic_fibre_stitching_a_new_self-healing_method_for_carbon-epoxy_composites (accessed Feb. 18, 2020).
- [92] T. Yang, C. H. Wang, J. Zhang, S. He, and A. P. Mouritz, "Toughening and self-healing of epoxy matrix laminates using mendable polymer stitching," *Composites Science and Technology*, 2012, doi: 10.1016/j.compscitech.2012.05.012.
- [93] T. Yang, C. H. Wang, J. Zhang, S. He, and A. P. Mouritz, "Toughening and self-healing of epoxy matrix laminates using mendable polymer stitching," *Composites Science and Technology*, 2012, doi: 10.1016/j.compscitech.2012.05.012.
- [94] T. Yang, J. Zhang, A. P. Mouritz, and C. H. Wang, "Healing of carbon fibre-epoxy composite T-joints using mendable polymer fibre stitching," *Composites Part B: Engineering*, 2013, doi: 10.1016/j.compositesb.2012.08.022.
- [95] A. M. Peterson, H. Kotthapalli, M. A. M. Rahmathullah, and G. R. Palmese, "Investigation of interpenetrating polymer networks for self-healing applications," *Composites Science and Technology*, 2012, doi: 10.1016/j.compscitech.2011.11.022.
- [96] S. Feih and A. P. Mouritz, "Tensile properties of carbon fibres and carbon fibre-polymer composites in fire," *Composites Part A: Applied Science and Manufacturing*, 2012, doi: 10.1016/j.compositesa.2011.06.016.
- [97] ASTM D3039, "ASTM D3039 Standard Test Method for Tensile Properties of Polymer Matrix Composite Materials -D3039 2008, Annual Book of ASTM Standards", doi: 10.1520/D3039_D3039M-17.

- [98] “ASTM D5528 - 01 Standard Test Method for Mode I Interlaminar Fracture Toughness of Unidirectional Fiber-Reinforced Polymer Matrix Composites.” <https://www.astm.org/DATABASE.CART/HISTORICAL/D5528-01.htm> (accessed Dec. 14, 2019).
- [99] L. K. Jain and Y. W. Mai, “On the effect of stitching on mode I delamination toughness of laminated composites,” *Composites Science and Technology*, 1994, doi: 10.1016/0266-3538(94)90103-1.
- [100] “ASTM D7264 / D7264M - 07 Standard Test Method for Flexural Properties of Polymer Matrix Composite Materials.” <https://www.astm.org/DATABASE.CART/HISTORICAL/D7264D7264M-07.htm> (accessed Dec. 14, 2019).



Performance Improvement of Genetic Algorithm Based Exam Seating Solution by Parameter Optimization

Fatih Agalday ^{1*} , Ali Nizam ² 

^{1*} Department of Computer Engineering, Mardin Artuklu University, 47060, Mardin, Turkey

² Department of Computer Engineering, Fatih Sultan Mehmet Foundation University, 34445, Istanbul,

Abstract

Exam seat allocation has become a complex problem, with an increasing number of students, subjects, exams, departments, and rooms in higher education institutions. The requirements and constraints of this problem demonstrate characteristics similar to extensively researched exam timetabling problems. They plan for a limited capacity effectively and efficiently. Additionally, exam seating requires a seating arrangement to reduce the number of cheating incidents. In the literature, several genetic algorithm-based methods have been recommended to prevent students, who are close friends, from sitting close during the exams while providing the best exam session arrangement. We improved the performance of the genetic algorithm using parameter optimization and a new elitism method to increase the saturation rate and accuracy. The algorithm was tested on a real-world dataset and demonstrated high potential for the realization of a high-quality seating arrangement compatible with the requirements of educational institutions.

Keywords: Data science applications in education, Genetic algorithm, Multi-parameter optimization.

Cite this paper as: Fatih A. and Ali N. (2022). Performance improvement of genetic algorithm based exam seating solution by parameter optimization, 6(2):220-232.

*Corresponding author: Ali Nizam

E-mail: ali.nizam@fsm.edu.tr

Received Date: 07/10/2021
Accepted Date: 26/07/2022 ©
Copyright 2022 by
Bursa Technical University.
Availableonline at
<http://jise.btu.edu.tr/>



The works published in the journal of Innovative Science and Engineering (JISE) are licensed under a Creative Commons Attribution-NonCommercial 4.0 International License.

1. Introduction

Cheating during academic examinations is a form of plagiarism that decreases education quality, reduces student satisfaction, and subverts the course evaluation system [1]. However, recent research has revealed that cheating is prevalent and has increased dramatically over the last thirty years [2]. According to [3], 54 percent of US and 45 percent of Canadian faculties report observing cheating during the exam, and 22 percent of US and 19 percent of Canadian students self-report serious test/exam cheating. Research in the US and Britain has repeatedly shown that more than half of university students cheat during their undergraduate years [4]. Preventing cheating in the first place is the best way to ensure fairness among students by measuring their academic achievements fairly [5].

Friendship was listed among the top five reasons as “My friend wants me to help” in the research on cheating in exams at universities [6]. In other research, the rate of copying from the closest seated colleague was higher than 50 percent, and helping others to cheat was more than 70 percent [7]. The faculty reporting rate of using an electronic device for cheating (11 percent) was lower than copying from another student with their knowledge (33 percent) and helping someone else cheat on a test (29 percent) [3]. Communication during the exam is significantly higher among neighbors who are also friends outside the examination room and unfamiliar neighbors will be less confident in interacting, which partially inhibits unwanted communication [8]. Additionally, detecting and punishing student whispering is often difficult and subjective. The easiest method to decrease cheating is to spread students out, leaving an empty seat between them in each row. Unfortunately, classroom size may not be sufficient to spread students effectively [9].

This study aims to provide the best session arrangement to prevent placing familiar students in a close location during an exam to minimize the possibility of cheating prevailing in central exams via GA. We investigated the best methods for passing elite individuals to the next population in the exam seating problem domain. In addition, we tuned the GA parameters, such as the mutation probability, crossover probability, and population size to determine reasonable settings. It reduces time consumption and manual human dependency and optimizes the usage of classroom spaces. We employed multiple parameters such as graduation from the same department or school, living with the same relative, or the same birthplace to identify friendship.

The remainder of this paper is organized as follows. Section 2 presents the motivation for the study and problem definition and describes various research works that have been conducted on exam scheduling and seating problems using GA and other methods. Section 3 discusses the selection mechanism, crossover and mutation operators, and parameters of the existing and proposed methods. Section 4 presents results that demonstrate the effectiveness of the proposed method. Finally, concluding remarks and discussions are presented in Section 5.

2. Background and Related Works

The steps of the exam scheduling process include examination timetabling, room assignment, and student seat placement. Examination timetabling begins by listing exams that cannot be scheduled in the same time slot, generating available examination time slots; and identifying available exam rooms and courses that need to be scheduled [10]. A large number of events to be scheduled and constraints imposed on timetabling make the search space for the problem extremely large. Indeed, a manual solution can require considerable effort or is nearly impossible [11]. Many constraints should be satisfied, as a course taught at many places must have the same exam

date and an invigilator can be assigned to any campus [12]. Timetabling problems have attracted the attention of the scientific community and interest in this field has increased [8]. However, the lack of room for information in currently used datasets means that the optimization function used to measure solutions does not incorporate all necessary issues [13].

The problem of assigning exams to classrooms has been investigated in research using seating capacity in the classroom as a hard constraint [14]. Some researchers have focused on the invigilation schedule which aims to assign rooms or invigilators after the exam timetable has been approved; however, it has received less attention from the research community because of the lack of available datasets [15]. There is relatively little research on the assignment of exams to classrooms by targeting the minimization of the total used capacity [16].

Generally, student placement on the seat is not considered when generating examination timetables. Some studies have focused on minimizing student movement between rooms by assigning them to the same room when they are scheduled to sit consecutive examinations on the same day [10]. Students should not undergo two examinations simultaneously over a designated period within a finite area of space. A viable solution must satisfy this ‘hard’ constraint [17].

When the focus shifts to the prevention of cheating, the successful distribution of seats in an exam is one of the primary concerns of a well-prepared exam hall, ensuring the maximum distance between students while making the best use of seats. The general aim is to replace friends separately during an exam and place non-befriended students next to each other as much as possible [8]. However, exam seats are usually allocated manually based on the basic rules [18]. Many institutes perform this task manually using Excel sheets causing excessive wastage of time and manpower [19].

Social network analysis has been used to detect student friendships and avoid cheating [8]. Friendships constructed by a friend’s friend create a complex network topology [20]. Because not every student has a public social media account, we determined the friendship level via the student’s department, program, and birthplace parameters using a real-world dataset.

3. Methods

This section explains the proposed method, its advantages, and the differences between the proposed and previous methods.

3.1. Genetical Algorithm Basic Structure

The solution to exam seating is constraint programming, which solves a given set of variables, a finite set of possible values that can be assigned to each variable, a list of constraints, and values of the variables that satisfy every constraint as the timetabling problem [21]. GA, which is a suitable optimization technique for solving hard and highly constrained problems, is a popular meta-heuristic method that addresses the university timetabling problem [22]. GA was chosen to solve the exam seating problem because of its robustness in many studies [23–26]. In addition, in some studies, the selection strategies of GA were incorporated into other algorithms, such as bee colony optimization, to increase the effectiveness of the solution to the examination timetabling problem [27].

GA which was first introduced by John Holland [28] allows the building of a solution inspired by nature. It aims to find the best solution for the survival of living organisms that adapt to the natural environment and the elimination

of living organisms that cannot adapt [29]. The population is composed of chromosomes, and the population size (PS) is the chromosome number. The initial population is generated from random values [30] and interchanges to produce new individuals (chromosomes). The population is assigned a suitability value by comparing each solution with other solutions using a fitness function for each generation number (GN) and the best individuals of the population are transferred to the next generation. This iteration continues to try solutions until the fitness value is zero or the maximum number of generations (GN_{max}) is reached.

The natural selection process can be clogged somewhere and circulates the same solution. Crossing and mutation are two important genetic operators used to create new solutions [31]. In the crossover operation, the bits of the first chromosome and the other chromosome shift according to a predefined rule to produce chromosomes with different structures and increase chromosome richness, as shown in Figure 1a.

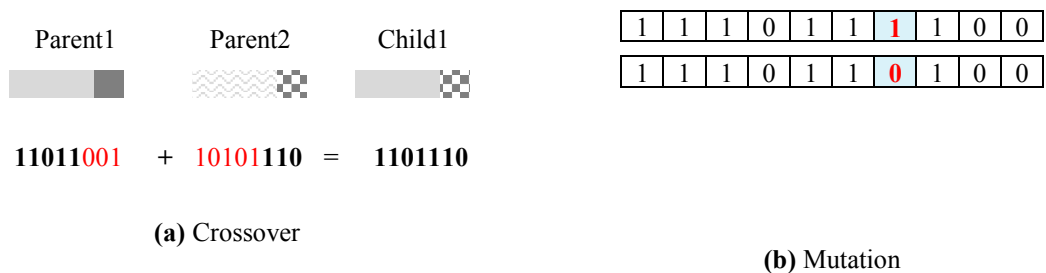


Figure 1. Operators in GA.

The mutation operator changes the homogeneous structure in the vicious circle formed when searching for the best solution. If all chromosomes are identical or similar, the optimum mean fit value may not be reached. Randomly selected genes in the chromosome are changed as shown in Figure 1b.

3.2. Applying Genetical Algorithm to Exam Seating

The exam seating problem has a variety of constraints similar to those of the timetabling problem. When searching for an optimal solution, E events can be allocated to P places in P^E ways that create an NP-hard problem [32]. Heuristic algorithms are used to solve NP problems in polynomial time or approximate it. Therefore, GA was applied to exam seating in the literature [33]. The students were placed into classrooms with different capacities as a matrix layout as shown in Figure 2.

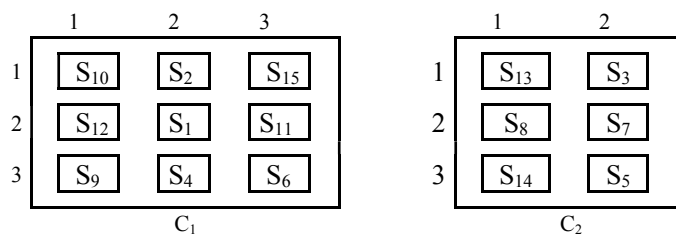


Figure 2. The session layout in the classrooms.

The initial population, chromosome encoding, and fitness function structures are arranged to solve the exam seating problem. The pseudo-code of the proposed GA method is shown in Figure 3.

```

begin
  Data: Create the initial population
  Result: F
while do
  Calculate F while (GNi < GNmax): The modified fitness function is applied on each chromosome;
  Cumulative Probability Calculation: Roulette wheel transfer to the intermediate population;
  CrossOver: Selection of chromosome pairs with an integrated repair algorithm;
  Mutation: Permutation coding;
  Elitism: Replace the worst members of the existing population with the best members of the intermediate
  population;
end

```

Figure 3. The proposed GA for exam seating

3.3. Chromosome Encoding and The Initial Population

Each chromosome was constructed by using a random distribution of student information to create an initial population. The initialization procedure is an important issue in GA implementation because it supports the fact that individuals across the first generation spread across the entire search space with as much diversity as possible [34]. The index information can be given by:

$$c \in \{1, \dots, R\} \text{ where } R \text{ is the number of classrooms} \tag{1}$$

$$i \in \{1, \dots, L\} \text{ where } L \text{ is the number of students} \tag{2}$$

$$t \in \{1, \dots, T\} \text{ where } T \text{ is the total number of seats} \tag{3}$$

$$s_i = (a_1, a_2, \dots, a_n) \text{ where } s_i \text{ is a tuple containing the attribute } (a) \text{ of } i\text{th student} \tag{4}$$

The form and definition of the chromosome structure are very important to improve the performance of the algorithm. One student was placed in each row or a chromosome $index = i$ represents $(ClassId, RowId, ColumnId)$ information [36]. The other information about the student such as undergraduate program, birthplace, and residence information has been stored in another list and referenced using student identity to reach a light and high-performance structure. Figure 4 shows an example distribution of a chromosome structure for 15 students and 2 classrooms.

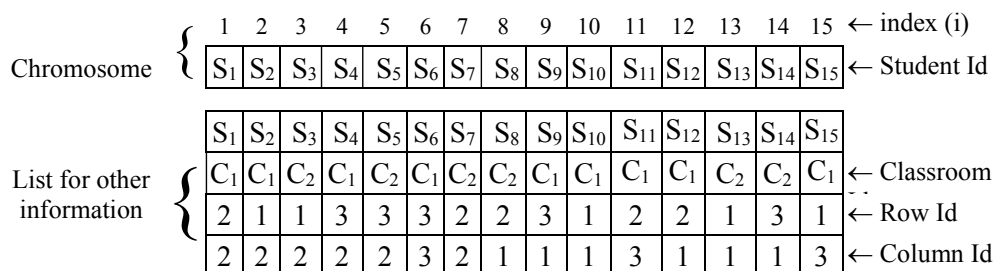


Figure 4. Chromosome structure

3.4. The Fitness Function

The system creates a penalty when two students are likely to recognize each other sitting back-to-back or next to each other in a chromosome. The fitness function $F(k)$, which represents the total penalty for k th generation, is given by Equation (5) as

$$F(k) = \sum_{i=1}^L \sum_{j=i+1}^L proximity(s_i, s_j) \tag{5}$$

To detect proximity, the relationship immediately behind and to the right of each student's seat is examined. When proximity is detected, the chromosome receives a $proximity(s_i, s_j)$ score representing the degree of proximity between the i th and j th students' locations as s_i and s_j . In Equation (6), the first row indicates that the j th student sits next to the seat of the i th student and they have the same proximity attributes. The second row indicates the j th student sitting behind the i th student. Only the seat behind the student is examined in the rightmost column of the classroom and only the seat next to the student is examined in the last row of the classroom. The proximity calculation for the fitness function is

$$proximity(t_i, t_j) = \begin{cases} 1 & \text{if } i = j + 1 \wedge (s_1 = s_2) \\ 1 & \text{if } i = j + N \wedge (s_1 = s_2) \\ 0 & \text{otherwise} \end{cases} \tag{6}$$

The classroom contains a total of M rows and N columns. We accepted all friendship parameters to be the same and the similarity coefficients as 1. The fitness function is subject to the following additional constraint: more than one student cannot be assigned to one seat:

$$\sum_{i=1}^L v_{it} \leq 1 \text{ for each } i \in 1, \dots, L \tag{7}$$

v_{it} 1 if student i is assigned to seat t and 0 otherwise.

The target solution must minimize the fitness value to zero or near zero.

3.5. The Crossover Operator

After determining the initial population, the chromosomes are crossed according to their fitness values, and new offspring individuals are obtained at the end of each iteration to determine which individuals are the correct solution, as shown in Figure 5. s_1, s_3, s_6 have a friendship; thus, *Chromosome₂* has one close seat (s_1, s_3) and $F = 1/3$. *Chromosome₃* has two close seats ($(s_1, s_3), (s_1, s_3)$) and $F = 2/3$.

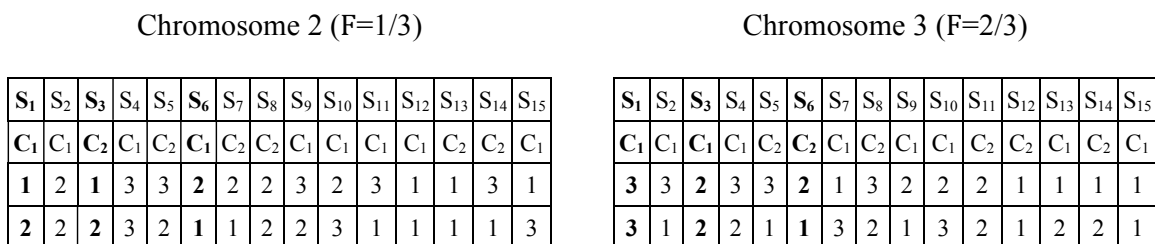


Figure 5. The crossover of chromosomes

i .th chromosome roulette selection probability function is given in Equation (8):

$$P(i) = \frac{F(i)}{\sum_{j=0}^{CN} F(j)} \tag{8}$$

Chromosome number (CN) defines the crossing point. Candidate chromosomes for selection are determined by generating a random number using a crossing point. For example, when random point 5 is determined, the first five genes of $Chromosome_2$ and the last ten genes of $Chromosome_3$ combine to form the *NewChromosome*.

Chromosomes that will survive in the next population are determined by cumulative ratio values using a randomly generated number between 0 and 1 in the roulette wheel selection method. Crosspoint selection is implemented by generating random values for chromosomes that address the locations of the chromosome pairs to be crossed. For example, the first pair of chromosomes to be crossed is 7 and 2, when random numbers (7 – 2 – 5 – 8 – 1 – 4 – 3 – 6) are generated in a population. The genes after the crossing point of the first and second chromosomes are combined to obtain the second offspring.

S ₁	S ₂	S ₃	S ₄	S ₅	S ₆	S ₇	S ₈	S ₉	S ₁₀	S ₁₁	S ₁₂	S ₁₃	S ₁₄	S ₁₅
C ₁	C ₁	C ₂	C ₁	C ₂	C ₂	C ₁	C ₂	C ₁	C ₁	C ₂	C ₂	C ₁	C ₂	C ₁
1	2	1	3	3	2	1	3	2	2	2	1	1	1	1
2	2	2	3	2	1	3	2	1	3	2	1	2	2	1

Figure 6. Crossover in SPCM

The direct implementation of GA crossover causes genes to repeat in the chromosome, as shown in Figure 6 [32]. When a crossover is performed without considering the repeating genes in the chromosome structure, over 20 percent of the chromosome structures are repeated causing the same student to be replaced in more than one place in the room or two different students to be replaced in the same seat [37]. In the example above, the students, s_5 and s_8 , were in the third seat of the second classroom. Therefore, this settlement plan cannot be applied in the real world. During the exchange process, the generic partially mapped crossover operator performs no feasibility check by default, and a repair mechanism is required to make each child chromosome feasible [34]. An improved crossover model was designed to eliminate an additional repair function as satisfying the constraints of the problem [37]. The crossover of i th gene in chromosomes X and Y is given by equation (9):

$$PMX = \{X_{Y[i]} = X_i \text{ then } X_{[i]} \leftrightarrow Y_{[i]}\} \tag{9}$$

The process begins with selecting random crossover points on the parents. The gene on the first chromosome is copied on the same chromosome to the location of the corresponding gene on the second chromosome when transferring the segment from the first parent to the first offspring. The same procedure is repeated for the second chromosome with the parents’ roles reversed. This prevents the replication of the same seating position on the same chromosome, as shown in Figure 7.



Figure 7. Partially matched crossover [37]

The genes (7,8,4) in Chromosome₁ were crossed with the genes (9,2,1) in Chromosome₂. Gene 9 in Chromosome₂ was replaced 7 in Chromosome₁. Gene 9 in Chromosome₁ was placed at the location of gene 7 in Chromosome₁. The same process was applied to others.

3.6. Elitist Selection

Elitist selection based on cloning the best single individual from one generation to the next is popular [36]. The average fitness of the population will increase by transferring the best chromosomes to the next generation. Thus, in a previous work [37], the best chromosome of the generation, which had the best fitness value, was selected as the elite and transferred to the next generation. Although an elitist procedure is sufficient for many GA applications, there may be some cases that benefit from selection schemes that provide different types of search capabilities [36]. Our observations showed that the method of preventing repeated genes by identifying transfer location using gene values [37] caused the distribution of genes to different points during the transition and slowed down the saturation in the crossover operator. To improve system performance, this paper explores several elitist procedures for the design of GA-based exam seating. We attempted to replace a number of the worst chromosomes of the previous generation with the best chromosomes from the new generation. We evaluated the effects of varying the number of replaced chromosomes against generation number.

The effects of the MR, CR, and PS values on the results of the previous algorithms were examined in detail and then applied to our elitist selection to compare the results. We determined the best values for the parameters step-by-step and used them as the initial values for the next step. We evaluated the saturation process by observing the penalty score of each algorithm over generations until the saturation point was reached. Each test was repeated 10 times, and the results of the analysis were averaged to reduce the error rate to less than 10 [38]. The proposed algorithm was implemented using Python.

The data obtained from the distance education application and research center of a university were used in this study. The data contained 68 unique undergraduate programs, 157 birthplaces, and 138 residential addresses.

4. Results and Discussion

Although there is no common judgment on the most suitable parameter values, we used David Schaffer's experimental study values as 0.75 – 0.95 for CR, 0.005 – 0.01 for MR, and 20 – 30 for PS [39]. In addition, it is recommended to take PS as an average of 10, in which PS affects the performance [40]. Thus, PS the value was

chosen as 12, as described in [37].

The effect of the parameter values on the saturation process of the previous algorithm is shown in Figure 8a-c. When the number of generations increased, the production of defective genes in the chromosome increased respectively until the saturation point was reached. The maximum number of generations that supported reaching the maturation point was detected as in the range of 50 to 500.

It was claimed that increasing MR has a positive contribution to the solution of the problem [41]. Thus, our investigation focused on MR parameter values having a range between 0.05 and 0.3 as in [37]. However, the results indicated that low MR values provided better saturation rates as shown in Figure 8a. We evaluated the effect of PS on the results using the best CR values determined as 0.01 as shown in Figure 8b. Thus, after testing different values, the parameter values providing the best session order were chosen inside the limits mentioned in the literature [39] as CR= 0.9, MR = 0.01, and PS=20.

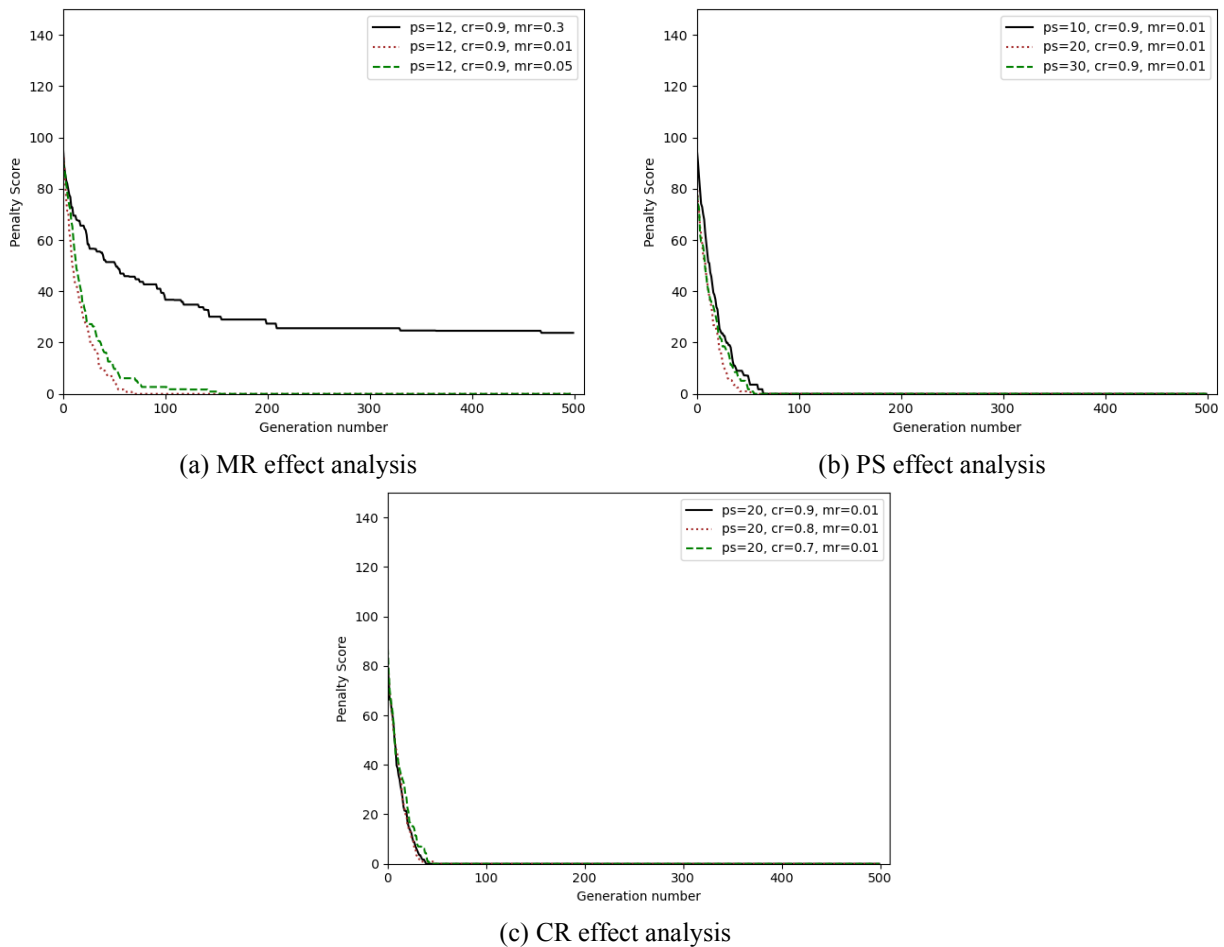


Figure 8. The effect analysis of the parameters

Figure 9 shows the parametric analysis of the proposed elitism procedure. We have added the results of the previous algorithm for the determined parameter values above to allow a comparison of the results of different elitisms to the figure.

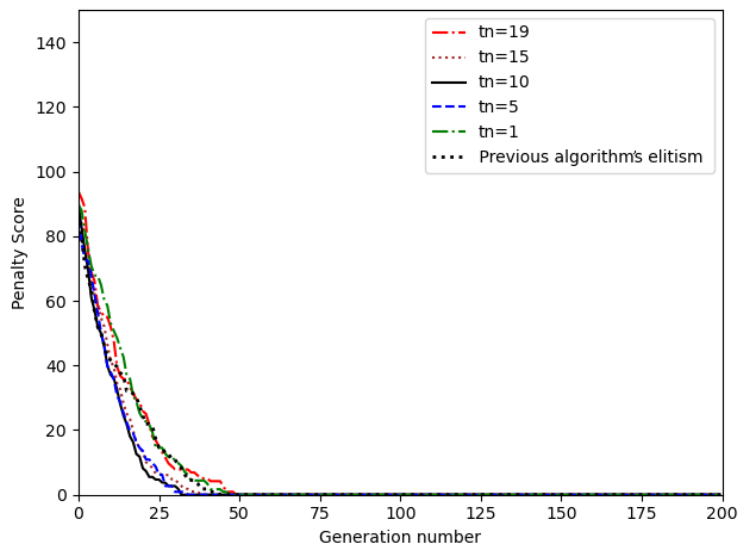


Figure 9. Demonstration of chromosomes in SPCM

The penalty scores decreased to zero for the 30th generation compared to the 50th generation in the previous algorithm, as shown in Figure 9. The TN values yielded better results when approximately 50 percent of the genes were altered.

Our comparative analysis results suggest that the proposed elitism method provides better saturation rates and lower penalty scores than the previous algorithms. The saturation rate decreases when the number of transferred chromosomes is low, and the elitism results correlate with those of the previous algorithm [37]. In addition, the model result did not contain any misplacement of students as appeared in the study [32].

Despite the important improvements, there are still some potential threats to the validity of our study. We evaluated the effects of parameter values step by step and transferred the best values to the next evaluation stage to decrease the size of the test attempts. This could have caused some parameter combinations to be missed. Trying combinations of all possible parameter values can provide slightly improved results. Additionally, the dataset on which the model was tested was small, considering the number of students in the centralized exams. This limits the evaluation of the algorithm performance against large examination datasets.

5. Conclusion

The principal contribution of this study is the parametric optimization of GA-based exam seating by analyzing the effect of parameter values on the system performance and saturation rate. The accuracy and performance of the algorithm were evaluated by using the student dataset from a university. The results indicated that the parametric optimization and improved elitism methods fulfilled two purposes simultaneously: increasing the robustness of the algorithm and preventing unrealistic seating plans.

The proposed model has important theoretical and practical implications. From a theoretical perspective, researchers can use the method and dataset as inputs for new exam seating, timetabling, and GA research. From a practical perspective, our process model can increase the speed of preparing reliable plans with optimal session orders for centralized exams where thousands of people are held simultaneously.

Some limitations of our study should be addressed to strengthen its applicability further. First, the effects of different parameters, such as school friendship and class friendship on exam seating accuracy and performance

should be evaluated in detail. Second, the determination of the minimum and maximum classroom spaces should be addressed to determine the optimum space allocation for exams. Finally, the integration of exam timetabling and seating should be investigated to develop a comprehensive plan for seat placement.

6. Acknowledgements

We thank the Academic Management Office of Mardin Artuklu University for providing the examination data.

References

- [1] Walker J. (1998). Student plagiarism in universities: What are we doing about it? *High Educ Res Dev*, 21(1), pp. 89–106.
- [2] McCabe D.L., Klebe L.T., Butterfield K.D. (2010). Cheating in Academic Institutions: A Decade of. *Ethics Behav.*, 8422, pp. 37–41.
- [3] Mccabe D.L. (2005). Cheating among college and university students: A North American perspective. *Int J Educ Integr*, 1(1).
- [4] Newstead S. (1996). Individual differences in student motivation. *J Educ Psychol.*, 88(2), pp. 229–41.
- [5] Yee K, MacKown P. (2009). Detecting and preventing cheating during exams. *Pedagogy, not Policing*.
- [6] Wang J., Tong Y., Ling M., Zhang A., Hao L, Li X. (2015). Analysis on test cheating and its solutions based on extenics and information technology. *Procedia Comput Sci.*, 55(2015):1009–14. DOI:10.1016/j.procs.2015.07.102
- [7] David L.T. (2015). Academic cheating in college students: relations among personal values self-esteem and mastery. *Procedia - Soc Behav Sci.*, 187, pp. 88–92, DOI:10.1016/j.sbspro.2015.03.017
- [8] Topîrceanu A. (2017). Breaking up friendships in exams: A case study for minimizing student cheating in higher education using social network analysis, *Comput Educ.*, 115, pp. 171–87, DOI: 10.1016/j.compedu.2017.08.008
- [9] Danielsen R.D., Simon A.F., Pavlick R. (2006). The culture of cheating: From the classroom to the exam room. *J Physician Assist Educ.* , 17(1), pp. 23–9.
- [10] Ayob M., Malik A. (2011). A new model for an examination-room assignment problem. *J Comput Sci.*, 11(10):187–90.
- [11] Güler M.G., Geçici E. (2020). A spreadsheet-based decision support system for examination timetabling. *Turkish J Electr Eng Comput Sci.*, 28(3): pp. 1584–98.
- [12] Elsaka T. (2017). Autonomous generation of conflict-free examination timetable using constraint satisfaction modelling. In: *IntArtificial Intelligence and Data Processing Symposium (IDAP)*, p. 1–10.
- [13] Vasupongayya S., Noodam W., Kongyong P. (2013). Developing examination management system: Senior Capstone Project, a case study. *Int J Comput Inf Eng.*, 7(7), pp. 1046–52.
- [14] Dammak A., Elloumi A., Kamoun H. (2006). Classroom assignment for exam timetabling. *Adv Eng Softw.*, 37(10), pp. 659–66.
- [15] Mohmad Kahar M.N., Kendall G. (2014). Universiti Malaysia Pahang examination timetabling problem: Scheduling invigilators, *J Oper Res Soc.*, 65(2), pp-214–26.

- [16] Elloumi A., Kamoun H., Jarbouli B., Dammak A. (2014). The classroom assignment problem: Complexity, size reduction and heuristics, *Appl Soft Comput J.*, 14 (PART C), pp-677–86. DOI: 10.1016/j.asoc.2013.09.003
- [17] Burke E.K., Mccollum B., Mcmullan P., Qu R. (2006). Examination timetabling: A new formulation, In *Proceedings of the 6th International Conference on the Practice and Theory of Automated Timetabling*, Brno, pp. 373-375.
- [18] Chaki P.K. (2016). Algorithm for efficient seating plan for centralized exam system, *Int Conf Comput Tech Inf Commun Technol.*, pp. 320–5.
- [19] Inamdar A., Gangar A., Gupta A., Shrivastava V. (2018). Automatic Exam Seating & Teacher Duty Allocation System, *Second Int Conf Inven Commun Comput Technol. (Icicct)*, pp. 1302–6.
- [20] Wang X.F., Chen G. (2003). Complex networks: Small-world, scale-free and beyond, *IEEE Circuits and Systems Magazine*, 2003, 3(1), pp. 6–20.
- [21] Brailsford S.C., Potts C.N., Smith B.M. (1999). Constraint satisfaction problems: Algorithms and applications, *European Journal of Operational Research*, Vol. 119, pp. 557–81.
- [22] Hosny M., Fatima S. (2011). A Survey of Genetic Algorithms for the University Timetabling Problem A Survey of Genetic Algorithms for the University Timetabling Problem Manar Hosny and Shameem Fatima, *Int Conf Future Inf Technol IPCSIT 13.*, pp. 34–9.
- [23] Abdelhalim E.A., Khayat G.A. El. (2016). A Utilization-based Genetic Algorithm for Solving the University Timetabling Problem (UGA), *Alexandria Eng J*, 55(2), pp.1395–409. DOI: 10.1016/j.aej.2016.02.017
- [24] Karova M. (2004). Solving Timetabling Problems Using Genetic Algorithms, *2Th Int'l Spring Seminar on Electronics Technology*, pp. 20–2.
- [25] Rozaimiee A., Shafee A.N., Anissa N., Hadi A., Mohamed M.A. (2017). A Framework for University's Final Exam Timetable Allocation Using Genetic Algorithm, *World Appl Sci J.*, 35(7), pp. 1210–5.
- [26] Pillay N., Banzhaf W. (2010). An informed genetic algorithm for the examination timetabling problem, *Appl Soft Comput J.*, 10(2), pp. 457–67.
- [27] Abdullah S., Alzaqebah M. (2013). A hybrid self-adaptive bees algorithm for examination timetabling problems, *Appl Soft Comput J.*, 13(8), pp. 3608–20. DOI: 10.1016/j.asoc.2013.04.010
- [28] Holland J.H. (1992). *Adaption in Natural and Artificial Systems: An Introductory Analysis with Applications to Biology, Control, and Artificial Intelligence*, MIT Press
- [29] Şen Z. (2004). *Genetik Algoritmalar ve En İyileme Yöntemleri*, İstanbul, Su Vakfı Yayınları
- [30] Karaboğa D. (2004). *Yapay Zekâ Optimizasyon Algoritmaları*, İstanbul, Atlas Yayınevi, pp. 75–112.
- [31] Negnevitsky M. (2005). *Artificial intelligence: A guide to intelligent systems*, Systems (2nd Edition), Pearson Education.
- [32] Tindell K.W., Burns A, Wellings A.J. (1992). Allocating hard real-time tasks: An NP-Hard problem made easy, *J Real-Time Syst.*, (4), p. 145.
- [33] Bulut F., Subaşı Ş. (2015). Best Seating Plan For Central Exams Using Genetic Algorihtms. *Dokuz Eylül Üniversitesi Mühendislik Fakültesi Fen ve Mühendislik Derg.*, 17(51), pp. 122–37.
- [34] Beligiannis GN, Moschopoulos C, Likothanassis SD. (2009). A genetic algorithm approach to school timetabling, *J Oper Res Soc.*, 60(1), pp. 23–42.

- [35] Akkan C., Gülcü A. (2018). Computers and Operations Research A bi-criteria hybrid Genetic Algorithm with robustness objective for the course timetabling problem, *Comput Oper Res.*, 90:pp. 22–32. DOI:10.1016/j.cor.2017.09.007
- [36] Soremekun, G., Gürdal, Z., Haftka, R. T., & Watson, L.T. (2001). Composite laminate design optimization by genetic algorithm with generalized elitist selection. *Computers & structures*, 79(2), 131-143.
- [37] Ağalday, M. F. (2018). Genetik algoritma ile merkezi sınavlarda tek ve çok boyutlu yakınlığa göre en iyi oturma planının oluşturulması (Master's thesis, Fatih Sultan Mehmet Vakıf Üniversitesi, Mühendislik ve Fen Bilimleri Enstitüsü).
- [38] Nadeau C., Bengio Y. (2003). Inference for the Generalization Error. *Mach Learn Norwell Kluwer Acad Publ*, 52(3), pp. 307–13.
- [39] Schaffer J.D. (1989). A study of control parameters affecting online performance of genetic algorithms for function optimization. In: 3rd International Conference on Genetic Algorithms. San Mateo, CA: Morgan Kaufmann, p. 51–60.
- [40] Aksu Ö. (2008). Yeni Bir Paralel Genetik Algoritma Modeli Ve Analog Devre Tasarımına Uygulanması Yüksek Lisans Tezi, Kayseri Erciyes Üniversitesi.
- [41] Grefenstette J.J. (1992). Genetic algorithms for changing environments. *Parallel Probl Solving from Nat.*, 2, pp. 137–44.



An Application of Non-Dominated Sorting Genetic Algorithm for Reversible Data Hiding Based on Histogram Shifting in Neuroimages

Fusun Er ^{1*} , Yildiray Yalman ² 

¹ *Piri Reis University, Department of Information Systems Engineering, 34940, Turkey*

² *Piri Reis University, Department of Information Systems Engineering, 34940, Turkey*

Abstract

This paper presents an application of a multi-objective non-dominated sorting genetic algorithm with a modified chromosome encoding for histogram shifting-based multiple reversible data hiding scheme in neuroimages which aims to minimize distortion and maximize capacity. The modified chromosomes encoding scheme is designed according to the zero-bin characteristic of the intensity histogram of the structural magnetic resonance imaging scans of the human brain. A detailed experimental study has been carried out for assessing the effect of non-dominated sorting for multi-objective optimization compared to Euclidian distance, the convenience of modified chromosome encoding scheme for medical images compared to non-medical images. The performance of the proposed method has been measured in terms of the peak signal-to-noise ratio (PSNR) for image quality and the bits per pixel (bpp) for capacity assessments. The experimental results show that the proposed method is better than its counterparts.

Keywords: Genetic algorithm, information security, magnetic resonance imaging, reversible data hiding

Cite this paper as: Fusun, E. and Yildiray, Y. (2022). An application of non-dominated sorting genetic algorithm for reversible data hiding based on histogram shifting in neuroimages. 6(2):233-247

*Corresponding author: Fusun Er
E-mail: fer@pirireis.edu.tr

Received Date: 25/06/2022
Accepted Date: 26/08/2022
© Copyright 2022 by
Bursa Technical University.
Available online at
<http://jise.btu.edu.tr/>



The works published in the journal of Innovative Science and Engineering (JISE) are licensed under a Creative Commons Attribution-NonCommercial 4.0 International License.

1. Introduction

Data hiding is the process of sending confidential data covertly embedded into a digital media, such as digital images, video, and signals [1]. The idea behind the utilization of digital images as a carrier in data hiding technologies is based on the inability of people to notice small changes in digital images by naked eye. Many data hiding schemas have been proposed in the literature that successfully employed various kinds of images in several application areas, including medical images. The Health Insurance Portability and Accountability Act (HIPAA) of 2003 and 2005 include a set of privacy and security rules that forces medical professionals and institutions to ensure patient confidentiality and privacy, even in digital media [2]. Since medical images contain critical information for diagnosis, the applied data hiding technique must ensure the reversibility of the cover image. Nowadays, it is of great interest to study data hiding techniques to hide identification information inside magnetic resonance images for establishing more secure data transmission channels. Most of the existing reversible data hiding schemes are based on histogram shifting (HS), which was initially proposed by Ni et al. [1]. Kurnaz et al. proposed an histogram-shifting based method that does not require shifting while preserving the visual quality of stego images [3]. A typical HS-based data hiding scheme starts by selecting one or more pairs of peak and zero bins in the histogram of a cover image. Then, it shifts the bins between peak bin and zero bin by one toward the zero bin. The main purpose is to create a gap for hiding a secret message in the size of the frequency of the peak bin, which the frequency of the selected bin determines the hiding capacity. On the other hand, the image distortion depends on the total number of shifted pixels. In a single-pair HS-based scheme, the peak bin with the highest frequency is matched to its nearest zero bin, thus, the number of pixels affected by shifting is the smallest [4]. A multiple embedding scheme should be considered in order to achieve a higher capacity, which consecutively employs more than one embedding procedure on pairs of different peaks and zero bins [5]. If it is aimed to increase the embedding capacity despite the high distortion in embedded images, the same pair selection procedure for a single pair can be repeated for multiple HS-based schemes by matching the next highest peak bin with its closest zero bin in case of a small number of zero bins existing in a histogram. However, multiple HS-based data hiding is a non-deterministic polynomial-time (NP)-hard problem when the size of the solution space is too large to find the best mapping of peak and zero bins. This problem is known as the rate-distortion optimization problem. Several algorithms have been proposed in the literature to find an optimal set of peak and zero pairs [6], [7] for multiple pair histogram shifting. Tian's algorithm searches for redundancy in digital images to achieve high embedding capacity while keeping the distortion low [8]. In practice, when the solution space is too large to find an optimal solution in a reasonable time, heuristic algorithms [9] are recommended to search for an optimal solution [10]. Recently, Wang et al. proposed a genetic algorithm-based embedding scheme in order to automatically determine the number of peak and zero bin pairs and their corresponding values [11], [12] and [13]. Furthermore, dynamic programming-based reversible data hiding algorithms were proposed to solve the optimization problem [14], [15].

This study aimed to implement a reversible and high-capacity HS-based data hiding technique for magnetic resonance imaging (MRI), which is one of the most widely used medical imaging tools. MRI is a non-invasive technology that produces detailed anatomical and functional images of the inner body without any exposure to radiation. Thus, a genetic algorithm model is proposed in this paper for solving a rate-distortion optimization problem for HS-based multiple reversible data embedding schemes.

The paper is organized as follows: Section 2 provides background information on the medical imaging techniques that were used to obtain the data that are included in this study. Section 3 describes the dataset used to evaluate the proposed model. The framework for rate-distortion optimization on HS-based data hiding is demonstrated in subsection 3.2. Then, experimental test results are presented and discussed. Final remarks are summarized in the Conclusion Section.

2. Background and Motivation

This section provides brief information about in vivo imaging of the human brain and how its intensity histogram characteristics inspired the chromosome structure of the proposed genetic algorithm (GA) model.

A. Structural imaging of the human brain

The human brain is the most complex organ of the human body and a part of the central nervous system (CNS). The brain is composed of two types of tissue: white matter (WM) and grey matter (GM). In addition, cerebrospinal fluid (CSF) is a clear plasma-like fluid that fills the brain ventricles. Grey matter contains relatively fewer myelinated neurons compared to white matter, which is mainly distributed on the surface of the brain cortex. The white matter appears white due to the abundance of the fatty substance (myelin) in its structure [16]. Magnetic resonance imaging is a widely used in vivo imaging technique for studying the human brain. Different tissue types have different longitudinal (or spin-lattice) relaxation times (T_1) that is a measure of the time taken for spinning protons to recover about 63% of the magnetization along the longitudinal direction. T_1 -weighted (T_1 -w) imaging is one of the basic pulse sequences in MRI, which exhibits contrast differences between different tissue types. The excited hydrogen nuclei in fat recover more rapidly along the longitudinal axis; thus, regain much longitudinal magnetization during the repetition time (TR) interval. Due to the lipid composition of myelin, white matter has higher intensity values and appears lighter than grey matter in T_1 -weighted images of the healthy human brain. The lowest signal intensity is obtained from protons in the water molecules of CSF. Hereby, CSF appears black in T_1 -w imaging of the brain [17].

B. Motivation

The histogram of T_1 -weighted imaging of the healthy human brain is characterized by three main mounds that correspond to three main tissue types: cerebrospinal fluid, grey matter, and white matter, respectively [17]. In this study, a group of non-zero neighboring bins delimited by zero bins of the histogram is called a "cluster", and similarly, a group of zero neighboring bins delimited by non-zero bins is called a "gap". A typical intensity histogram of a structural MRI image has either narrow gaps between thick clusters that create many candidate peak points per zero points or wider gaps between thin clusters that form many unmatched zero locations. This characteristic is the main motivation behind the algorithmic design of the presented algorithm. The chromosome structure of this study is designed to encode the selection of zero-bin pairs for histogram shifting, such that adjacent zero-bins within a gap are matched with the non-zero bins of the neighboring cluster.

C. Materials and Methods

The efficiency of the proposed Genetic Algorithm (GA) is presented on axial slices of a set of T1-weighted imaging scans belonging to healthy elderly. Additionally, the proposed approach is compared with a non-heuristic schema. Furthermore, the proposed schema is tested for widely used non-medical images: Lena, Baboon, and Peppers.

Experimental Dataset

A total of 30 healthy elderly subjects have been included in this study. For each subject, their spatially normalized and skull-stripped anatomical MRI brain scans were downloaded from the Alzheimer's Disease Neuroimaging Initiative (ADNI) data archive. The scans are three-dimensional 16-bit depth magnetic resonance images with a size of $110 \times 110 \times 110$ and a resolution of $2 \text{ mm} \times 2 \text{ mm} \times 2 \text{ mm}$. The experiments were performed on the 60th axial slice of the volumes at a size of 110×110 . Fig.1 presents an axial slice of one of the MRI scans used in the experimental evaluation of the proposed model.

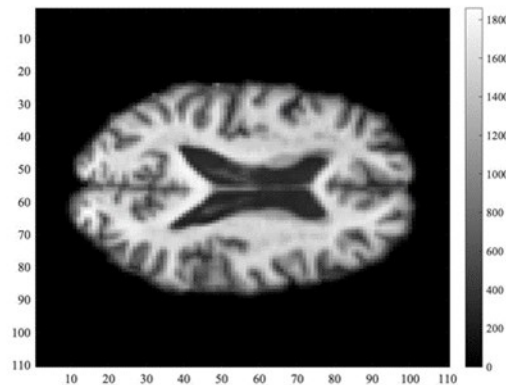


Figure 1. An axial slice of the dataset used in the experiments.

Proposed model for reversible data-hiding

The conventional phases of a genetic algorithm have been performed, which includes (1) initial population generation, (2) parent selection, (3) crossover, (4) mutation, and (5) next population selection. The overall GA schema requires three system parameters and one input: the size of the population (n_p), the number of epochs (n_e) and the mutation probability (r_m) are the system parameters; the histogram model of the cover image (H) is the input parameter. The aim of this GA model is to find an optimum set of zero-nonzero bin pairs based on the histogram model of a particular cover image. In this study, the model proposes a new chromosome encoding scheme based on the histogram structure, and employs a non-dominated sorting algorithm to find the best individual for the next population.

Chromosome encoding based on the intensity histogram of the image

The proposed chromosome structure is highly related to the histogram model of the cover image. The data structure of a histogram model (H) is composed of gaps (G) and clusters (C) denoted as $H = (G, C)$, where the number of gaps is represented by $|G| = n_g$ and the number of clusters is represented by $|C| = n_c$.

G is a sorted sequence of gaps that are labelled as g_i in such a way that $G = \langle g_1, \dots, g_{n_g} \rangle$. Each gap g_i

corresponds to one of the zero-bin gaps of the histogram in ascending order that g_m represents bins with smaller numbered bins than what g_n represents when $m < n \leq n_g$. Thus, a single gap g_i is implemented as a sequence of consecutive zero bin-numbers (ZB_i). The number of zero-bins in a gap is at least one, but the size may vary according to the histogram of the image ($|ZB_i| > 0$).

Similarly, C is used to represent all clusters of sequential non-zero bin-numbers $C = \langle c_1, \dots, c_{n_c} \rangle$ in ascending order. A single cluster c_i has one or more non-zero bins associated with its intensity as a sequence of pairs (NZB_i) in opposite to gaps since all intensities are zero in gaps. Thus, NZB_i represents non-zero bins of the cluster c_i as $NZB_i = \langle \langle b_{i1}, q_{i1} \rangle, \dots, \langle b_{ik}, q_{ik} \rangle \rangle$, where b's are the bin numbers and q's are the corresponding intensities of the bin numbers such that $k = |NZB_i| > 0$ is the number of non-zero bins in the cluster c_i .

Since, we included the bin number 0 (zero) that does not exist in the ROI of the image and the bin number "one plus the highest intensity value of the image", a histogram model starts and ends with a gap, which yields $|G| = n_g$ that is always equals to $(|C| = n_c) + 1$ and the bin numbers of g_i is always followed by the bin number of c_i . The following figure Fig.2 illustrates a symbolic histogram of an arbitrary image with a size of 10×10 and with intensity levels in the range of $[1-36]$. The bin numbers zero and 37 (one more than the highest intensity) are artificially added to the histogram to guarantee that it will start and end with a gap. Therefore, the sample histogram has four gaps ($n_g = 4$) and three clusters ($n_c = 3$). The gaps have three, six, six and three bin numbers in such that $ZB_1 = \langle 0, 1, 2 \rangle$, $ZB_2 = \langle 9, 10, 11, 12, 13, 14 \rangle$, $ZB_3 = \langle 23, 24, 25, 26, 27, 28 \rangle$ and $ZB_4 = \langle 35, 36, 37 \rangle$, respectively. The clusters are implemented as two-dimensional tuples that $NZB_1 = \langle \langle 3, 5 \rangle, \langle 4, 6 \rangle, \langle 5, 4 \rangle, \langle 6, 3 \rangle, \langle 7, 6 \rangle, \langle 8, 4 \rangle \rangle$, $NZB_2 = \langle \langle 15, 2 \rangle, \langle 16, 5 \rangle, \langle 17, 8 \rangle, \langle 18, 7 \rangle, \langle 19, 5 \rangle, \langle 20, 5 \rangle, \langle 21, 3 \rangle, \langle 22, 4 \rangle \rangle$ and $NZB_3 = \langle \langle 29, 4 \rangle, \langle 30, 6 \rangle, \langle 31, 5 \rangle, \langle 32, 7 \rangle, \langle 33, 6 \rangle, \langle 34, 5 \rangle \rangle$. As a crosscheck, the sum of intensities of all clusters ($\sum_{i=1}^{n_c} \sum_{j=1}^k q_{ijk}$) is equals to the number of pixels ($10 \times 10 = 100$).

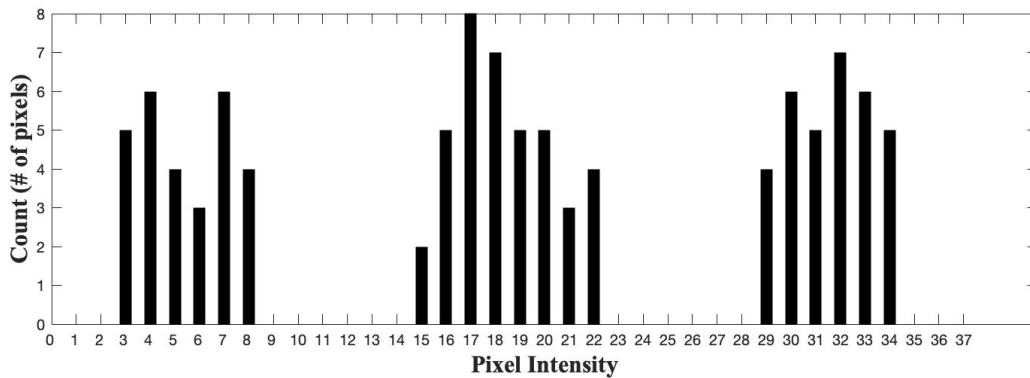


Figure 2. An illustration of an intensity histogram of an arbitrary image with a size of 10×10 .

The proposed chromosome encoding scheme based on the histogram model is a series of gene segments that are located in gaps. A gene segment is composed of zero or more encoder-genes and a regulatory gene, as illustrated in Fig.3. Each encoder gene is associated with one of the successive bins of the gap on which it is located. A regulator gene can take a boolean value that expresses (or suppresses) the corresponding encoder-genes. In addition to genes, a gene segment can be either left-handed or right-handed that determines the cluster for matching bin numbers, which is called "encode-direction". If a gene segment of the gap g_i is left-handed then bins of the gap are matched with the bins of the cluster c_i otherwise they match with the cluster c_{i+1} . Each gap may hold zero or one

left-handed gene segment and zero or one right-handed gene segment except the first and the last gaps. The first gap may contain zero or one right-handed gene segment, and the last gap may contain zero or one left-handed gene segment. Therefore, an individual chromosome may have at most $(2 \times (n_g - 2)) + 1 + 1 = 2 \times n_g - 2 = 2 \times (n_g - 1) = 2 \times n_c$ numbers of gene segments.

There exist some constraints that must be considered during the training of genetic algorithm (GA) model. The first one says that two gene segments can not overlap, therefore the same zero bin will not be paired with more than one nonzero bin. The second one says the total number of encoder-genes of gene-segments that share the same cluster is limited by the number of bins of the cluster. The final one deals with where the gene-segment is placed in the gap, because a shorter distance between the matching points results in a higher PSNR value in the data embedded-image.

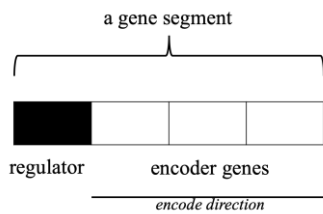


Figure 3. A gene segment

The Fig.4 illustrates an instance of the proposed chromosome structure with three gene segments. The first gene segment is a left-handed gene segment that matches the zero-bins in the range of 9-13 with some non-zero bins of the first cluster. The second gene segment is inactivated. The last gene segment is an active and left-handed segment that has only three zero-bins to match with the bins of the third cluster.

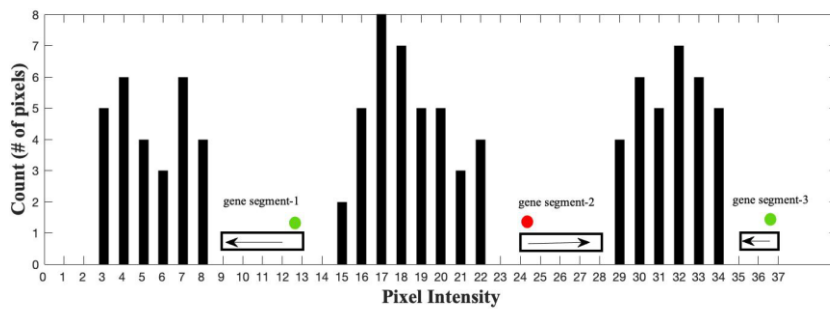


Figure 4. An instance of chromosome encoding on the sample histogram

D. Training of the GA model

The training procedure of the proposed GA model for the given histogram model is given in Algorithm 1. The procedure runs for the given number of epochs (n_e). In each epoch, all individuals in the population are sorted using a non-dominated multi-objective sorting algorithm. The last two-thirds of the population having high scores are randomly paired to generate two offspring. The generated offspring are exposed to mutation with the given mutation probability (r_m). This GA model employs customized implementations of crossover and mutation

according to the proposed chromosome algorithm.

Algorithm 1: Training initial population for n_e numbers of epochs

```

function GA_TRAIN( $n_p$ ,  $n_e$ ,  $r_m$ , H) : P
  Input:  $n_p$ ,  $n_e$ ,  $r_m$  are system parameters; H is the histogram model of the image
  Output:  $P = \{P_i \mid i = 1..n_p\}$  is a sequence of trained individual chromosomes.
  1  /* Initialization */
  2  for  $i \leftarrow 1$  to  $n_p$ 
  3    |  $P_i \leftarrow$  randomly generated chromosome
  4  end
  5  /* Training */
  6  for epoch  $\leftarrow 1$  to  $n_e$ 
  7    |  $P \leftarrow$  SORT_NSA( $P$ )
  8    |  $Q \leftarrow \emptyset$  // Q will keep generated offspring
  9    |  $k \leftarrow \lfloor n_p \times (2/3) \rfloor$  // k is the number parents
 10   |  $I_x \leftarrow$  a random permutation of  $\{n \mid n = 1, 2, \dots, k\}$ 
 11   | for  $i \leftarrow 1$  to  $k$  by 2
 12   | | offspring  $\leftarrow$  CROSSOVER( $P_{I_{x_i}}, P_{I_{x_{i+1}}}$ )
 13   | | if random_number(0,1)  $\leq r_m$ 
 14   | | | offspring  $\leftarrow$  MUTATE(offspring)
 15   | | end
 16   | |  $Q \leftarrow Q \cup$  offspring
 17   | end
 18   |  $P \leftarrow$  SORT_NSA( $P \cup Q$ )
 19   |  $P = \{P_i \mid i = 1..n_p\}$  // get better  $n_p$  number of individuals
 20  end
 21  return P
 22 end function

```

E. Sub procedures of Training GA Model

E.1. SORT_NSA Procedure: A non-dominated sorting algorithm (NSA) is applied to a population P that consists of n_p number of individuals denoted by $\{P_i \mid i = 1..n_p\}$, assigning each individual to one of the k number of Pareto Fronts $F = \{F_i \mid i = 1..k\}$. The pareto index (i), is the ranking of the pareto front, where the pareto front F_m provides better solutions than F_n for a particular multi-objective optimization problem if $1 \leq m < n \leq k$. On the other hand, the solutions of a Pareto front do not dominate each other. In this study, an iterative approach is followed in the implementation of NSA to sort solutions of the given population aiming to maximize both peak signal-to-noise ratio (PSNR) and data embedding capacity. Initially, all solutions of a population compose a set of remaining solutions. In each iteration of a loop with a counter variable (i) is incremented by one starting from one; the unassigned solutions that are not dominated by any other unassigned solutions are assigned to the Pareto front F_i , until there are no more solutions to assign. Fig.5 illustrates the first three iterations of a NSA procedure for an example population with ten individuals. At the end of the first iteration, two solutions marked with red-cross are selected for the Pareto Front F_1 , which are better solutions than all the remaining eight solutions, but they do not dominate each other. One of the red-crossed solutions is better in PSNR and the others offer higher capacities. Then, the second iteration runs for the remaining eight solutions to compose the second Pareto front F_2 in the same way. At the end of the third iteration, only one solution remained, which will be assigned to the last and fourth Pareto front. If sorting within solutions of a Pareto front is needed, then crowd-distance is applied to measure the surrounding density of a solution.

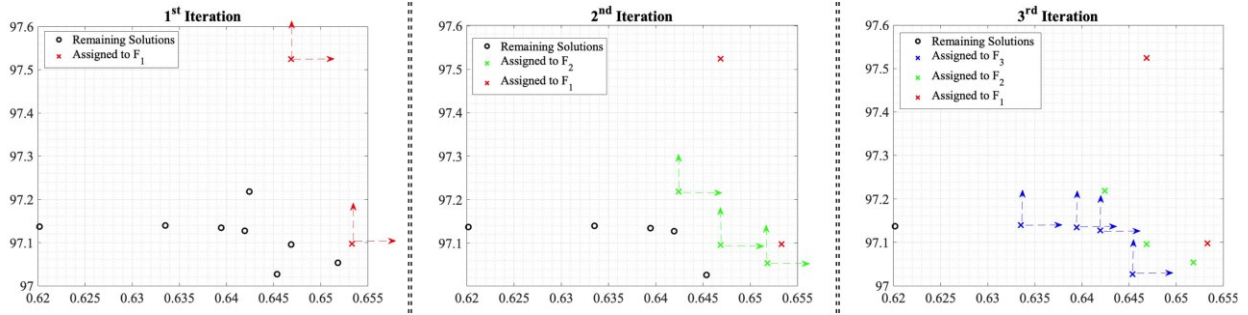


Figure 5. An illustration of non-dominated sorting procedure for a population with ten solutions

The distance value of a particular solution among all solutions in a multi-objective optimization environment is defined as the sum of the differences between the values of the nearest two neighboring solutions when sorted separately according to each objective function. The crowding distance of solutions having the lowest and highest values in an objective function is considered with infinite values so that they are excluded. In this study, solutions with a smaller crowding distance are preferred to achieve optimum solutions in both objectives rather than just one purposive dominant one. This measurement is applied in the selection of the better n_p solutions for the next generation as it is in the 18th line of the Algorithm 1 only for the Pareto front of N th solution.

The Algorithm 2 summarizes the procedure in pseudocode to calculate the crowding distance for all solutions of a particular Pareto front. The algorithm gets individuals (S) in a given Pareto and returns corresponding crowding distance values (CD). Initially all individuals have zero crowd-distance value. Then the algorithm considers each objective separately as an outer loop start in the sixth line. The individuals are sorted according to their j^{th} objective function values. Afterwards, the individuals having the highest and lowest values are excluded with infinite crowded distance values. Finally, the absolute distance of its two neighboring solutions is added to its corresponding crowding distance values in the 11th line.

Algorithm 2: Calculate crowding distances of individuals having the Pareto P_r

```

function CROWDING_DISTANCE(S) : CD
    Input: S = {si | i = 1,2,...,n} is a sequence of n number of solutions in a given Pareto
    Output: CD = {cdi | i = 1,2,...,n} is a sequence of crowding distances of individuals
    1    /* Initialization */
    2    for i ← 1 to n
    3        | cdi ← 0
    4    end
    5    M = {mi,j | i = 1,2,...,n and j = 1..2} // M is a sequence of objective function
        of n number of solutions in a two-objective involving two objective environment.
        mi,j stands for the jth objective function value of si
    6    for j ← 1 to 2
    7        M', T ← SORT(M*,j) // T = {ti | i = 1,2,...,n} and M' = {m'i | i = 1,2,...,n}
            // in such that m'i = mti,j
    8        cdt1 ← ∞
    9        cdtn ← ∞
    10       for k ← 2 to (n - 1)
    11           | cdtk = cdtk + |m'tk-1 - m'tk+1|
    12       end
    13    end
    14    return CD
    15 end function
    
```

E.2. CROSSOVER Procedure: As a part of the presented algorithm, the crossover method was designed to preserve the proposed chromosome structure and to comply with the defined constraints. The crossover method starts with a randomly selected twenty-percent of all regulated gene segments of the first parent, which are inherited by the first offspring. The clusters belonging to the remaining clusters of the second parent were transferred to the first offspring (and vice versa for the second offspring). The intersecting encoder genes of the overlapping gene segments are cropped in favor of a randomly chosen one.

Fig.6 illustrates the proposed crossover technique based on the histogram model used in Fig.2. Two different solutions of the histogram (*Parent-A* and *Parent-B*) are crossed over that generated *Offspring-A* and *Offspring-B*. The third of the three clusters is selected as crossover point to exchange gene-segments among parents, so that, the *Offspring-A* inherited its first and second gene-segments from *Parent-B* and its third and fourth gene-segments are inherited from *Parent-B*.

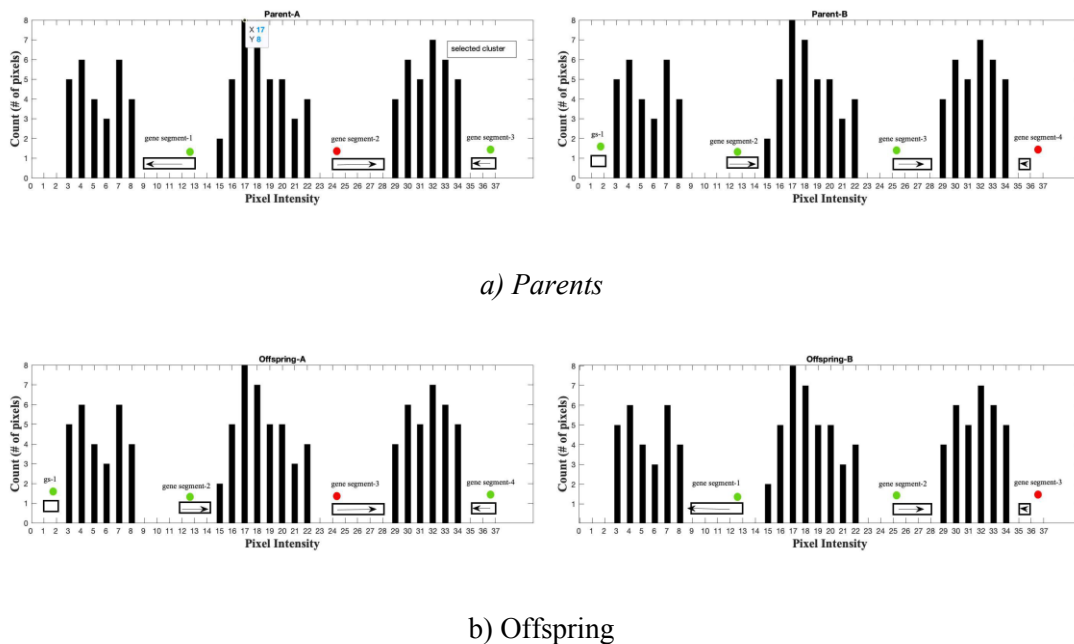


Figure 5. Illustration of a Crossover Operation

E.3. MUTATE Procedure: The mutation affects both regulator genes and encoder-genes. The mutation of regulator genes is a simple procedure in which the regulator genes of randomly selected ten percent of the gene-segments are toggled. Since the previously expressed regulator genes will begin to be suppressed and vice versa, this kind of mutation affects the total capacity. On the other hand, twenty percent of the gene segments were mutated by deleting the encoder-gene next to the regulator gene and entailing it to its complement gene segment. This kind of mutation does not change the capacity. On the other hand, since it affects the matching between zero-bins and peak-bins, such a mutation is related to the distortion.

F. Alternative Distance Measure as opposed to NSA

An Euclidean distance-based fitness value is used to sort individuals in a population as a comparison to NSA in the third and fifteenth lines of Algorithm 1. The fitness value of the chromosome is defined as the magnitude of the vector v in such that $fitness = |\vec{v}| = \langle c, p \rangle^T$, where c and p are scalars in the range of $[0 - 1]$.

The scalar p stands for the ratio of PSNR to the maximum possible PSNR value of the image; and, the scalar c is

the ratio of the capacity in bits to the maximum possible capacity of the image.

In this study, PSNR is calculated for 16-bit data as $PSNR = (20 \times \log_{10}(2^{16} - 1)) - (10 \times \log_{10} MSE)$, where MSE is the mean squared error between the original image and the data embedded-image. The maximum possible PSNR value is calculated by assuming MSE is equal to the epsilon that indicates the minimum distortion occurred by moving only one pixel by one, which is around 135 dB.

3. Results and Discussion

This section presents and discusses experimental results on the dataset explained in Section 2-C.

A. Histograms of the Images of the Experimental Dataset

As it is stated in the background and motivation section, this study is based on the characteristics of the histogram of a structural MRI image. In this section, the intensity histogram of one of the images of the dataset is presented in Figure 7. The histogram has 2125 bins, of which 335 of them are zero-valued bins that are around 16% of the total. Theoretically, the highest 335 peaks can be shifted to all zero locations, but, in practice, only 298 zero-bins are available for shifting due to the characteristics of the histogram.

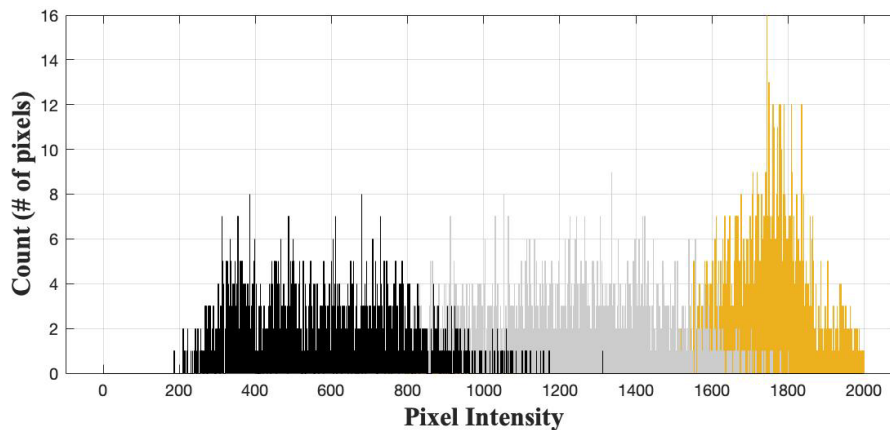


Figure 7. Pixel Intensity Histogram of an Image of the Dataset

The gap-cluster statistics of the histogram are summarized as follows: The wideness statistics of all 231 clusters were 7.74 ± 14.09 [1-171] (mean \pm std[min-max]). Among 335 zero locations, only 298 of them can be used for shifting, 224 of which can be used for either one of two neighbourhood clusters for shifting. The histogram statistics of the three mounds are given separately in Table 1. The mean signal intensities of cerebrospinal grey matter and white matter are 574, 1228 and 1749, in that order. All three mounds are almost symmetrical bell-shaped ($-0.5 \leq \text{skewness} \leq 0.5$) but tails are thinner than the normal distribution (kurtosis < 3) for cerebrospinal fluid and grey matter.

Table 1: Table explanation.

	Cerebrospinal fluid	Grey matter	White matter
Mean Value	574	1228	1749
Standard Deviation	199	220	122
Median Value	557	1238	1750
Minimum Value	186	744	1411
Maximum Value	1313	1800	2124
Mode	385	1336	1744
25th Percentile	400	1059	1666
75th Percentile	728	1403	1819
Skewness	0.4	-0.2	0.23
Kurtosis	2.52	2.17	3.22

B. Experimental Results

The system parameters are empirically set as $n_p = 100$, $n_e = 150$ and $r_m = 10$ for the proposed GA model. Fig.8 presents scatter plots of the embedding capacity and PSNR values (in dB) of the individuals of the initial population, the evolved population with the NSA method and the evolved population with the Euclidian distance method; in black, green, and red colors, respectively. The embedding capacity is presented in a rate of embedded data length in bits to the maximum capacity in bits (listed in Table 2). Since, all individuals of the evolved population with the Euclidian distance method provide the solutions with the same capacity and PSNR values, all individuals plotted on top of each other. The mean capacity of the individuals of the initial population is computed to be 0.54 bpp, with a standard deviation of 0.0094. After 150 epochs of training with a procedure using NSA sorting algorithm, the mean PSNR value of the individuals on the first Pareto front of the population was statistically significantly increased compared with the initial population ($p < 0.001$), with a mean \pm std of 99.82 ± 0.28 , while the capacity value remained same statistically. On the other hand, after 150 epochs of training with a procedure using Euclidian distance sorting algorithm, the capacity value improved significantly ($p < 0.001$), with a mean \pm std of 0.60 ± 0.00 , but, the PSNR value has decreased.

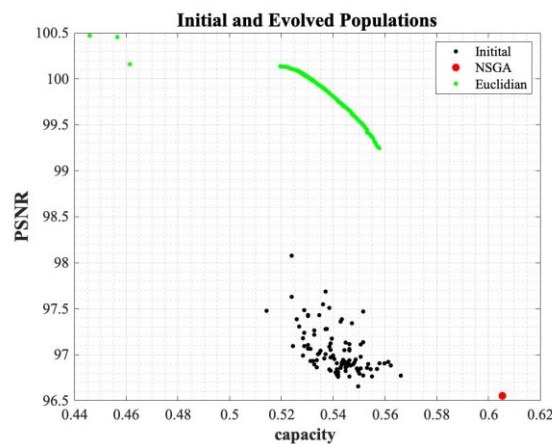


Figure 8. Distortion against capacity of the initial and evolved population tested on the T1-w MRI slice

Table 2 provides a summary of the cluster characteristics of the whole dataset. There exist various numbers of clusters in the range of [115-640] with a high standard deviation. The zero bin numbers are given in the format of “a(s)/t”, where t is the total number of zero bins that exist in the histogram. The number a indicates how many of the total t number of zero bins can be used for shifting. The number s denotes how many of the available zero bins can be paired with more than one cluster. The mean of the percentage of the ratio of the number a to the number t is 86.91 with a standard deviation of 0.06. In other words, around 13% of the total zero-bins are not considered to be used for shifting.

Table 1: Cluster Statistics.

	cluster count	clusterwidth (mean±std)	zero bins count (a(s)/t)*	maximum capacity
1	231	7.74±14.09	298(224)/335	2022
2	256	6.64±17.80	394(260)/439	2361
3	314	5.72±10.72	495(288)/588	2583
4	411	4.58±9.64	627(397)/744	2939
5	299	5.17±10.95	461(271)/496	2429
6	205	8.06±14.45	289(188)/326	1815
7	494	4.37±8.98	745(473)/886	3016
8	115	11.77±18.33	144(113)/181	1278
9	287	6.32±12.41	408(280)/463	2140
10	310	5.46±12.12	438(305)/479	2290
11	521	3.99±5.62	833(481)/967	3035
12	621	3.52±4.88	1020(564)/1317	3447
13	561	3.86±5.78	819(584)/872	2874
14	640	3.47±7.27	990(591)/1197	3400
15	178	8.59±12.90	266(160)/306	1725
16	118	12.76±23.80	145(122)/162	1130
17	222	7.25±16.49	300(233)/306	1771
18	360	5.46±7.05	516(368)/588	2260
19	327	5.82±8.79	490(312)/576	2390
20	198	8.17±11.40	257(216)/274	1468
21	383	5.27±11.06	604(379)/703	3202
22	325	5.60±8.31	464(320)/499	2192
23	291	6.21±12.86	405(274)/465	2313
24	151	10.56±23.20	206(163)/266	1777
25	458	4.50±7.03	704(446)/830	2937
26	132	11.20±35.07	182(137)/257	1887
27	249	7.11±18.39	344(240)/361	2063
28	348	5.54±9.66	475(366)/497	2268
29	308	5.91±11.93	435(288)/604	2667
30	262	6.86±10.26	351(279)/381	1914

* The number of zero bins are given in a(s)/t; t = total number of zero bins; a = available number of zero bins for shifting; s =among available bins, how many of them are shared by two clusters

Fig.9a and Fig.9b show the convergence characteristic curve of the capacity and PSNR values for training a GA model for 150 epochs. The populations rapidly converged to an approximate equilibrium almost 50 epochs later. The “multiple boxplot” MATLAB implementation of Ander Biguri (2021) was used to draw figures.

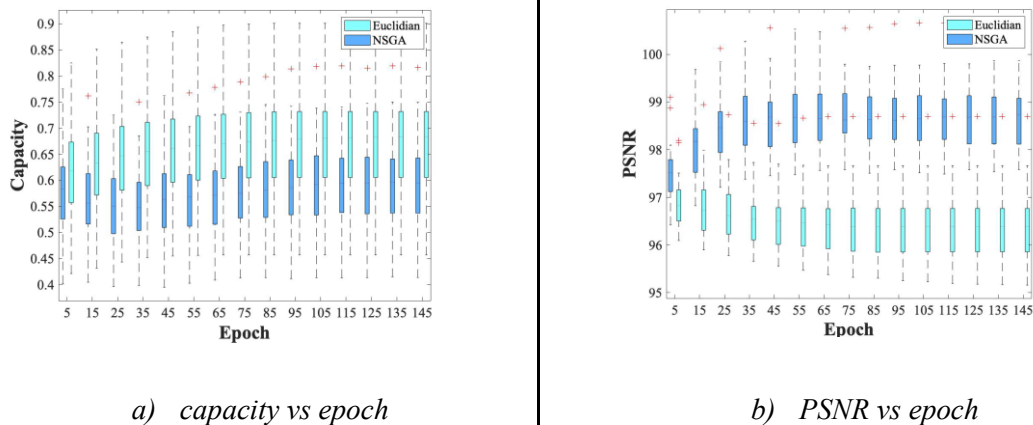


Figure 9. Convergence characteristics curves

Furthermore, the comparison of the performance obtained using the solutions proposed by the individuals of the first population and the evolved population is given in Table 3 in terms of PSNR values. Left-tailed t-tests confirmed that the proposed method significantly improved the populations ($p < 0.01$) when the NSA sorting method is applied. Only three cases of the experiment with Euclidian distance reported significant improvement in PSNR, nevertheless, less than the one with the NSA method.

C. Comparison with the case of using non-medical images

The histograms of the preprocessed non-medical test images Lena, Baboon and Pepper had a total of 308, 43 and 260 clusters, respectively. The Baboon image had fewer zero-bins than others with 85 zero-bins; on the other hand, only 65 percent of them could be included in the pairing procedure. Of the 424 zero bins, only 356 zero-bins were encoded in the GA model in the Lena image. After 150 epochs, the mean of the PSNR values of the individuals in the evolved populations is increased statistically significant compared to the initial populations for all three non-medical images, respectively, with a little improvement in the rate observed for the image Baboon.

D. Time complexity analysis

To compute $T(n)$, the running time of proposed model for the given N_p number of individuals and N_e number of epochs as inputs into the training procedure, the products of the cost and times of each line in algorithm 1 are added together. The cost of each statement is a constant c_i , where i indicates the line number of the statement. The running time of a statement depends on how many times the statement is repeated rather than the cost of the statement [18]. Lines 2-3 are repeated n_p times, if n_p is expressed as p times n then the first loop of line 2-3 takes a time roughly proportional to n . There is a second loop between lines 6 and 12, which has an inner loop between the line 10 and the line 11. By considering n_e is a constant, the inner loop will be the main determining factor for the time complexity. Thus, based on the complexity analysis of the GA training, the GA model has a running time of $O(n)$.

4. Conclusion

In this study, an evolutionary optimization algorithm for solving the rate-distortion trade-off in the HS-based multiple reversible data embedding algorithm is proposed. For this purpose, a specially designed genetic algorithm is proposed to determine the optimal pair of peak and zero bins for structural magnetic resonance imaging images. The chromosome encoding approach of the proposed GA model is inspired by the histogram characteristics of MR images. The proposed algorithm has been evaluated using a set of T1-weighted magnetic resonance images. The mean PSNR value of all individuals in the population after training with the proposed NSA-based GA procedure was statistically significantly increased up to 99.82. Experimental results show that the proposed algorithm yields higher quality embedded images without sacrificing embedding capacity in the field of medical imaging.

5. Acknowledgment



The data used in the preparation of this paper were obtained from the Alzheimer's disease Neuroimaging Initiative (ADNI) database (adni.loni.usc.edu). The ADNI was launched in 2003 as a public-private partnership, led by Principal Investigator Michael W. Weiner, MD. The primary goal of ADNI has been to test whether serial magnetic resonance imaging (MRI), positron emission tomography (PET), other biological markers and clinical and neuropsychological.

References

- [1] Zhicheng, N., Yun-qing, S., Ansari N, Su W. (2006) Reversible data hiding. *IEEE Transactions On Circuits And Systems For Video Technology* 16:354-362.
- [2] Kiel, J. (2012). HIPAA and its effect on informatics. *Comput Inform Nurs* 30:1-5.
- [3] Kurnaz, H., Konyar, M. Z., Sondaş, A. (2020). A new hybrid data hiding method based on near histograms, *Eur J Sci Technol*, 18:683-694.
- [4] Vazhoramalayil, M., Vedhanayagam, M. (2021). A novel image scaling based reversible watermarking scheme for secure medical image transmission. *Isa Transactions*, 108:269-281.
- [5] Wei-liang, T., Chia-ming, Y., Chin-chen, C. (2009). Reversible data hiding based on histogram modification of pixel differences. *Ieee Transactions On Circuits And Systems For Video Technology*, 19:906-910.
- [6] Hwang, H., Kim, H., Vasiliy, S., Joo, S. (2010). Reversible watermarking method using optimal histogram pair shifting based on prediction and sorting. *Journal of Transactions On Internet and Information Systems*, 4:655-670.
- [7] Kuo, W., Li, J., Wang, C., Wu, L., Huang, Y. (2016). An improvement data hiding scheme based on formula fully exploiting modification directions and pixel value differencing method. *IEEE Computer Society*.
- [8] Tian, J. (2003). Reversible data embedding using a difference expansion. *IEEE Transactions On Circuits And Systems For Video Technology*, 13:890-896.
- [9] Malhotra, R., Singh, N., Singh, Y. (2011). Genetic algorithms: Concepts, design for optimization of process controllers. *Comput Inf Sci*, 4:39-5.

- [10] Strossmayer, J. (2001). A Comparison of Several Heuristic Algorithms for Solving High Dimensional Optimization Problems 1.
- [11] Wang, J., Ni, J., Zhang, X., Shi, Y. (2017). Rate and distortion optimization for reversible data hiding using multiple histogram shifting. *Ieee Transactions On Cybernetics*, 47:315-326.
- [12] Wang, J., Ni, J. (10.1109/WIFS.2013.6707819). A GA optimization approach to HS based multiple reversible data hiding.
- [13] Wang, J., Chen, X., Shi, Y. (2019). Unconstraint optimal selection of side information for histogram shifting based reversible data hiding. *Ieee Access* 35564-35578.
- [14] Kuo-liang, C., Yong-huai, H., Wei-ning, Y., Yu-chiao, H., Chyou-hwa, C. (2009). Capacity maximization for reversible data hiding based on dynamic programming approach. *Applied Mathematics And Computation*, 208:284-292.
- [15] Qi, W., Li, X., Zhang, T., Guo, Z. Optimal Reversible Data Hiding Scheme Based on Multiple Histograms Modification. *Ieee Transactions On Circuits And Systems For Video Technology*, 2300-2312.
- [16] Wansapura, J., S., Dunn, R., Ball, W. (1999). NMR relaxation times in the human brain at 3.0 tesla. *Journal Of Magnetic Resonance Imaging*
- [17] Hazlewood, C., Yamanashi, W., Rangel, R., Todd, L. (1982). In vivo NMR imaging and T1 measurements of water protons in the human brain. *Magnetic Resonance Imaging*, 1:3-10.
- [18] Cormen, T.,H. (2009). Introduction to algorithms. MIT press, 658- 662.

Mechanical Properties of Thermoplastic Filament Stitched Carbon Fiber Reinforced Composites

Gokcenur Saglam ^{1*} , Ayse Celik Bedeloglu ² 

^{1*} *Ermetal Otomotiv ve Eşya San. Tic. A.Ş.*

² *Department of Polymer Materials Engineering, Bursa Technical University, 16310 Bursa, Turkey.*

Abstract

In recent years, the use of composites has attracted great interest in both academia and industry, especially due to their lightness and mechanical properties. In this study, acrylonitrile butadiene styrene (ABS), poly(ethylene-co-methacrylic) acid (EMAA) and ethylene vinyl acetate (EVA) filaments were produced in a single screw extruder. The produced filaments were integrated into composite materials by stitching method, and then, the mechanical properties of the filaments and composites were investigated. According to the tensile test results, it is concluded that the stitching process affects the mechanical properties of the composite material.

The strength of the composite material produced with EVA filament with a maximum diameter of 1mm increased by 23%. Apart from these, the composite materials produced with 1mm ABS and 0.6mm and 0.8mm EMAA filaments increased by an average of 15%. There was no significant change in the elongation of the composite material produced with 0.6mm, 0.8mm, and 1mm diameter filaments. The elongation of the composite material produced with only 1mm diameter ABS filament increased by 12%. The elongation values of the composite material prepared with 0.6mm diameter EMAA and EVA polymers decreased also by 15%.

Keywords: 3-Dimensional Reinforcement, Carbon Fibre-Reinforced Polymers (CFRPs), Stitching, Filament, Fibre-Reinforced Polymer Composites (FRPCs).

Cite this paper as:

Saglam, G., Celik Bedeloglu, A. (2022). *Mechanical Properties of Thermoplastic Filament Stitched Carbon Fibre Reinforced Composites*. Journal of Innovative Science and Engineering. 6(2): 248-258

*Corresponding author: Gokcenur Saglam
E-mail: gkc.nur_saglam@hotmail.com

Received Date: 05/08/2021
Accepted Date: 06/12/2022
© Copyright 2022 by
Bursa Technical University. Available
online at <http://jise.btu.edu.tr/>



The works published in Journal of Innovative Science and Engineering (JISE) are licensed under a Creative Commons Attribution-NonCommercial 4.0 International License.

1. Introduction

Fibre-reinforced polymer composites (FRPCs) are preferable in many areas due to their promising mechanical properties, such as high specific strength, high specific modulus, good fatigue resistance, high damage tolerance, and excellent processability [1–3]. For example, using carbon fibre-reinforced polymers (CFRPs), instead of metal in automotive, can result in a weight reduction of up to 15%. This feature has been proven to improve the fuel efficiency of vehicles [4]. FRPCs are mostly formed by overlapping fibre reinforcements or prepreg layers under the heat and pressure to form a complex three-dimensional network structure [5]. In addition, thermoplastic additives, such as particles, filaments, nanoflakes or nanotubes affecting the material properties, can be applied with different techniques to obtain improved properties in the composite materials [6].

The through-the-thickness stitching method with filament increases high in-plane strength, interlaminar fracture toughness, impact damage tolerance, [7] and tensile strength of composite materials [8–10]. It also has a higher resistance to delamination cracking under low energy, high energy, dynamic loading, and ballistic effects [11,12]. However, they suffer from damage by delamination cracking when the stitching needle passes through the prepreg tape or fabric, a gap is formed in the area, and the fibres are separated from each other. The type and structure of the stitch are the most important parameters affecting the composite performance. Four different types of stitches are applied: lock stitch, modified lock stitch, chain stitch, and double lock stitch [13,14]. While conventional lock stitches are used in the fabric industry, other stitch types are frequently used in the composite industry [13].

To develop stitched composites, the poly(ethylene-co-methacrylic) acid (EMAA) and ethylene vinyl acetate (EVA) and acrylonitrile butadiene styrene (ABS) polymers can be chosen because of their properties. EMAA is a hard, light, easily workable, thermoplastic polymer without the need for plasticizers. It also has applications in composite materials due to its low melting point, toughness, and high melt flow index. The most important feature is that it is an effective agent because it contains functional groups that are chemically reactive with the amine groups in the epoxy [15–22].

EVA is a transparent, high mechanical strength, flexible, rubbery thermoplastic copolymer. In addition, its structure consists of varying amounts of vinyl acetate (VA) and ethylene. Its crystallinity, melting point, and hardness depend on the VA content in its structure. Generally, the VA rate varies between 1-40%. As the VA content increases, its crystallinity decreases, so the melting temperature (T_m) decreases. It becomes softer and more elastic. Impact resistance and tear resistance increase. The glass transition temperature (T_g) in EVA is not affected by the VA ratio and is between (-35) and (-25). The EVA is a well-known adhesive and has a very low viscosity [23,24].

ABS is an opaque, amorphous polymer. It is one of the important engineering plastics consisting of the polymerization of styrene, acrylonitrile, and butadiene monomers. Each monomer in its structure has different properties. Acrylonitrile, heat and chemical resistance, long-term thermal stability, and toughness; Butadiene, impact resistance and maintaining its properties at low temperature; Styrene provides hardness, surface gloss, and easy workability [25]. Also, ABS has a pendant functionality from maleic anhydride and cyanate groups which may have been capable of interacting with the epoxy resin with the aromatic pendant group [14,26–28]

According to the literature review, there is no similar study with EVA and ABS filaments. The stitching method with EMAA filaments has been studied, but its mechanical properties has not been studied sufficiently.

Therefore, the aim of this study is to produce filaments with 0.6mm, 0.8mm, and 1mm diameters from EMAA, EVA, and ABS polymers and use them to stitch the preregs to improve the mechanical properties. In order to measure the mechanical properties, tensile and flexural tests were performed both on the stitched and un-stitched composites.

2. Material and Methods

In this study, EMAA, ABS, and EVA polymers which are suitable for injection method were preferred. The EMAA polymer has a density of 0.94 g/cm³, MFI value was 395 g/10 min, and trade name Nucrel® 2940 was obtained from DuPont. ABS polymer has a density of 1.02 g/cm³, MFI has a value of 12g/20min, trade name ABS HI100. EVA polymer, vinyl acetate content has a 19%, has a density of 0.941g/cm³ and has a MFI value of 2.5 g/10min and trade name Greenfleks ML 50 was purchased from RESINEX. The composite materials used in this study were fabricated by unidirectional carbon fibre-epoxy prepreg (VTM 264) was supplied by SPM Prepreg System.

2.1. Preparation of Thermoplastic Filaments

Extrusion Line (Polmak Plastik/Lab Extruder) 18MM device was used for filament production. In this study, the effects of two different parameters on the filaments were investigated as shown in Table 1. In the article, EMAA, EVA, and ABS filaments with diameters of 0.6 mm, 0.8 mm, and 1 mm were produced using the optimum parameters.

Table 1. Extrusion parameters of filaments

Filament Code	Extrusion rate (r/min)	Extrusion traction rate (r/min)
ABS06	2.5	8
ABS08	4	7.5
ABS1	4.5	4.6
EVA06	3.5	10
EVA08	5	7
EVA1	5.5	5.1
EMAA06	3.5	6
EMAA08	5	6.5
EMAA1	7.5	

2.2. Fabrication of Unstitched and Stitched Composites

The carbon fibre/epoxy composite prepreg was stitched manually in the thickness direction with EMAA, ABS, and EVA filaments, respectively. The demonstration of the stitched structure is shown in Fig.1. In the process, the stitch density

was 1.0 stitch/cm². The unstitched and stitched composites were hot press cured at 120°C under 0.05 MPa. Subsequently, all composite materials were post-cured in an air-circulated oven for 40 minutes at 150°C under 0.05 MPa [29]. In the stitching process, the process was easier as the EMAA and EVA filaments are very flexible and was more difficult because the ABS filament is hard.

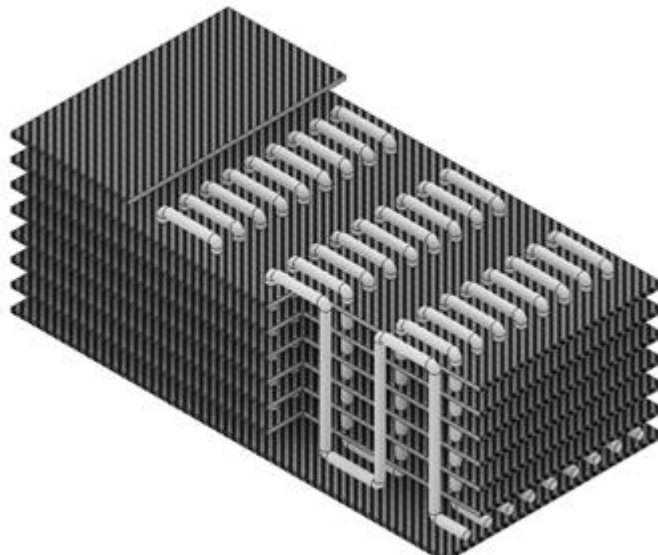


Figure 1. The demonstration of the stitches in the carbon fibre–epoxy composite

2.3. Characterization

The tensile strength, elastic modulus, yield strength and tensile strength tests of the filaments were performed with reference to ASTM D3822/D3822M-14 standard. The length of the filaments prepared in accordance with the standard is 150mm [30].

In order to measure the tensile strength and tensile modulus of elasticity of the composite materials, tensile tests were carried out according to the ASTM D 3039/D 3039M-00 standard. Composite materials were prepared as 25mm in width, 250 mm in length, and 2.5mm in thickness in accordance with the standard [31]. For each composite type, at least five samples were tested. Tensile tests of composite materials were carried out in accordance with the standards at 2 mm/min [30,31].

The flexural strength of the composites produced were tested in accordance with ASTM D 7264/D 7264M-07 standard. The width of the samples prepared in accordance with the ASTM D 7264/D 7264M-07 standard was 13 mm, and the thickness/gap ratio was taken as 1/32 [32].

3. Results and Discussion

3.1. Tensile Test Results of Filaments

As seen in table 2, the tensile stress of the 0.6 mm diameter EMAA filament is 25.21 MPa. The strength of the 0.8mm and 1.0mm diameter filaments decreased by 4% and 2%, respectively. Test results showed that filament diameters did not have a serious effect on strength [33].

The tensile strength of the 0.6 mm diameter EVA filament is 33.73 MPa. According to the test results, it was observed that as the diameter of the filaments increased, the strength increased by more than 30%.

The tensile strength of the 0.6 mm diameter ABS filament is 19.84 MPa. The strength of 0.8mm and 1.0mm diameter filaments increased by 70%. According to the results, there was a significant increase in mechanical values as the diameter increased for ABS [34,35].

Table 2. Stress-strain values obtained as a result of tensile tests of filaments

Material type	Filament diameters	Stress (MPa)	Standard deviation	Strain (%)	Standard deviation
EMAA	0.6	25.51	0.84	139.36	3.96
	0.8	24.23	0.39	329.4	14.16
	1	22.66	0.18	200.39	4.55
EVA	0.6	33.73	1.44	163.03	27.32
	0.8	21.05	1.28	146.96	17.29
	1	24.07	0.43	408.22	33.08
ABS	0.6	19.84	4.21	16.93	2.32
	0.8	33.59	0.46	47.35	23.12
	1	33.97	0.33	16.45	2.05

3.2. Tensile Test Results of Composites

As seen in Fig. 3, the tensile strength of the unstitched composite is 368 MPa. The strength of the stitched composite material prepared with 1 mm diameter ABS filament increased by 14%. The strength of composite materials produced with 0.6 mm and 0.8 mm diameter filaments decreased by 41% and 36%, respectively. When the chemical structure of ABS is examined, it contains unsaturated hydrocarbon and nitrile groups that react with epoxy groups. ABS has a high melting point. In this study, the process temperature was approximately 150°C, and ABS could not completely melt in the composite material, and it could not spread between the layers because its viscosity was too dense. For this reason, although ABS has functional groups that will react with the epoxy matrix, it has not been found to have an effect on the tensile strength since it cannot come into contact with the sufficient surface [36,37]. As a result, its strength decreased.

As shown in Fig. 2, the strength of the stitched composite material produced with EMMA filament with 0.6 mm and 0.8 mm diameters increased by 16% and 7%, respectively. The strength of the composite material produced with the filament used with a diameter of 1mm decreased by 6%. The test results reveal that the filament diameter did not have a great effect on the tensile strength. EMMA contains functional groups that are chemically reactive with amine groups in epoxy. As a result of the reaction, water is released, and the resulting water creates vapor pressure in the temperature environment. With this high pressure, EMMA spreads easily between the layers. As the diffusion of EMMA between layers increased, its chemical reaction amount with the epoxy matrix increased. [17,38,39]. Therefore, there was no significant change in the strength properties depending on the filament diameter.

The strength of stitched composite materials produced with 1 mm diameter EVA filaments increased by 23%, as shown in Fig. 2. The strength of composite materials produced with EVA filaments used in 0.6mm and 0.8mm diameters decreased by 7% and 16%, respectively. The composite manufacturing process temperature is above the EVA melting

temperature. EVA has a very low viscosity compared to EMAA and ABS and shows adhesive feature [40–42]. Therefore, the 1 mm diameter filament caused an increase in strength in the stitched composite.

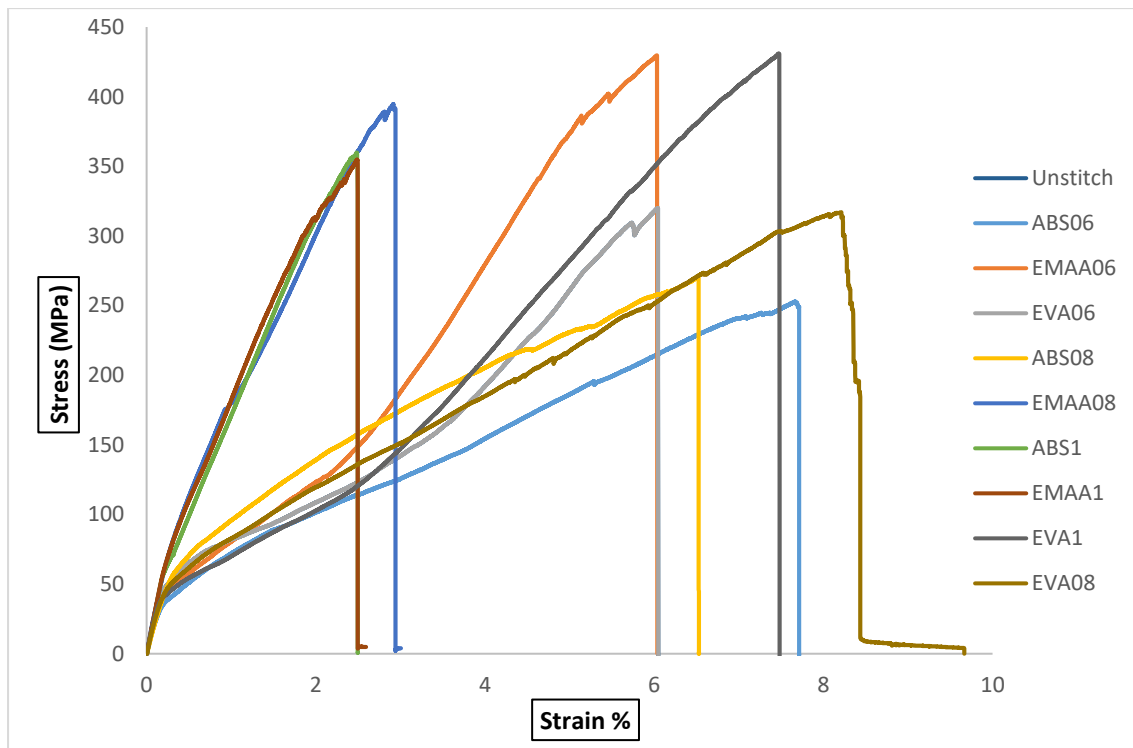


Figure 2. Stress-strain curves of composite materials produced with different filament diameters

3.3. Flexural Test Results of Composites

A three-point bending test was performed according to ASTM D 7264/D 7264M-07 test standards on both stitched and unstitched composites produced with filaments using different types and diameters. In this test, the specimen is in a support opening, and the load is applied to the midpoint by the loading nose [43].

As seen in Fig. 3, the flexural strength of the unstitched composite is 167.81 MPa. As shown in Fig. 3, the strength of the stitched composite material produced with ABS filament with a diameter of 0.8mm and 1mm increased by 119% and 147%, respectively, while the strength of the composite produced with a diameter of 0.6mm diameter decreased by 15%. No significant change was observed in the elongation of composite materials produced with filaments of 0.6mm and 0.8mm diameters. However, the elongation of the composite material produced with a 1mm diameter filament rose 12%, and the material became more ductile.

As shown in Fig. 3., the strength of the stitched composite material produced with EVA filament with a diameter of 0.6mm, 0.8mm, and 1mm increased by 140%, 129%, and 67%, respectively, No significant change was observed in the elongation of all composite materials. Only, elongation of the composite material produced with 0.6mm and 1mm diameter filament decreased 15% and 20%, respectively, and a more brittle structure was formed in the materials.

According to the results of the composite material prepared with EMAA filament, the strength of the composite material produced with 0.6 mm, 0.8 mm, and 1 mm diameter EMAA filament increased by 116%, 145%, and 109%, respectively. According to the elongation result, there was a 35% reduction in the elongation rate of the composite material produced with only 0.6mm diameter filament, and the material reached a more brittle structure. There was no significant change in the elongation of the composite material produced with 0.8mm and 1mm diameter filaments.

When the flexural and tensile test results are examined, it has been proven that all results are in parallel with the results of the tensile test of the filaments.

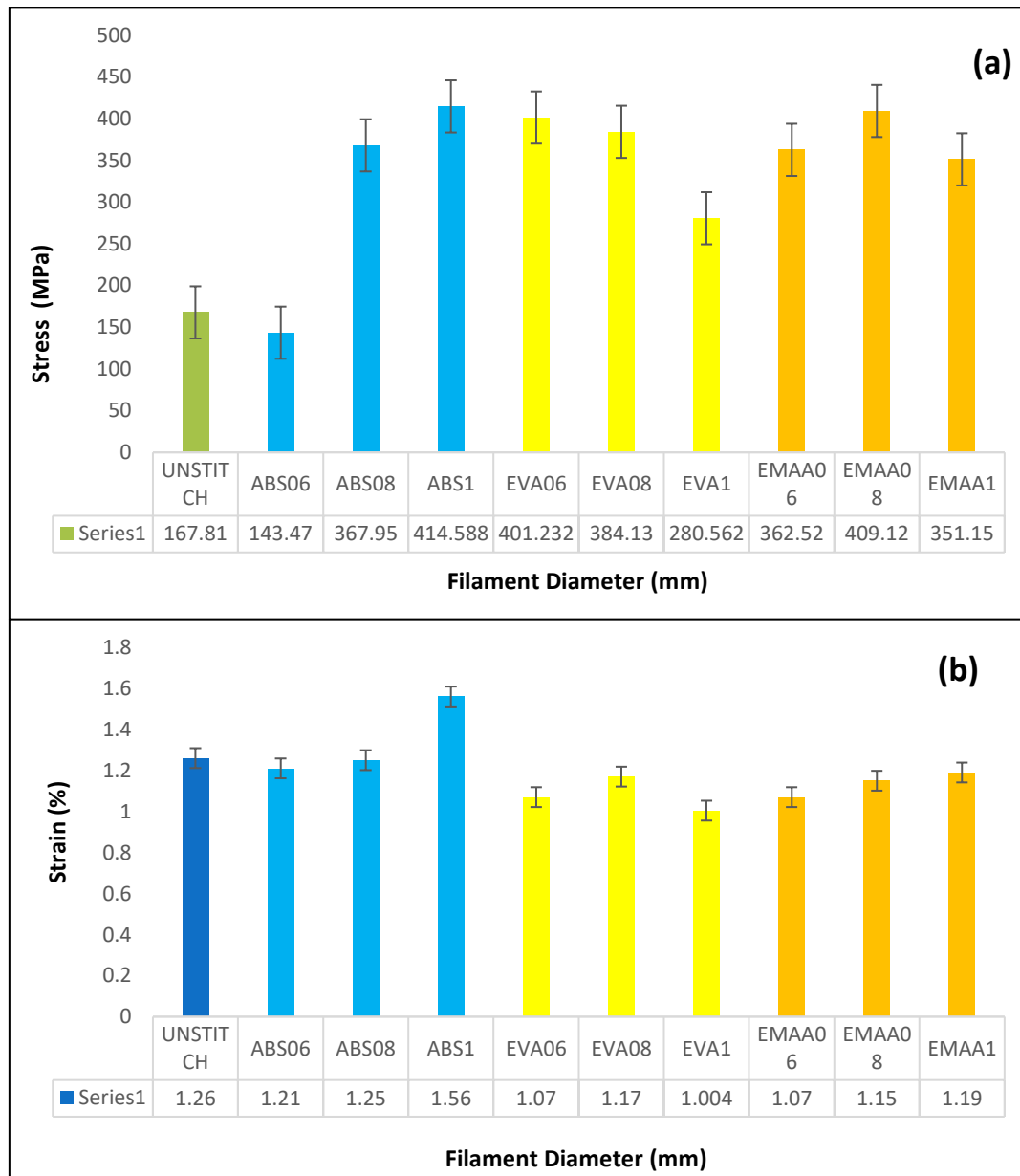


Figure 3. The variation of the stress(a) strain(b) graphs obtained as a result of the three-point bending test of the composite materials prepared with ABS, EMAA, and EVA filaments according to the filament diameter

4. Conclusion

In this paper, the effects of using EMAA, EVA, and ABS filaments in the composite materials with stitching process on the some mechanical properties of composites were presented. It has been proven that filaments of different types and diameters greatly affect the mechanical properties of the stitched composites. According to the test results, it has been concluded that the stitching process reduces the mechanical properties of the composite material. The strength of the stitched composite material produced with 1 mm diameter EVA filament increased by 23%. Apart from these, an average of 15% increase in tensile strength was achieved in stitched composite materials produced with 1mm ABS, 0.6mm and 0.8mm EMAA filaments. During the stitching process of the filament, the separation of the fibres from each other, the formation of resin-rich regions, porosity, fibre breakage, and the formation of cracks between the resin may have caused these results [10,44,45]; the decrease in the tensile strength of the composites. According to the 3-point bending test results, it has been found out that the stitching process increased the flexural mechanical properties of the composite material. There was no significant change in the elongation of the composite material produced with different type and diameter of filaments. The elongation of the composite material produced with only 1mm diameter ABS filament increased by 12%. The elongation values of the composite material prepared with 0.6mm diameter EMAA and EVA polymers also decreased by 15%.

References

- [1] Zakaria MR, Md Akil H, Abdul Kudus MH, Ullah F, Javed F, Nosbi N. Hybrid carbon fiber-carbon nanotubes reinforced polymer composites: A review. *Composites Part B: Engineering* 2019;176. <https://doi.org/10.1016/j.compositesb.2019.107313>.
- [2] Chung DDL. Processing-structure-property relationships of continuous carbon fiber polymer-matrix composites. *Materials Science and Engineering R: Reports* 2017;113:1–29. <https://doi.org/10.1016/j.mser.2017.01.002>.
- [3] Wang Z, Yang B, Xian G, Tian Z, Weng J, Zhang F, et al. An effective method to improve the interfacial shear strength in GF/CF reinforced epoxy composites characterized by fiber pull-out test. *Composites Communications* 2020;19:168–72. <https://doi.org/10.1016/j.coco.2020.03.013>.
- [4] Kim P. A Comparative Study of the Mechanical Performance and Cost of Metal, FRP, and Hybrid Beams. *Applied Composite Materials* 1998 5:3 1998;5:175–87. <https://doi.org/10.1023/A:1008830017745>.
- [5] Boon Y di, Joshi SC. A review of methods for improving interlaminar interfaces and fracture toughness of laminated composites. *Materials Today Communications* 2020;22. <https://doi.org/10.1016/j.mtcomm.2019.100830>.
- [6] Rajak DK, Pagar DD, Kumar R, Pruncu CI. Recent progress of reinforcement materials: a comprehensive overview of composite materials. *Journal of Materials Research and Technology* 2019. <https://doi.org/10.1016/j.jmrt.2019.09.068>.

- [7] Tada Y, Ishikawa T. Experimental evaluation of the effects of stitching on CFRP laminate specimens with various shapes and loadings. *Mechanical and Corrosion Properties Series A, Key Engineering Materials* 1989. <https://doi.org/10.4028/www.scientific.net/kem.37.305>.
- [8] Kang TJ, Lee S ho. Effect of Stitching on the Mechanical and Impact Properties of Woven Laminate Composite. *Journal of Composite Materials* 1994. <https://doi.org/10.1177/002199839402801604>.
- [9] Chung WC, Jang BZ, Chang TC, Hwang LR, Wilcox RC. Fracture behavior in stitched multidirectional composites. *Materials Science and Engineering A* 1989. [https://doi.org/10.1016/0921-5093\(89\)90355-9](https://doi.org/10.1016/0921-5093(89)90355-9).
- [10] Dransfield K, Baillie C, Mai YW. Improving the delamination resistance of CFRP by stitching-a review. *Composites Science and Technology* 1994. [https://doi.org/10.1016/0266-3538\(94\)90019-1](https://doi.org/10.1016/0266-3538(94)90019-1).
- [11] Jain LK, Mai YW. On the effect of stitching on mode I delamination toughness of laminated composites. *Composites Science and Technology* 1994. [https://doi.org/10.1016/0266-3538\(94\)90103-1](https://doi.org/10.1016/0266-3538(94)90103-1).
- [12] Mouritz AP. The damage to stitched GRP laminates by underwater explosion shock loading. *Composites Science and Technology* 1995. [https://doi.org/10.1016/0266-3538\(95\)00122-0](https://doi.org/10.1016/0266-3538(95)00122-0).
- [13] Saboktakin A. 3D textile preforms and composites for aircraft structures: A review. *International Journal of Aviation, Aeronautics, and Aerospace* 2019. <https://doi.org/10.15394/ijaaa.2019.1299>.
- [14] Mouritz AP, Leong KH, Herszberg I. A review of the effect of stitching on the in-plane mechanical properties of fibre-reinforced polymer composites. *Composites Part A: Applied Science and Manufacturing* 1997;28:979–91. [https://doi.org/10.1016/S1359-835X\(97\)00057-2](https://doi.org/10.1016/S1359-835X(97)00057-2).
- [15] Zhang P, Li G. Advances in healing-on-demand polymers and polymer composites. *Progress in Polymer Science* 2016. <https://doi.org/10.1016/j.progpolymsci.2015.11.005>.
- [16] Yuan YC, Rong MZ, Zhang MQ, Chen J, Yang GC, Li XM. Self-Healing Polymeric Materials Using Epoxy/Mercaptan as the Healant. *Macromolecules* 2008;41:5197–202. <https://doi.org/10.1021/ma800028d>.
- [17] Pingkarawat K, Wang CH, Varley RJ, Mouritz AP. Effect of mendable polymer stitch density on the toughening and healing of delamination cracks in carbon-epoxy laminates. *Composites Part A: Applied Science and Manufacturing* 2013. <https://doi.org/10.1016/j.compositesa.2013.02.014>.
- [18] Pingkarawat K, Wang CH, Varley RJ, Mouritz AP. Effect of mendable polymer stitch density on the toughening and healing of delamination cracks in carbon-epoxy laminates. *Composites Part A: Applied Science and Manufacturing* 2013. <https://doi.org/10.1016/j.compositesa.2013.02.014>.
- [19] Pingkarawat K, Wang CH, Varley RJ, Mouritz AP. Thermoplastic fibre stitching: a new self-healing method for carbon-epoxy composites 2013:708–11.
- [20] Khomkrit Pingkarawat. THERMOPLASTIC FIBRE STITCHING: A NEW SELF-HEALING METHOD FOR CARBON-EPOXY COMPOSITES 2013.
- [21] Pingkarawat K, Mouritz AP. Stitched mendable composites: Balancing healing performance against mechanical performance. *Composite Structures* 2015. <https://doi.org/10.1016/j.compstruct.2014.12.034>.

- [22] Hargou K, Pingkarawat K, Mouritz AP, Wang CH. Ultrasonic activation of mendable polymer for self-healing carbon-epoxy laminates. *Composites Part B: Engineering* 2013;45:1031–9. <https://doi.org/10.1016/j.compositesb.2012.07.016>.
- [23] Varley RJ, Craze DA, Mouritz AP, Wang CH. Thermoplastic healing in epoxy networks: Exploring performance and mechanism of alternative healing agents. *Macromolecular Materials and Engineering* 2013. <https://doi.org/10.1002/mame.201200394>.
- [24] Pingkarawat K, Bhat T, Craze DA, Wang CH, Varley RJ, Mouritz AP. Healing of carbon fibre-epoxy composites using thermoplastic additives. *Polymer Chemistry* 2013;4:5007–15. <https://doi.org/10.1039/c3py00459g>.
- [25] McKen LW. Styrenic Plastics. *Fatigue and Tribological Properties of Plastics and Elastomers* 2010:51–71. <https://doi.org/10.1016/B978-0-08-096450-8.00004-1>.
- [26] Pingkarawat K, Bhat T, Craze DA, Wang CH, Varley RJ, Mouritz AP. Healing of carbon fibre-epoxy composites using thermoplastic additives. *Polymer Chemistry* 2013. <https://doi.org/10.1039/c3py00459g>.
- [27] Yang T, Zhang J, Mouritz AP, Wang CH. Healing of carbon fibre-epoxy composite T-joints using mendable polymer fibre stitching. *Composites Part B: Engineering* 2013. <https://doi.org/10.1016/j.compositesb.2012.08.022>.
- [28] Pingkarawat K, Wang CH, Varley RJ, Mouritz AP. Self-healing of delamination fatigue cracks in carbon fibre-epoxy laminate using mendable thermoplastic. *Journal of Materials Science* 2012;47:4449–56. <https://doi.org/10.1007/s10853-012-6303-8>.
- [29] Yang T, Wang CH, Zhang J, He S, Mouritz AP. Toughening and self-healing of epoxy matrix laminates using mendable polymer stitching. *Composites Science and Technology* 2012. <https://doi.org/10.1016/j.compscitech.2012.05.012>.
- [30] ASTM International. ASTM D3822/D3822M - 14 Standard Test Method for Tensile Properties of Single Textile Fibers. Standards 2014.
- [31] ASTM D3039. ASTM D3039 Standard Test Method for Tensile Properties of Polymer Matrix Composite Materials -D3039 2008, Annual Book of ASTM Standards n.d. https://doi.org/10.1520/D3039_D3039M-17.
- [32] ASTM D7264/D7264M-07. Standard Test Method for Flexural Properties of Polymer Matrix Composite Materials. Annual Book of ASTM Standards, 2007.
- [33] Calderón-Villajos R, López AJ, Peponi L, Manzano-Santamaría J, Ureña A. 3D-printed self-healing composite polymer reinforced with carbon nanotubes. *Materials Letters* 2019;249:91–4. <https://doi.org/10.1016/J.MATLET.2019.04.069>.
- [34] Kim H, Park E, Kim S, Park B, Kim N, Lee S. Experimental Study on Mechanical Properties of Single- and Dual-material 3D Printed Products. *Procedia Manufacturing* 2017;10:887–97. <https://doi.org/10.1016/J.PROMFG.2017.07.076>.

- [35] Grabowik C, Kalinowski K, Ćwikła G, Paprocka I, Kogut P. Tensile tests of specimens made of selected group of the filament materials manufactured with FDM method. *MATEC Web of Conferences* 2017;112. <https://doi.org/10.1051/MATECCONF/201711204017>.
- [36] Nabi G, Malik N, Tahir MB, Raza W, Rizwan M, Maraj M, et al. Synthesis of graphitic carbon nitride and industrial applications as tensile strength reinforcement agent in red Acrylonitrile-Butadiene-Styrene (ABS). *Physica B: Condensed Matter* 2021;602:412556. <https://doi.org/10.1016/J.PHYSB.2020.412556>.
- [37] Pingkarawat K, Wang CH, Varley RJ, Mouritz AP. Healing of fatigue delamination cracks in carbon-epoxy composite using mendable polymer stitching. *Journal of Intelligent Material Systems and Structures* 2014;25:75–86. <https://doi.org/10.1177/1045389X13505005>.
- [38] Meure S, Wu DY, Furman SA. FTIR study of bonding between a thermoplastic healing agent and a mendable epoxy resin. *Vibrational Spectroscopy* 2010. <https://doi.org/10.1016/j.vibspec.2009.09.005>.
- [39] Meure S, Wu DY, Furman S. Polyethylene-co-methacrylic acid healing agents for mendable epoxy resins. *Acta Materialia* 2009;57:4312–20. <https://doi.org/10.1016/j.actamat.2009.05.032>.
- [40] Arsac A, Carrot C, Guillet J. Determination of Primary Relaxation Temperatures and Melting Points of Ethylene Vinyl Acetate Copolymers. *Journal of Thermal Analysis and Calorimetry* 2000 61:3 2000;61:681–5. <https://doi.org/10.1023/A:1010160105917>.
- [41] Almeida A, Possemiers S, Boone MN, de Beer T, Quinten T, van Hoorebeke L, et al. Ethylene vinyl acetate as matrix for oral sustained release dosage forms produced via hot-melt extrusion. *European Journal of Pharmaceutics and Biopharmaceutics* 2011;77:297–305. <https://doi.org/10.1016/J.EJPB.2010.12.004>.
- [42] Schneider C, Langer R, Loveday D, Hair D. Applications of ethylene vinyl acetate copolymers (EVA) in drug delivery systems. *Journal of Controlled Release* 2017;262:284–95. <https://doi.org/10.1016/J.JCONREL.2017.08.004>.
- [43] ASTM D7264 / D7264M - 07 Standard Test Method for Flexural Properties of Polymer Matrix Composite Materials n.d. <https://www.astm.org/DATABASE.CART/HISTORICAL/D7264D7264M-07.htm> (accessed December 14, 2019).
- [44] Drake DA, Sullivan RW, Clay SB, DuBien JL. Influence of stitching on the fracture of stitched sandwich composites. *Composites Part A: Applied Science and Manufacturing* 2021;145:106383. <https://doi.org/10.1016/J.COMPOSITESA.2021.106383>.
- [45] Dransfield K, Baillie C, Mai YW. Improving the delamination resistance of CFRP by stitching—a review. *Composites Science and Technology* 1994;50:305–17. [https://doi.org/10.1016/0266-3538\(94\)90019-1](https://doi.org/10.1016/0266-3538(94)90019-1).

A Comparative Study on the Performance Analysis of Feature Extractors Used in Augmented Reality Applications under Various Image Conditions

Ceren Akman ^{1*} , Ergun Gumus ² 

¹ Kirsehir Ahi Evran University, Department of Computer Engineering, Kirsehir, Turkey

² Bursa Technical University, Department of Computer Engineering, Bursa, Turkey

Abstract

Until today, various approaches have been proposed in order to create Augmented Reality (AR) environment where virtual-real integration takes place. One of these approaches is vision-based model, and it is divided into two branches as Marker-Based Augmented Reality (MBAR) and Markerless Augmented Reality (MAR). In the use of MBAR model, a reference image is introduced to the system before, and when this image enters the camera view, an AR environment is created. However, in MAR model, no image is introduced to the system before. Instead, it uses natural characteristics present in the image, such as edges, corners, and geometrical shapes to create an AR environment. In order to use MAR model, it is necessary to use algorithms which require high processing power and memory capacity. Within the scope of this study, MAR model was chosen as reference and an evaluation on combinations of descriptive extractors (such as ORB, SIFT, and SURF) and matchers (such as Bruteforce, Bruteforce-Hamming, and Flannbase) was presented. In this context, it was aimed that we could obtain knowledge about i) the number of key points and detection time with the use of different descriptor extractors, and ii) the number of matching key points and the amount of positional deviation of a virtual object placed on a real world scene with the use of different matchers. In line with this goal, analyses were made, using different image scales and brightness levels on both PC and mobile platforms. Results showed that, for both platforms, combinations using ORB method could work faster with less deviation than the combinations using other methods in all conditions. In addition, RANSAC algorithm was also used to reduce the total mean deviation ratio, and it was seen that the rate could be reduced from 70% to 4.5%..

Keywords: Augmented reality, Markerless augmented reality, Performance analysis, ORB, SIFT, SURF.

Cite this paper as: Ceren A. and Ergun G. (2022). A comparative study on the performance analysis of feature extractors used in augmented reality applications under various image conditions, 6(2):259-278.

*Corresponding author:
Ceren Akman

E-mail:ceren.akman@ahievran.edu.tr

Received Date:31/01/2022

Accepted Date:18/10/2022

© Copyright 2022 by
Bursa Technical University.
Availableonline at
<http://jise.btu.edu.tr/>



The works published in the journal of Innovative Science and Engineering (JISE) are licensed under a Creative Commons Attribution-NonCommercial 4.0 International License.

1. Introduction

Rapid advances in technology has brought innovations to our daily life. Augmented Reality (AR) is one of the leading ones among these innovations. AR technology is based on enriching the virtual environment by adding virtual objects on existing real world assets. While Azuma [1] defines AR concept as overlapping real and virtual data, providing a simultaneous interaction between the enriched environment and the user, Milgram et al. [2] state that AR concept emerges in the part where real environment starts to become virtual. With the help of AR technology built on the real world, 2D or 3D objects created in the virtual environment can be placed on real images, thus adding the feeling of being a part of the real world to the perception of the user [3, 4].

Supporting the content with 3D data with the help of AR technology has enabled this technology to be used in many areas, especially in the field of education. Research carried out within the scope of this study shows that old-fashion teaching techniques may be insufficient for these young people due to the fact that Generation Z grows together with technology. Especially, the increase in the preference of mobile devices, such as tablets and smart phones, has provided these devices to enter the field of education and resulted in the emergence of the concept of mobile learning. Keskin et al. [5] stated that efficiency in the education process will increase thanks to the fact that students can access information practically regardless of time and place by mobile learning. Korucu et al. [6] also studied mobile learning technique and stated that positive effects occur in the field of education as the technique increases the situations such as supporting personal learning, excitement, curiosity, and the desire to research by considering the learning process with a student-centered approach. In another study, Avci et al. [7] used AR technology to teach the periodic table, which is one of the basic subjects of chemistry course. They stated that students' interest and curiosity increased by using the developed application due to the possibility of seeing and interacting all elements in 3D environment. Uzun et al. [8] developed an AR application to explain human skeletal system to children with disabilities. In the application, human anatomy and skeletal system were supported with 3D visuals, and it was observed that disabled children learned the skeletal system more easily. In the light of this finding, by examining the studies in the field of education, it can be seen that AR technology has much to add to mobile learning process.

Especially with the arrival of Generation Z, use of mobile devices, such as tablets and phones, has increased. The ease of using these devices, the possibility of performing operations with voice commands, and the increasing usage ratio among children have accelerated the integration of AR technology to mobile platforms. At the same time, having sensors such as GPS, accelerometer, and compass, mobile devices have gained many advantages in location-based AR model [9]. AR environment can easily be created by processing the data gathered from sensors. The most frequently used application in this area has been Wikitude AR [10–12].

Apart from location-based AR technology, there are AR types such as projection-based, superimization-based, and vision-based. In vision-based AR applications, images or frames of a video shot by a camera are processed. By using feature extraction methods, coordinate data of the reference object in the image is tracked, and 2D or 3D objects are virtually positioned over this reference object. Vision-based AR technology is divided into two as Marked-Based AR (MBAR) and Markerless AR (MAR).

In order to ensure real&virtual integration with MBAR applications, a marker must be introduced to the system beforehand. When the marker gets into the view of the camera of the device, application becomes active and AR

environment gets created. In the use of the MBAR model, video stream taken from the camera is separated into frames and a previously introduced marker is searched in each frame. The search continues till the marker gets found in a frame; at this point, a virtual object is positioned on the real-world coordinate of the marker in the frame. Finally, AR environment is created by integrating virtual reality.

When examining applications of AR technology in the field of education, we can see that MBAR model has a wide usage. However, due to its dependence on defining and using of a specific marker, it lacks potential of what?. In order to eliminate this disadvantage, MAR model, which provides environment and marker independence, can be preferred. In this model, natural targets in the image are used as reference instead of introducing a marker to the system beforehand. However, in order to create an AR environment using natural targets, feature detection, extraction and matching algorithms which require high processing power and memory capacity should be used in the background. This model is disadvantageous for mobile devices with low memory capacity and processing power. On the other hand, with proper choices on parameters, fore-mentioned algorithms can be efficiently used on mobile platforms.

Within the scope of this study, the aim was to create an AR environment by using MAR model, which provides independence from the environment and the marker. For this purpose, analyses were made on PC and mobile platforms with various combinations of feature extraction and matching algorithms on video images with different brightness, scale, and color levels. During this process, i) the number of key points in the source image, ii) the detection time of key points, iii) the number of matching key points and the required time for matching between consecutive frames, and iv) the amount of positional deviation of the repositioned virtual object depending on the key points were all examined. Performance measurements were achieved, and the most appropriate algorithm combination was selected along with proper parameters. In the second, third, and fourth sections of this study, materials and methods used in the study are clearly explained, experiments along with results are presented, and discussion on the results are given, respectively.

2. Material and Method

In order for the video frames used in the AR environment to get recognized and associated in the digital environment, there is a need to determine the descriptors, such as key points, and extract the feature vectors, which are accepted as the digital signature of these descriptors. Generally, detection operations are performed, using natural descriptors such as edges, corners, and geometric shapes in video frames. Once these descriptors are found, feature vectors, which are considered as the digital signature of the image that enables what? It is not clear. Will you please write the noun instead of the pronoun here? to be used in the virtual environment, are obtained by using feature extraction methods.

There are various methods proposed for this purpose in the literature. Within the scope of this study, Oriented FAST and Rotated BRIEF (ORB), Scale-Invariant Feature Transform (SIFT), and Speeded-Up Robust Features (SURF) key point detection and feature extraction methods were employed. Also, at the matching phase, Bruteforce, Bruteforce-Hamming, and Flannbase matchers were used to match points detected in consecutive frames. In this section, these methods are briefly mentioned.

2.1. Key point Detection and Feature Extraction

2.1.1. Scale-Invariant Feature Transform (SIFT)

SIFT, by David Lowe [13], is an algorithm that basically consists of four steps which enable detection of key points on images and extraction of corresponding feature vectors. In the use of the algorithm, first of all, a Gaussian filter is applied to different scales of the pattern and appropriate key points are determined (Figure 1) [13, 14].

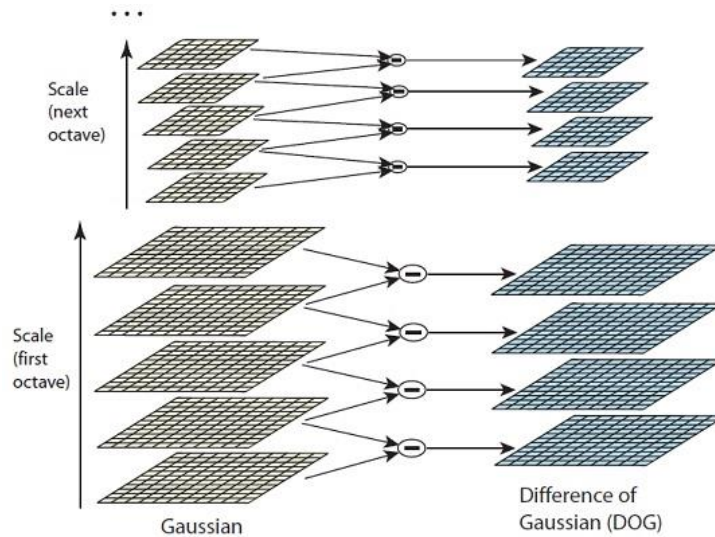


Figure 1. Using DoG at different scales [13].

Not all identified key points are stable. For this reason, locations of stable key points are determined by eliminating unstable and low-contrast points by using a quadratic Taylor series in Difference of Gaussians (DoG) space. A direction is assigned to each key point so that it is not affected by the rotation effect. In order not to get affected by other changes, a 16×16 pixel-size window is created for each key point, having the key point in the center. Then, 16 sub-windows of 4×4 size are obtained from this window; gradients are calculated for each sub-window and stored in histograms of 8 parts. By this way, 128 feature vectors having stable descriptors are extracted. SIFT algorithm is resistant to changes in rotation, scale, illumination, and perspective transformations in the image area thanks to the steps performed [13]. However, the use of this algorithm requires high computing power and memory sources. For this reason, this algorithm might be inefficient in smart mobile devices with insufficient memory capacity and processing power.

2.1.2. Speeded-Up Robust Features (SURF)

In 2006, Bay et al. [15] proposed SURF algorithm that is based on integral images and Hessian matrix as an alternative to SIFT. Similar to SIFT algorithm, SURF is resistant to changes in scale and rotation; however, it requires less computation time for key point detection and feature extraction stages as compared to SIFT. Instead of DoG method used in SIFT, box filtering method is used in SURF algorithm. In DoG method, an iterative scaling technique is used that is the result of the previous scaling is expected so that the next scaling can be performed. However, in the box filtering method, candidate key points are determined by performing different scaling operations directly on the original image instead of iterative scaling. All candidate key points are determined by using the determinant of the Hessian matrix in the current scale space, and in order to eliminate unstable candidates, the “suppress the weak one” approach is used at each scale close to $3 \times 3 \times 3$ (Figure 2). In this approach, each

candidate key point in the center is compared with a total of 26 neighboring candidate key points in all 3 scales, and if the current value of the candidate is low, it gets eliminated [16].

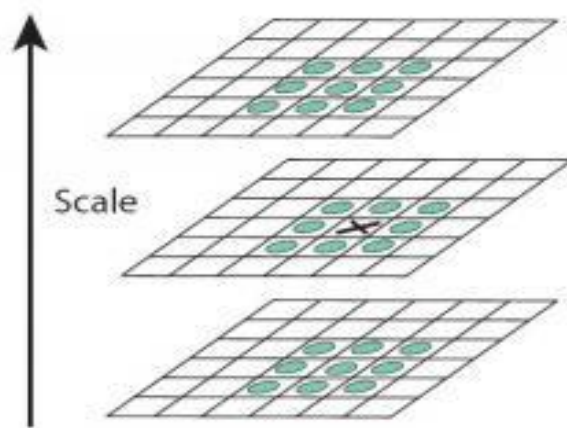


Figure 2. SURF keypoint detection [16].

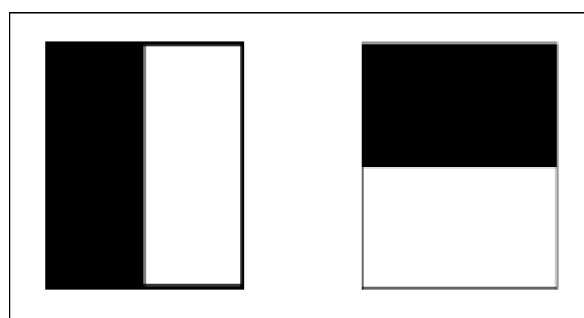


Figure 3. Haar wavelet model [16].

In SURF algorithm, a pair of Haar wavelets, shown in Figure 3, is used for x and y directions on the input image in order to increase stability of the feature vector extraction process and reduce computation time. In this model, for each key point, a neighborhood of size $20S \times 20S$ with the key point in the center is created where S is the scale level. This area is then divided into sub-regions of 4×4 . By applying Haar wavelets to these sub-regions, wavelet responses d_x and d_y values on x and y directions are obtained, respectively. Then, in order to be sensitive to rotation, wavelet responses are weighted by $2S$ Gauss, and sum of the absolute values of d_x and d_y values are found (Figure 4). Thus, the quadruple (VSURF) shown in Equation 1 is obtained for each 4×4 sub-region. A combination of all quadruples forms the final feature descriptive vector [16, 17].

$$V_{SURF} = (\sum d_x, \sum d_y, \sum |d_x|, \sum |d_y|) \quad (1)$$

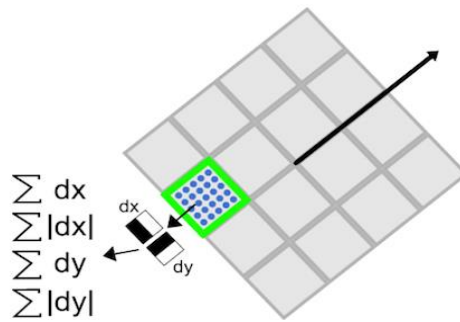


Figure 4. Descriptive component diagram [16].

2.1.3. Oriented FAST and Rotated BRIEF (ORB)

ORB is yet another key point detection and feature extraction algorithm based on FAST [18] and BRIEF [19] algorithms. It was developed by Rublee et al. [20] as an alternative to SIFT and SURF algorithms. ORB gains scale invariance by using the scale pyramid. For each scale, key points are determined by using FAST, and top N key points are quickly found by using the Harris corner metric. FAST has no orientation feature. To overcome this problem, ORB uses “Center of Gravity” method. In order to obtain the orientation vector, density centroid of the corners (C) is calculated by using Equation 2 where I is the image itself [21].

$$m_{pq} = \sum_{x,y} x^p y^q I(x,y), \quad C = \left(\frac{m_{10}}{m_{00}}, \frac{m_{01}}{m_{00}} \right) \quad (2)$$

After that, an \overrightarrow{OC} vector is obtained from point C to point O, which is the geometric center of the vertices. Using Equation 3, direction of this vector is determined by finding the angle θ between points O and C. Thus, ORB gains the feature of orientation.

$$\theta = \arctan \left(\frac{m_{01}}{m_{10}} \right) \quad (3)$$

BRIEF, which is another component of ORB, does not provide good results in terms of rotation. To overcome this problem, a randomly chosen pixel dataset around each key point is formed. By applying an intensity-based binary test to all pixel pairs in this dataset, a new matrix P containing binary test results is obtained. Then, for orientation angle θ , rotation matrix R_θ (Equation 4) is calculated and used in Equation 5, to find the oriented matrix P_θ [19, 20].

$$R_\theta = \begin{bmatrix} \cos \theta & -\sin \theta \\ \sin \theta & \cos \theta \end{bmatrix} \quad (4)$$

$$P_\theta = R_\theta \cdot P \quad (5)$$

2.2. Descriptor Matching

Matching phase is the next step that should be applied after key point detection and feature extraction in order to create an AR environment. In this phase, descriptor matchers such as Bruteforce, Bruteforce-Hamming, and FLANN-based matching [22, 23] are used to determine the correspondence between descriptors in different perspectives of a particular object. By this way, it is ensured that operations of great importance such as detection

and tracking of the object are carried out. The main idea behind these matchers is based on K-Nearest Neighbors algorithm which finds top K-nearest neighbors (in query image) of each descriptor from the reference image. However, the proximity values detected between two images may be erroneous due to noise. In order to prevent this error and provide a stable matching process, usually a screening system based on a predetermined threshold is used. In this system, a metric which is defined as the ratio of distance between closest pairs to distance between second closest pairs shows whether the match is correct or not. If this ratio is less than the threshold, it is considered as an acceptable match; otherwise, the next pair is evaluated.

2.3. Random Sample Consensus (RANSAC)

RANSAC algorithm was developed by Fischler and Bolles [24] to predict a strong and successful model from the dataset by eliminating outliers according to the input data. Matches found by using descriptor matching methods are not always expected to be reliable due to the noise in the image. Therefore, by using the RANSAC method, whose steps are given in Algorithm 1, this handicap can be eliminated and most accurate matches can be obtained, allowing a stable homograph estimation [25–27].

Algorithm 1: Steps of RANSAC algorithm.

- 1- S samples are randomly chosen from the dataset X consisting of correct matches, and the model parameter is determined according to selected samples.
- 2- Points within a specified threshold value t are assigned to the model parameter and the dataset X_i is determined according to these assigned values. The dataset X_i is the consensus of the sample data.
- 3- If the size of X_i is greater than threshold t , then, the model is re-estimated by using all points in X_i and the process is finished.
- 4- If the size of X_i is less than threshold t , again, S samples are randomly chosen from dataset X and previous steps are repeated.
- 5- After N trials, the largest consensus set X_i is selected, and the model is recreated by using all points in the X_i dataset.

3. Results and Discussion

Numerical data associated with the figures in this section can be found at <https://github.com/akmanrcn/article-graphics-results>.

AR assisted education is one of the common application fields of AR technology and is chosen as the subject of this study. By the literature review, it was seen that majority of the applications developed for this area is based on MBAR, which relies on a predefined specific marker. However, relying on such a marker restricts the practicality of applications. Because of this disadvantage, MAR, which accepts natural features in the view as reference and provides environment and marker independence, is studied instead.

MAR model, as mentioned in the previous sections, is composed of key point detection, feature extraction, and matching processes. These processes of MAR use algorithms which require high computation power and memory resource. In order to compensate these needs and create a stable AR environment, tests were performed on both PC

and mobile platforms with reasonable sources. PC platform had a 6-cores CPU running at 4.50GHz, and 16GB RAM while the mobile platform had a 4-cores CPU running at 2.0GHz, and 2GB RAM.

In order to create an AR environment on mentioned platforms, a 433-frames long video with the resolution of 1280×800 pixels were shot using the mobile platform. The first frame was selected as the reference image, and the remaining 432 frames were accepted as query images. These images were processed with key point detection and feature extraction algorithms such as ORB, SIFT, and SURF under different brightness (Figure 5), and scaling conditions, both on mobile and PC platforms. After that, the performance of these algorithms was compared by using test results obtained from all query images.

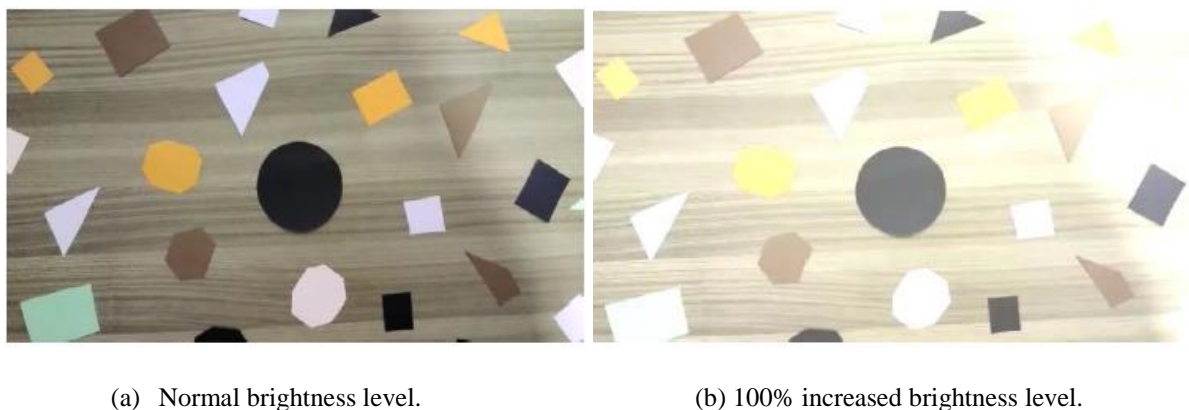


Figure 5. Different brightness levels of the sample video.

First of all, average runtimes on PC platform (average of runs at 10 different times) for different scaling levels of the query images were examined. In the examination, current brightness level was kept constant (normal brightness).

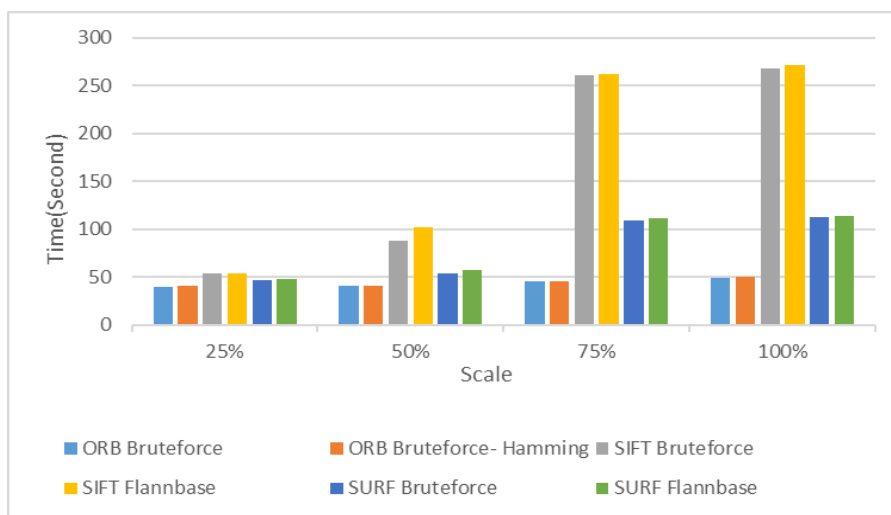


Figure 6. Average runtimes at normal brightness level on PC platform.

Figure 6 shows runtimes of various combinations of detection, extraction, and matching algorithms on PC platform for four different scaling levels when the brightness is kept at normal level. It can be clearly seen that ORB-based combinations were the fastest and SIFT-based combinations were the slowest ones in terms of running time.

When the brightness level was increased by 100%, average runtimes (average of 10 different runs) of various combinations of detection, extraction, and matching algorithms on PC platform for four different scaling levels were found as shown in Figure 7.

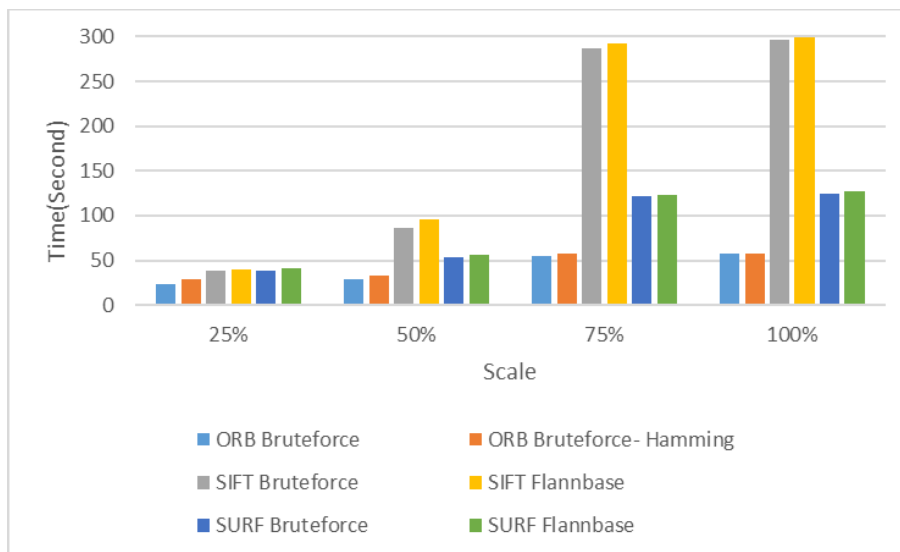


Figure 7. Average runtimes at 100% increased brightness level on PC platform.

As seen in Figure 7 as well, ORB-based combinations were the fastest and SIFT-based combinations were the slowest ones when there was a 100% increase in brightness level. Compared to Figure 6, a negligible increase in average runtimes was observed when the brightness level was increased.

In a similar fashion, Figure 8 and 9 show average runtimes of combinations of detection, extraction, and matching algorithms on mobile platform, under normal and 100% increased brightness levels, respectively.

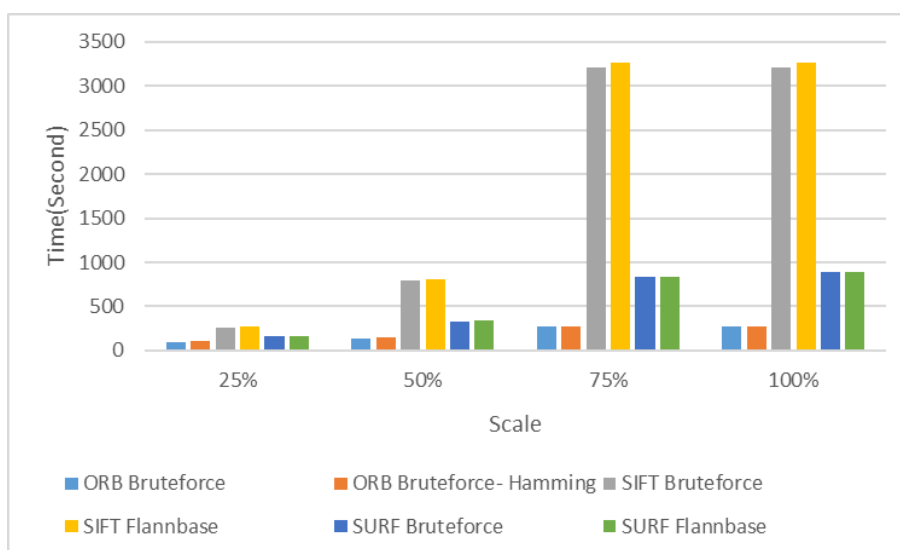


Figure 8. Average runtimes at normal brightness level on mobile platform.

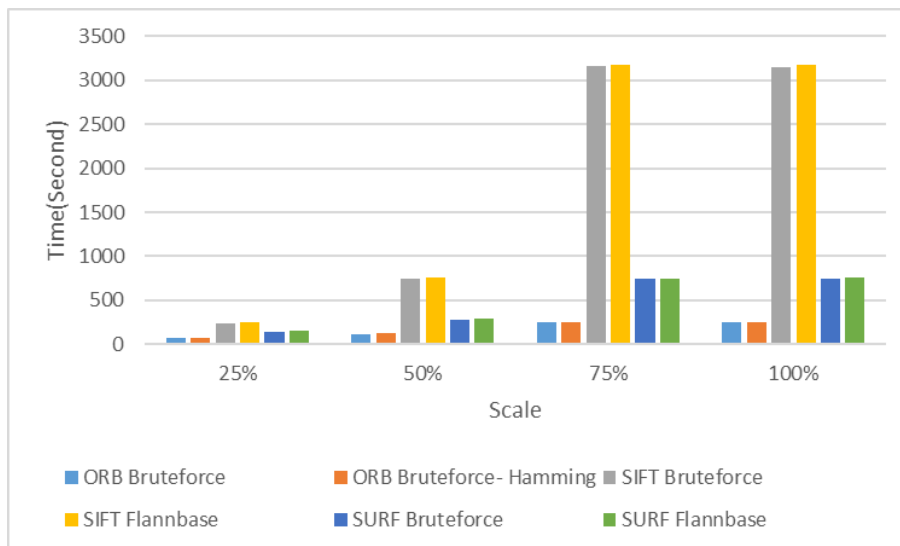


Figure 9. Average runtimes at 100% increased brightness level on mobile platform.

As similar to the previous results, ORB-based combinations were the fastest and SIFT-based combinations were the slowest ones under different brightness levels on mobile platform. However, considering average runtimes, it was observed that the time spent on mobile platform was much higher than the time spent on PC platform. Considering the figures, it is obvious that runtimes can be reduced by decreasing the scaling level, which is an advantage for mobile platforms.

Key point detection and feature extraction processes directly affect average runtime (average of 10 different runs). For normal brightness (NP) and increased brightness (AP) levels, average detection times of all key points on the PC platform are given in Figure 10.

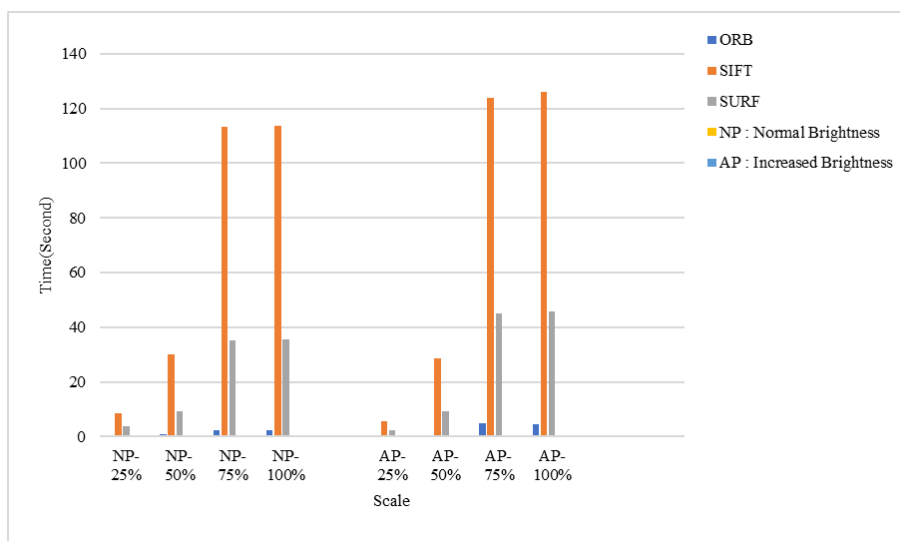


Figure 10. Average keypoint detection times under NP/AP conditions on PC platform.

When average key point detection times for both platforms were examined, it was observed that the process was completed at the slowest pace by using SIFT and fastest using ORB. Test runs were also performed on mobile platform. It was observed that the application on mobile platform runs 13 times slower than the one on PC platform. However, ratios of runtimes of algorithms remained the same.

Another factor affecting the total runtime is feature extraction process. For PC and mobile platforms, average times to extract the feature vector at normal brightness and increased brightness levels are given in Figure 11 and Figure 12, respectively. Examining the figures, it was observed that feature extraction process was again completed, at the slowest pace by using SIFT and at the fastest pace by using ORB.

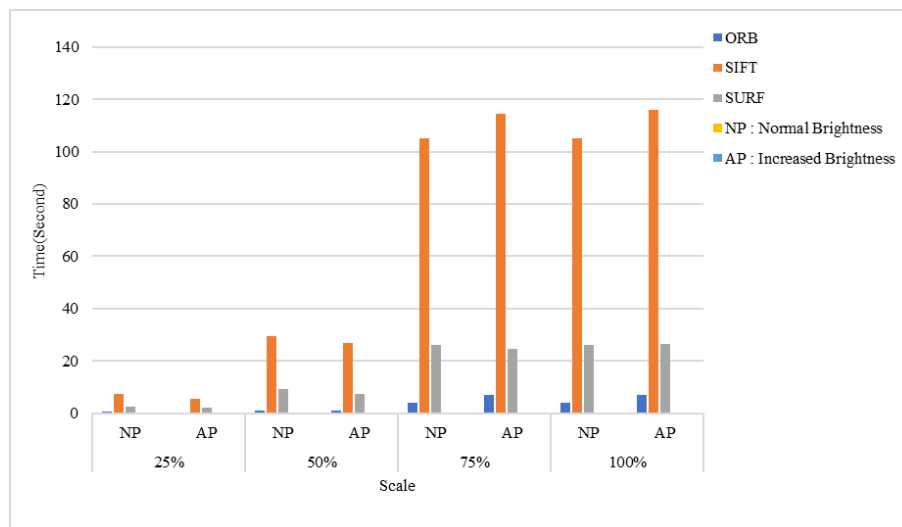


Figure 11. Feature extraction times under NP/AP conditions on PC platform.

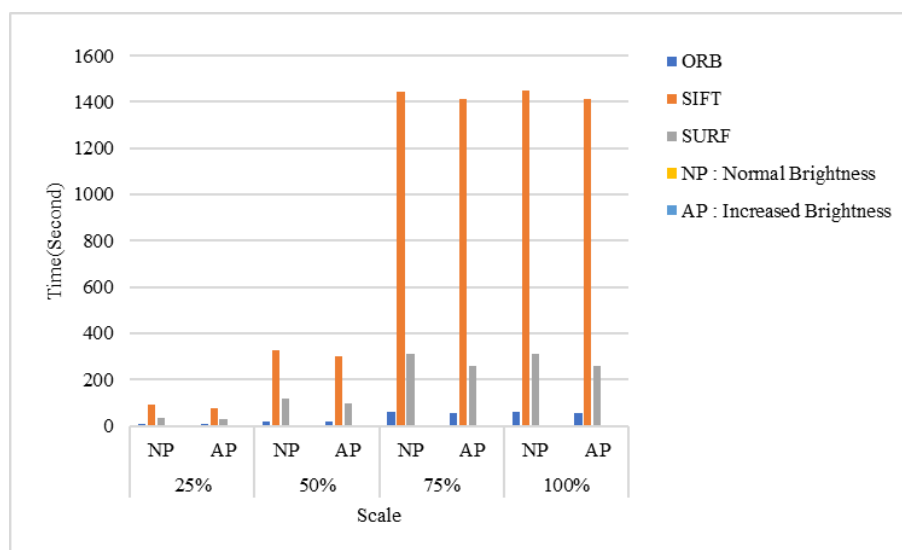


Figure 12. Feature extraction times under NP/AP conditions on mobile platform.

Number of key points obtained from all query images at normal brightness level was the same for both platforms, as shown in Figure 13. The same conclusion can be made for the increased brightness level, the results of which are given in Figure 14. In terms of the number of key points, it was seen that SURF detected the most while ORB detected the least. Figure 10 reveals that, SIFT was the slowest algorithm, while SURF detected more key points than any other algorithms. This shows that box filtering approach used in SURF is more advantageous than Gaussian filtering approach used in SIFT. Similar results have been reported in studies in the literature [29-30].

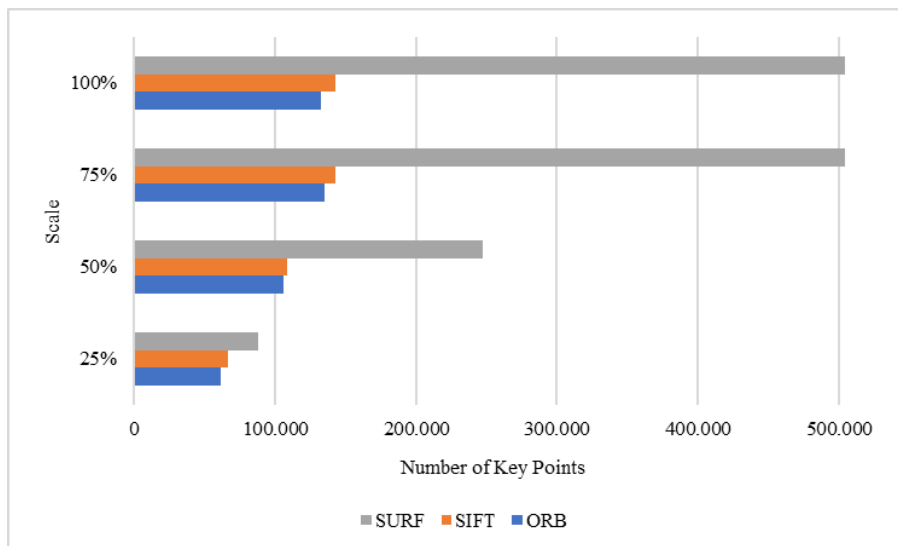


Figure 13. Number of key points at normal brightness level on PC/mobile platform.

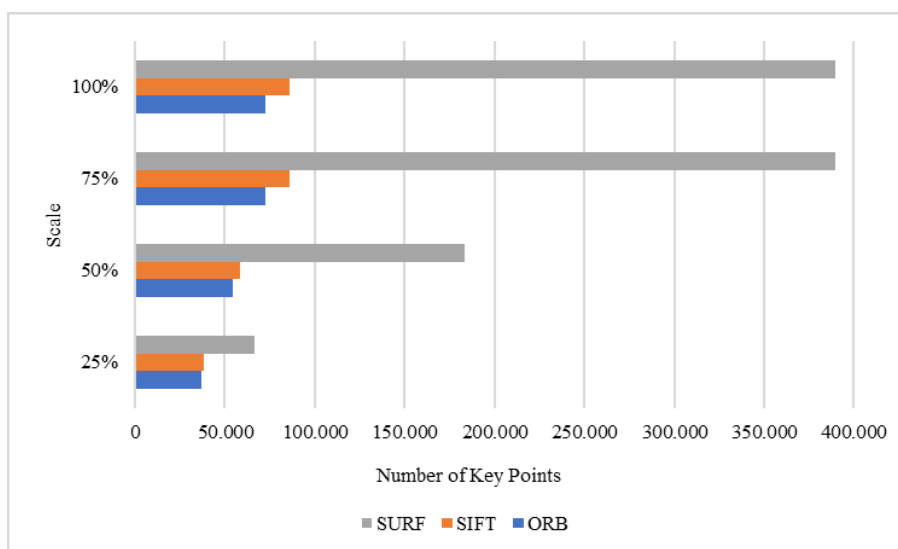
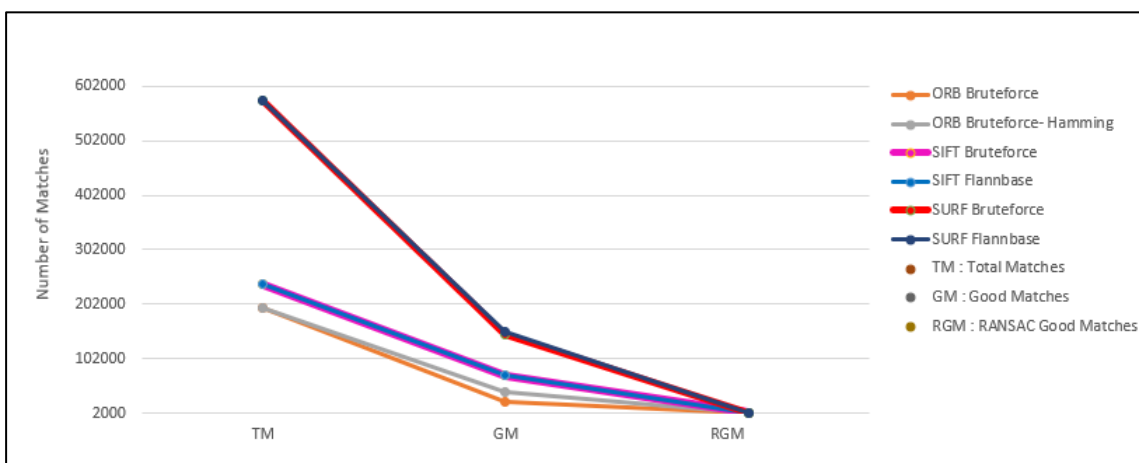


Figure 14. Number of key points at increased brightness level on PC/mobile platform.

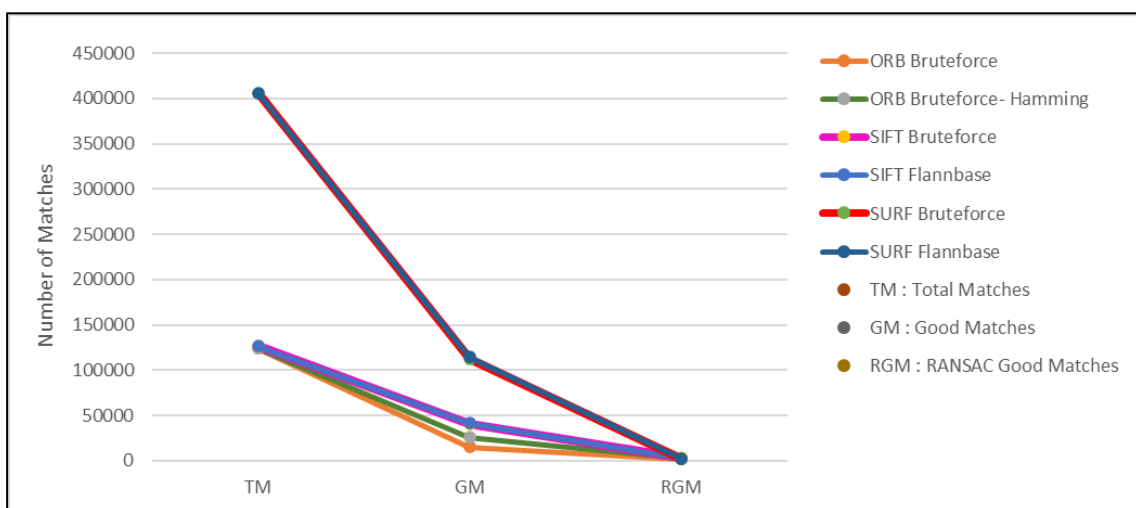
Increasing the brightness level at all scaling levels for mobile platform and at 25%, 50% scaling levels for PC platform reduced the average runtime. However, increasing the brightness level at 75%, 100% scaling levels on PC platform also resulted in an increase in the average runtime (Figure 7). While the increase and decrease in runtimes were negligible, it is not possible to reach the same conclusion for the number of key points. When the brightness level was increased, the number of detected key points decreased to a level that could not be neglected (Figure 13 vs. Figure 14). Thus, it can be seen that, although increasing the brightness level may seem advantageous in terms of operating time, this may be a disadvantage in terms of the detected key points, causing loss of valuable data. This is a trade of for mobile platforms.

Following the key point detection and feature extraction steps, matching methods are used for scene tracking. For this step, Bruteforce, Bruteforce-Hamming, and Flannbase matchers were used together with K-Nearest Neighbors (KNN) algorithm. Using this algorithm, each descriptor (Q) in the query image is matched with the two nearest neighbor descriptors (R1 and R2) in the reference image. By this way, images obtained from the sample video were

compared with the reference image, and the matching process was completed. However, detected matches were not entirely correct. Therefore, the distance between matching descriptors was compared to a preselected threshold value. Considering the present studies in literature, this value is generally chosen as 0.8 [28]. In the calculation process, if the distance between Q and R1 was less than $\text{threshold} \times \text{the distance between Q and R2}$, then, Q-R1 pair was accepted as a correct matching pair represented by GM (Good Matches). However, all GM were still not reliable due to the noise in images. At this point, in order to overcome the problem, researchers have shown that absolute correct matches can be detected by using RANSAC algorithm [29-30]. Thus, in this study, RANSAC algorithm was used to make a more accurate homograph estimation. The most accurate matching pairs obtained by using RANSAC are expressed by RGM (RANSAC Good Matches). For both brightness levels, the number of matches obtained in all cases (TM: Total matches, GM: Good Matches, RGM: RANSAC based Good Matches) are given in Figures 15, 16, and 17. Figure 15 shows results for 100% and 75% scaling levels, Figure 16 shows results for 50% scaling level, and Figure 17 shows results for 25% scaling level.



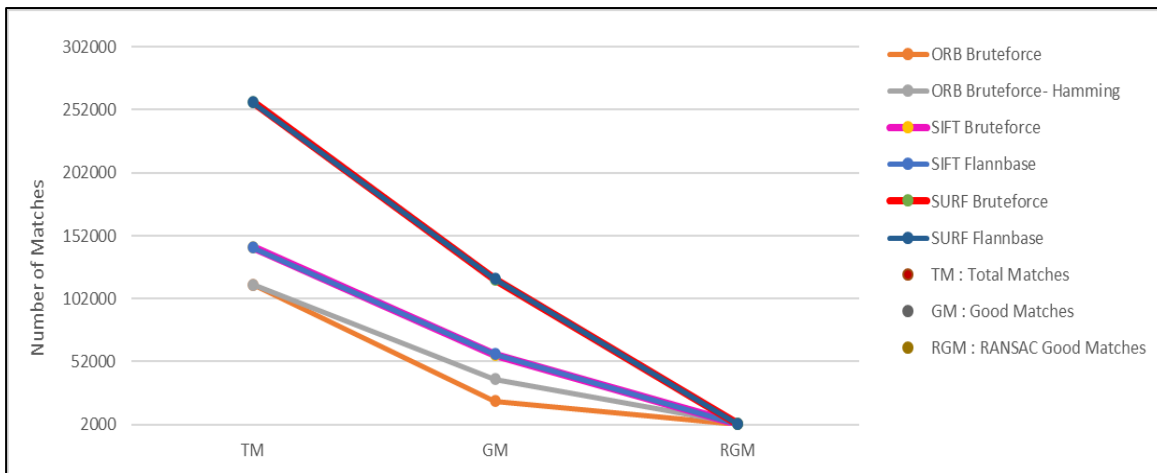
(a) Normal brightness.



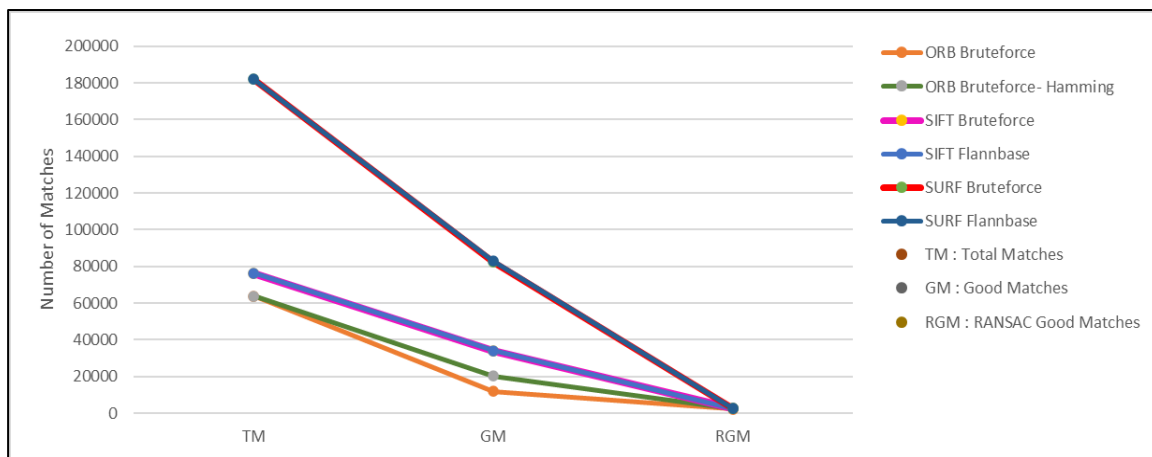
(b) Increased brightness.

Figure 15. Number of matches for 100% and 75% scales on both platforms.

(a): Normal brightness, (b): Increased brightness



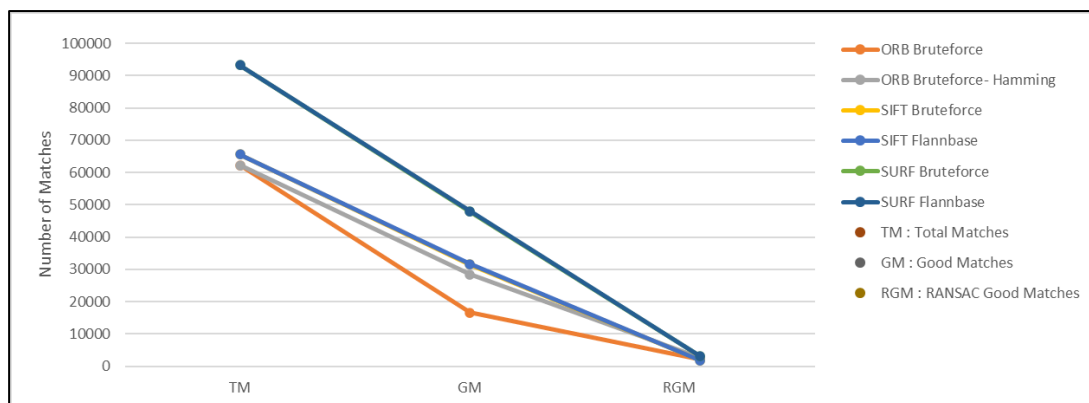
(a) Normal brightness.



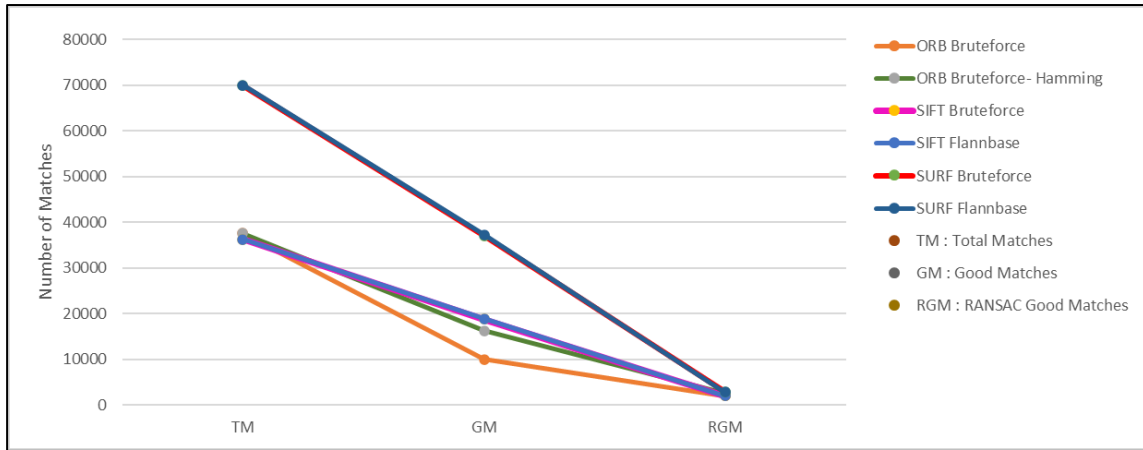
(b) Increased brightness.

Figure 16. Number of matches for 50% scale on both platforms.

(a): Normal brightness, (b): Increased brightness



(a) Normal brightness.



(b) Increased brightness.

Figure 17. Number of matches for 25% scale on both platforms.

(a): Normal brightness, (b): Increased brightness

Considering the number of total matches, matching after SURF gives the highest number of matches while matching after ORB gives the lowest. By applying Equations 6 and 7, proportional GM% and proportional RGM% rates were also obtained (Figure 18), respectively. These values are the same for both PC and mobile platforms. It was observed that GM% was the highest for SIFT-derived descriptors at 100% and 75% scaling levels, and for SURF-derived descriptors at 50% and 25% scaling levels. However, when examining RGM%, it was observed that RGM% was the highest for ORB-derived descriptors at all scaling levels. This reveals that RANSAC algorithm chooses more descriptors derived by ORB than SIFT or SURF. GM% and RGM% rates for the increased brightness level are also given in Figure 19.

$$GM\% = GM/TM * 100 \tag{6}$$

$$RGM\% = RGM/GM * 100 \tag{7}$$

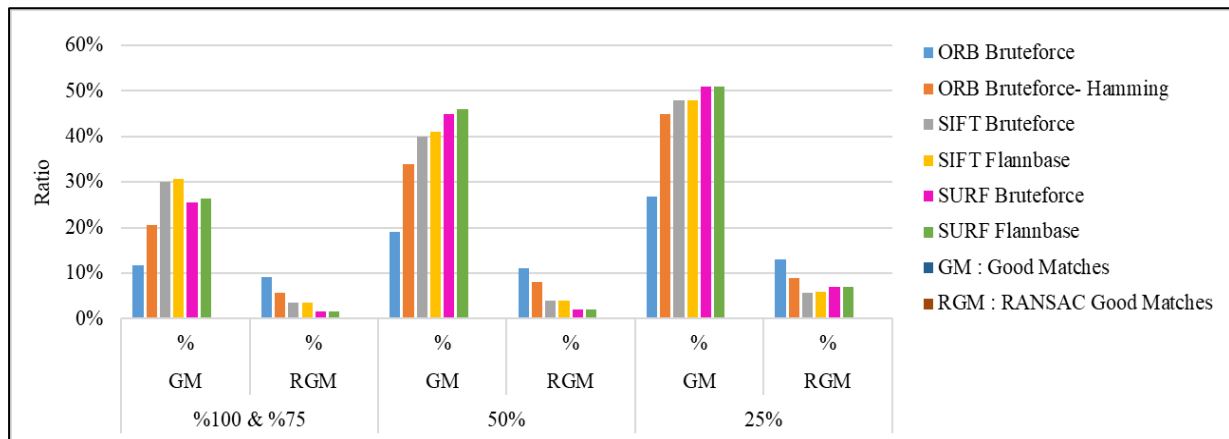


Figure 18. Matching rates at normal brightness level.

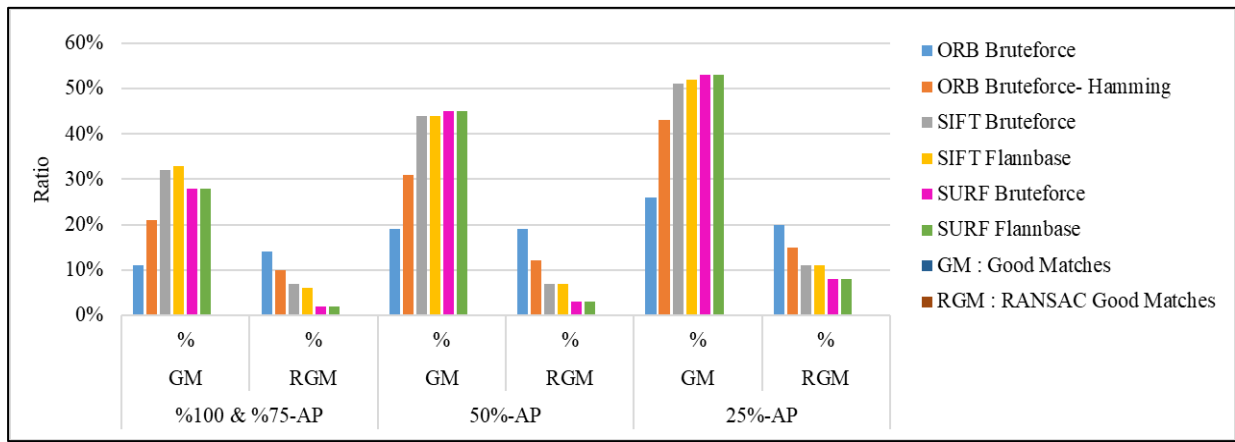


Figure 19.. Matching rates at increased brightness level.

Another subject of the study is to compare the performance of detection&matching combinations in terms of positioning a virtual object. For this purpose, a virtual object was placed in the center of the black circle shown in Figure 5 which is the first frame (reference image) of the video. Then, this object was repositioned on following 432 frames (query images) of the video by using various descriptor&matcher combinations such as OB (ORB Bruteforce), OBH (ORB Bruteforce-Hamming), SB (SIFT Bruteforce), SFL (SIFT Flannbase), SFFL (SURF Flannbase), and SFB (SURF Bruteforce). At each repositioning step, one might expect to see the virtual object maintaining its position in the very center of the black circle; however, this does not happen all the time causing a deviation. In order to measure the amount of this deviation, the distance between the new position of the object and the center of the circle should be calculated at each repositioning step. For this, the center of the circle in each image was determined by using HoughCircle method provided by OpenCV 2.4.11 library. The amount of deviation changes depending on the used descriptor&matcher combinations, brightness level, and scaling level (Figure 20).

	Scale Size			
	25%	50%	75%	100%
δ	320*200	640*400	960*600	1280*800

Figure 20. δ value for each scaling level.

By using Equations 8 and 9, pixel-based deviation value (DV) and deviation ratio subject to the image scale (DRS) were calculated for each query image, respectively. Afterwards, a total of 10 query images with the lowest and highest deviations were determined as outliers and got eliminated. Then, a mean deviation ratio (MDR) over all query images was calculated.

$$DV = \frac{\sqrt{x^2+y^2}}{\delta} \tag{8}$$

$$DRS = DV * 100 \tag{9}$$

The mean deviation ratios at each scaling level were examined separately for both platforms, at normal brightness level, and without using RANSAC. For 100% scaling level, it was observed that the highest MDR occurred by using SIFT-based descriptor&matcher combinations, while the lowest MDR occurred by using ORB-based descriptor&matcher combinations (Figure 21).

Matching rates and the number of key points are numerically the same for 75% and 100% scaling levels (see Figures 13-14, 18-19). However, the resolution obtained as a result of scaling on the image is different. Therefore, MDR differs for these two scaling levels. Examining Figure 21, it can be said that the decrease in the scaling level reduced the deviation ratio for SURF-based descriptor&matchers while this is not valid for other combinations. On the other hand, when the deviation ratio axis is examined, one can see that there are deviations above 100%. This indicates that the virtual object deviates too much or even goes off the screen.

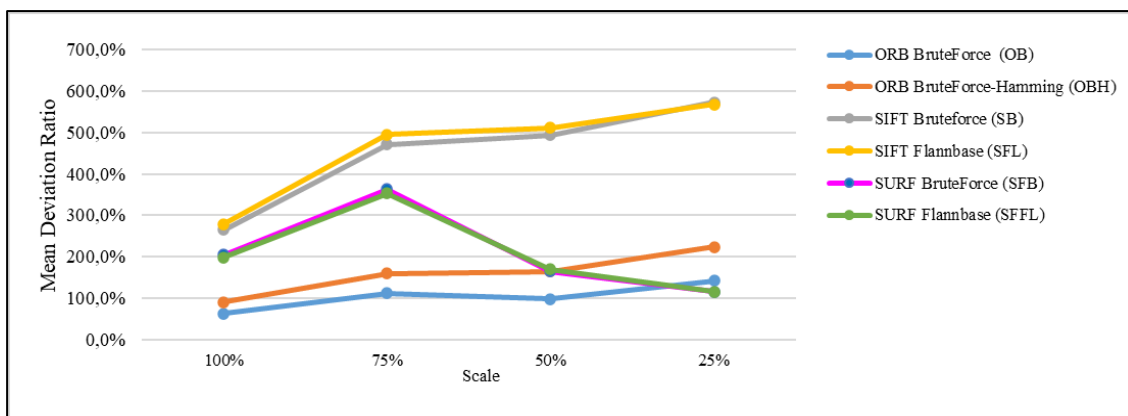


Figure 21. MDR without RANSAC at normal brightness level on both platforms.

MDR values in Figure 22 were obtained by using RANSAC algorithm at normal brightness level for both platforms. Paying attention to the deviation ratio axis, one can see that the virtual object remained on the screen for all descriptor&matcher combinations at all scaling levels, even if it deviated from the position it should be. It is observed that, for all combinations, there is less deviation when using the original 100% scaling level and more deviation at 25% scaling level.

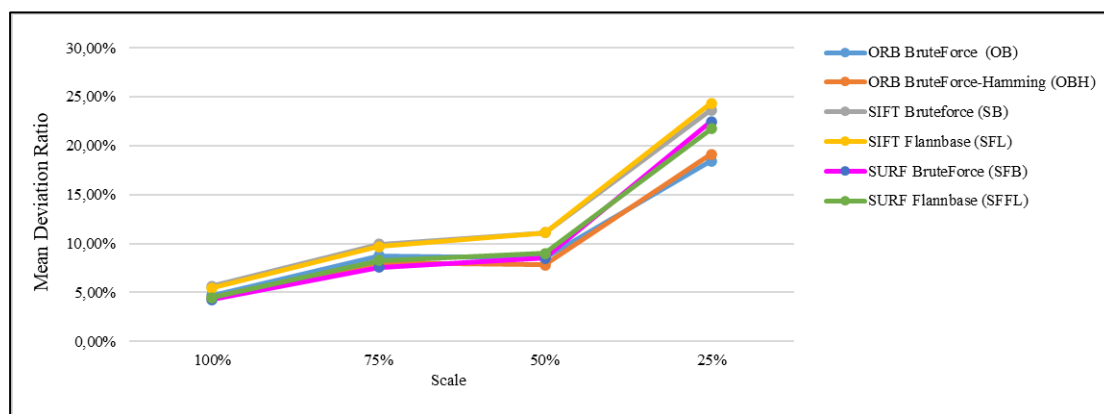


Figure 22. MDR with RANSAC at normal brightness level on both platforms.

Similar tests were done, using the test video with the increased brightness. When the deviation ratio axis in Figure 23 is examined, without using RANSAC, MDR value is observed to be less than MDR value obtained by using the normal brightness level. However, MDR values are mostly above 100%. This indicates that the virtual object usually moves on screen and is mostly off-screen. When deviations of all combinations at various scaling levels were examined, it was observed that the least deviation occurred in OOB combination at 100% scaling level, and the highest deviation occurred in SFSFL combination at 75% scaling level.

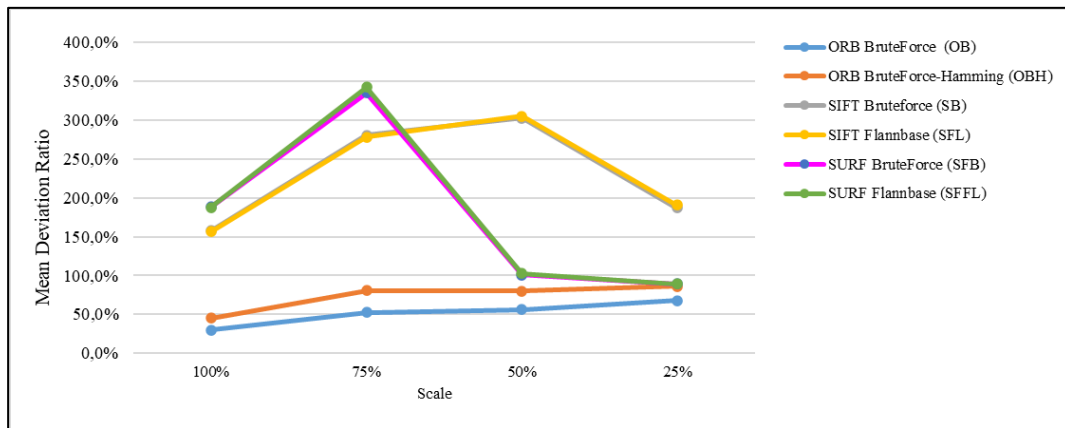


Figure 23. MDR without RANSAC at increased brightness level on both platforms.

MDR values in Figure 24 were obtained by using RANSAC algorithm at increased brightness level for both platforms. When the deviation ratio axis is examined for all combinations, the virtual object is seen to deviate from its intended position but remains on the screen at all scaling levels. It is also observed that the virtual object deviates the least at 100% scaling by using OOB combination, and the most at 25% scaling level by using SSFL combination. RANSAC algorithm seems to be effective in reducing the deviation and gives more accurate results as resolution approaches to its original scale level.

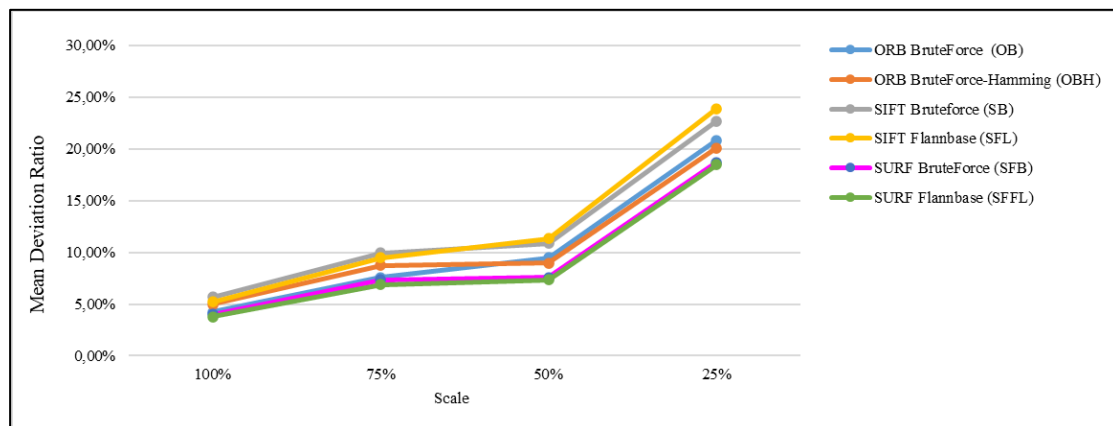


Figure 24. MDR with RANSAC at increased brightness level on both platforms.

4. Conclusion

The comparative analysis of the feature extractors used in this study is compatible with the results of previous studies [30-31]. A comparative performance analysis of the combinations of various key point detectors, feature extractors, and matcher algorithms at different brightness/scale levels has been made on mobile and PC platforms. By using these combinations, key points and corresponding feature vectors in frames of a test video were extracted and matched. The time spent extracting and matching the key points, the number of key points detected, the number of matches and the amount of deviation of the virtual object added to the image are the main areas of interest of the study.

In key point detection and feature extraction algorithms used in the study, according to the hardware used,

brightness level and scale levels, gave various results in outputs such as the number of key points, runtime, and match rate. When all the results are examined, the increase in the brightness level is observed to have a reducing effect on the number of key points detected and the key point extraction time, but it has no significant effect on the amount of deviation. This shows that the increase in the brightness level naturally leads to elimination of weak key points. This can be interpreted as an advantage for mobile platforms with low processing power.

Rather than the reduction in runtime, the most important issue is the match rate in the output, so RANSAC algorithm was used to improve stability. With the use of the algorithm, mean deviation ratio was reduced to approximately 5% for all descriptor&matcher combinations at 100% scaling level. However, when the scale level was reduced to a quarter, it was observed that the mean deviation ratio increased approximately four folds. This shows that a MAR model that makes use of the aforementioned algorithms will be significantly affected by the image scale. At this point, especially for mobile platforms, the use of ORB-based detector & matcher combination with RANSAC may be a suitable choice due to the advantages in runtime, key point matching rate, and low deviation ratio.

As future work, it is aimed to hybridize the current study with deep learning networks used for object recognition.

References

- [1] Azuma, R. T. (1997). A Survey Of Augmented Reality. *Presence: Teleoperators & Virtual Environments*, 6(4), 355-385.
- [2] Milgram, P., & Kishino, F. (1994). A Taxonomy Of Mixed Reality Visual Displays. *IEEE Transactions On Information And Systems*, 77(12), 1321-1329.
- [3] Ufkes, A., & Fiala, M. (2013, May). A Markerless Augmented Reality System For Mobile Devices. In 2013 International Conference On Computer And Robot Vision (pp. 226-233). IEEE.
- [4] Gonzato, J. C., Arcila, T., & Crespín, B. (2008). Virtual Objects On Real Oceans. In *Graphicon'2008* (Pp. 49-54).
- [5] Keskin, N. Ö., & Kiliç, A. G. H. (2015). Mobil Öğrenme Uygulamalarına Yönelik Geliştirme Platformlarının Karşılaştırılması ve Örnek Uygulamalar. *Açıköğretim Uygulamaları Ve Araştırmaları Dergisi*, 1(3), 68-90.
- [6] Korucu, A. T., & Biçer, H. (2019). Mobil Öğrenme: 2010-2017 Çalışmalarına Yönelik Bir İçerik Analizi. *Trakya Eğitim Dergisi*, 9(1), 32-43.
- [7] Avcı, A. F., & Taşdemir, Ş. (2019). Artırılmış Ve Sanal Gerçeklik ile Periyodik Cetvel Öğretimi. *Selcuk University Journal Of Engineering Sciences*, 18(2), 68-83.
- [8] Uzun, Y., Bilban, M., & Kalaç, M. Ö. (2018). Artırılmış Gerçeklik Kullanılarak Engelli Çocukların Öğrenme Yeteneklerinin Geliştirilmesi. *Uluslararası Engelsiz Bilişim Kongresi*.
- [9] Schall, G., Grabner, H., Grabner, M., Wohlhart, P., Schmalstieg, D., & Bischof, H. (2008, June). 3d Tracking In Unknown Environments Using On-Line Keypoint Learning For Mobile Augmented Reality. In 2008 IEEE Computer Society Conference On Computer Vision And Pattern Recognition Workshops (Pp. 1-8). IEEE.
- [10] Kağan, G. Ü. L., & Şahin, S. (2017). Bilgisayar Donanım Öğretimi İçin Artırılmış Gerçeklik Materyalinin Geliştirilmesi ve Etkililiğinin İncelenmesi. *Bilişim Teknolojileri Dergisi*, 10(4), 353-362.
- [11] İçten, T., & Güngör, B. A. L. (2017). Artırılmış Gerçeklik Üzerine Son Gelişmelerin ve Uygulamaların İncelenmesi. *Gazi Üniversitesi Fen Bilimleri Dergisi Part C: Tasarım ve Teknoloji*, 5(2), 111-136.
- [12] Kaleci, D., Demirel, T., & Akkuş, I. (2016). Örnek Bir Artırılmış Gerçeklik Uygulaması Tasarımı. xviii.

Akademik Bilişim Konferansı, Aydın, Türkiye.

- [13] Lowe, D. G. (2004). Distinctive Image Features From Scale-Invariant Keypoints. *International Journal Of Computer Vision*, 60(2), 91-110.
- [14] https://docs.opencv.org/3.4/da/df5/tutorial_py_sift_intro.html [Accessed: April 4th, 2021].
- [15] Bay, H., & Tuytelaars, T. (2006). Luc Van Gool. Surf: Speeded Up Robust Features, 14.
- [16] Evans, C. (2009). Notes On The Opensurf Library. University Of Bristol. Tech. Rep.
- [17] Li, A., Jiang, W., Yuan, W., Dai, D., Zhang, S., & Wei, Z. (2017). An Improved Fast+ Surf Fast Matching Algorithm. *Procedia Computer Science*, 107, 306-312.
- [18] Viswanathan, D. G. (2011). Features From Accelerated Segment Test (Fast) Deepak Geetha Viswanathan 1.
- [19] Calonder, M., Lepetit, V., Strecha, C., & Fua, P. (2010, September). Brief: Binary Robust Independent Elementary Features. In *European Conference On Computer Vision* (Pp. 778-792). Springer, Berlin, Heidelberg.
- [20] Rublee, E., Rabaud, V., Konolige, K., & Bradski, G. (2011, November). Orb: An Efficient Alternative To Sift Or Surf. In *2011 International Conference On Computer Vision* (Pp. 2564-2571). IEEE.
- [21] Rosin, P. L. (1999). Measuring Corner Properties. *Computer Vision And Image Understanding*, 73(2), 291-307.
- [22] Muja, M. (2009). Approximate Nearest Neighbors With Automatic Algorithm Configuration. In *Proc. Int. Conf. On Computer Vision Theory And Applications*, Lisbon, 2009.
- [23] https://docs.opencv.org/4.x/dc/dc3/tutorial_py_matcher.html [Accessed: Augustth 29, 2021].
- [24] Fischler, M. A., & Bolles, R. C. (1981). Random Sample Consensus: A Paradigm For Model Fitting With Applications To Image Analysis And Automated Cartography. *Communications Of The Acm*, 24(6), 381-395.
- [25] Dihkan, M. (2019). Uzaktan Algılanmış Görüntülerin Surf Özellik Verileri Ve Ransac Algoritması Ile Otomatik Çakıştırılması. *Gümüşhane Üniversitesi Fen Bilimleri Enstitüsü Dergisi*, 9(3), 425-432.
- [26] Erdöl, E. S. (2019). Anahtar Noktası Ve Yama Eşleşme Yöntemleri Ile Doku Bazlı Görüntü Sahteciliği Tespiti (Doctoral Dissertation, Karadeniz Teknik Üniversitesi).
- [27] Çömert, R., & Avdan, U. Yersel Lazer Tarayıcı Verilerinden Basit Geometrik Yüzeylerin Otomatik Olarak Çıkarılması.
- [28] A. Jakubović and J. Velagić, "Image Feature Matching and Object Detection Using Brute-Force Matchers," 2018 International Symposium ELMAR, 2018, pp. 83-86, doi: 10.23919/ELMAR.2018.8534641.
- [29] Li, H., Qin, J., Xiang, X., Pan, L., Ma, W., & Xiong, N. N. (2018). An efficient image matching algorithm based on adaptive threshold and RANSAC. *IEEE Access*, 6, 66963-66971.
- [30] S. A. K. Tareen and Z. Saleem, "A comparative analysis of SIFT, SURF, KAZE, AKAZE, ORB, and BRISK," 2018 International Conference on Computing, Mathematics and Engineering Technologies (iCoMET), 2018, pp. 1-10, doi: 10.1109/ICOMET.2018.8346440.
- [31] Karami, E., Prasad, S., & Shehata, M. (2017). Image matching using SIFT, SURF, BRIEF and ORB: performance comparison for distorted images. *arXiv preprint arXiv:1710.02726*.

Influence of Bridge Piers on Velocity under Unsteady Flows

Gokcen Bombar 

İzmir Katip Çelebi University, Department of Civil Engineering, Çiğli, İzmir, Turkey.

Abstract

It is reported that every year hundreds of bridges collapse due to the dynamic forces acting on the piers, particularly during floods and the scour around the foundations. Since the determination of the velocity distribution upstream of the pier is directly related to this force, it is important to predict the effect of a presence and diameter of a bridge pier on velocity and turbulence parameters. In this study, the time variation of point velocities in the stream-wise and vertical direction at a point upstream of a bridge pier was obtained under clear-water and unsteady flow conditions. The presence of the bridge pier causes the velocity profile to be steeper. The increase in pier diameter decreased the maximum stream-wise velocity whereas it increased the vertical velocity in the down flow direction particularly near the bed. The turbulence intensity in stream-wise direction increases in the rising limb and decreases in the falling limb, more prominently near the bottom. The maximum percent reductions in the stream-wise velocities at peak flow were calculated as 6% and 11% for the small and big piers, respectively. The reduction in stream-wise velocity at peak flow increases with depth especially for the pier with greater diameter.

Keywords: Flood flow, Bridge pier, Velocity time series, Velocity profile.

Cite this paper as:

Bombar, G. (2022). *Influence of Bridge Piers on Velocity under Unsteady Flows*. Journal of Innovative Science and Engineering, 6(2): 279-296

*Corresponding author: Gokcen Bombar
E-mail: gokcen.bombar@ikcu.edu.tr

Received Date: 25/02/2022
Accepted Date: 24/08/2022
© Copyright 2022 by
Bursa Technical University. Available
online at <http://jise.btu.edu.tr/>



The works published in Journal of Innovative Science and Engineering (JISE) are licensed under a Creative Commons Attribution-NonCommercial 4.0 International License.

1. Introduction

The collapse of a bridge usually results in a loss of life and property where almost 60% of these failures result from scour and other hydraulic-related causes [1]. Especially, after a heavy rainfall inducing a flood flow, the dynamic forces acting on the piers increase rapidly which are directly related to the velocity and its vertical distribution [2]. Therefore, the stability and structural design of bridges must be obtained from the velocity distribution at the upstream of the pier, to predict the drag forces correctly, principally when the velocity is not constant but a function of time.

Since the bridge pier in the flow acts as an obstacle, the flow decelerates as it approaches the pier and it is reduced to zero on the upstream side of the pier [3, 4]. The velocity flow field and turbulence parameters in steady flows around bridge piers have been investigated by many researchers both experimentally [5, 6] and numerically [7, 8]. Baker [9, 10, 11] and Yulistiyanto [12] obtained the stream-wise and vertical velocity components, turbulence intensity and vorticity for the non-scoured fixed bed base. Melville [13] and Melville and Raudkivi [3] studied the relationship between horseshoe vortex and scour hole. Qadar [14] and Sarker [15] studied the flow characteristics around cylindrical piers on a scoured bed. Ahmed and Rajaratnam [16] worked on smooth, rough and mobile beds to examine the velocity distribution around the circular pier. Istiarto [17], Dey and Raikar [18] and Das et al. [19] have experimentally determined the velocity, turbulence intensity, turbulent kinetic energy and bottom shear stress distribution around the circular bridge. Unger and Hager [6] used Particle Image Velocimetry (PIV) in their study. Barbhuiya and Dey [20] measured the turbulent flow field at a vertical semicircular cylinder with a flat plate attached to the sidewall of a rectangular channel and at a wing-wall abutment. Yulistiyanto [4] investigated the velocity field around a cylindrical bridge pier in various planes while there is no scour and Istiarto [17] made relevant measurements under equilibrium scour. Akib et al. [21] focused on the relationship between scour depth in complex pier groups and combined piles bridge and various parameters including the variation of inflow velocity, distance, and time.

In nature, unsteady flows are the most common type of open channel flow. The flow features like average velocity, and turbulence intensity. Reynolds stress [22-27], the suspended material [28] and the bed load [29-32] are the issues investigated in unsteady flow conditions [33-35].

Studies related to bridge piers under unsteady flow conditions are relatively scarce [36-38], particularly the investigations on the velocity and turbulence characteristics in the presence of a bridge pier [39]. To the authors knowledge, experimental studies dealing with the velocity variation with time—on the presence of the bridge piers for unsteady flow is scarce. Gargari et al. [40] investigated the flow passed a circular pile in gradually-varied unsteady flow. Erdog [41] and Erdog et al. [42] investigated the hysterical effects in flow structure behind a finite array of cylinders under gradually varying unsteady flow conditions. Therefore, it was decided to conduct an experimental study dealing with the velocity variation with time in front of the bridge piers for unsteady flow. In this study, the time variation of instantaneous velocity was investigated at clear-water and unsteady flow conditions in a water column in front of the

piers. Three cases were taken into consideration namely, without a pier, with a pier having a diameter of 6 cm, and a pier with a diameter of 9 cm. The variation of mean and fluctuating components of the velocity and the reduction in velocity due to the presence of the pier were calculated and interpreted.

2. Experimental Setup and Procedure

The experiments were conducted in a rectangular recirculating flume of 0.7 m wide (B) and 18 m long, having a slope of 0.004 (Fig. 1). The bed was composed of cohesionless sediment with a median diameter $d_{50} = 0.43$ mm. The total sediment depth was 22 cm and sediment transport was not observed during the experiments. Coarse sediments were placed at the bed surface of the first 1.7 m of the flume in order to develop a fully turbulent flow and to prevent the local scour at the entrance of the flume [43, 44].

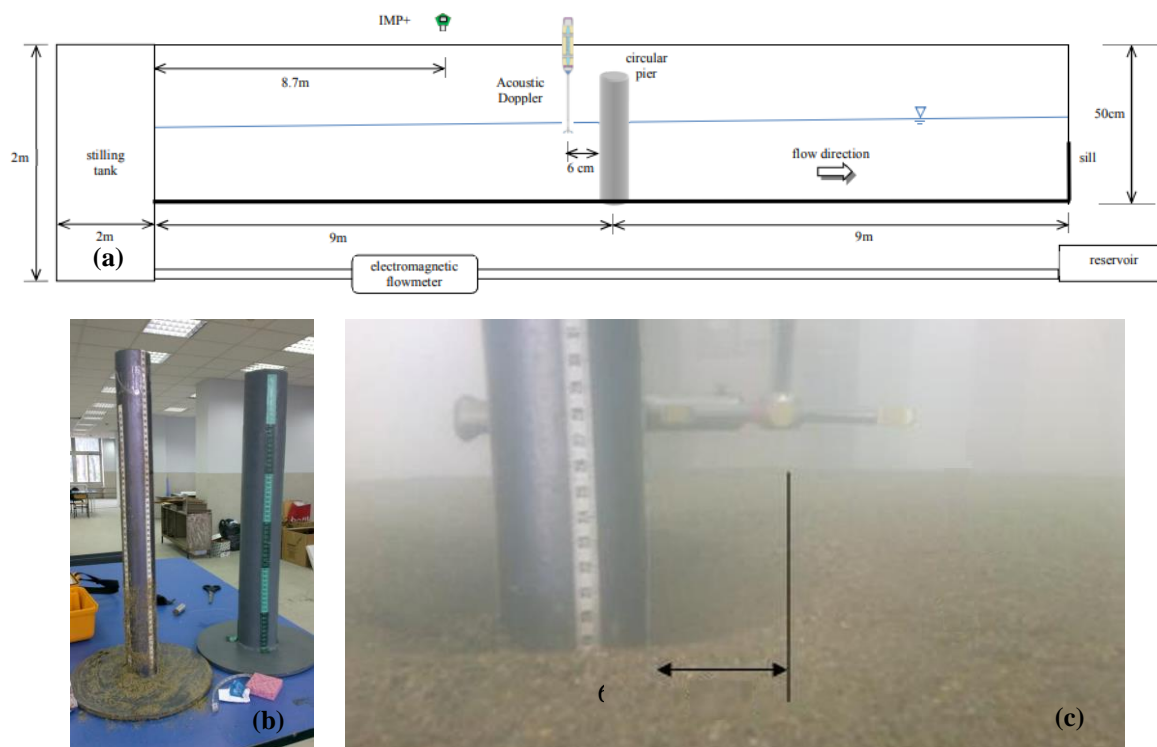


Figure 1.(a) Scheme of the experimental set-up, (b) piers, (c) location of the Flow Tracker

The flow rate in the flume was adjusted using a pump speed control unit (PSCU). The hydrographs were generated by increasing and/or decreasing the revolution rate of the pump as a percentage at desired time increments with this device. The advantage of the well-known fact was taken that the pump speed of a pump and the flow rate are directly and linearly proportional with each other.

Three triangular shaped asymmetrical hydrographs namely U1, U2 and U3 with rising durations of 1.5 min, 4.5 min and 9 min were generated. The falling duration of all experiments was the same and it was 1 minute.

The instantaneous point velocities were measured by a side looking ultrasonic instrument (Flow Tracker, Sontek) at $x = 8.94$ m where x is the distance from the flume entrance. To obtain the velocity time series at various locations within the flow depth, the instrument was first fixed at a specific location above the original sediment bed level and the hydrograph was generated and the velocity was measured throughout the duration of the hydrograph. Then the instrument was shifted to a neighboring vertical location, the same hydrograph was generated, and another velocity time series related to this neighboring point with a different height from the bottom sediment bed is obtained. The hydrograph generation at each vertical location is denoted as a run and resulting with a time series particularly for that elevation.

The velocity measurements were realized at the location of the bridge pier prior to its installation. Each experiment conducted in the absence of bridge piers was denoted by “a”. This step is aimed at obtaining velocity data of the flow unperturbed by the cylinder. The data serve as a reference with which the measured data around the cylinder shall be compared. Two circular piers with diameters of $b = 6$ cm and $b = 9$ cm were used in the flume located at $x = 9$ m. The experiments with a pier diameter of 6 cm were denoted as “b” and with a pier diameter of 9 cm as “c”. The velocity measurements were taken 6 cm upstream of the bridge pier. It was noted that the velocity measurements at points closer about 4.5 cm to the pier were not possible.

The variation of approach flow depth with time was measured at $(B-b)/2$ upstream part of the piers according to Oliveto and Hager [45], which was 8.7 m from the entrance by means of an ultrasonic level meter with a precision of 1 mm. The flow rate was measured by an electromagnetic flow meter mounted on the pipe for each run and averaged to determine the time variation of the flow rate for one experiment.

3. Methodology for Data Treatment

For the treatment of velocity time series in the stream-wise and vertical axis, the following procedure and equations were adopted.

The instantaneous point velocities $u(t)$ and $w(t)$ can be decomposed into their time-varying mean values $\bar{u}(t)$ and $\bar{w}(t)$, and their fluctuating components as $u'(t)$ and $w'(t)$ in longitudinal (x -axes) and vertical (z -axes) directions, respectively, as given in Eq. (1.a) and Eq. (1.b).

$$u(t) = \bar{u}(t) + u'(t) \quad (1.a)$$

$$w(t) = \bar{w}(t) + w'(t) \quad (1.b)$$

where (t) denotes the variable as a function of time as for the unsteady flows.

The obtained instantaneous point velocity time series $u(t)$ at each vertical location were smoothed by using the moving average algorithm to get the time varying mean $\bar{u}(t)$ and the fluctuating components $u'(t)$. The mean value at any instant was calculated by taking the average of the previous and proceeding 10 data as in Eq. (2). Same procedure was applied to calculate the $\bar{w}(t)$ and $w'(t)$.

$$\bar{u}_n = \sqrt{\frac{1}{21} \sum_{i=n-10}^{n+10} u_i} \tag{2}$$

The turbulence intensity of the stream-wise and vertical velocities are determined by calculating the root-mean-square (rms) of the fluctuating component which also has a time varying character. The $rms(u)$ and $rms(w)$ for n^{th} data were calculated by taking the mean average of the previous and proceeding 10 data as

$$[rms(u)]_n = \sqrt{\frac{1}{21} \sum_{i=n-10}^{n+10} (u_i - \bar{u}_i)^2} \tag{3}$$

Reynolds stress, τ can be calculated by the equation given below,

$$\tau = -\rho \overline{u'w'} \tag{4}$$

where the u' and w' are the fluctuating components, ρ is the density of water.

4. Experimental Results

For all experiments, the base values of flow depth h_{base} , flow rate Q_{base} and mean velocity V_{base} were 12.2 cm, 2.1 L/s and 2.4 cm/s, respectively. The variation of the flow rate with time is depicted in Fig. 2. Table 1 gives details of the experiments in which Q_{peak} and h_{peak} are the peak values of flow rate and flow depth. Time to the peak value of the flow rate is denoted by t_{rQ} . Since the same hydrograph is measured for all cases a, b, and c, the peak values of flow rate are the same.

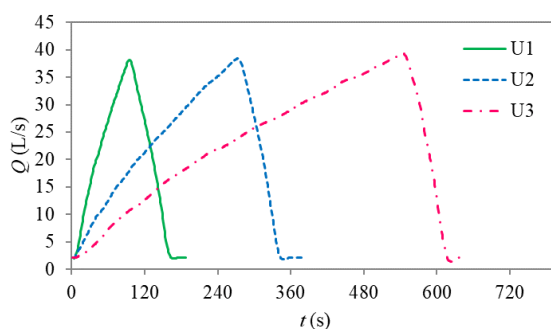


Figure 2. Variation of flow rate with time.

Table 1. The peak values of flow rate and flow depth, time to peak value of flow rate and the unsteadiness parameter.

Parameter	U1	U2	U3
Q_{peak} (L/s)	38.2	38.4	39.3
h_{peak} (cm)	19.5	20.6	20.8
t_{rQ} (s)	96	273	544
α	0.0049	0.0021	0.0011

The unsteadiness of a hydrograph can be defined by the change of flow depth within a specified time interval [22]. The dimensionless unsteadiness parameter α , as given below, was proposed by Nezu and Nakagawa [46] and used by Nezu et al. [22], Onitsuka and Nezu [47] and Nezu and Sanjou [48].

$$\alpha = \frac{1}{U_c} \frac{\Delta h}{t_{rQ}} \tag{5}$$

where $\Delta h = h_{peak} - h_{base}$, $U_c = (V_{base} + V_{peak})/2$, V_{peak} is the peak mean velocities. Nezu and Sanjou [42] divided the open channel flows into two categories, as if $\alpha < 0.001$, then the flow is considered as low unsteady flow otherwise it has high unsteadiness characteristics [22].

The variation of instantaneous point velocities with time and time-varying means denoted as raw and smoothed data of experiments U2b measured at $z/h_{base} = 0.45$ are depicted in Fig. 3. The negative vertical velocity values indicate the down-flow towards the bed.

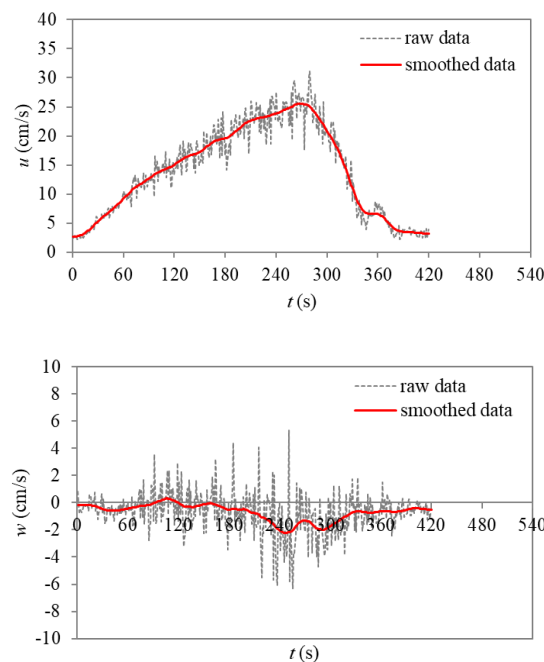


Figure 3. Variation of instantaneous point velocities and their time varying mean values.

The maximum velocity values of the smoothed data were obtained from each time series through the water column. The peak values of the time time-varying mean velocities for the cases without a pier, with small pier ($b = 6$ cm) and big pier ($b = 9$ cm) are calculated and given in Table 2, for $z/h_{base} = 0.4$ and $z/h_{base} = 1.0$.

Table 2. The peak values of the time-varying mean velocities for the cases without a pier and with the piers of diameter $b = 6$ cm and $b = 9$ cm (All velocity values are in cm/s).

peak value	z/h_{base}	U1a	U1b	U1c	U2a	U2b	U2c	U3a	U3b	U3c
\bar{u}	0.4	23.70	22.93	20.34	26.05	24.05	22.90	27.79	24.10	23.36
	1.0	28.84	23.62	22.73	30.10	26.05	25.31	30.58	26.09	23.80
\bar{w}	0.4	-0.91	-1.93	-2.62	-1.07	-1.77	-2.59	-1.36	-2.73	-3.11
	1.0	-1.23	-1.33	-2.53	-1.10	-1.74	-2.20	-1.07	-2.31	-2.35

It is revealed that the maximum value in the stream-wise direction decreases with the presence and even with the increase in pier diameter for stream-wise direction at all depths. The maximum value in the vertical direction on the other hand, increases its magnitude as a downflow. The stream-wise velocities are all greater near the surface than the ones near the bed. The maximum values of vertical velocity are the same at all depths for most of the experiments. A prominent effect of the unsteadiness on the maximum values was not noted.

The stream-wise velocity profiles are given in Fig. 4, at various dimensionless times as $t/t_{r,Q}$ equal to 0.25, 0.50 and 1.0 as peak time. The flow depth for U3 experiments is the highest for the corresponding time of other U2 experiments and U1 experiments.

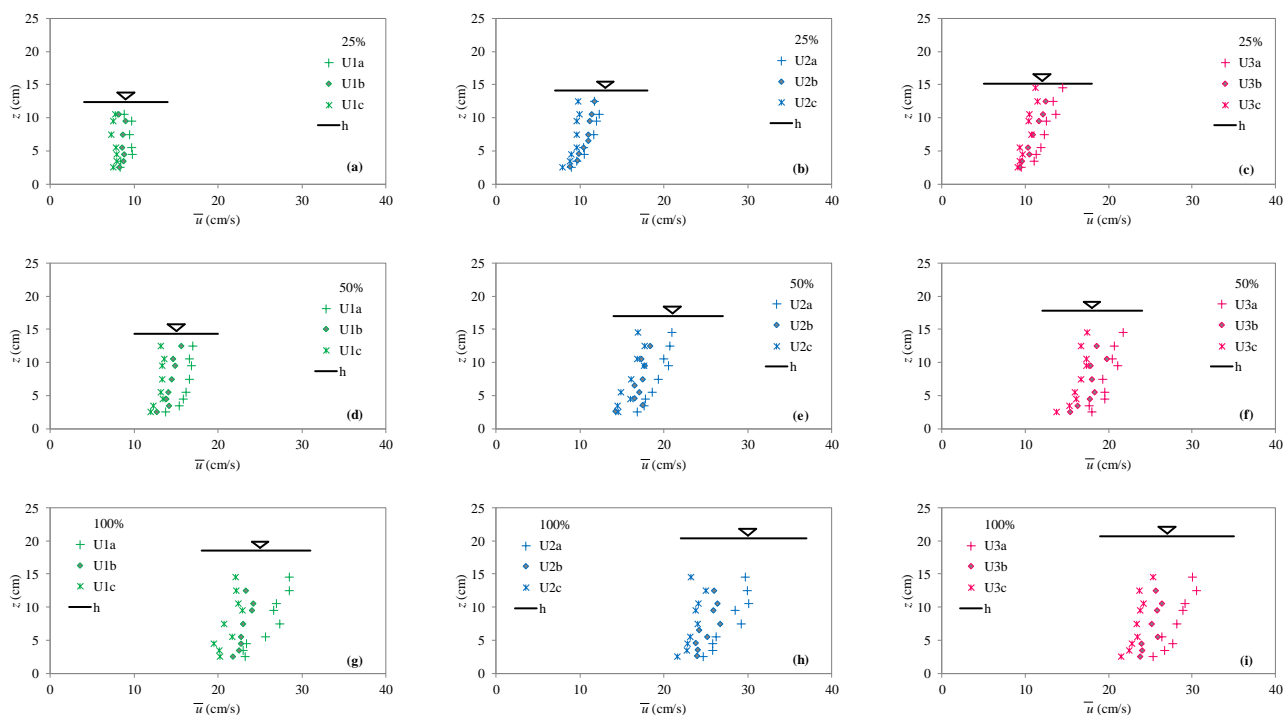


Figure 4. Velocity profiles in longitudinal direction $t/t_{r,Q} = 0.25$ for (a) U1, (b) U2, (c) U3, 0.50 for (d) U1, (e) U2, (f) U3, 1.0 for (g) U1, (h) U2, (i) U3.

It is revealed that for all hydrographs, the presence of the bridge pier results in a retardation of the point velocities. For all dimensionless times, it is observed that the hydrograph U1 has the velocity profile having the lowest velocity values, whereas the profiles in U2 and U3 are greater. As seen from the graphs, the greater the diameter of the pier is, the steeper the velocity profile is. The maximum value of the point velocity occurred at a vertical elevation z equal to around 12.5 cm for most of the experiments. This is in accord with Song and Graf [49] who revealed that the maximum velocity occurs below the water surface.

Song and Graf [49] revealed that during the passage of the hydrograph, the velocities in the rising limb are greater than the ones in the falling limb for equal depths. The velocity profiles of the same flow depth regarding the rising and falling durations are depicted in Fig. 5. The flow depth of 16 cm was selected since it is the average base and peak flow depths and occurs at $t = 62$ s, 108 s, 170 s in the rising and $t = 165$ s, 348 s, 620 s in the falling limbs of the experiments U1, U2, and U3, respectively. It is observed that for the same depth, the profiles in the rising limb are always greater than the falling limb. This is more prominent for the ones with higher unsteadiness, particularly for U1. The effect of the presence of the bridge pier retards the flow resulting in more uniform, steeper, and small velocity profiles.

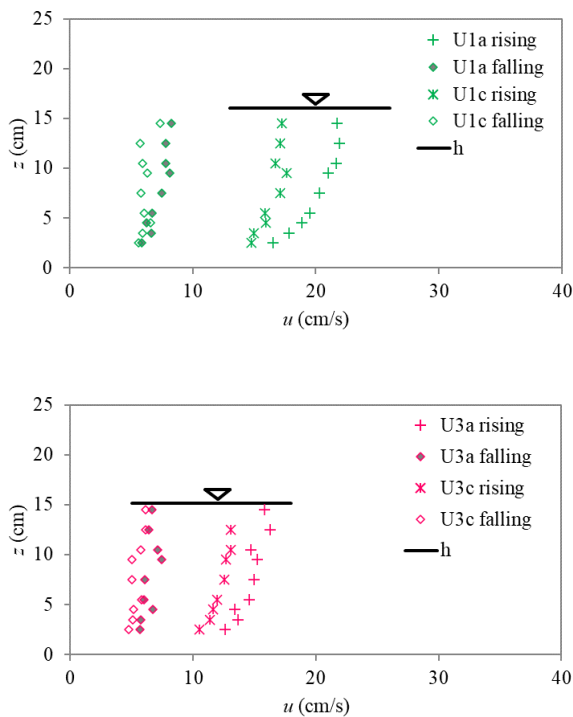


Figure 5. Velocity profiles in longitudinal direction of same flow depth (a) U1a & U1c and (b) U3a & U3c, without a pier and with 9 cm pier, respectively.

The velocity profiles of vertical component w at the dimensionless times 0.5 and 1.0 are depicted in Fig. 6 for U2 experiments. It is observed that in the absence of the bridge pier, the average vertical flow is nearly equal to zero in the water column. The presence of small pier increases the magnitude of the down flow prominently greater near the bed. These results are concluded for other experiments as well.

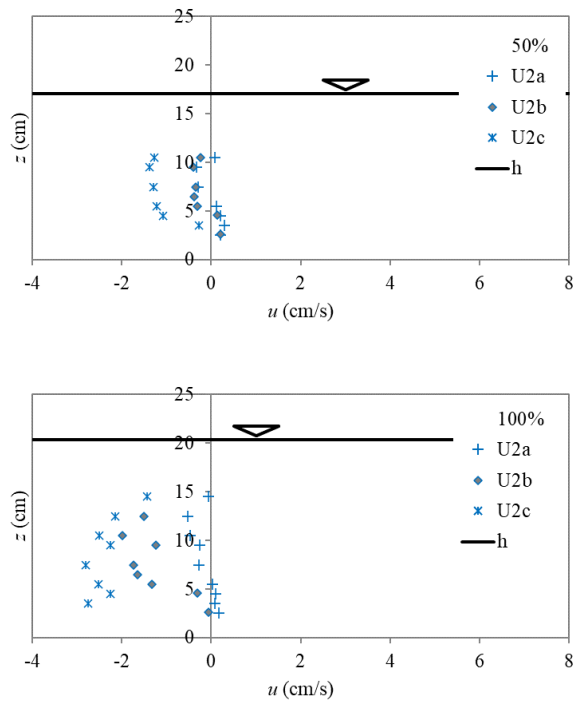


Figure 6. Velocity profiles in vertical direction at the dimensionless times (a) 0.5 and (b) 1.0.

The time variation of the fluctuating component of stream-wise and vertical velocities are calculated for U3a at $z/h_{base} = 0.4$ and $z/h_{base} = 1.0$ and for U3c at $z/h_{base} = 0.4$ as given in Fig. 7a, 7b and 7. c, respectively, as an example. The negative values are due to the decrease in instantaneous velocity with respect to mean velocity, whereas the positive values represent the increase. As depicted in Fig. 7.a and 7. c, both u' and w' have an increasing characteristic with time in the rising duration. In order to analyze this result, the rising duration was divided into three equal time intervals, namely the initial, middle, and peak phases. The band limits are depicted on the same figure as the extreme values i.e. minimum and maximum. The standard deviations were calculated within each time interval and summarized in Table 3 and Table 4 for $z/h_{base} = 0.4$ and $z/h_{base} = 1.0$, respectively, including the falling duration. The extreme bands become wider in time for $z/h_{base} = 0.4$ whereas this is not observed at locations near the water surface. The standard deviation for the fluctuating values of u' and w' , are depicted in Fig 7. a and 7 .c, in blue and orange colors respectively for each phase. The standard deviation values did not differ for the initial, middle, and peak values for both stream-wise and vertical velocities near the surface. As illustrated in Fig 7 .b, the average standard deviation for three phases are 1.80 cm/s and 1.43 cm/s, for u' and w' , respectively. For most of the experiments, the standard deviation is in general less than the one corresponding to peak time. The presence of the pier did not considerably change this behavior of the fluctuation components close to the water surface (Table 4) whereas the standard deviation of stream-wise component is suppressed for those close to bed (compare Fig 7.a and 7. c).

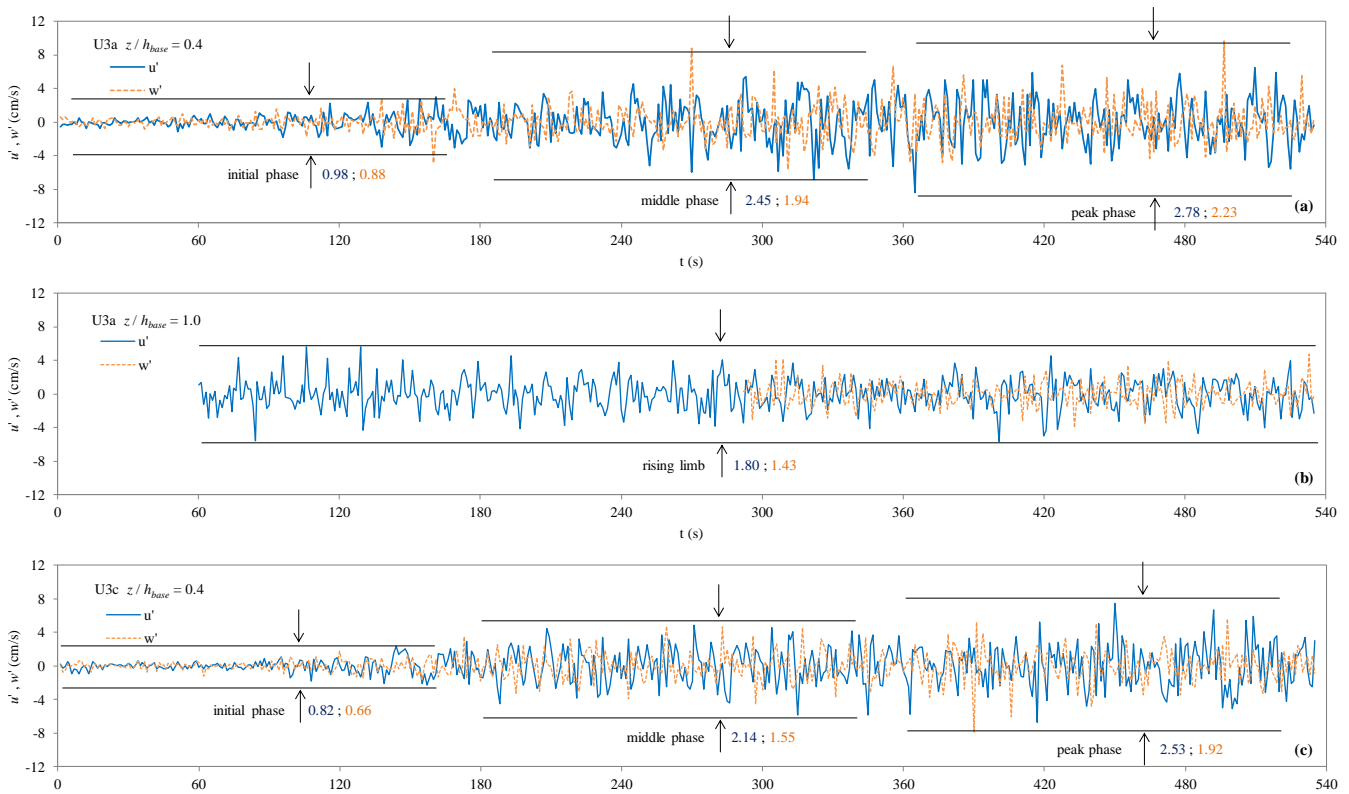


Figure 7. Variation of u' and w' with time (a) U3a at $z/h_{base} = 0.4$, (b) U3a at $z/h_{base} = 1.0$, and (c) U3c at $z/h_{base} = 0.4$

The standard deviation values calculated for the time intervals at $z/h_{base} = 0.4$.

	u'				w'			
	initial	middle	peak	falling	initial	middle	peak	falling
U3a	0.98	2.45	2.78	1.72	0.88	1.94	2.23	2.51
U3b	1.09	2.00	2.74	2.39	0.86	1.82	2.38	1.79
U3c	1.97	2.14	2.53	2.25	1.48	1.55	1.92	1.34
U2a	0.73	2.04	3.07	1.68	0.66	1.76	1.65	1.38
U2b	0.72	2.32	2.86	2.09	0.80	1.87	2.47	1.85
U2c	0.64	1.96	2.79	2.76	0.46	1.61	1.95	1.83
U1a	1.50	1.24	2.47	2.19	0.39	1.47	2.20	1.76
U1b	1.17	1.16	2.74	2.04	0.25	1.12	1.90	1.48
U1c	1.17	0.84	2.87	2.52	0.39	1.47	2.20	1.80

The standard deviation values calculated for the time intervals at $z/h_{base} = 1.0$.

	u'				w'			
	initial	middle	peak	falling	initial	middle	peak	falling
U3a	1.84	1.72	1.82	1.49	-	1.48	1.39	1.30
U3b	1.60	1.67	1.81	1.56	-	1.35	1.40	1.17
U3c	1.67	1.56	1.94	1.54	-	1.09	1.57	1.31
U2a	1.89	1.77	1.62	1.47	-	1.35	1.34	1.13
U2b	1.90	1.86	1.58	1.65	-	-	1.40	1.57
U2c	1.52	1.67	1.81	1.14	-	1.52	1.45	1.28
U1a	-	-	1.81	1.45	-	-	1.23	1.56
U1b	-	-	1.94	1.70	-	-	1.14	1.94
U1c	-	-	1.63	1.76	-	-	1.23	1.22

The obtained time variation of stream-wise $rms(u)$ and vertical $rms(w)$ point velocities for all experiments corresponding to the elevation $z/h_{base} = 0.4$ are shown in Figs. 8.a,b,c and Figs. 8.d,e,f, respectively. It is observed that the presence of the piers did not have an influence on $rms(u)$ or $rms(w)$. The $rms(u)$ values increase the rising limb and decrease in the falling limb. The turbulence intensity in the stream-wise direction attenuates when approaching the bed surface. Neither the presence of the pier nor the unsteadiness affected the intensity near the surface and near the bed. For the vertical velocity case, the $rms(w)$ had a constant value throughout the hydrograph duration. In this direction, the intensity attenuates when approaching the bottom while remaining the same near the surface with the increase in pier diameter.

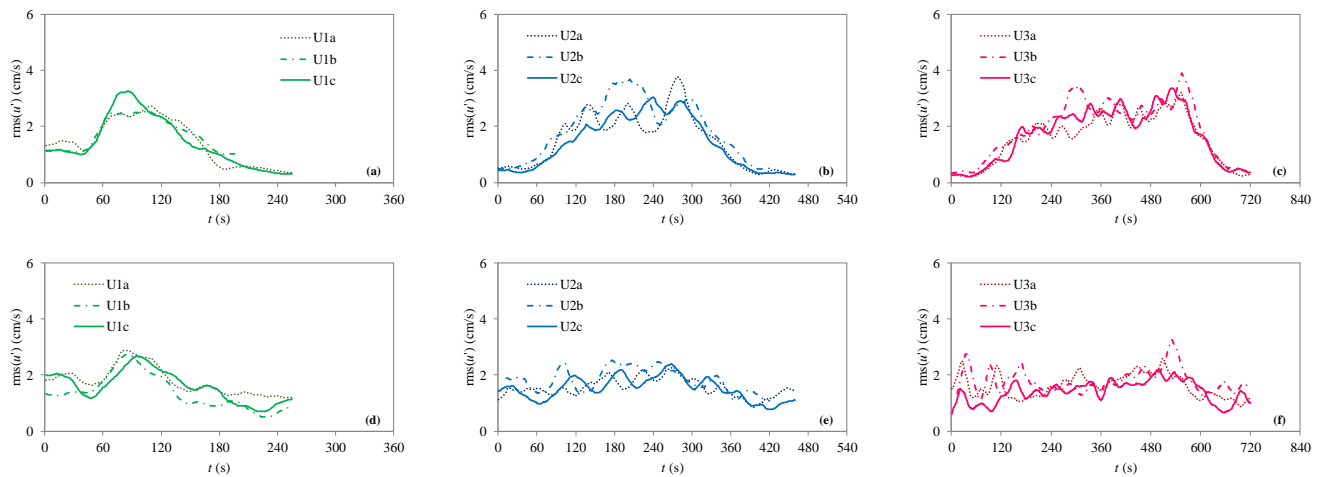


Figure 8. Variation of (a), (b) and (c) $rms(u)$ with time for U1, U2 and U3, respectively and (d), (e) and (f) $rms(w)$ with time for U1, U2 and U3, respectively.

The variation of u' with w' is plotted for U2 and U1 in Fig. 9, considering the initial, middle and peak phases additionally the falling phase. For all cases, the sweep and ejection events dominate throughout the hydrograph. In all graphs, it is also observed that the fluctuation values in the stream-wise direction are all greater than the ones in the vertical direction.

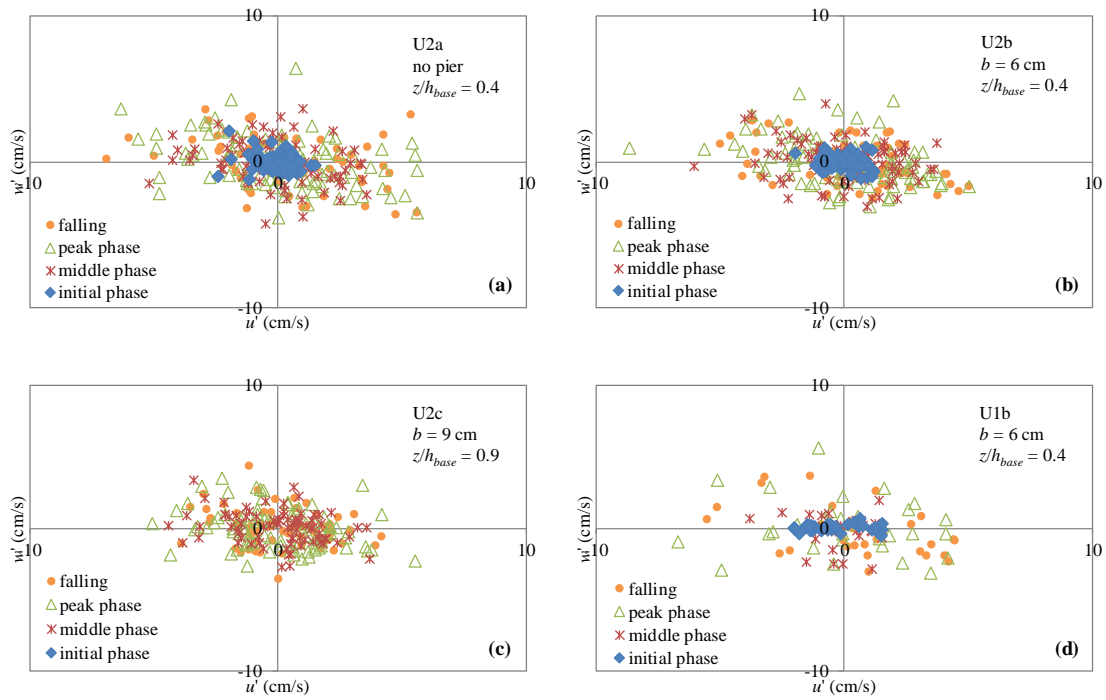


Figure 9. The variation of u' with w' for (a) U2a, (b) U2b, (c) U2c, (d) U1b.

By using the fluctuating components, the time variation of $u'w'$ is calculated and given in Fig 10. Whether there is a pier or not the $u'w'$ has its maximum value near the bottom and decreases towards the water surface. For all the experiments, the $u'w'$ increases in the rising limb and decreases in the falling limb. The unsteadiness of the hydrograph did not affect considerably but the presence of the pier decreased the maximum values of the $u'w'$.

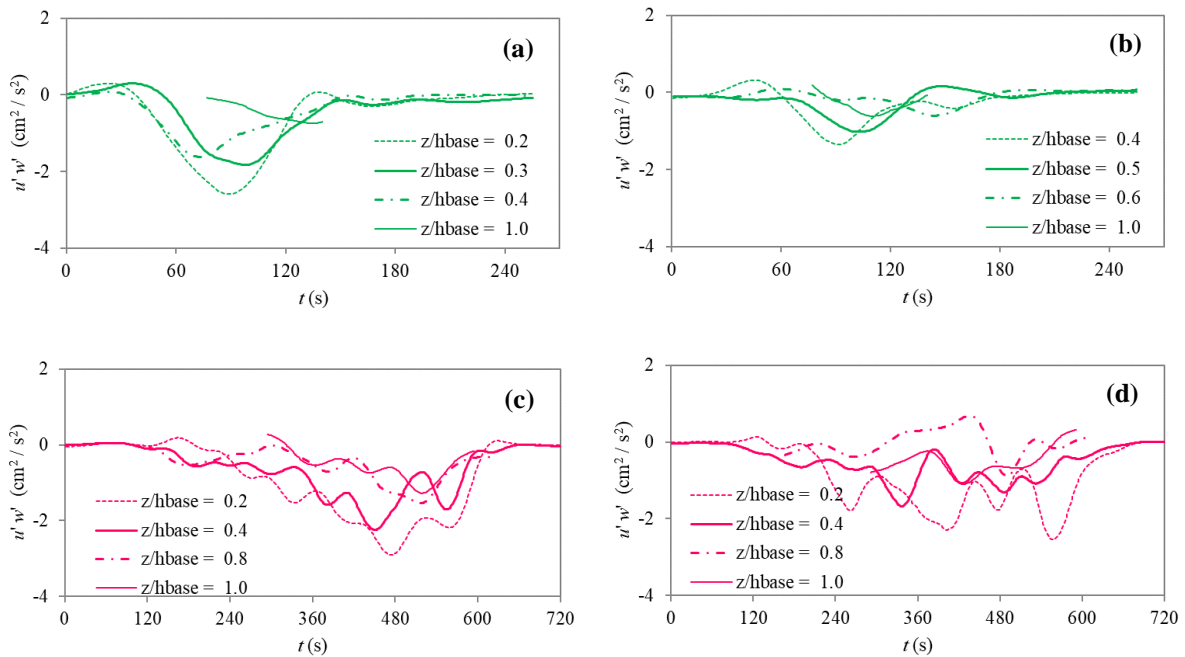


Figure 10. The time variation of $u'w'$ for (a) U1a, (b) U1c, (c) U3a, (d) U3c.

The presence of the pier decreased the velocity in stream-wise and increased the down flow velocity in the vertical direction as depicted in Fig. 11.a and 11.b, respectively. The average differences for cases b and c were calculated as subtracting the time average velocity value at a specific time from that of corresponding to the case a. Therefore, the curves are given only for experiments b and c as time variation of $\text{avg}(\overline{\Delta u})$ and $\text{avg}(\overline{\Delta w})$. It is observed that the unsteadiness of the hydrograph did not influence the average change in the stream-wise. The maximum average reduction for pier width of 6 cm is 3.1 cm/s (average of 3.1 cm/s, 3.3 cm/s and 3.0 cm/s for U1b, U2b and U3b, respectively) and 4.3 cm/s (average of 4.4 cm/s, 4.3 cm/s and 4.2 cm/s for U1c, U2c and U3c, respectively) for the pier width 9 cm in stream-wise direction. The corresponding maximum percent changes at peak were calculated as 6% and 11%. In vertical direction, the maximum average increase in down-flow was calculated as 0.5 m/s and 1.5 cm/s for the small and big piers.

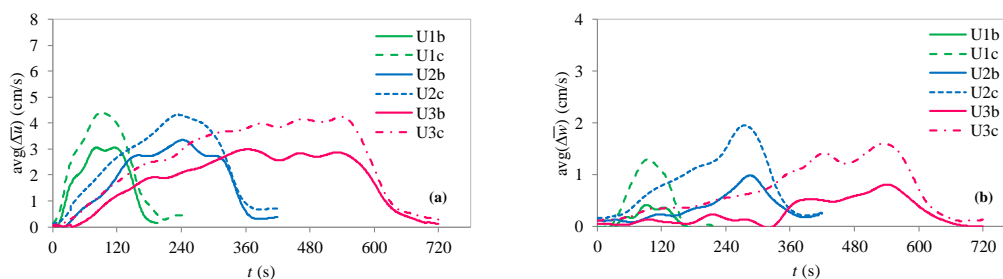


Figure 11. Average reduction in maximum velocity due to the presence of pier (a) in stream-wise and (b) vertical directions.

The reductions in point velocities at peak are calculated and given in Fig. 12. It is revealed that the reduction increases with z due to both piers but prominently for the pier with $b = 9$ cm for the velocity in stream-wise direction. The increase in down-flow does not change with depth but is greater for the pier with a greater diameter.

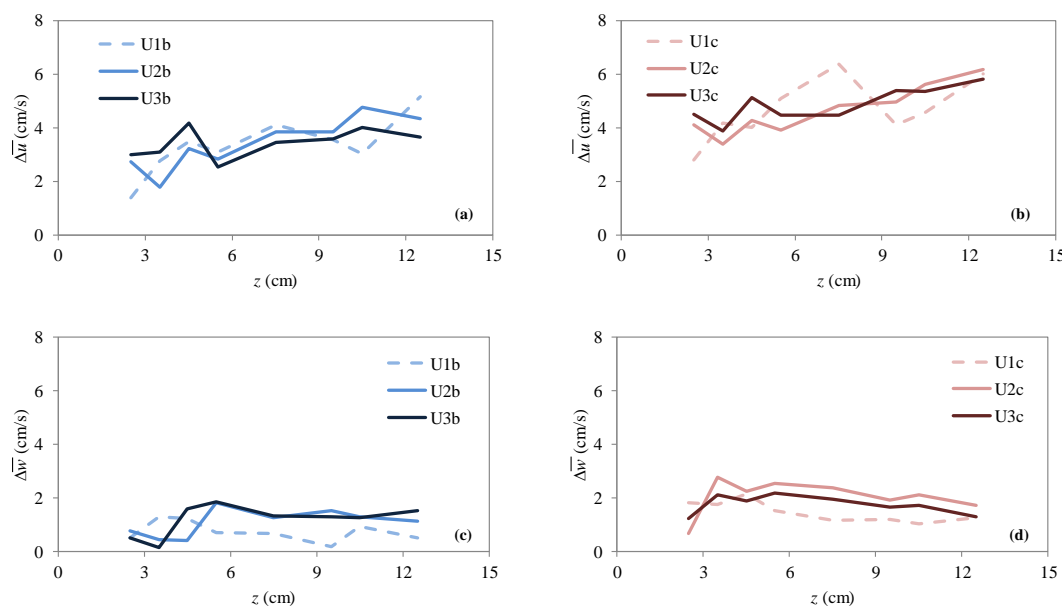


Figure 12. Variation of change in maximum velocity due to presence of pier with depth, (a) 6 cm pier diameter and (b) 9 cm pier diameter in stream-wise direction and (c) 6 cm pier diameter and (d) 9 cm pier diameter in vertical direction.

5. Conclusion

The time variation of point velocities in a stream-wise and vertical direction at a point upstream of a bridge pier were investigated at clear-water conditions under unsteady flow conditions. Three triangular-shaped hydrographs with approximately the same peak discharges but with different rising durations were generated. The effect of two circular bridge piers which are 6 cm and 9 cm in diameter on the flow properties was discussed in which the measurements were also conducted in the absence of any pier. The main findings can be summarized as follows;

- The presence of the pier decreased the stream-wise velocity while increasing the magnitude of vertical velocity towards the bed, prominently greater near the bed.
- The greater the diameter of the pier is, the steeper the stream-wise velocity profiles are.
- It was observed that for the same depth, the profiles in the rising limb are always greater than the falling limb. This is more prominent for the ones with higher unsteadiness.
- The standard deviation of the stream-wise fluctuating components near the bed increases in the rising limb with time, while it remains constant near the surface.
- The standard deviation of the vertical velocity fluctuating components did not differ throughout the hydrograph duration. The presence of the pier did not considerably change this behavior.
- The sweep and ejection events dominate throughout the duration of all hydrographs.
- For all the experiments, the $u'w'$ increase in the rising limb and decrease in the falling limb. Whether there is a pier or not the $u'w'$ has its maximum value near the bottom and decreases towards the water surface. The presence of the pier certainly decreased the maximum values of the $u'w'$.
- The maximum percent reduction at peak flow was calculated as 6% and 11%, for the piers with a width of 6 cm and 9 cm, respectively.
- The reduction in stream-wise point velocities at peak flow increases with depth. The greater the pier diameter is, the more the reduction is.
- The change in a vertical direction at peak flow due to the pier is constant throughout the depth.
- The results of this study could be used to verify the numerical studies for unsteady flows with bridge piers.

In future studies, the flow conditions and turbulence structures around the bridge piers can be determined by using symmetrical and asymmetrical hydrographs with different unsteadiness and by using different bridge pier diameters with different shapes and different types of sediments. The evolution of coherent structures under unsteady flow conditions would be a novel topic in this field.

Acknowledges

The author would like to express her gratitude to Prof. Dr. Şebnem ELÇİ for supplying the ultrasonic velocity meter used during the execution of the experiments.

List Of Notations

$\text{avg}(\Delta \bar{u})$	average value of the change in stream-wise velocity due to bridge pier [LT ⁻¹];
$\text{avg}(\Delta \bar{w})$	average value of the change in vertical velocity due to bridge pier [LT ⁻¹];
b	bridge pier diameter [L];
B	flume width [L];
d_{50}	median size of sediment [L];
h_{base}	flow depth at base flow [L];
h_{peak}	flow depth at peak flow [L];
$\text{rms}(u)$	root-mean-square of the velocity in stream-wise direction [LT ⁻¹];
$\text{rms}(w)$	root-mean-square of the velocity in vertical direction [LT ⁻¹];
t	time [T];
t_{rQ}	time to peak value of the flow rate [T];
u	instantaneous point velocity in stream-wise direction [LT ⁻¹];
u'	fluctuating components of point velocity in stream-wise direction [LT ⁻¹];
\bar{u}	time varying mean of point velocity in vertical direction [LT ⁻¹];
w	instantaneous point velocity in vertical direction [LT ⁻¹];
w'	fluctuating components of point velocity in vertical direction [LT ⁻¹];
\bar{w}	time varying mean of point velocity in stream-wise direction [LT ⁻¹];
x	distance from the flume entrance [L];
z	elevation from the bed surface [L];
U_c	average of V_{base} and V_{peak} $U_c = (V_{base} + V_{peak})/2$ [LT ⁻¹];
V_{base}	approach velocity at base flow [LT ⁻¹];
V_{peak}	approach velocity at peak flow [LT ⁻¹];
Q_{base}	flow rate at base flow [L ³ T ⁻¹];
Q_{peak}	flow rate at peak flow [L ³ T ⁻¹];
Δh	difference between the base and peak flow depths [L];
$\Delta \bar{u}$	change in stream-wise velocity due to bridge pier [LT ⁻¹];
$\Delta \bar{w}$	change in vertical velocity due to bridge pier [L T ⁻¹];
α	dimensionless unsteadiness parameter [-];


References

- [1] Landers, M. N., (1992). Bridge Scour Sata Management. Published in Hydraulic Engineering: Saving a Threatened Resource—In Search of Solutions: *Proceedings of the Hydraulic Engineering sessions at Water Forum '92. Baltimore, Maryland, August 2–6.*
- [2] Franzini, J. B. and Finnemore, E. J.(1997). *Fluid Mechanics with Engineering Applications*, (McGraw-Hill), ISBN 0-07-021914 1.
- [3] Melville, B. W. and Raudkivi, A. J. (1977). Flow characteristics in local scour at bridge piers. *J. Hydraul. Res.*, 15 373–380.
- [4] Yulistiyanto, B. (1997), Flow around a cylinder installed in a fixed-bed open channel, PhD thesis no 1631, École Polytechnique Fédérale de Lausanne, Switzerland.
- [5] Breusers, H. N. C., Nicollet, G. and Shen, H. W. (1977). Local scour around cylindrical piers. *J. Hydraul. Res.*, 15: 211–252.
- [6] Unger, J. and Hager, W. E. (2007). Down-flow and horseshoe vortex characteristics of sediment embedded bridge piers, *Experiments in Fluids*, 42: 1–19.
- [7] Ettema, R., Kirkil, G. and Muste, M., (2006). Similitude of large scale turbulence in experiments on local scour at cylinders. *J. Hydraul. Eng.*, 132: 33–40.
- [8] Kirkil, G., Constantinescu, S. G. and Ettema, R. (2008). Coherent structures in the flow field around a circular cylinder with scour hole. *J. Hydraul. Eng.*, 134: 572–587.
- [9] Baker, C. J. (1979). Laminar horseshoe vortex. *J. Fluid Mech.* 95: 347–367.
- [10] Baker, C. J. (1980). The turbulent horseshoe vortex. *Journal of Wind Engineering Industrial Aerodynamics*, 6 9–23.
- [11] Baker, C. J. (1985). The position of points of maximum and minimum shear-stress upstream of cylinders mounted normal to flat plates. *Journal of Wind Engineering Industrial Aerodynamics*, 18: 263–274.
- [12] Yulistiyanto, B. (2009). Velocity measurements on flow around a cylinder, *Dinamika Teknik Sipil*, 9: 111–118.
- [13] Melville, B. W. (1975). Scour at bridge sites. Report No 117, School of Engineering, University of Auckland, Auckland, New Zealand.
- [14] Qadar, A. (1981). The vortex scour mechanism at bridge piers. *J. Proc. of Inst. Civ. Engrs*, 71: 739–757.
- [15] Sarker, M. A. (1998). Flow measurement around scoured bridge piers using Acourstic Doppler Velocimeter (ADV). *Flow Measurement and Instrumentation*, 9: 217–227.
- [16] Ahmed, F. and Rajaratnam, N. (1998). Flow around bridge piers. *J. Hydraul. Eng.*, 124: 288–300.
- [17] Istiarto, I. (2001). Flow around a cylinder on a mobile channel bed. Ph.D. Thesis, no. 2368, EPFL, Lausanne, Switzerland.
- [18] Dey, S. and Raikar, V. R., (2007). Characteristics of horseshoe vortex in developing scour holes at piers. *J. Hydraul. Eng.*, 133: 399–413.

- [19] Das, S., Das, R. and Mazumdar, A. (2013). Comparison of characteristics of horseshoe vortex at circular and square piers. *Research Journal of Applied Sciences, Engineering and Technology*, 5: 4373–4387.
- [20] Barbhuiya, A. K. and Dey, S. (2003). Velocity and turbulence at a wing-wall abutment. *Sadhana*, 28: 35–56.
- [21] Akib, S., Jahangirzadeh, A., and Basser, H. (2014). Local scour around complex pier groups and combined piles at semi-integral bridge. *J. Hydrol. Hydromech.*, 62: 108–116.
- [22] Nezu, I., Kadota, A. and Nakagawa, H. (1997). Turbulent structure in unsteady depth varying open-channel flows, *J. Hydraul. Eng.*, 123 752–763.
- [23] Song, T. (1994). Velocity and turbulence distribution in non-uniform and unsteady openchannel flow. PhD thesis no 1324, Ecole Polytechnique Fédérale de Lausanne, Switzerland.
- [24] Tu, H. (1991). Velocity distribution in unsteady flow over gravel beds, PhD thesis no 911, École Polytechnique Fédérale de Lausanne, Switzerland.
- [25] Bares, V., Jirak, J. and Pollert, J. (2008). Spatial and temporal variation of turbulence characteristics in combined sewer flow. *Flow Measurement and Instrumentation*, 19: 145–154.
- [26] Bombar, G. (2016). The hysteresis and shear velocity in unsteady flows. *Journal of Applied Fluid Mechanics*, 9(2): 839–853.
- [27] Khuntia, J. R., Devi, K., Khatua, K. K. (2021). Turbulence characteristics in a rough open channel under unsteady flow conditions, *ISH Journal of Hydraulic Engineering*, 27:sup1, 354-365, <https://doi.org/10.1080/09715010.2019.1658549>.
- [28] de Sutter, R., Verhoeven, R. and Krein, A., (2001). Simulation of sediment transport during flood events: Laboratory work and field experiments. *Hydrological Sciences Journal*, 46: 599–610.
- [29] Suzka, L. (1987). Sediment transport at steady and unsteady flow: a laboratory study, PhD thesis no 704, École Polytechnique Fédérale de Lausanne, Switzerland.
- [30] Qu, Z. (2002). Unsteady open-channel flow over a mobile bed. PhD thesis no 2688, École Polytechnique Fédérale de Lausanne, Switzerland.
- [31] Güney, M. Ş., Bombar, G. and Aksoy, A. Ö., (2013). Experimental study of the coarse surface development effect on the bimodal bed-load transport under unsteady flow conditions. *J. Hydraul. Eng.*, 139: 12–21.
- [32] Francalanci, S., Paris, E. and Solari, L., (2013). A combined field sampling-modeling approach for computing sediment transport during flash floods in a gravel-bed stream. *Water Resour. Res.*, 49: 6642–6655.
- [33] Nanson, G. C. (1974). Bed load and suspended load transport in a small, steep, mountain stream, *Am. J. Sci.*, 274 471–4
- [34] Kuhnle, R. A. (1992). Bedload transport during rising and falling stages on two small streams, *Earth Surf. Proc. Land.*, 17: 191–197.
- [35] Çokgör, S. and Diplas, P. (2001). Bed load transport in gravel streams during floods. *Proceedings of World Water and Environmental Resources Congress, ASCE*, 1, 47.
- [36] Lopez, G., Teixeira, L., Ortega-Sanchez, M. and Simarro, G. (2006). Discussion of ‘Further results to time-dependent local scour at bridge elements’. *J. Hydraul. Eng.*, 132: 995–996.

- [37] Lai, J. S., Chang, W. Y. and Yen, Y. L. (2009). Maximum local scour depth at bridge piers under unsteady flow. *J. Hydraul. Eng.*, 135: 609–614.
- [38] Hager, W. H. and Unger, J. (2010). Bridge pier scour under flood waves. *J. Hydraul. Eng.*, 136: 842–847.
- [39] Bombar, G. (2014). Clear-water bridge scour under triangular-shaped hydrographs with different peak discharges, *Proceedings of River Flow 2014 Conferece, Lausanne, Switzerland*
- [40] Erdog, E. (2014). The influence of unsteadiness degree on hydraulic characteristics in open channel flow. Istanbul Technical University Graduate School of Science Engineering and Technology, M.Sc. Thesis, May 2014, 356137.
- [41] Gargari, M. K., Kırca V. S. Ö., Yagcı, O., (2022). Experimental investigation of gradually-varied unsteady flow passed a circular pile. *Coastal Engineering*, 168 (2021) 103926, <https://doi.org/10.1016/j.coastaleng.2021.103926>.
- [42] Erdog, E., Yagcı, O., Kırca, V. S. Ö. (2022). Hysterical effects in flow structure behind a finite array of cylinders under gradually varying unsteady flow conditions. *Journal of Ocean Engineering and Marine Energy*, <https://doi.org/10.1007/s40722-022-00229-y>.
- [43] Saçan, C., Çetin, O.K., Bombar, G., (2013). Investigation of the scour inception around a circular bridge pier. *Proceedings of the Second International Conference on Water, Energy, and the Environment, ICWEE, Kusadası, Turkey September 21-24, 2013.*
- [44] Çetin, O. K., Saçan, C., Bombar, G., (2016). Investigation of the relation between bridge pier scour depth and vertical velocity component, *Pamukkale Universitesi Muhendislik Bilimleri Dergisi*, 22(6):427-432, <https://doi.org/10.5505/pajes.2015.76768>.
- [45] Oliveto, G. and Hager, W. H. (2002). Temporal evolution of clear-water pier and abutment scour, *J. Hydraul. Eng.*, 128: 811–820.
- [46] Nezu, I. and Nakagawa, H. (1993). *Turbulence in open-channel flows*, IAHR Monograph Series, (A.A. 619 Balkema Publishers), Rotterdam, The Netherlands.
- [47] Onitsuka, K. and Nezu, I. (1999). Effect of unsteadiness on von Karman constant in unsteady open channel flows. *D1-Turbulent Channel Flows with Macro Roughness Vegetation, 28 th Congress of IAHR, Graz, Austria, Conf. Proceedings.*
- [48] Nezu, I. and Sanjou, M. (2006). Numerical calculation of turbulence structure in depth varying unsteady open-channel flows. *J. Hydraul. Eng.*, 132: 681–695.
- [49] Song, T. and Graf, W. H. (1996). Velocity and turbulence distribution in unsteady open-channel flows. *J. Hydraul. Eng.*, 122: 141–154.

Local Adaptive Phase Correction Algorithm For 3-D Profilometry Systems Based on Phase Shifting Method

Mustafa Ozden 

Bursa Technical University, Department of Electrical and Electronics Engineering, Bursa, Turkey.

Abstract

The method of reflecting sinusoidal phase-shifted patterns to the surface, based on the demodulation technique of phase information, has been a popular method to obtain 3-D surface depth using 2-D images. The phase information that is extracted with this method is wrapped; so it must be unwrapped. Even though the phase information is unwrapped, there will be some errors because of the possibility of non-sinusoidal characteristics of phase patterns, surface discontinuities, low sample rates, and technical handicaps (poor calibration and hardware malfunctions, and so on). To deal with these errors resulting from the phase unwrapping process, there are some computationally expensive and complex methods that have been presented. In this paper, a fast and low complex local adaptive phase correction algorithm based on the four-step phase shifting method is implemented. The method is firstly validated by using synthetic data. After the validation process, an optic test system is realized, and a few experiments are performed by using physical real data. For the optical system used to physically acquire the data, a lookup table-based calibration technique has also been developed to obtain accurate surface phase information. The performance of the method is evaluated with simulation results and real data, and visually compared to popular unwrapping methods.

Keywords: 3-D reconstruction, fringe patterns, phase shifting, phase unwrapping.

Cite this paper as:

Ozden, M. (2022). *Local Adaptive Phase Correction Algorithm For 3-D Profilometry Systems Based on Phase Shifting Method*. Journal of Innovative Science and Engineering. 6(2): 297-313

*Corresponding author: Mustafa Ozden
E-mail: mustafa.ozden@btu.edu.tr

Received Date: 04/08/2021
Accepted Date: 16/10/2022
© Copyright 2022 by
Bursa Technical University. Available
online at <http://jise.btu.edu.tr/>



The works published in Journal of Innovative Science and Engineering (JISE) are licensed under a Creative Commons Attribution-NonCommercial 4.0 International License.

1. Introduction

It is very convenient that using non-contact optical methods in determining 3-D surface profiles is common in Computer Aided Manufacturing (CAM) systems. The most popular method of these optical techniques is projecting the beam patterns (fringe patterns) onto the surface to get 3-D information. This method is also known as shadow moire method [1]. Patterns keep the depth information belonging to the 3-D surface as phase information which is modulated. Therefore the fringe patterns also called as phase patterns.

There are some methods for the extraction of the demodulated phase information from the modulated phase patterns. Fourier fringe analysis technique, direct phase demodulation, and phase shifting method are some examples for these analysis methods [2-4]. If the surface to be reconstructed is not dynamic, phase shifting technique is practically convenient. The method does not require complex computations. In this method, at least three phase patterns, which have equal phase intervals, are projected onto the surface so that different phase images can be obtained.

The extracted phase information is wrapped because the sinusoidal function is subjected to the arctangent function (as expressed in Equation 1). Therefore, there are discontinuities in the phase function. Typically the unwrapping process intends to transform the wrapped phase function into the continuous form. There is a basic method for the unwrapping process; however, as some unwanted issues such as surface discontinuities, low SNR, low sample rates or non-ideal sinusoidal fringe patterns may be encountered with the use of this method, the unwrapped phase will have some errors. Especially these errors are static or propagative. To overcome this problem, a number of phase correction algorithms have been implemented. Zhao and others, developed a method for the spatial light modulators which has the advantages of high-precision pixel-wise phase correction against environmental disturbance. This method relies on gamma correction and shape aberration correction, using manufacturer's gamma lookup table [5]. Thang et al. propose a method based on local 1-D phase correction by using multi-frequency phase heterodyne. The method determines whether a phase map needs to be corrected by calculating the deviation between the predicted and actual phase according to the slope of the projected standard fringe pattern and has the best effect to eliminate jump like phase errors [6]. Zheng et al. propose a fast self-correction algorithm to reduce the nonlinear phase error by using average intensity value of the captured fringe images which have nonlinear response parameters and also use multi-frequency heterodyne algorithm [7].

Song et al. propose three wavelength grating method which uses the phase information of three different wavelengths for phase unwrapping and phase correction superior than the traditional multi-frequency heterodyne method [8]. Zhang et al. address multipath problem in phase shifting profilometry applications [9]. Feng et al., present a study for phase similarity based on light field reconstruction method. Their method also uses multi-frequency heterodyne algorithm for unwrapping the phase data. Different from other studies, this light field imaging method, which is an emerging method for 3-D reconstruction studies, needs a calibration step addition to fringe projection step [10]. In addition to new analyses,

there are also studies where algorithms that will produce good results in noisy conditions are developed. Zhao et al. developed a simple and robust unwrapping algorithm, using the transport of intensity equation (TIE) and fast cosine transform. They report that their algorithm produces satisfactory unwrapping results even in a notably noise condition [11].

In fact, if there were no problems in surface phase functions mentioned above, it would be enough to use the basic unwrapping method and would need no phase unwrapping algorithms. Other processes to obtain 3-D height of the object surface after phase unwrapping process are to eliminate the slope and to use the appropriate calibration function for phase-to-height relation.

Except for Zhao's work [11], other methods that are not mentioned here, besides including quite hardware development studies requiring a calibration phase, treat the phase data in 1-D. In this study, a new Four-Step Phase Shifting Method with phase error correction algorithm is developed for optical 3-D measuring. Here, 1-D unwrapping process is applied as 2-D for phase unwrapping in the algorithm. A 2-D adaptive correction algorithm is also developed to cancel phase noises. Besides, a lookup table-based calibration algorithm is implemented to obtain accurate sinusoidal phase patterns. This calibration algorithm can be used when working with the real data, i.e. when using a physical optical system. Because of the distortions of the optical systems, especially gamma function of the optic device and surface characteristics, gray-level differences may occur between the phase patterns created on the computer and the phase patterns projected onto the surface. These distorting effects are observed as unwanted slopes and undulations on the object surface. For optic test setup, a DLP light commander module for projecting fringe patterns onto the surface and a high resolution CCD/CMOS camera for capturing images from the surface are used. After getting the accurate phase patterns, the desired phase unwrapping algorithms is then implemented and described in the sections below.

2. 3-D Reconstruction Technique Based On Phase Shifting Method

In a typical fringe projection system (Figure 1), a computer generates fringe patterns of vertical sinusoidal stripes and sends them to a projector, called a light modulator, which will reflect them onto objects. As the result of Shadow Moire principle [1], the reflected fringe image patterns are modulated and contain surface 3-D information as phase values. Then reflected images are captured by a video camera. 3-D information is determined by using the triangulation technique according to the Shadow Moire principle. As the fringe patterns are sinusoidal, each vertical fringe stripe consists of phase information of the objects.

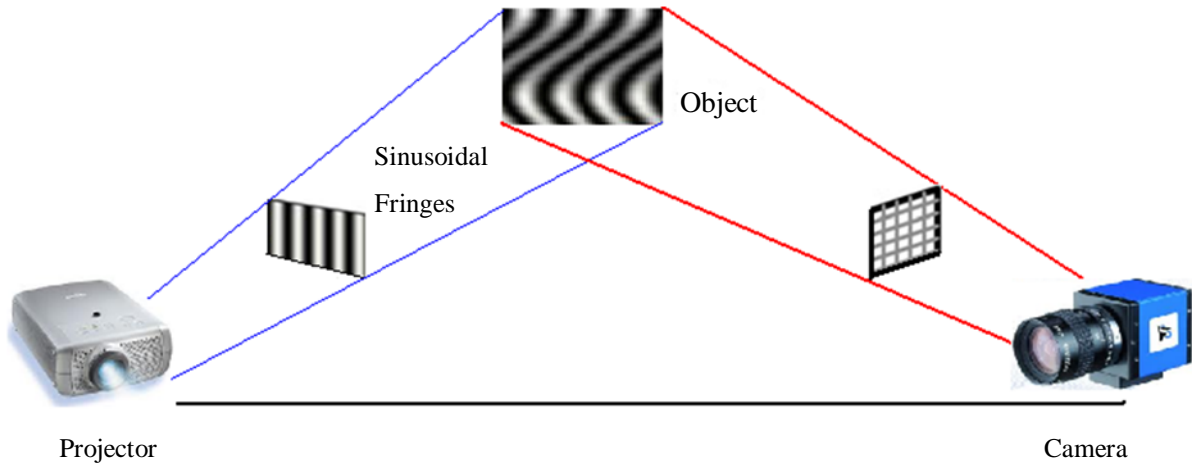


Figure 1.Real-time 3-D imaging system with fringe analysis.

Fringe patterns mentioned above are in sinusoidal form and can be expressed as [12]:

$$I(x, y) = a(x, y) + b(x, y) \cos(2\pi f_0 x + \phi(x, y)) \tag{1}$$

Where $a(x, y)$ is the background illumination, $b(x, y)$ is the amplitude of the fringe phase modulation, f_0 is the spatial carrier frequency, and $\phi(x, y)$ is the phase value of the fringes in each value of (x, y) position. In order to calculate $\phi(x, y)$, there are several techniques mentioned in the introduction section, and in this study four-step phase shifting technique is used.

2.1. Four-step Phase Shifting Method

The four-step phase shifting method have some advantages, such as high measurement speed, low computational complexity, cancellation of background illumination, detail accuracy, and ease of automation. In this technique, four independent equations is used to eliminate $a(x, y)$ and $b(x, y)$ [1]. Practically this is implemented as using $\pi/2$ phase shifted images and expressed mathematically as below:

$$\begin{aligned} I_1(x, y) &= a(x, y) + b(x, y) \cos(2\pi f_0 x + \phi(x, y)) \\ I_2(x, y) &= a(x, y) + b(x, y) \cos(2\pi f_0 x + \phi(x, y) + \frac{\pi}{2}) \\ I_3(x, y) &= a(x, y) + b(x, y) \cos(2\pi f_0 x + \phi(x, y) + \pi) \\ I_4(x, y) &= a(x, y) + b(x, y) \cos(2\pi f_0 x + \phi(x, y) + \frac{3\pi}{2}) \end{aligned} \tag{2}$$

By using Equation 2, following expression can be extracted for calculating the phase value $\phi(x, y)$:

$$\Psi(x, y) = \tan^{-1}\left(\frac{I_4 - I_2}{I_1 - I_3}\right) = 2\pi f_0 x + \phi(x, y) \tag{3}$$

where $\Psi(x,y)$ is the wrapped phase and consists of 2π jumps. Spatial carrier frequency f_0 causes a tilt in the reconstructed image, and it must be eliminated. That is achieved with subtraction of the unwrapped reference plane from the unwrapped phase values of $\Psi(x,y)$, which is subjected to desired unwrapping algorithm mentioned in following section.

2.2 Local Adaptive Phase Error Correction Algorithm

In Equation 3, wrapped phase map values range from $-\pi$ to π because of the nature of the arctan function. The classical approach for phase unwrapping problem is to add or subtract 2π in the phase map. The main reason behind this is to make the result of unwrapping process as the same as the original true phase value $\emptyset(x,y)$.

For 1-D case, unwrapping process can be expressed mathematically as [13]:

$$U[\Psi(n)] = \Psi(n) + 2\pi k \quad (4)$$

where k is an integer and $U[\Psi(n)]$ is the unwrapped phase to be calculated. Unwrapping process basically follows the steps below:

1. Start with the second sample of $\Psi(n)$.
2. Calculate the difference, $\Delta\Psi(n) = \Psi(n+1) - \Psi(n)$.
3. If $\Delta\Psi(n) > \pi$, subtract 2π from this sample and from all the following samples.
4. If $\Delta\Psi(n) < -\pi$, add 2π to this sample and to all the following samples.
5. Repeat these 1 to 4 steps for all samples of $\Psi(n)$.

In fact, if there were no corrupt data in the wrapped phase map, 1-D unwrapping technique could be applied for columns and rows of the wrapped phase value, and so it could be easy to obtain unwrapped phase value $U[\Psi(n)]$ as the same with $\emptyset(x,y)$. Since the ideal cases cannot be supplied, there will be error propagations in result of the classical unwrapping process. Therefore, for 2-D case, several algorithms which use binary stripe [14] and color-coded stripes [15] have been proposed for the unwrapping problem. These algorithms can be classified into two major groups as local and global unwrapping algorithms [16]. In these algorithms, accuracy is well-proportioned with complexity; however, execution time increases.

In this study, due to its low complexity of 1-D unwrapping method, 2-D phase unwrapping method is implemented by applying 1-D processes both to columns and rows of the wrapped phase map. As the resulting unwrapped phase map may have errors which cause artifacts in the reconstructed image, they are eliminated with the developed two-step recursive algorithm in this study. The algorithm tries to find the artifacts and correct them by using adjacent uncorrupted phase pixel values. This process is applied for whole pixel values of the wrapped phase image respectively. This approach has very low computational complexity and runs very fast; the pseudo code of the algorithm is given below.

- Apply 1-D unwrapping process to each columns of the wrapped phase map.
- Assign each row vector to a blank row of an empty matrix.
- For each pixel in the row of matrix,
 - Calculate the differences between gray value of consecutive pixel

$$D_i = p(x, y) - p(x + i, y) \quad (5)$$

If the absolute difference is greater than the threshold level ($|D_i| > \varepsilon$) which is determined by the user,

- assign the gray level value of the corresponding pixel of i th, to a variable of m_1 ,
- $$m_1 = p(x + i, y) \quad (6)$$
- start a new seek along a user defined 1D window length (m)
 - calculate the difference between the gray levels of the pixels in the window (W) and m_1
 - If the absolute difference is greater than the threshold level, which may be different from the above, continue seeking along the window length

$$Dw_k = m_1 - W(i), \quad \hat{i} = 0..m, k = 1..m \quad (7)$$

- If the absolute difference is lower than the threshold level, assign the gray level value of the corresponding pixel of k th, to a variable of m_2

$$\text{if } |Dw_k| < \varepsilon, \quad m_2 = W(\hat{i}) \quad (8)$$

- change the gray levels of the pixels among i and k with equal intervals of m_1 and m_2

$$p(x + c, y) = \left\lceil \frac{m_2 - m_1}{k - i} \right\rceil, \quad c = i, \dots, k, \mid c, i, k \in Z \quad (9)$$

- If the absolute difference is lower than the threshold level which is determined by the user,
 - continue the seeking process along the row matrix length.
- Repeat the same steps for each column of the matrix.

The pseudo code reveals that the algorithm has a threshold level and a window length parameter for operation. These values can be set by the user and changed for the application to get optimum results. Because of changing the row data along the algorithm steps, it works clearly fast. Since the scanning process is performed according to the difference between gray-level value and the threshold level, the algorithm works adaptively.

Figure 2 shows the corrective effect of the algorithm on the wrapped phase map. Reconstructed 3-D image obtained from 1-D unwrapping process is given in Figure 2a. As can be seen from the figure, there are phase errors needed to be eliminated. After applying proposed adaptive algorithm, corrected unwrapping result is obtained as shown in Figure 2c. Figure 2b and Figure 2d indicate selected row data from 3-D images on left.

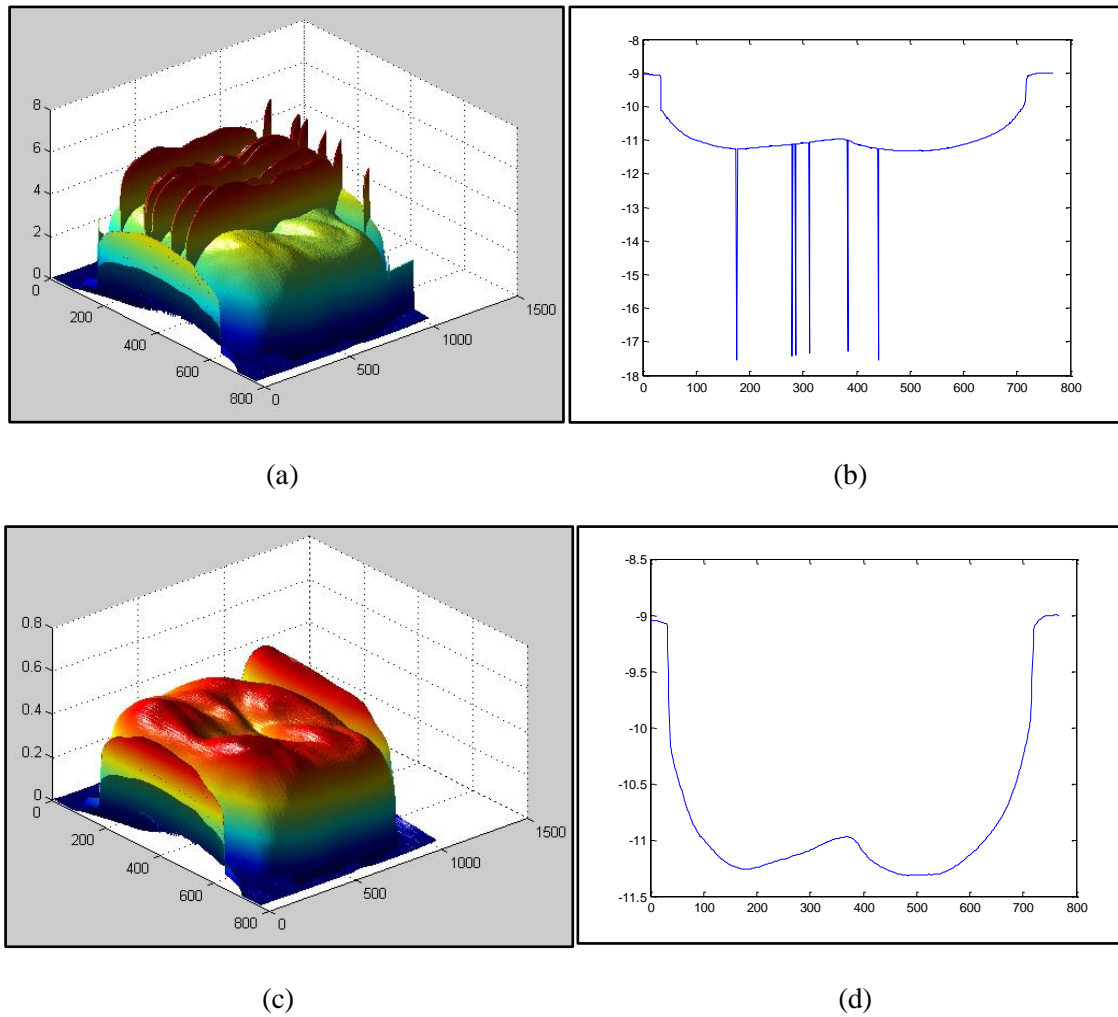


Figure 2. Results obtained with and without the proposed algorithm. a-b) 3-D image and selected row data of it obtained without proposed method. c-d) 3-D image and selected row data of it obtained with proposed method.

3. System Setup And Calibration

In order to obtain a 3-D surface profile of the physical object models by applying the phase shift method, a system consisting of a projector, a computer and a camera has been established.

3.1. System Setup for Acquiring Real Data

The system setup, shown in Figure 3, includes a light commander (DLP), an industrial camera and two laptops. Test system is set to obtain 3-D information of a white object which is placed in a 30 x 30 cm view area and 50 cm far from the system plane. Resolution of the camera is 5MP, it has noise cancellation ability, and image capture speed is 120 fps. The angle between the camera and projector is adjustable with a special platform. The generated fringe patterns are projected via a laptop, and the projected images are recorded via another one.



Figure 3.System setup.

There are corruptions in the images captured by the optical test system because of the optical reasons, light effects, and the surface characteristics of the real object. In Figure 4, the light profile captured from the surface and reconstructed 3-D surface using this profile is shown. It is significant that an unwanted slope occurs on the reconstructed 3-D surface, so the calibration process described in the following section is applied to eliminate such type of distortions.

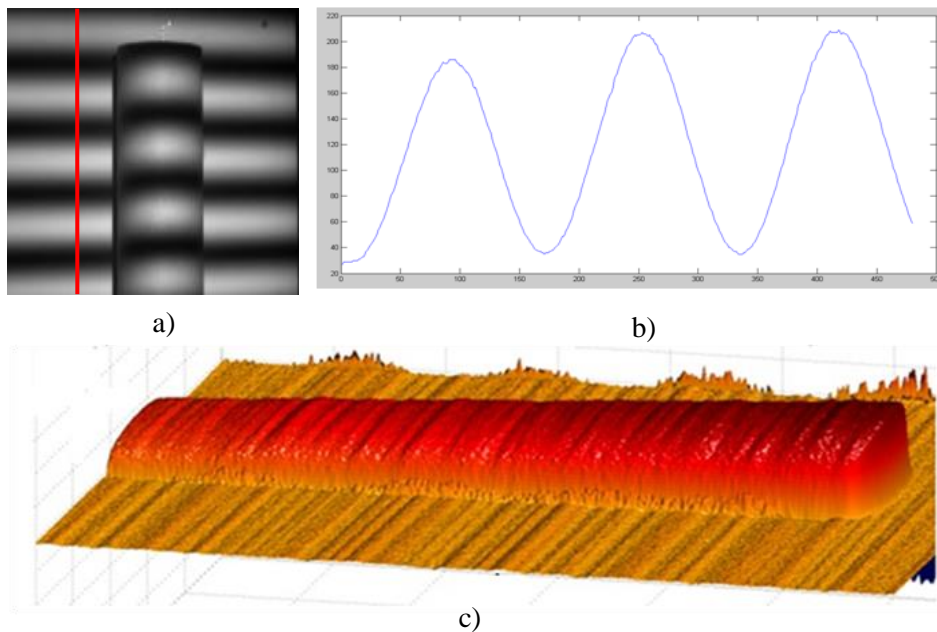


Figure 4. An example of light disturbances: a) Fringe image, (b) Cross-sectional light distribution profile on the plane, (c) Reconstructed 3-D object.

3.2 Lookup Table-Based Calibration Algorithm

In order to reconstruct the 3-D object accurately and also to achieve high performance from any phase unwrapping algorithm, it is very important to obtain the sinusoidal fringe patterns properly, so the system needs to be calibrated. In

this study, both real and synthetic data are used. While the real data is obtained through the established system, the synthetic data is obtained by using the 3-D CAD program. For the synthetic data, there is no need for system calibration because the fringe patterns can be accurately obtained. Since there may be obvious differences between the sinusoidal fringe patterns captured on the plane and generated from the light modulator, a lookup table-based calibration algorithm is proposed based on the adjustment of gray level values to make the fringe pattern on the plane ideally sinusoidal [17]. Figure 5 shows the block diagram of the lookup table-based calibration algorithm.

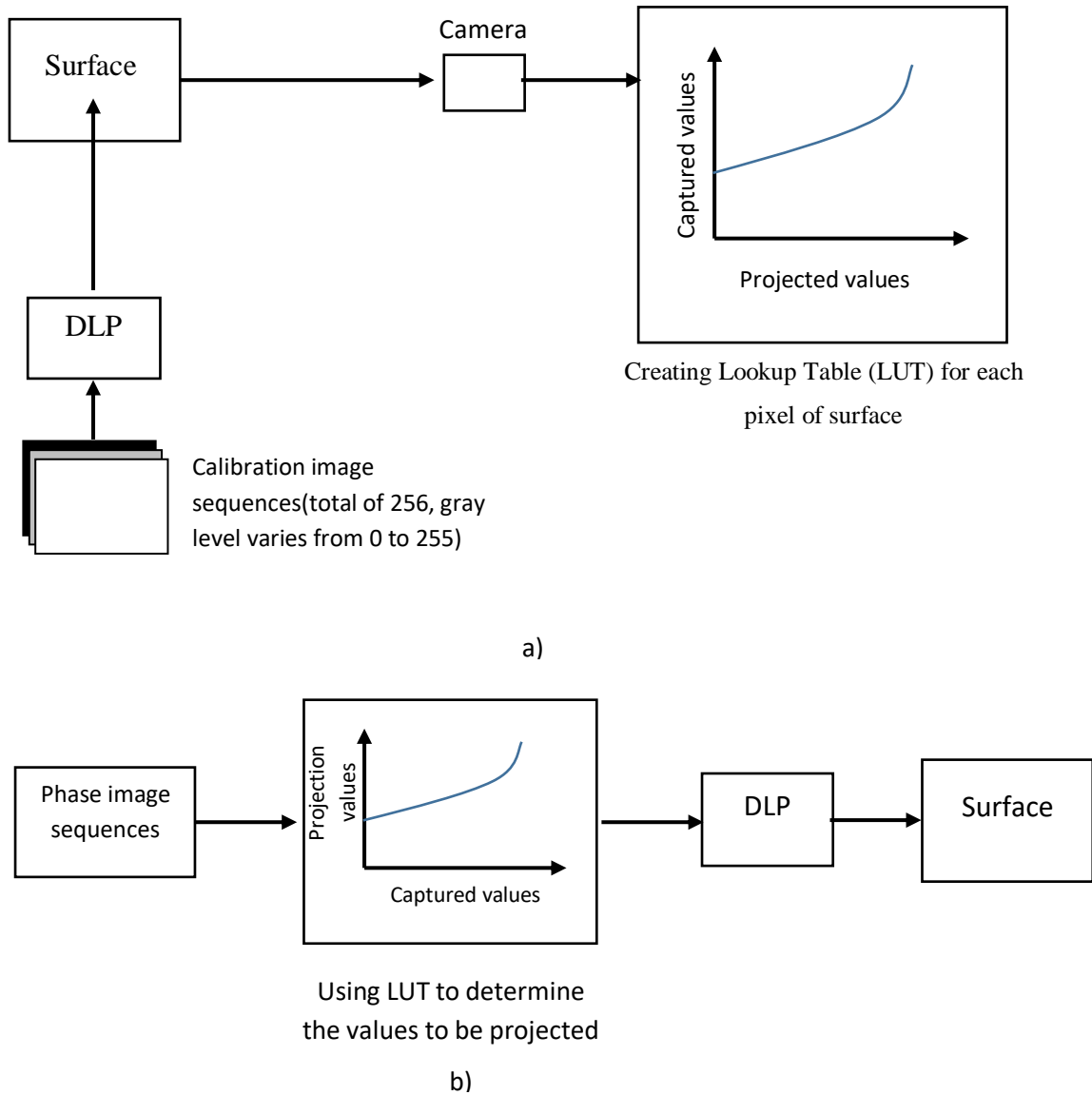


Figure 5. Lookup table-based calibration algorithm: a) Creating the LUT, b) Using the LUT for phase image projection

Although the camera used in the setup meets the focusing requirement in the specified range, lens distortions affect the system as well as in all camera systems. The MATLAB Camera Calibration Toolbox [18] is used to eliminate these lens distortions, which usually occur at the edges of the lens rather than the center. The calibration process is completed by projecting the chessboard pattern on the plane and obtaining the distortion pattern of the lens according to the reference pattern. After determining the distortion model for the lens, this distortion model is applied inversely to obtain a corrected

image. The light Commander Module can produce different calibration patterns, so that the calibration procedure may be performed easily.

Since the reference object used in the system is in the center of the image plane and is small enough to be exposed to less camera distortions, projection-induced distortions emerge as a more important problem than camera-induced distortions. Un-calibrated projector-induced distortion effects appear as an undesirable tilt and undulations on reconstructed objects as shown in Figure 4. Therefore, in addition to the camera calibration, the projection system (Light Commander) must also be calibrated.

Projector-related limitations are generally related to the fact that the reference pattern gray level is practically not achieved in the 0-255 range uniformly. This results in data loss and fluctuations on objects due to rounding the same value in a given range of levels in 3-D reconstruction.

The system is capable of linear operation in the gray-level sensitivity range from 50 to 160. The first step to eliminate this problem is to set the gray-level values of the patterns to this gray-level range. The system also points out that the slope in the light profile is caused by the lens of the projector optics. In order to solve these problems, a distortion function made by the projector lens for each pixel should be determined. For this purpose, a greyscale test image sequence is generated, each of which has the same values between 0 and 255. These images are then sequentially projected onto the object-free surface. A MATLAB-based algorithm which calculates the lookup table value to obtain the required reference image is developed. In this algorithm, the values required for each pixel and the values generated by the projection system are calculated by matching with a lookup table-based method, and this is applied to the reference pattern. Thus, the desired image is obtained, and unwanted tilts (or slopes) in the light profile can be largely eliminated. The flow chart of the algorithm is given in Figure 6.

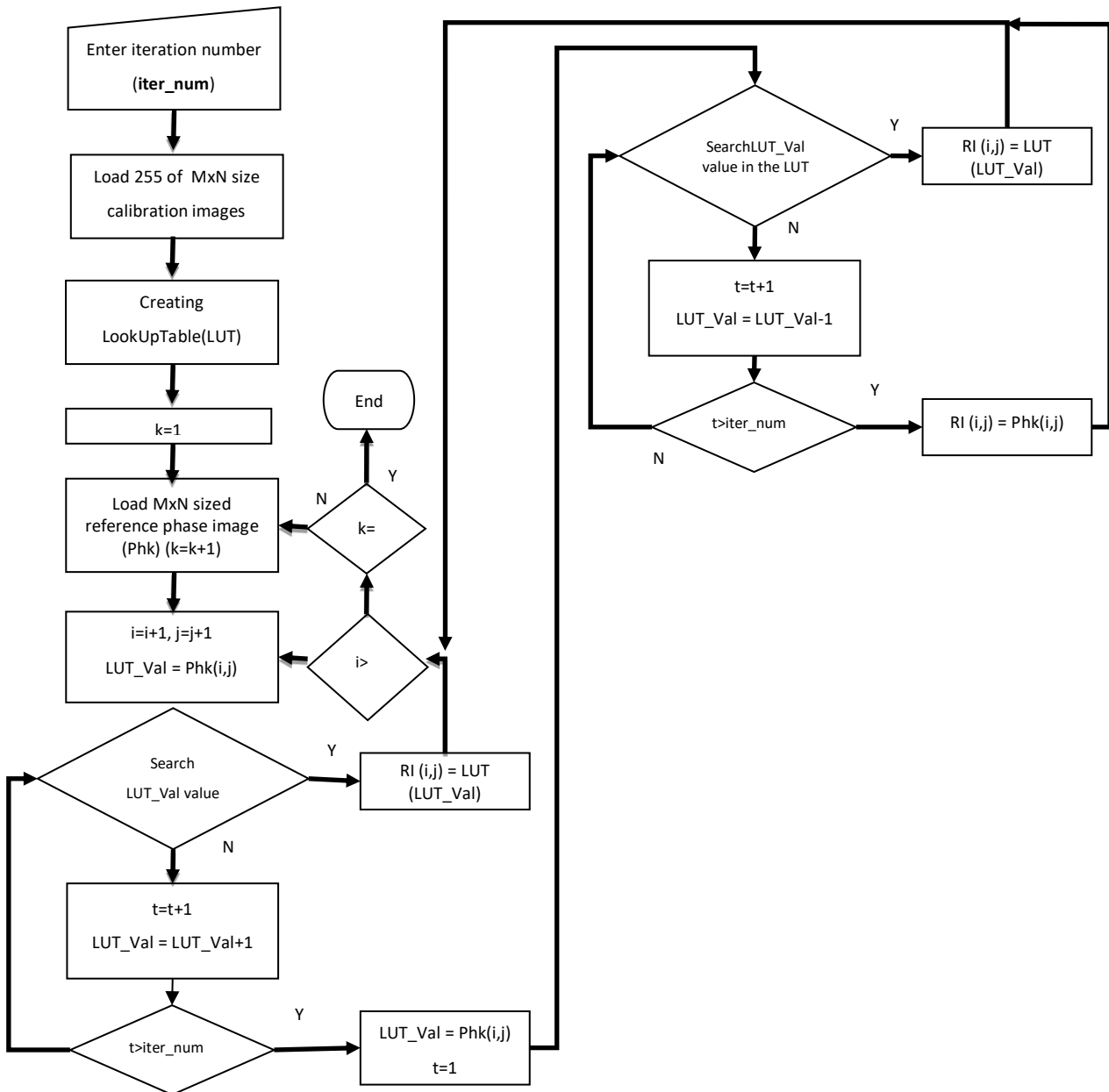


Figure 6. Algorithm flowchart.

The reference pattern obtained by using the proposed algorithm and the corrected phase pattern are shown in Figure 7.

This algorithm is needed to perform the calibration process before the first use of the system.

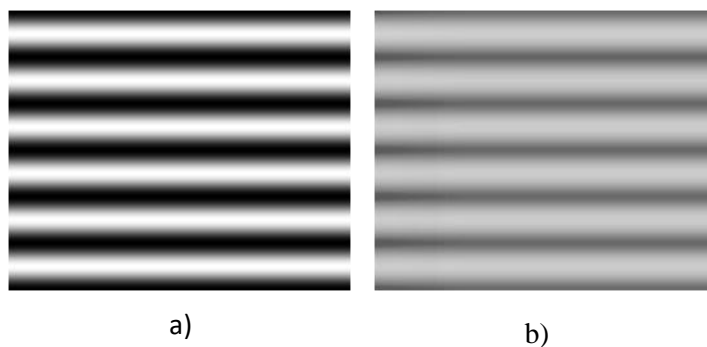


Figure 7. Result of proposed calibration algorithm: (a) Reference phase pattern, (b) Corrected phase pattern resulted from proposed algorithm to obtain reference pattern of (a).

4. Simulation Results

In the simulation studies, the proposed algorithm are tested with synthetic data containing phase images of 3-D object models. Synthetic object model (tooth model) samples are created in the Mudbox (trial version) program on the computer, and these models are transferred to the 3D Studio Max (trial version) scene to simulate the optical system setup. All the images used in this setup have 1024x768 pixels resolution. In order to obtain phase images, phase shifted fringe patterns are produced in MATLAB and then transferred to 3D Studio Max scene. By determining the angle between camera and light modulator, fringe patterns are projected onto the 3-D object models. All of four phase shifted fringe patterns (0, 90, 180 and 270 degree) are projected successively. The camera in the virtual optic setup captures modulated fringe patterns which are reflected from 3-D object model, then wrapped phase image is obtained by using four-step phase shifting algorithm technique. This wrapped phase image is unwrapped using the proposed method, and 3-D data is obtained. Figure 8 and Figure 9 show the original 3-D object models, the wrapped phase images, and the reconstruction results obtained by proposed method, respectively.

For the reconstruction of the image, 1-D phase unwrapping process is applied to the columns of the wrapped phase image, and the scaling factor [19] is used in order to transform the unwrapped phase values into the 3-D data (height) values. The resulting 3-D data consist of a tilt because of the carrier frequency f_0 , which is mentioned in Equation 3 and needs to be eliminated to obtain tilt-free 3-D data. As shown in Figure 10, this is done by subtracting the unwrapped phase image of the reference plane from the unwrapped phase image of object.

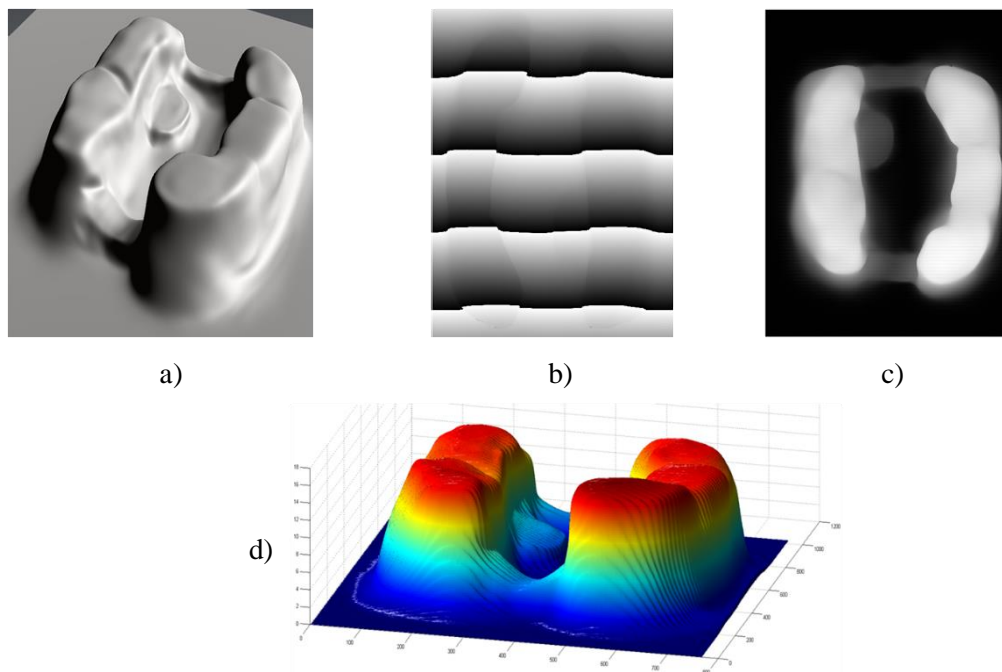


Figure 8. Four step phase shifting result for proposed method: (a) Original synthetic 3-D object model-1, b) Wrapped phase image, (c) Phase unwrapped and tilt removed result, (d) 3-D reconstruction result.

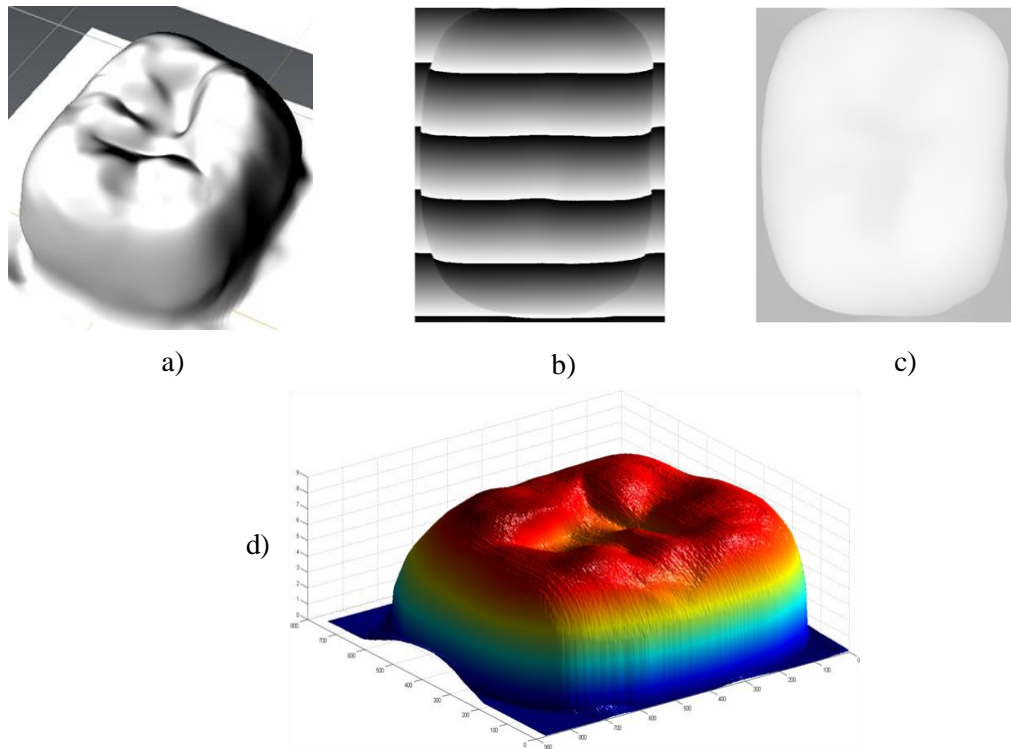


Figure 9. Four step phase shifting result for proposed method: (a) Original synthetic 3-D object model-2, b) Wrapped phase image, (c) Phase unwrapped and tilt removed result, (d) 3-D reconstruction result.

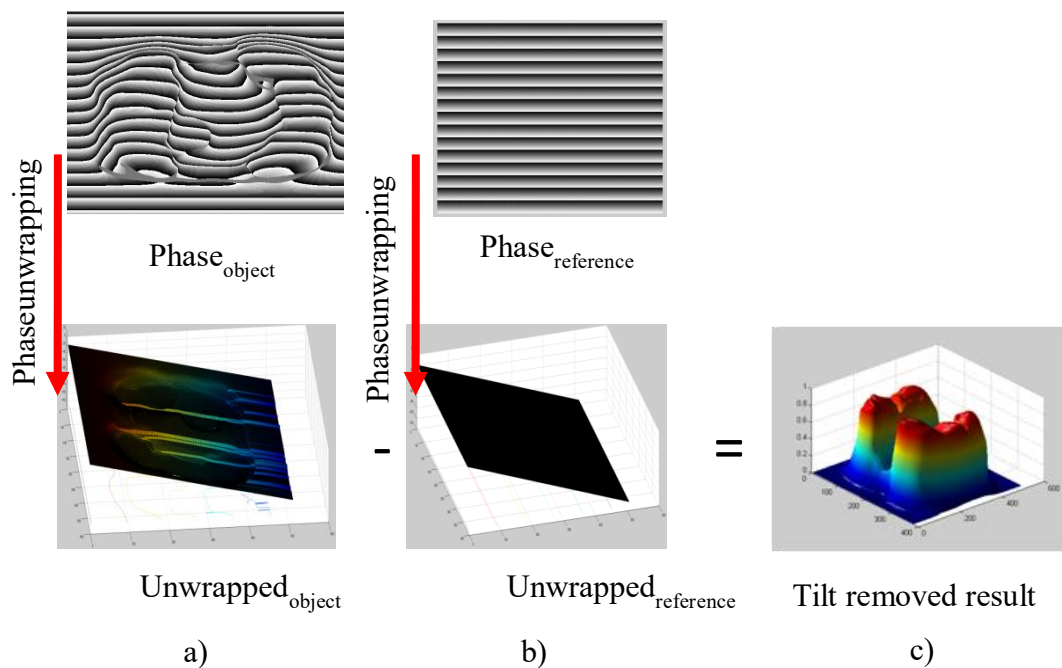


Figure 10. Tilt removing from the 3-D data: (a) Resulting image of 1-D unwrapping process to wrapped phase image, (b) Resulting image of 1-D unwrapping process to reference plane, (c) Unwrapped object with tilt removed.

In order to compare the performance of the proposed method with known methods, comparisons are made in this study with both synthetic and real data. In the tests, to determine the system angle and the number of fringes to be used, some analyses are made. Since using lower fringe numbers results in higher sensitivity and less edge noise, the fringe number

8 is chosen for all tests. The selection of the projection angle is another important issue; and at higher angle values, shadows are formed in the fringe image; and therefore, a lot of important phase information is lost. At low angles, it is observed that notches are formed on the obtained surface but can be removed with a smoothing filter. An angle of 5 to 10 degrees determined to be the right choice for the system angle for best performance.

For comparison, phase test data set consisting of 4 synthetic and 2 real data are processed with classical unwrapping (Itoh method [20]), Goldstein unwrapping method [21], Zhao’s method [11], and the proposed method, and the results are presented in Figure 11. In the test process, the data and other operations are the same for all methods, but there is a difference only in terms of the unwrapping method.

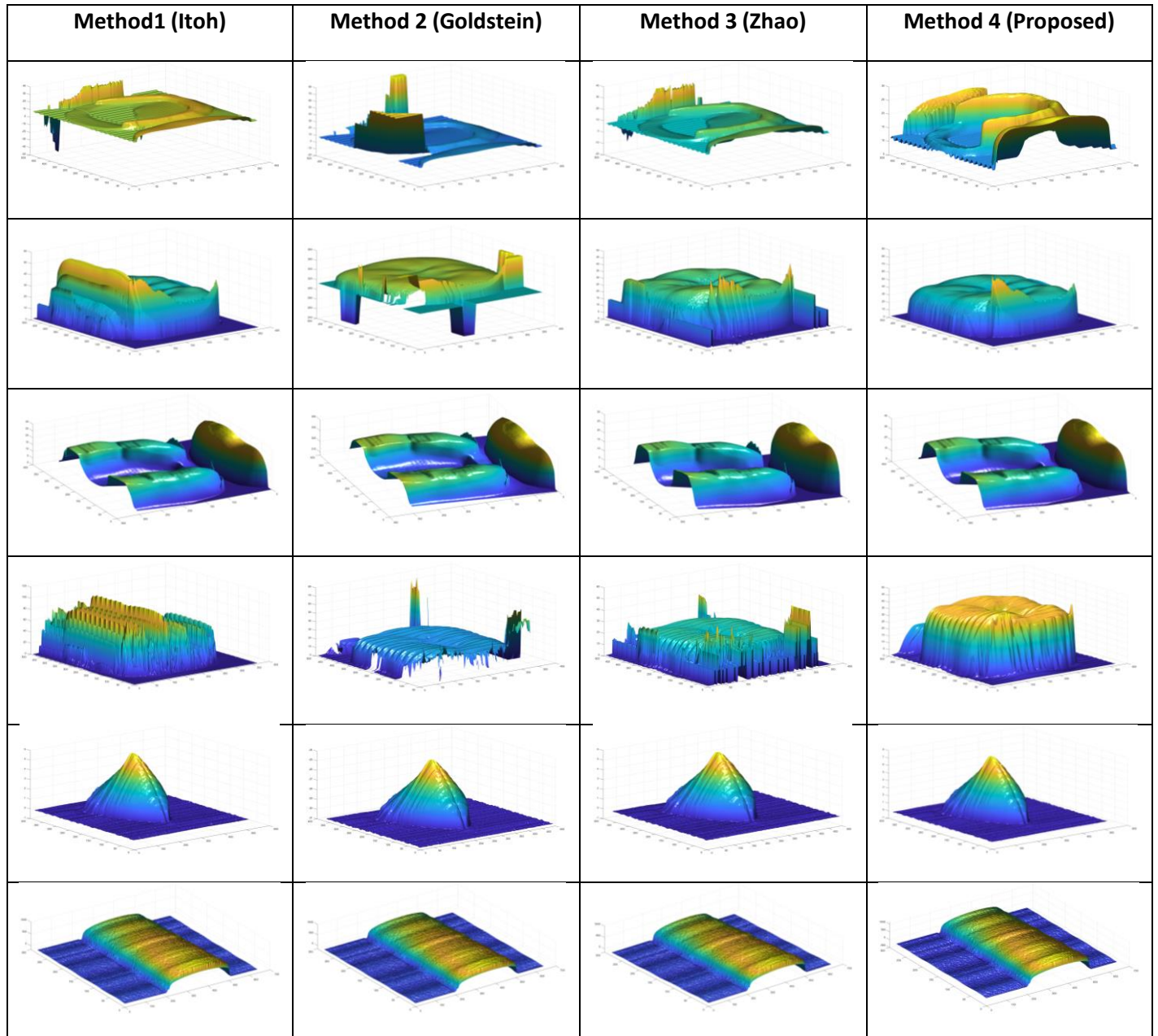


Figure 11. Comparison of the proposed method with the methods of Itoh, Goldstein, and Zhao. The first 4 rows show the results for the synthetic data, and the last two rows show the results for the real data. From left to right, the first column shows the results obtained by Itoh’s method, the second column refers to Goldstein’s and the third column to Zhao’s methods, respectively, while the last column reveals the results obtained by the proposed method.

The simulations in the study are done with a laptop of Pentium Core i5 3 GHz processor, 8.0 GB RAM, and the MATLAB version is 2019b. Except for the Goldstein algorithm, other algorithms obtain the results under 1 second, while the Goldstein algorithm has an average of 10 seconds to obtain the result. The Quality Guided unwrapping method [22] is also used in the study; however, this method needs a user input for the correct phase information, and the unwrapping process takes quite a long time (over 6 minutes). Therefore, it is not included in the comparison results.

When the results are compared visually, it is seen that all algorithms produce the same correct result for real data. While obtaining the phase image of the real data, the lookup table-based calibration algorithm developed in this study is used. Since the fringe data is obtained properly and relatively simple objects are used, it seems normal to achieve this success. However, when the results obtained by using the phase images of complex artifacts, which are taken as properly calibrated, are compared, it is seen that the proposed method achieves very good results compared to the other 3 methods. Window size is selected as 10% of image size, and threshold value is selected as 20% of local gray (phase) value for all the phase images.

5. CONCLUSION

A new local adaptive phase correction algorithm based on phase shifting method for 3-D reconstruction applications is presented in this study. While the method developed for the phase unwrapping process in this study is applied as modifications of the results of the basic phase unwrapping technique, other methods such as Goldstein, Quality Guided, and Least Squares [23] make some changes on the phase data before applying the unwrapping process.

For this reason, Itoh and Zhao's methods, which have similar approaches, seem to be more important in terms of comparisons. Although the fastest method is Itoh's method, robustness of this method is notably low. Therefore, there is not much difference between Zhao's and Goldstein's methods in terms of obtaining reliable results, yet the Goldstein method has the disadvantage of long processing time. The proposed method is both fast like the Itoh's and Zhao's methods and more reliable than the other methods compared. For reconstructed 3-D data, Z_{\min} is -0,5077, and Z_{\max} is 8,0483, and the difference between two consecutive points is 0,0020. This means that 8,54 mm object can be reconstructed with 2 μm sensitivity in the physical setup.

In recent years, superior results have been obtained thanks to the technical developments in 3-D profilometry systems. On the other hand, phase shift profilometry systems are still an area of interest due to their advantages of fast operation, hardware simplicity, low cost, and simultaneous multi-measurement features. The proposed algorithm adaptively corrects the raw phase data for phase shifted system. As the simulation studies show the result that proposed method has an efficient execution time and low complexity, it is thought that it can be used in real-time applications.

References

- [1] R.Zhao, H.Lu, M.Zhao, and C.Sun, "Surface Profiling Using a Modified Shadow Moire Technique", 11th Int. Symposium on, Advanced Packaging Materials: Processes, Properties and Interface, 151-154, 2006.
- [2] W.Chen, X.Su, Y.Cao, Z.Qc, and L. Xiang, "Method of Eliminating Zero Spectrum in Fourier Transform Profilometry", Optics and Lasers in Engineering, vol.43, pp1267-1276, 2005.
- [3] Y.Ichioka, and M. Inuiya, "Direct Phase Detection System", Applied Optics, 11:1507-1514, 1972.
- [4] P.S. Huang, and H. Guo, "Phase shifting shadow moiré using the Carré algorithm", Proceedings of Spie,7066:1-7, 2008.
- [5] Yicheng Zhao, Wenxiang Yan, Yuan Gao, Zheng Yuan, Zhi-Cheng Ren, Xi-Lin Wang, Jianping Ding , and Hui-Tian Wang, "High-Precision Calibration of Phase-Only Spatial Light Modulators", IEEE Photonics Journal, 14(1), 2022
- [6] J. Tang et al., "Local Phase Correction Method Based on Multi-Frequency Phase Heterodyne", 26th International Conference on Automation and Computing (ICAC), pp. 1-6, 2021.
- [7] Z. Zheng, J. Gao, J. Mo, L. Zhang and Q. Zhang, "A Fast Self-Correction Method for Nonlinear Sinusoidal Fringe Images in 3-D Measurement", IEEE Transactions on Instrumentation and Measurement, 70, 1-9, 2021
- [8] Limei Song et al, "Structured-Light Based 3D Reconstruction System for Cultural Relic Packaging", Sensors, 18(9), 1-13, 2018.
- [9] Y. Zhang, D. L. Lau and Y. Yu, "Causes and Corrections for Bimodal Multi-Path Scanning With Structured Light", CVPR, 4426-4434, 2019,
- [10] Wei Feng, Junhui Gao, Tong Qu, Shiqi Zhou and Daxing Zhao, "Three-Dimensional Reconstruction of Light Field Based on Phase Similarity", Sensors, 21, 1-12, 2021.
- [11] Zixin Zhao et al, "Robust 2D phase unwrapping algorithm based on the transport of intensity equation", Measurement Science and Technology, 30, 015201, 2019
- [12] H. Zhang, and H. Su "A Phase Unwrapping Algorithm for 3D Reconstruction", SPND'07, 611-615, 2007.
- [13] G.S. Siva, and L.K. Rao, "New Phase Unwrapping Strategy for Rapid and Dense 3D Data Acquisition in Structured Light Approach", 5th Int. Workshop on Automatic Processing of Fringe Patterns, Stuttgart, Germany, 2005.
- [14] H.B. Wu, Y. Chen, M. Y. Wu, C. R. Guan, and X. Y. Yu, "3D Measurement Technology by Structured Light Using Stripe-Edge-Based Gray Code", Journal of Physics Conference Series, 48:537-541, 2006.
- [15] P. Wissmann, R. Schmitt, and F. Forster, "Fast and accurate 3D scanning using coded phase shifting and high speed pattern projection", IEEE Conf. on 3DIMPVT, 108-115, 2011.
- [16] D. Ghiglia and M. Pritt, "Two-dimensional phase unwrapping theory, algorithms and applications", John Wiley & Sons, 1998.
- [17] J. Geng, "Structured-light 3D surface imaging: a tutorial", Advances in Optics and Photonics, 3:128-160, 2011.
- [18] Internet: "Camera Calibration Toolkit for Matlab", <https://www.vision.caltech.edu/bougetj/calib.doc>.

- [19] B.A. Rajoub, D.R. Burton, and M.J.Lalor “A new phase-to-height model for measuring object shape using collimated projections of structured light”, *Journal of Optics A: Pure and Applied Optics*, 4:368-375, 2005.
- [20] K. Itoh, “Analysis of the phase unwrapping problem,” *Applied Optics*, (21):14,2470,1982.
- [21] R. Goldstein, H. Zebker, C. Werner, “Satellite radar interferometry—two-dimensional phase unwrapping”, *Radio Sci.*, 23(4), 713–720, 1988
- [22] Ming Zhao, Lei Huang, Qican Zhang, Xianyu Su, Anand Asundi, and Qian Kemao, “Quality-guided phase unwrapping technique: comparison of quality maps and guiding strategies, ” *Appl. Opt.*, 50, 6214-6224, 2011.
- [23] M.D.Pritt, “Comparison of Path-Following and Least-Squares Phase Unwrapping Algorithms”, *IEEE Conf. on IGARSS*, 2:872-874, 1997.